

# Facies-based rock properties distribution along the Harvey 1 stratigraphic well

Claudio Delle Piane<sup>1</sup>, Hugo K.H. Olierook<sup>2</sup>, Nick E. Timms<sup>2</sup>, Ali Saeedi<sup>2</sup>, Lionel Esteban<sup>1</sup>, Reza Rezaee<sup>2</sup>, Vassili Mikhaltsevitch<sup>2</sup>, Stefan Iglauer<sup>2</sup>, Maxim Lebedev<sup>2</sup>

<sup>1</sup>CSIRO Earth Sciences and Resource Engineering, PO Box 1130, Kensington WA 6151, Australia

<sup>2</sup>Curtin University, GPO Box U1987, Perth, WA 6845, Australia

Final project report EP133710

June 2013

Australian National Low emissions Coal Research and Development (ANLEC R&D)  
Dr. James Underschultz



Curtin University

### Citation

Delle Piane, C., Olierook, H.K.H., Timms, N.E., Saeedi, A., Esteban, L., Rezaee, R., Mikhaltsevitch, V., Lebedev, Maxim. 2013. Facies-based rock properties distribution along the Harvey 1 stratigraphic well. CSIRO Report Number EP133710

### Copyright and disclaimer

© 2012 CSIRO To the extent permitted by law, all rights are reserved and no part of this publication covered by copyright may be reproduced or copied in any form or by any means except with the written permission of CSIRO.

### Important disclaimer

CSIRO advises that the information contained in this publication comprises general statements based on scientific research. The reader is advised and needs to be aware that such information may be incomplete or unable to be used in any specific situation. No reliance or actions must therefore be made on that information without seeking prior expert professional, scientific and technical advice. To the extent permitted by law, CSIRO (including its employees and consultants) excludes all liability to any person for any consequences, including but not limited to all losses, damages, costs, expenses and any other compensation, arising directly or indirectly from using this publication (in part or in whole) and any information or material contained in it.





# Contents

Contents .....	i
<b>Acknowledgments</b>	<b>vi</b>
<b>Executive summary</b>	<b>vii</b>
<b>Preliminary Notes</b>	<b>ix</b>
<b>1 Module 1: Sedimentary logging and facies analysis of cored intervals</b>	<b>1.1</b>
1.1 Summary .....	1.2
1.2 Introduction .....	1.2
1.3 Geological Background.....	1.3
1.4 Analytical Techniques/Approach .....	1.5
1.4.1 Core logging .....	1.5
1.4.2 Facies analysis .....	1.5
1.4.3 Sample selection .....	1.7
1.5 Results .....	1.10
1.5.1 Downhole facies distribution .....	1.10
1.5.2 Cumulative and continuous facies thickness .....	1.15
1.5.3 Facies and core gamma comparison.....	1.16
1.6 Discussion.....	1.19
1.6.1 Depositional environment .....	1.19
1.6.2 Cumulative and continuous thickness characteristics of facies .....	1.20
1.6.3 Comparison with the sedimentology of the Lesueur Sandstone in Pinjarra-1.....	1.20
1.6.4 Core gamma and lithofacies .....	1.21
1.6.5 Preliminary feasibility studies .....	1.22
1.7 Conclusions .....	1.22
<b>2 Module 2: Petrographic and mineralogical analysis</b>	<b>2.23</b>
2.1 Summary .....	2.24
2.2 Introduction .....	2.24
2.3 Analytical Techniques/Approach .....	2.24
2.3.1 Thin section preparation.....	2.24
2.3.2 Petrography .....	2.25
2.3.3 Mineralogy: X-ray diffraction .....	2.25
2.3.4 Hylogging™ data interpretation.....	2.25
2.3.5 Quantitative grain size analysis.....	2.26
2.4 Results .....	2.27
2.4.1 Petrography and mineralogy .....	2.27
2.4.2 Diagenetic cements and distribution.....	2.33
2.4.3 Quantitative grain size distribution .....	2.34

2.5	Discussion.....	2.34
2.5.1	Provenance .....	2.34
2.5.2	Diagenesis .....	2.35
2.5.3	Mineral reactions.....	2.37
2.6	Conclusions .....	2.38
<b>3</b>	<b>Module 3: Wireline log analysis of Harvey 1</b>	<b>3.39</b>
3.1	Summary .....	3.40
3.2	Introduction .....	3.41
3.3	Data Collection .....	3.41
3.4	Data Quality Control.....	3.41
3.5	Petrophysical Evaluation .....	3.43
3.5.1	Volume of Shale (Vsh).....	3.44
3.5.2	Porosity .....	3.44
3.5.3	Water Saturation .....	3.48
3.5.4	Pore water resistivity (Rw).....	3.48
3.5.5	Permeability.....	3.49
3.5.6	Porosity and permeability relation .....	3.53
3.6	Summary of Petrophysical Evaluation Results.....	3.54
3.7	Conclusions .....	3.56
<b>4</b>	<b>Module 4a: Petrophysical core plug characterization</b>	<b>4.57</b>
4.1	Summary .....	4.58
4.2	Introduction .....	4.58
4.3	Analytical Techniques/Approach .....	4.58
4.3.1	X-ray Computer Tomography .....	4.58
4.3.2	Core porosity and permeability .....	4.58
4.4	Results .....	4.60
4.4.1	X-ray CT .....	4.60
4.4.2	Helium porosity and Permeability .....	4.60
4.4.3	Mercury injection porosimetry .....	4.63
4.4.4	NMR .....	4.65
4.4.5	NMR porosity and permeability.....	4.66
4.5	Discussion and conclusions .....	4.67
<b>5</b>	<b>Module 4b: Core Flooding</b>	<b>5.71</b>
5.1	Summary .....	5.72
5.2	Introduction .....	5.72
5.3	Experimental Techniques.....	5.72
5.3.1	Material.....	5.72
5.3.2	Experimental conditions .....	5.75

5.3.3	Experimental apparatus.....	5.75
5.3.4	Experimental procedure .....	5.77
5.4	Results and discussion.....	5.80
5.4.1	Sample 206647 .....	5.81
5.4.2	Sample 206660 .....	5.83
5.4.3	Sample 206669 .....	5.84
5.4.4	Shale Disk 1 .....	5.85
5.5	Summary and Conclusions .....	5.86
<b>6</b>	<b>Module 5a Geomechanical-ultrasonic core plug characterization</b>	<b>6.91</b>
6.1	Summary .....	6.92
6.2	Introduction .....	6.92
6.3	Analytical Techniques/Approach .....	6.92
6.3.1	Geomechanical tests.....	6.92
6.3.2	Ultrasonic tests .....	6.96
6.4	Results .....	6.97
6.4.1	Mechanical data.....	6.97
6.4.2	Rock physics data.....	6.101
6.5	Discussion.....	6.104
6.5.1	Mechanical behavior.....	6.104
6.5.2	Vp Vs relationships from the laboratory compared with empirical regression lines .....	6.105
6.5.3	Elastic wave velocities: Log and Lab .....	6.106
6.5.4	Gassmann Fluid substitution .....	6.107
6.6	Conclusions .....	6.109
<b>7</b>	<b>Module 5b Low-frequency laboratory measurements of samples from Harvey 1.</b>	<b>7.111</b>
7.1	Summary .....	7.112
7.2	Apparatus .....	7.113
7.3	Method and operation.....	7.115
7.4	Measurement Results .....	7.117
7.4.1	Description of samples.....	7.117
7.4.2	Sample 206603 (Yalgorup Member) .....	7.118
7.4.3	Sample 206642 (Yalgorup Member) .....	7.120
7.4.4	Sample 206663 (Wonnerup Member).....	7.121
7.4.5	Sample 206664 (Wonnerup Member).....	7.123
7.5	Discussion and conclusions .....	7.125
<b>8</b>	<b>Summary and conclusions</b>	<b>8.135</b>
	<b>Appendix A</b>	<b>8.139</b>
	<b>Appendix B</b>	<b>8.140</b>

<b>Appendix C</b>	<b>8.141</b>
<b>Appendix D</b>	<b>8.142</b>
<b>Appendix E</b>	<b>8.143</b>
<b>Appendix F</b>	<b>8.144</b>
<b>Appendix G</b>	<b>8.147</b>
Yalgorup samples.....	8.147
Wonnerup samples .....	8.148
<b>References</b>	<b>Error! Bookmark not defined.</b>





# Acknowledgments

The authors would like to acknowledge contributions to the South-West Hub Flagship project by the Western Australian Department of Mines and Petroleum (including the Geological Survey of Western Australia), the Western Australian Royalty for Regions Program and the Commonwealth Department of Resources, Energy and Tourism. The authors wish to acknowledge financial assistance provided through Australian National Low Emissions Coal Research and Development (ANLEC R&D). ANLEC R&D is supported by Australian Coal Association Low Emissions Technology Limited and the Australian Government through the Clean Energy Initiative.

The authors would like to thank Geotechnical Services PTY LTD for laying out of the cored intervals and granting access to their facility for the sedimentary logging of the cores; GSWA, in particular Arthur Mory and Alan Millar, for supplying core gamma, XRD mineralogy, mercury injection and well log data in support of this project and for sharing their geological expertise in front of the cores. Lena Hancock, Department of Mines and Petroleum, is thanked for her expertise in quality checking the Hylogger data.

Discussions and cooperation with colleagues in and out of CSIRO made the development and completion of this project possible, particular gratitude goes to Linda Stalker and Cedric Griffiths for their additional efforts on the internal review of the report.

We also would like to acknowledge the help from Weatherford Petroleum Consultants for granting us the access to their core-flood interpretation software package, Sendra.

The experimental program would not have been possible without the meticulous attention and technical support of Shane Kager, David Nguyen, Leigh Kiewiet and Bruce Maney at CSIRO.

Finally, gratitude goes to Jim Underschultz, Sandeep Sharma and Mohammad Bahar for their comments and suggestions leading to the final version of the report.

# Executive summary

The South West CO<sub>2</sub> Geosequestration Hub project (the SW-Hub) consists of a public and private partnership linking the Western Australia State government and the major industrial emitters of CO<sub>2</sub> in the region. The potential geosequestration site is located in a deep saline aquifer within the Lesueur Sandstone. It is planned to collect CO<sub>2</sub> from a number of industrial emitters, where the injection masses are expected to be in the order of 6.5 million tonnes per year for the 40 years of active injection part of the project.

In support of the project the Geological Survey of Western Australia (GSWA) drilled an onshore stratigraphic well (GSWA-Harvey-1, hereafter Harvey-1) at 115° 46' 28.4"E and 32° 59' 34.2"S in proximity to the town of Harvey. The well reached a depth of 2945m and was used to collect a series of wireline logs and recover cores for laboratory analyses. In this framework the Australian National Low Emissions Coal Research & Development (ANLEC) provided support for the research and scientific examination of the well data.

The goal of the multidisciplinary work presented here is to help enable and further understand the geological and geophysical parameters that will affect the safe and efficient storage of CO<sub>2</sub> at the proposed SW-Hub site in the Southern Perth Basin. In particular, the areas of interests covered by this work are related to the characterization of the geological units intersected by Harvey-1 in terms of storage capacity; injectivity and containment potential; elastic and mechanical properties and heterogeneity of the formations encountered.

The workflow adopted for this work is composed of a series of work units including:

- Sedimentary logging of the cored sections of the well;
- Petrographic and mineralogical analysis of the sedimentary units and evaluation of their diagenetic history;
- Evaluation of the wireline logs collected from Harvey-1;
- Experimental measurements of the petrophysical properties of core plugs from Harvey 1 and comparison with those from the neighbouring well Pinjarra-1;
- Core flooding of Harvey-1 samples;
- Experimental measurement of geomechanical properties of samples representative of the units intersected by Harvey-1;
- Experimental measurements of elastic properties and their dependency upon stress, fluid content and frequency; and
- Data integration.

The present work feeds into and supports a wider program aimed at the integrated evaluation of the SW-Hub encompassing a detailed analysis of the seismic data available in the region; an assessment of the potential for fault reactivation around the proposed injection area; a study of the possible fluid-rock interactions at reservoir conditions and the forward stratigraphic modelling of the area.

The specific outcomes of this work consist of:

1. A new lithofacies scheme adopted to describe and classify the sedimentary units, their distribution and thickness along the borehole and in the context of the geological history of the Perth Basin;
2. An interpretation of the available wireline logs supported by experimental measurements on core plugs;
3. Comprehensive petrophysical evaluation of the core plugs and interpretation based on the adopted lithofacies scheme;

4. Assessment of relative permeability (to brine and supercritical CO<sub>2</sub>) under in-situ reservoir conditions;
5. Evaluation of the achievable levels of the scCO<sub>2</sub> capillary residual trapping; and
6. Appraisal of geomechanical and elastic properties of the sedimentary units of the Perth Basin.

The outcomes of the work indicate significant differences between the Upper and Lower Members of the Lesueur Sandstone in terms of sedimentology, petrophysical, geomechanical and elastic properties.

Good reservoir properties are recorded in the lower Member (Wonnerup 1380-2895m depth) of the Triassic Lesueur Sandstone with encouraging values of porosity (7 to 19%) and permeability (0.01 to 580 mD) and lithofacies homogeneity with depth. Permeability anisotropy measured in the laboratory can be very significant at the tentatively predicted injection levels: across bedding permeability ranges between 0.01 and 3mD while along bedding permeability ranges between 38-580mD, resulting in anisotropy of up to 3 orders of magnitude. Core flooding tests also give positive indications for residual trapping (25 to 45%) as a principal containment mechanism. However, a marked decrease of permeability (up to 50%) was observed after sample flooding was also inferred from the tests

By contrast the overlying Yalgorup (704-1380m) is far more heterogeneous, and due to poor core conditions of the shaly layers, the characterization work only focused on the sandy intervals and the results cannot be regarded as representative of the whole stratigraphic unit. Uncertainties remain regarding the geomechanical properties and containment potential of the different lithofacies within the Yalgorup. Nevertheless the presence of interbedded sands and shale layers could be beneficial in terms of storage. Also no data have been collected on a further potential seal for the geosequestration site: the Eneabba formation. Further research should be focused on the integrated characterization of the two units to match the level of understanding now attained for the Wonnerup Member.

# Preliminary Notes

The report is organised in chapters describing the analytical approach and results of each work unit; the chapters' sorting reflects the chronological evolution of the project. Each chapter was prepared to be self-standing.

The nomenclature of the samples reflects the identification code provided by GSWA. Formation names and Formation tops are taken from the post-drilling documents circulated by the GSWA. Any reference to sample depth used in this report is based on the indications provided on the casing of the retrieved cores corresponding to measured depth relative to the rotary table (MDRT) provided by GSWA.

Details of the researchers' contributions to the work presented in this report are as follows:

Module 1	Hugo K.H. Olierook, Nick E. Timms, Claudio Delle Piane
Module 2	Hugo K.H. Olierook, Nick E. Timms, Claudio Delle Piane
Module 3	Reza Rezaee
Module 4a	Hugo K.H. Olierook, Lionel Esteban, Claudio Delle Piane
Module 4b	Ali Saeedi, Stefan Iglauer, Claudio Delle Piane, Lionel Esteban
Module 5a	Claudio Delle Piane
Module 5b	Vassili Mikhaltsevitch, Maxim Lebedev



# 1 Module 1: Sedimentary logging and facies analysis of cored intervals

## 1.1 Summary

The Perth Basin consists of rocks that form aquifers and reservoirs and has recently been studied for CO<sub>2</sub> geosequestration. Harvey-1 is a 2945 m deep stratigraphic hole drilled proximal to Harvey (Western Australia), with 6 cored sections totaling 217 m in length. The cored intervals cut through the Yalgorup and Wonnerup Members of the Lesueur Sandstone. The primary objective of the work presented here was to characterize the local sedimentology, using a facies scheme, to assess reservoir and seal thickness and distribution. This informed the selection of samples from a range of facies and depths to be used in subsequent experimental studies. A facies scheme developed for the central Perth Basin was applied to Harvey-1. The Yalgorup Member consists of mixed-thickness, interbedded high to low energy channel-fill facies, and swampy /overbank deposits and palaeosols. The Wonnerup Member consists of thick, continuous, high energy channel-fill facies, with minor intercalations of moderate to low energy channel-fill/stacked rippleforms and rare swampy deposits.

Total intensity core gamma response, in counts per second, was compared to lithofacies interpreted from core logging in order to set parameters for extrapolation to un-cored intervals in Harvey-1. There was a moderate correlation (50-90% probability) between low (10-50) core gamma (coarse-grained sandstones, facies Ai-Aiii), moderate (50-80) core gamma (fine to medium-grained sandstones, facies B-C) and high (70-100+) core gamma (fine sandstones, siltstones, mudstones, facies E-G), in counts per second.

The analysis indicates that the potential reservoir in the Wonnerup Member is continuous and thick. The Yalgorup Member and intercalations may act as a baffles to upwards fluid migration due to the mixed nature of the mudstone and sandstone succession.

## 1.2 Introduction

The Perth Basin comprises rocks that form aquifers and reservoirs and has recently been studied for CO<sub>2</sub> geosequestration. In particular, the South West Hub, near Harvey, has been assessed as a possibility for long term storage of carbon dioxide. Due to poor outcrop geology in the Perth Basin, the site assessment solely relies on geophysical methods and the analysis of sparse core material extracted from deep wells. The stratigraphic hole Harvey-1, drilled in early 2012 near the south west town of Harvey, with a total depth of 2945 m, is the deepest hole the Geological Survey of Western Australia (GSWA) has ever drilled. It was planned to provide subsurface data to support the evaluation of the SW-Hub carbon capture and storage (CCS) Project, the planning of further data acquisition in the area, as well as determining the petroleum and geothermal potential for the South Perth Basin.

Before assessment of petrophysical properties of the buried rocks, such as porosity and permeability, an understanding of the extent and distribution of their geological characteristics is required. Selection of samples from a wide range of rock types and depths can then be made for subsequent petrophysical investigations. The obtained data can then be extrapolated to the geometry and distribution of rock types (facies) in cored sections. An extrapolation of cored intervals to the wireline data of the entire Harvey-1 can then be made to provide an estimate of the porosity and permeability distribution of the Harvey-1 hole.

The first objective of the work presented here was to characterize the local sedimentology, using a facies scheme, to assess reservoir and seal thickness and distribution. The second objective was to select samples from a range of rock types (facies) and depths to be used in subsequent experimental studies. Due to the time and cost constraints, core plug samples are limited to 90 samples.

The results of module 1 include: (a) an evaluation of the geology of the cored sections of Harvey-1, in terms of its reservoir and seal capacities; (b) a selection of sample locations based on a wide variety of rock types (lithofacies) at a range of depths, to be used in subsequent modules; (c) an attempt to correlate core gamma to lithofacies, which may further be used to evaluate the un-cored areas of Harvey-1.



### 1.3 Geological Background

The Perth Basin is a north-south elongate extensional basin stretching along the western coastline of Western Australia between latitudes 27°00'S and 34°30'S (Mory and Iasky, 1996). The basin contains mainly continental clastic rocks of Permian and younger age deposited in a developing rift system that culminated with the breakup of Gondwana in the Late Cretaceous (Mory and Iasky, 1996; Song and Cawood, 2000; Crostella and Backhouse, 2000). During the Permian, the Perth Basin was the eastern half of a rift valley that formed due to extension in a south-westerly direction, with sinistral movement (Song and Cawood, 2000; Crostella and Backhouse, 2000). Extension continued until the Jurassic leading to the central zone subsiding as a series of grabens and half-grabens, with marine ingression and deposition of transgressive marine sediments (Song and Cawood, 2000). During the early Cretaceous, dextral transtension dominated to the northwest (Mory and Iasky, 1996). The Perth Basin architecture is dominated by listric, extensional, north to north-west trending faults that formed during the breakup of Gondwana and controlled the distribution of the sediments, compartmentalizing the Perth Basin into a series of sub-basins (Mory and Iasky, 1996; Song and Cawood, 2000; McPherson and Jones, 2005). It is considered that sedimentation broadly kept pace with accommodation space during faulting and subsidence (Mory and Iasky, 1996).

Harvey-1 is a 2945 m deep stratigraphic hole drilled in February 2012 by GSWA at a location proximal to Harvey, Western Australia (Fig. 1.1a). It has the following coordinates: Lat: 32°59'30.79"S Long: 115°55'39.23"E. The stratigraphy of Harvey-1 has been revised by GSWA after drilling, and consists from top to bottom of unconsolidated sandstone and laterite, the Guildford Formation, the Early Cretaceous Leederville Formation, the Early Jurassic Eneabba Formation, the Late-Middle Triassic Lesueur Sandstone and the Early Triassic Sabina Sandstone (Fig. 1.1b). Formations were identified using correlation from other wells through breaks on the induction-electrical, gamma-ray and sonic logs. Formations and Members are summarized in Table 1.1. A total of 217 m of core was retrieved from 6 intervals in Harvey-1. The cored intervals of Harvey-1 consist of the Yalgorup Member (cores 1-4) and Wonnerup Member (cores 5-6) of the Lesueur Sandstone. Cored depths are summarized in Table 1.2.

Formation	Age	Formation top (m)	
		MDRT	TVDSS
Sandstone and laterite	Quaternary	Start of hole	+24.5
Guildford Formation	Quaternary	5.18	+19.3
Leederville Formation	Early Cretaceous	36	-11.5
Eneabba Formation	Early Jurassic	250	-225.5
Basal Eneabba Shale	Early Jurassic	625	-600.5
Lesueur Sandstone	Late Triassic	704	-679.5
Yalgorup Member	Late Triassic	704	-679.5
Wonnerup Member	Middle Triassic	1380	-1335.5
Sabina Sandstone	Early Triassic	2895	-2870.5
Dry Hole Total Depth		2945	-2920.5

**Table 1.1. Summary of formation tops within Harvey-1 (formation tops provided by Geological Survey of WA). MDRT: measured depth relative to the rotary table; TVDSS True Vertical Depth SubSea.**

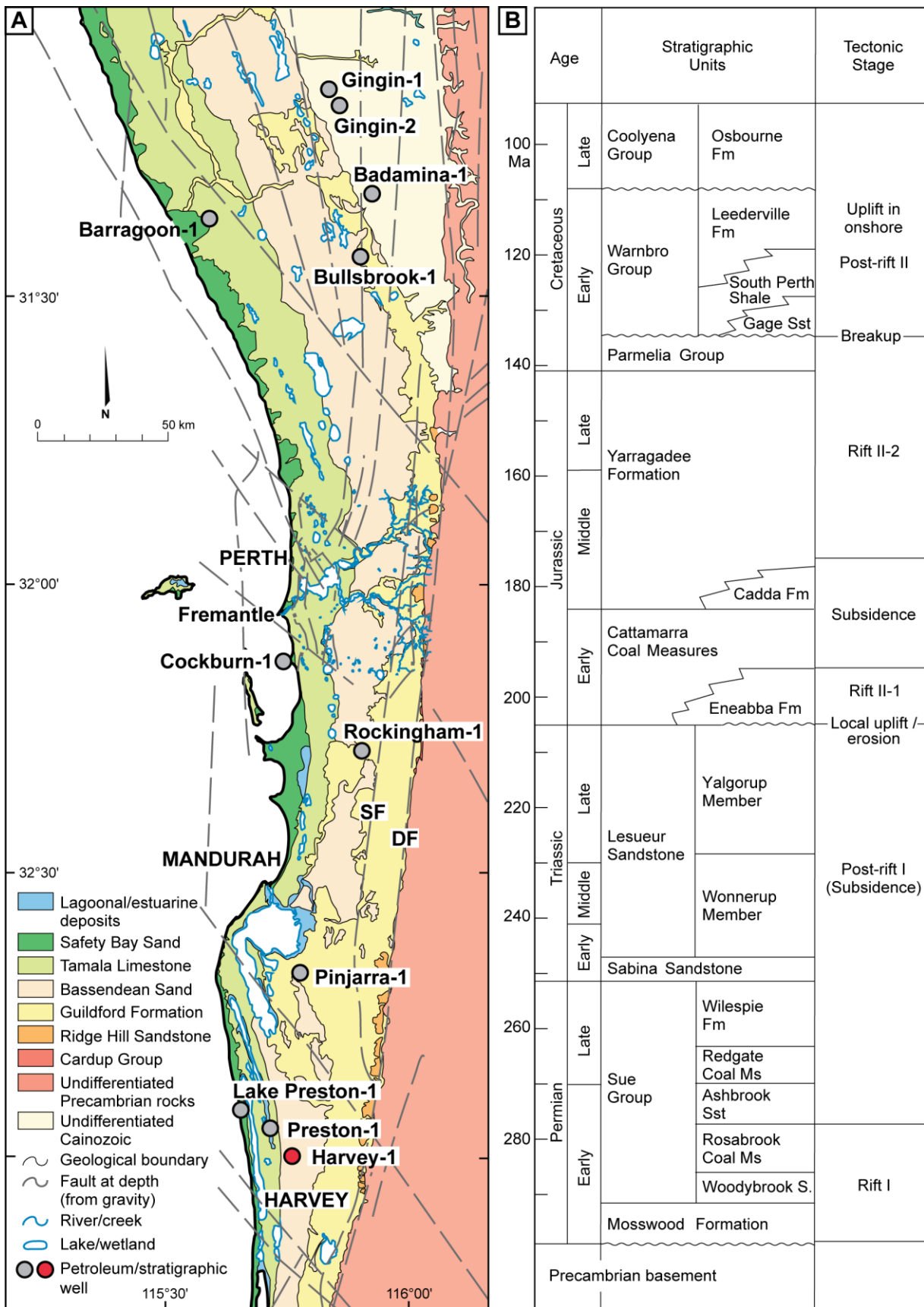


Figure 1.1. (a) Geological map of the central Perth Basin showing the location of onshore exploration wells. Harvey-1 is shown in red. Geology after Playford et al. (1976). 'Faults at depth' control pre-Cretaceous basin architecture and are interpreted from the vertical gradient of isostatic residual gravity, after Wilkes et al. (2011). (b) Generalised stratigraphy of the Perth Basin, after Crostella & Backhouse (2000). Tectonic stages after Song and Cawood (2000).

Core	Member/Formation	Core top heights, below surface (m)		Length (m)
		Start of core	End of core	
1	Yalgorup Mbr (Upper Lesueur Fm)	895	931.5	36.5
2	Yalgorup Mbr (Upper Lesueur Fm)	1266	1319.2	53.2
3	Yalgorup Mbr (Upper Lesueur Fm)	1320	1335	15
4	Yalgorup Mbr (Upper Lesueur Fm)	1336	1344	8
5	Wonnerup Mbr (Lower Lesueur Fm)	1896	1947.7	51.7
6	Wonnerup Mbr (Lower Lesueur Fm)	2480	2532.5	52.5

**Table 1.2. Summary of cored sections within Harvey-1.**

Correlation of stratigraphic surfaces from existing wells in the area and available seismic surveys shows that the Guildford Formation is conformable with the overlying Quaternary sands, but unconformable with the underlying Leederville Formation. The Leederville formation is unconformable with the Eneabba Formation. The Eneabba Formation, Lesueur Sandstone and Sabina Sandstone are conformable.

## 1.4 Analytical Techniques/Approach

### 1.4.1 CORE LOGGING

Preliminary sedimentary logging was initially undertaken at the core shed of Geotechnical Services Pty Ltd (Geotech) on the whole cored section subdivided into 1m segments and removed from its casing prior to slabbing. This helped define sampling locations based on identified lithofacies. The core material from Harvey-1 was then slabbed and had 90 core plugs drilled and then moved to the Core Library of GSWA in Carlisle. Refinement of preliminary core logs on both sections of the slabbed core was done at the Core Library. Sedimentological data was recorded in terms of lithology, colour, sedimentary structures, grain size, sorting, roundness/sphericity, core breaks and additional comments.

The hard copy sedimentary logs were digitized using Adobe Illustrator and subsequently combined into a single, downhole sedimentary log (Appendix A). This visual approach allowed a thorough overview of the sedimentology and facies distribution of the cored sections of Harvey-1.

### 1.4.2 FACIES ANALYSIS

Sedimentary rocks were subdivided into lithologically different facies. Each lithofacies has distinct physical characteristics, such as grain size, sorting, sedimentary structures and colour, so that they are recognisably different in core and/or outcrop. The environment of deposition exerts a primary control on these characteristics and so a lithofacies scheme is commonly interpreted in terms of sedimentary environment. Note that because sedimentary structures have a key role in lithofacies analysis, this approach is generally restricted to observations made in outcrop and drill core rather than drill cuttings. Lithofacies analysis provides a physical property-based rock classification framework and a context for the interpretation of petrophysical tests, such as measurements of porosity and permeability.

Reconnaissance logging and integration with provenance studies of the Perth Basin showed that a braided fluvial-dominated facies scheme fits the sedimentology best (Fig. 1.2) (Miall, 1996; Mory and Iasky, 1996; Cawood and Nemchin, 2000). A braided fluvial-dominated facies scheme developed by Miall (1996) was modified for the logging of other wells in the Perth Basin (Cockburn-1, Gingin-1, Gingin-2 and Pinjarra-1) and was subsequently applied to Harvey-1 (Timms et al., 2012). Nine distinct lithofacies were identified, as shown in Fig. 1.3:

Ai – High energy channel fill, commonly cross bedded, gravelly to very coarse sandstone;

Aii – High energy fluvial channel barforms, medium to very coarse cross bedded sandstone with significant grain size variation between beds;

Aiii – Fluidized fluvial barforms, massive, coarse sandstone;

B – Moderate energy fluvial barforms, massive, medium sandstone with flaser cross lamination;

C – Moderate to low energy stacked rippleforms, fine to medium cross laminated sandstone, with common organic fragments and flaser-drapes;

D – Floodplain palaeosols (often vertisols), fine to medium homogenized sandstone with rootlets, desiccation cracks and slickensides;

E – Swampy/lagoonal deposits, under waterlogged conditions, muddy bioturbated sandstone with slumps and dewatering structures;

F – Crevasse splays and overbank deposits, interbedded silty fine sandstone and siltstone with trough cross lamination;

G – Swampy/ overbank deposits, muddy laminated silt with plant fragments and thin laminated fine sandstone.

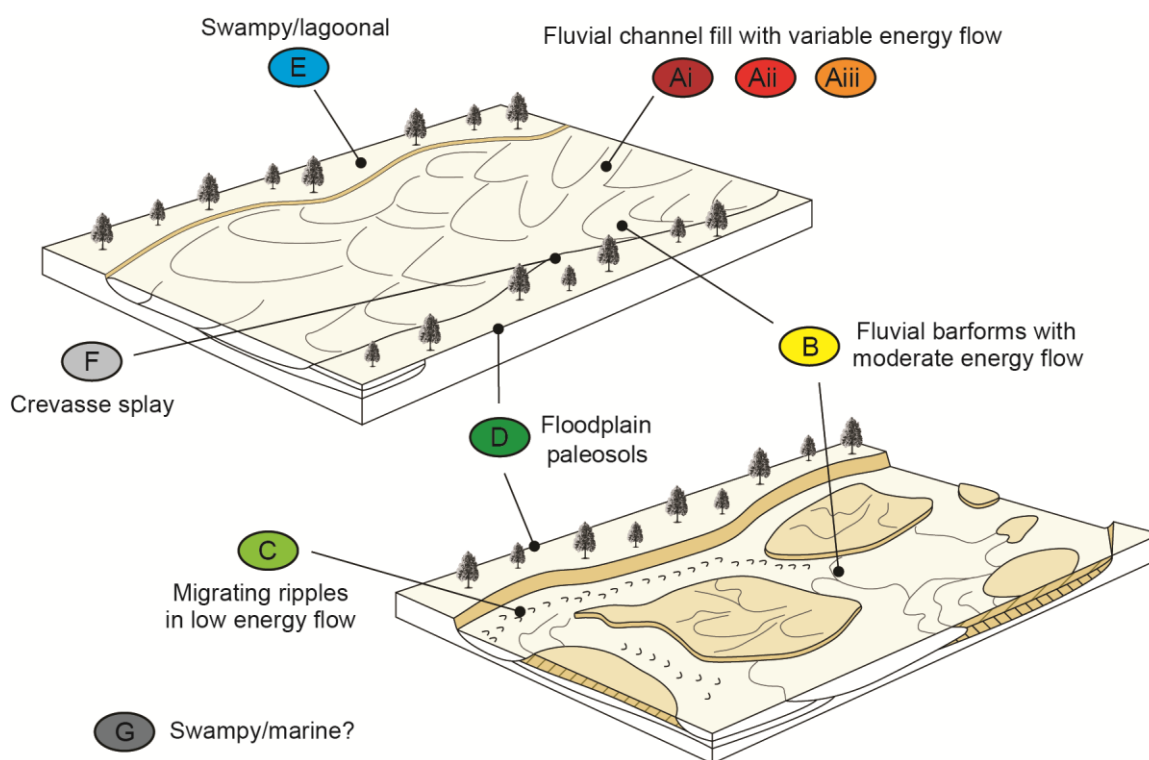


**Figure 1.2. Block diagrams to illustrate the sedimentary depositional environment and architecture of lithofacies Ai-G. After Miall (1996).**

The facies data was processed to determine statistical characteristics of facies in Harvey-1, including: (a) the downhole facies distribution; (b) the cumulative thickness per facies; (c) the continuous thickness per facies, and; (d) the characteristics of core gamma response for each facies type. These data will provide a useful comparison to well log analysis and important inputs for flow and sedimentary modeling.

Finally, the distribution of lithofacies in Harvey-1 core was compared with that of the Lesueur Sandstone in the Pinjarra-1 well, approximately 42 km to the northwest. Pinjarra-1 is a 4572 m deep petroleum exploration well drilled proximal to Pinjarra, Western Australia (Fig. 1.1). It intersects the Eneabba Formation between 1192-2361 m below sea level and the Upper Triassic Lesueur Sandstone between 2361-

4562 m below sea level (Jones and Nicholls, 1966). Core from Pinjarra-1 totaled 60 m from 28 intervals (with ~150 m spacing), and spans the Lesueur Sandstone, Eneabba Formation and Cattamarra Coal Measures. A lithofacies analysis of Pinjarra-1 core is given in Timms et al. (2012).

### **1.4.3 SAMPLE SELECTION**

Sample locations were selected targeting all facies identified during core logging, across a wide range of depths. Samples were also selected at locations where the integrity was deemed to be cohesive when plugged. A sample catalogue may be found in Appendix B. Samples localities were also marked on the digital logs (found in Appendix A).

90 samples were selected and plugged. Eight of these were picked to be used for geochemical characterization in project 7-1111-0200. The remaining 82 have first been analyzed by the Geological Survey of Western Australia. A subset of 29 samples was used by CSIRO for petrophysical, geomechanical, acoustic core plug characterization and for core flooding tests.

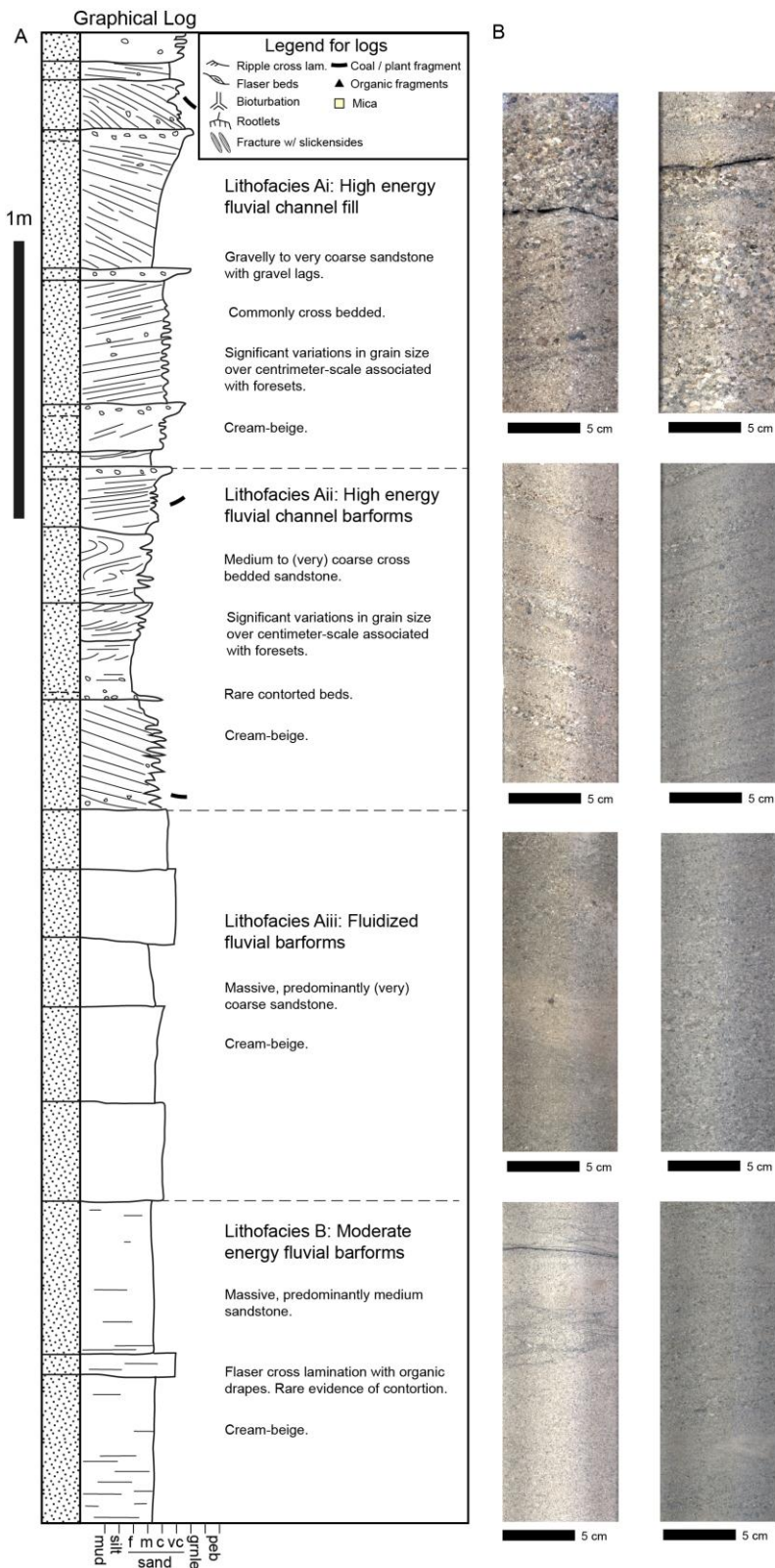


**Figure 1.3 A summary of the lithofacies scheme developed for the Mesozoic stratigraphy of the central Perth Basin. (A) Graphical sedimentary logs and descriptions. (B) Example core photographs from Harvey-1.**

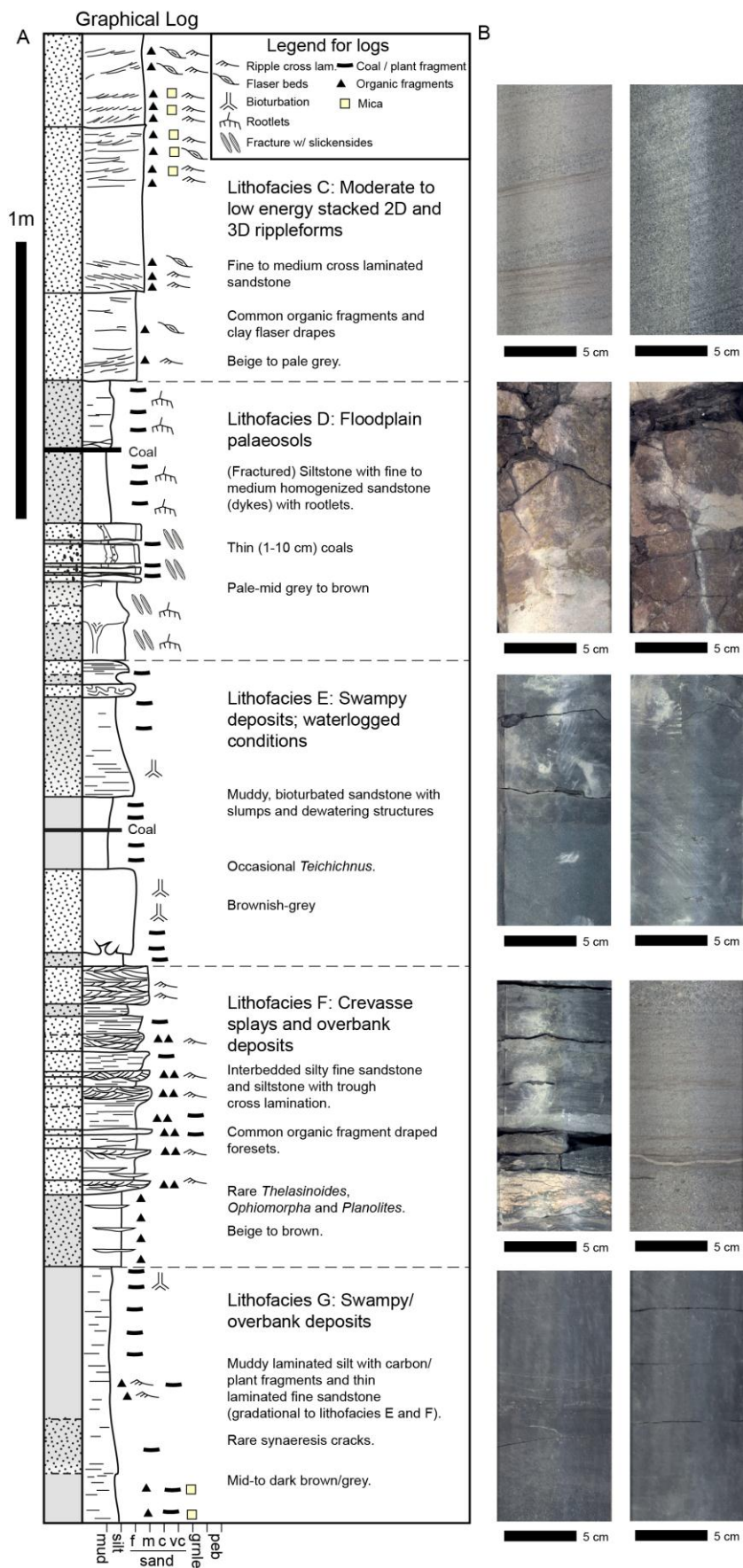


**Figure 1.3. continued: A summary of the lithofacies scheme developed for the Mesozoic stratigraphy of the central Perth Basin. (A) Graphical sedimentary logs and descriptions. (B) Example core photographs from Harvey-1.**

Measurements of Gamma-ray intensity were undertaken by GSWA on the recovered cores. Values were measured as total intensity, in counts per second. The core gamma logger was a Scintrex GRS-500 with a GeoGamma NaI(Tl) detector. The detector size is 76 by 76 mm. Gamma response was measured on the Al-cased core at 5 cm intervals.

## 1.5 Results

### 1.5.1 DOWNHOLE FACIES DISTRIBUTION

The facies scheme developed for the central Perth Basin is directly applicable to Harvey-1, with only a small modification to palaeosols (facies D) from Timms et al. (2012) (Fig. 1.3). Variations within lithofacies include grain size (indicated by bedding and lamination), bioturbation, mineralogy (indicated by colour and texture), plant fragments and fractures.

Six cored sections were taken from Harvey-1, all of which intersect the Lesueur Formation (Fig. 1.4 and Fig. 1.5). The Lesueur Formation is split into the Yalgorup (cores 1-4; Fig. 1.4) and Wonnerup (cores 5-6; Fig. 1.5) Members. The Yalgorup Member exhibits mixed sandstone/siltstone/mudstone layers, whereas the Wonnerup Member consists predominantly of interbedded coarse, very coarse and gravelly sandstone. The following section outlines the lithofacies interpreted from core logging, which can be visualized using the downhole distribution per core (Fig. 1.6).

#### Yalgorup Member

Core 1 (895-931.5 m) consists of mixed coarse to gravelly, high energy channel fill (facies Ai to Aiii) and fine to medium grained moderate energy channel barforms and rippleforms (facies B and C; Fig. 1.4). Siltstone and mudstone beds are rare, with the exception of one 2m-thick bed. The coarsest sandstones (facies Ai) are very poorly sorted, whereas the fine to medium-grained, interbedded facies (B and C) are moderately sorted.

Cores 2 to 4 (1266-1344 m), which are almost continuous, consist primarily of siltstones and sandstones in a palaeosol (vertisol) depositional environment (facies D) (Fig. 1.4). These rock types are mainly fractured and filled silty mudstone, with thin layers of medium-grained sandstone, and uncommon very coarse grained sandstone layers. Medium-grained fracture-fills resemble a poorer-sorted moderate energy channel barforms (facies B). Rarer coarser grained sandstones resemble poorly-sorted high energy channel fill (facies Ai-Aiii). Vertical to sub-vertical, trans-bedform fractures are pervasive in mudstones; they are typically planar to irregular, and can extend from 5 cm to several meters. These fractures are typically filled with medium-grained sandstone and occasionally very coarse grained sandstone, creating sub-vertical sandstone 'dykes', which could act as permeable pathways through otherwise relatively impermeable mudstone. Open, gently inclined, fractures often occur as conjugate sets, exhibiting prominent slickenlines (Fig. 1.7). These are orientated with an acute angle of intersection through the horizontal such that the inferred maximum stress direction is horizontal. The top of core 2 contains fracture-filled silty mudstone and sandstone beds. Sandstones have a similar composition to the fracture-fills that are immediately above. Towards the middle of core 2, sandstone becomes more common, forming poorly sorted horizons that extend up to 3m in thickness. Like the top of core 2, these sandstones have a similar composition to those immediately below, suggesting that material has filled in from above. Towards the base of core 2, and within cores 3 and 4, mudstone/siltstone is the dominant lithotype, with sandstone limited to 'dykes' and sparse high energy channel fill (facies Ai) and moderate energy channel barforms (facies B) horizons.

#### Wonnerup Member

Core 5 (1896-1947.7 m) consists primarily of interbedded coarse to gravelly sandstones, indicating high energy channel fill and barforms (facies Ai-Aii). Crossbeds, defined by alternating grain sizes, range between 1-5 cm thick (Fig. 1.5). Foreset thicknesses range between 0.4-1.5 m in thickness. These continuous facies are occasionally punctuated by fine to medium, cross-laminated sandstone, indicative of low-moderate energy stacked rippleforms (facies C) and medium-grained moderate energy barforms (facies B). Thin



siltstone and mudstone beds are rare and are interpreted to be swampy/overbank deposits (facies G). Clay content varies slightly within crossbedded sandstones particularly near the middle of core 5.

Core 6 (2480-2532.5 m) consists primarily of interbedded coarse to gravelly sandstones, which suggest high energy channel fill and barforms (facies Ai-Aii), with crossbeds, defined by alternating grain sizes, between 1-10 cm thick (Fig. 1.5). Foreset thicknesses range between 0.3-1.8 m. There are intercalations of meter-scale, massive, coarse-grained, high energy fluidized barforms (facies Aiii), massive, medium grained, moderate energy channel barforms, (facies B), and finely crossbedded, fine to medium stacked rippleforms (facies C). Thin punctuations of ~1-20 cm thick siltstone/mudstone layers are rare. These are occasionally laminated and finely interbedded, indicative of crevasse splays (facies F), or bioturbated and showing dewatering structures (facies E), but more commonly swampy/overbank deposits (facies G).

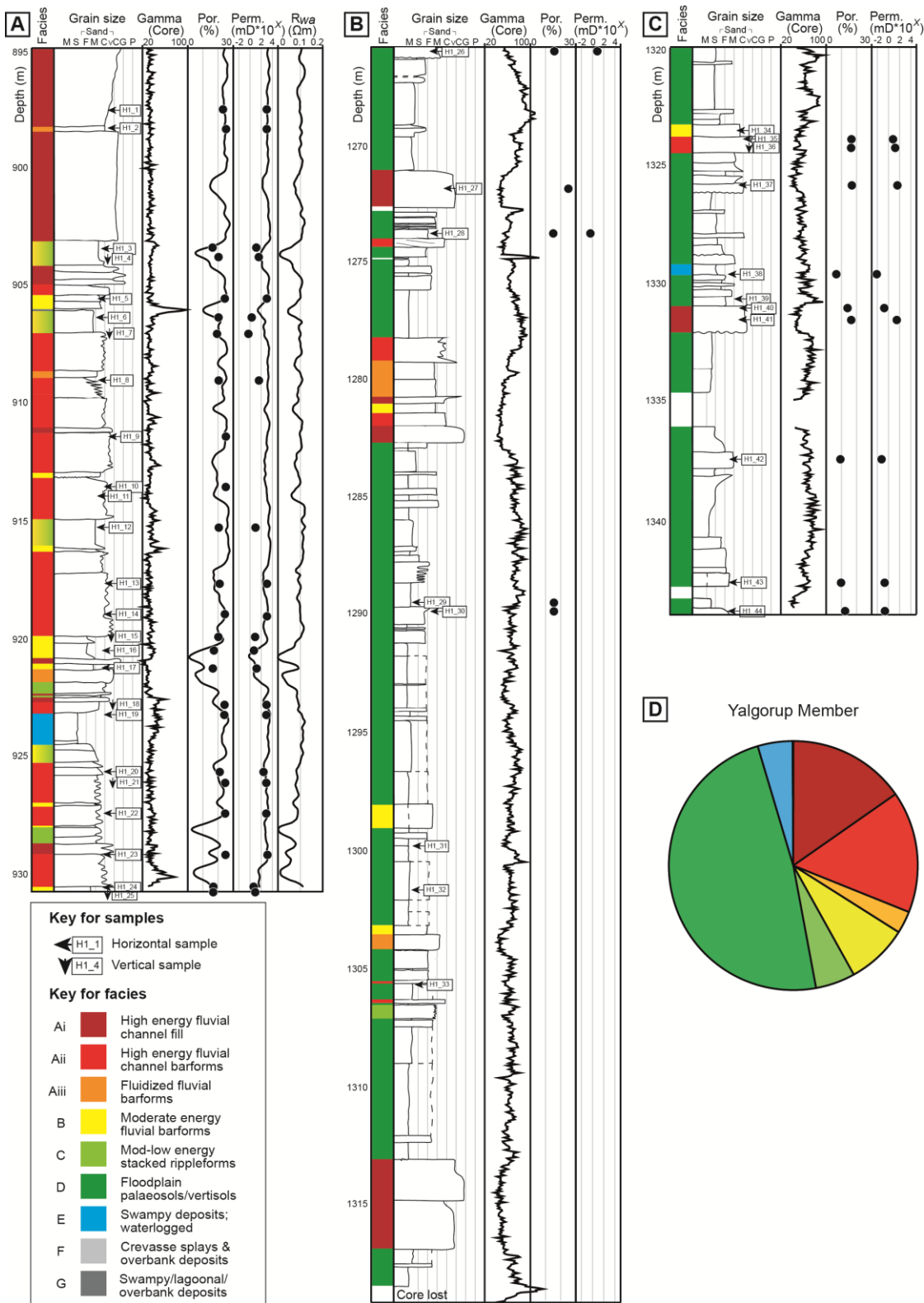
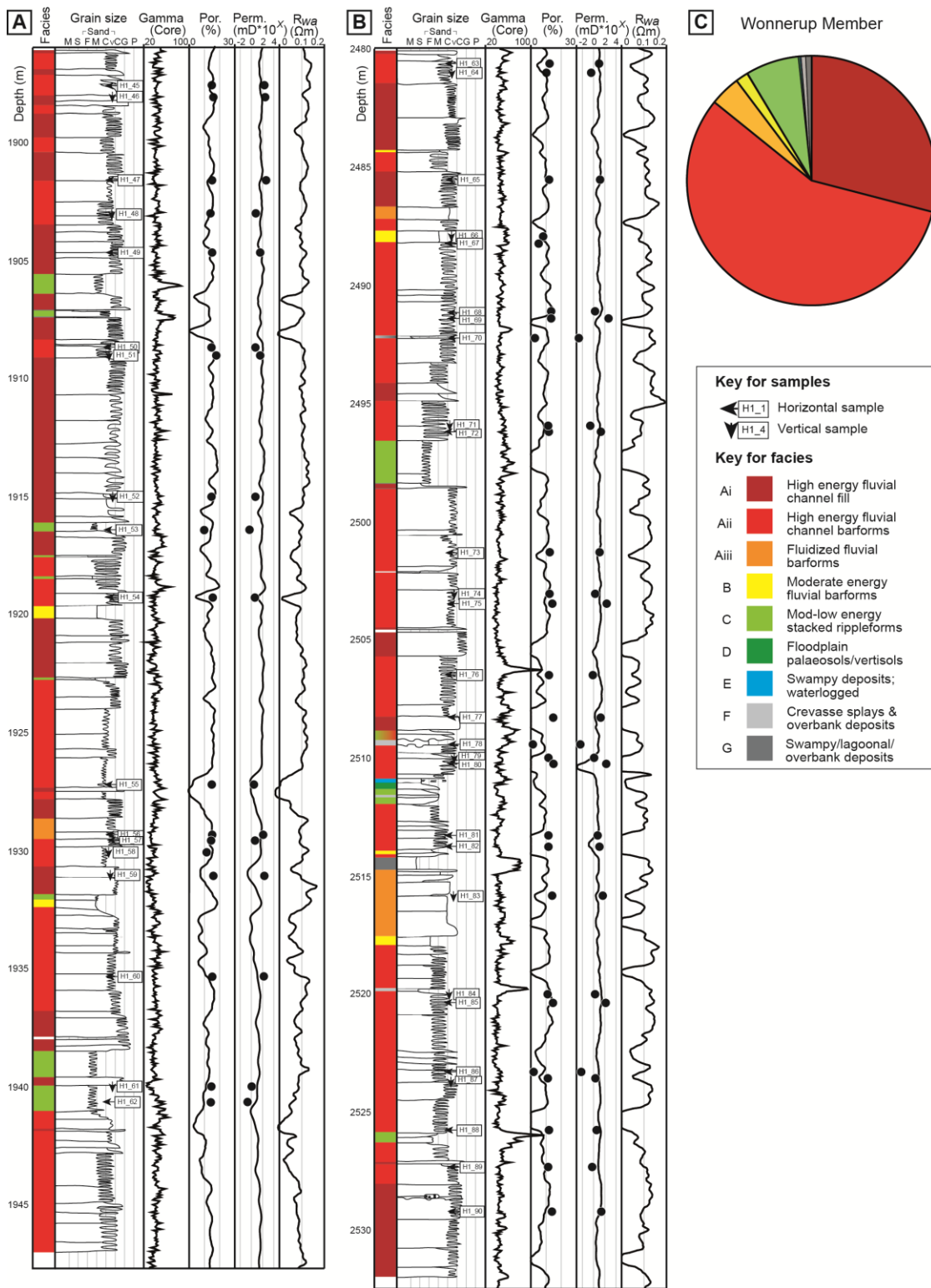


Figure 1.4. (A-C) Distribution of rock properties in the Yalgorup Member cored intervals of Harvey-1: (A) Core 1 – 895-931.6 m; (B) Core 2 – 1266-1319 m, and; (C) Core 3 and 4 – 1320-1344 m. Facies were determined through a facies model developed by Timms et al. (2012), modified from Miall (1996). Gamma was taken at 5 cm intervals on whole core, in counts per second. Porosity (Por.) and permeability (Perm.) distribution models were determined from average neutron-density porosity, not shown for B and C due to poor data; helium-injection of core plugs provided statistical data at sample localities. Pore water resistivity (Rwa) was calculated through Archie’s law, not shown for B and C due to poor data. (D) Pie chart showing the relative abundance of each facies of the Yalgorup Member.



**Figure 1.5. (A-B)** Distribution of rock properties in the Wonnerup Member cored intervals of Harvey-1: (A) Core 5 – 1896-1847.7 m, and; (B) Core 6 – 2480-2532.5 m. Facies were determined through a facies model developed by Timms et al. (2012), modified from Miall (1996). Gamma was taken at 5 cm intervals on whole core, in counts per second. Porosity (Por.) and permeability (Perm) distribution models were determined from average neutron-density porosity; helium-injection of core plugs provided statistical data at sample localities. Pore water resistivity (Rwa) was calculated through Archie’s law; and (C) Pie chart showing the relative abundance of each facies of the Wonnerup Member.

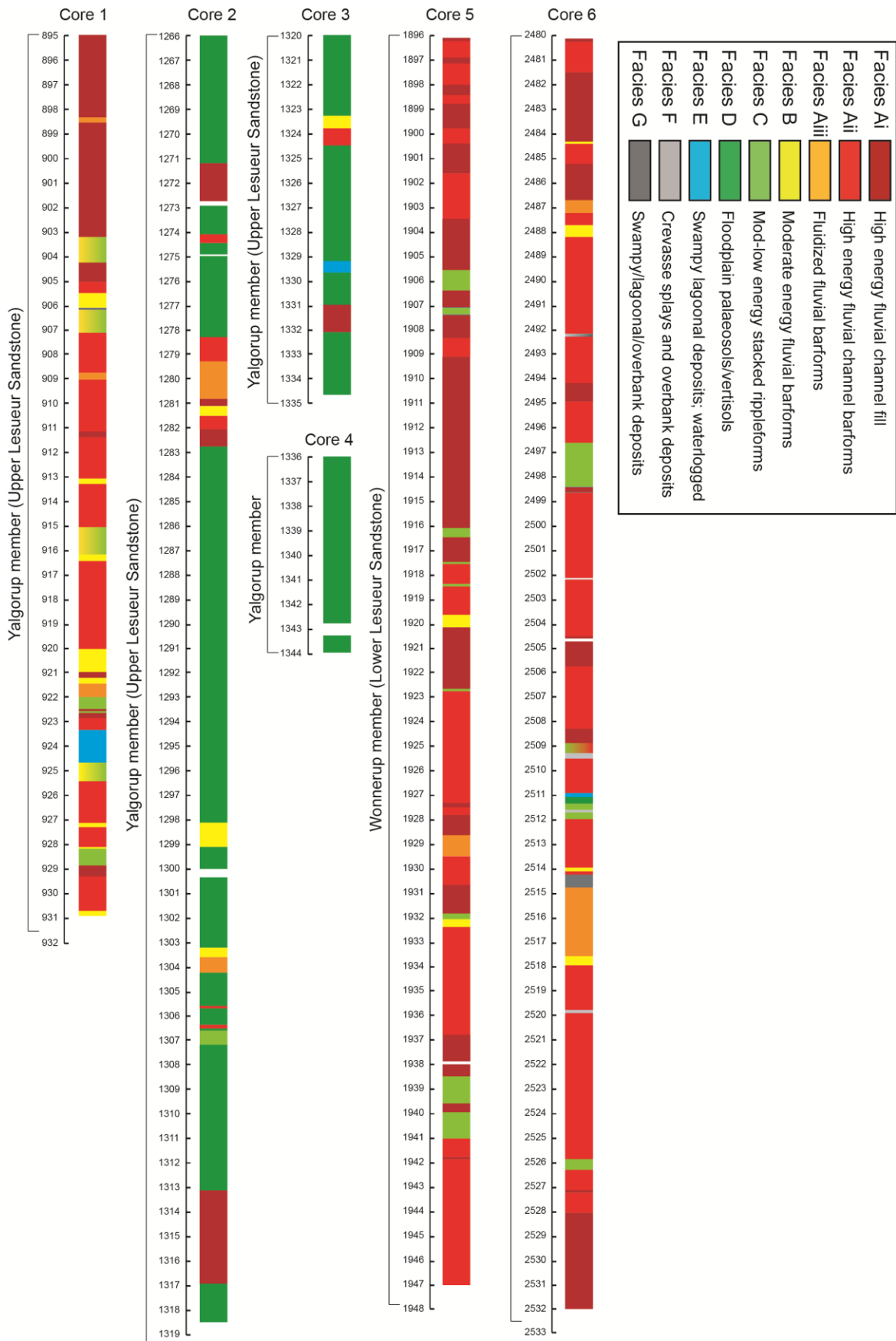


Figure 1.6. A summary of the lithofacies Ai-G assigned to cored intervals from sedimentary logging.



**Figure 1.7** Core image of sandy siltstone deposited as floodplain palaeosols, showing conjugate fracture sets with slickenlines. The image is approximately 10 cm across.

### 1.5.2 CUMULATIVE AND CONTINUOUS FACIES THICKNESS

Cumulative and continuous thicknesses of lithofacies characteristics help to estimate the reservoir potential and sealing capacity of targeted intervals. Cumulative lithofacies thicknesses measure the proportions of each lithofacies, Ai to G, of the Lesueur Sandstone, split into the Yalgorup and Wonnerup Members.

Continuous lithofacies thicknesses measure the individual thicknesses of lithofacies, which are then statistically processed to determine the mean, median, first and third quartiles, and minima and maxima. This helps determine the rate of facies switching and therefore the rate of porosity-permeability variation at core scale.

The Lesueur Sandstone contains over 60% of high energy channel fill and barforms (facies Ai-Aiii) across its 6 cored intervals. When split into its two Members, the Yalgorup Member and Wonnerup Member contain approximately 35% and 85% facies Ai-Aiii, respectively (Fig. 1.4 and 1.5). The Yalgorup Member is dominated by floodplain palaeosols (facies D) in cores 2-4, but otherwise mixed, consisting of between 5-15% of the other facies. The Wonnerup Member is dominated by facies Ai and Aii, with 1-10% of all other facies.

The continuous thicknesses of facies in the Lesueur Sandstone average about 1-2 meters (Fig. 1.8). The Yalgorup Member is relatively evenly distributed, with the mean varying between 0.7 m and 1.5 m, with the exception of facies D and E, where the mean is between 2.5-3 m, and facies G, where the mean is less than 0.1 m. With the exception of facies D, 50% of thicknesses fall within 0.5 m of the mean. The Wonnerup Member has thick continuous intervals of facies Ai to Aiii, with 50% of the thicknesses falling within 1-2 m

of the mean. Facies B to G have a mean of less than 0.2 m, with the exception of facies C, which has a mean of 0.5 m.

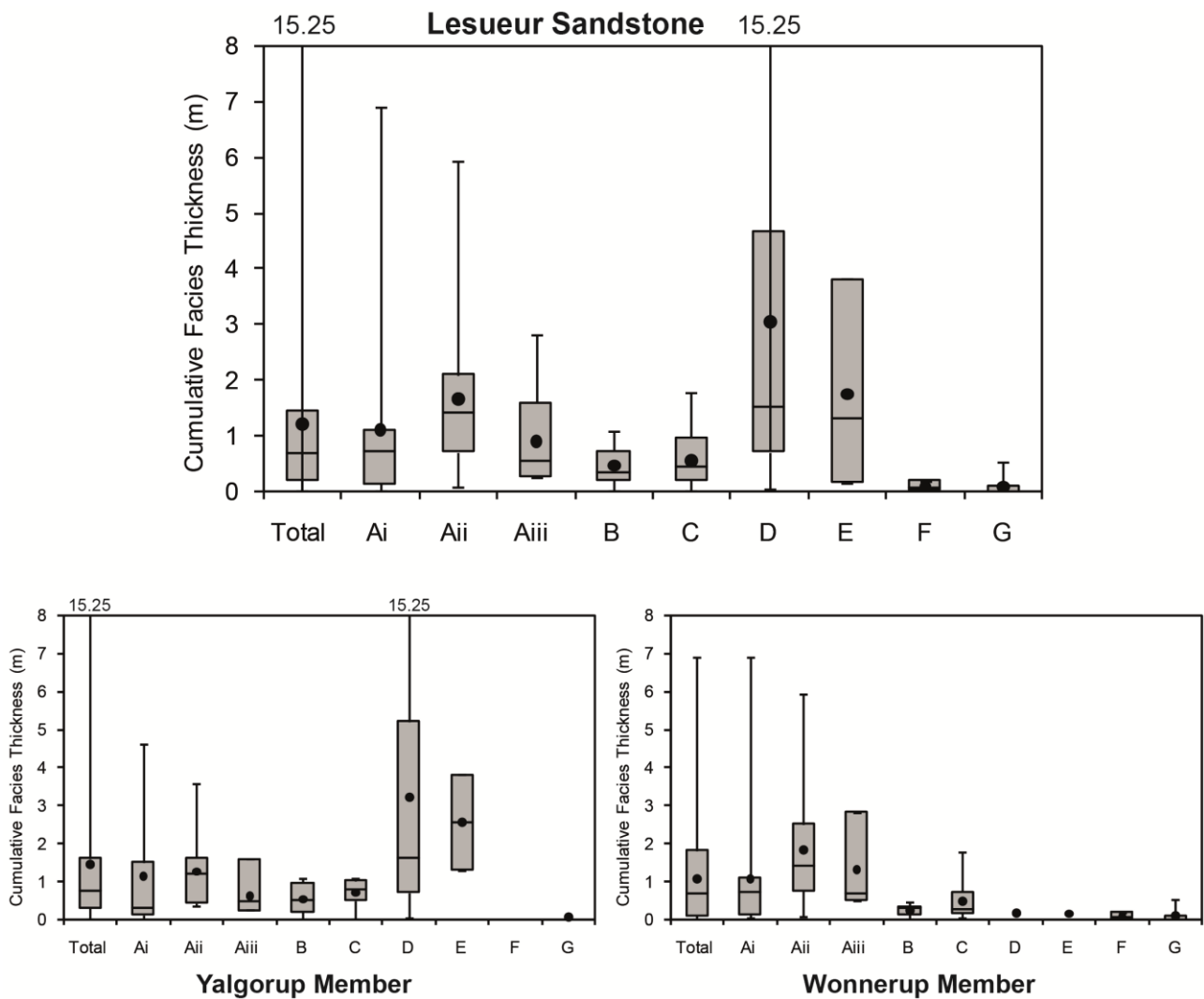


Figure 1.8 Box and whiskers plots of continuous thicknesses of different lithofacies for cored intervals of each stratigraphic Formation/Member. The graph shows the minimum (base of error bar), first quartile (base of rectangle), median (within rectangle), third quartile (top of rectangle), maximum (top of error bar) and mean (dot).

### 1.5.3 FACIES AND CORE GAMMA COMPARISON

Core gamma measurements were compared to the interpreted facies scheme. High to moderate energy, clean, channel fill and barforms (facies Ai to B) typically exhibit the lowest gamma response; facies C to D are intermediate, and facies E to G have higher gamma response (Fig. 1.9 and 1.10). However, there are overlaps in the gamma response from different facies types. Fig. 1.10 shows that the probability of facies Ai-Aiii is more likely to occur at gamma ray values between 10-50 counts per second. Facies B to D typically have intermediate values between 50 and 90 counts per second. For facies E to G, gamma ray values are most commonly in the range of 70 to 90 counts per second.

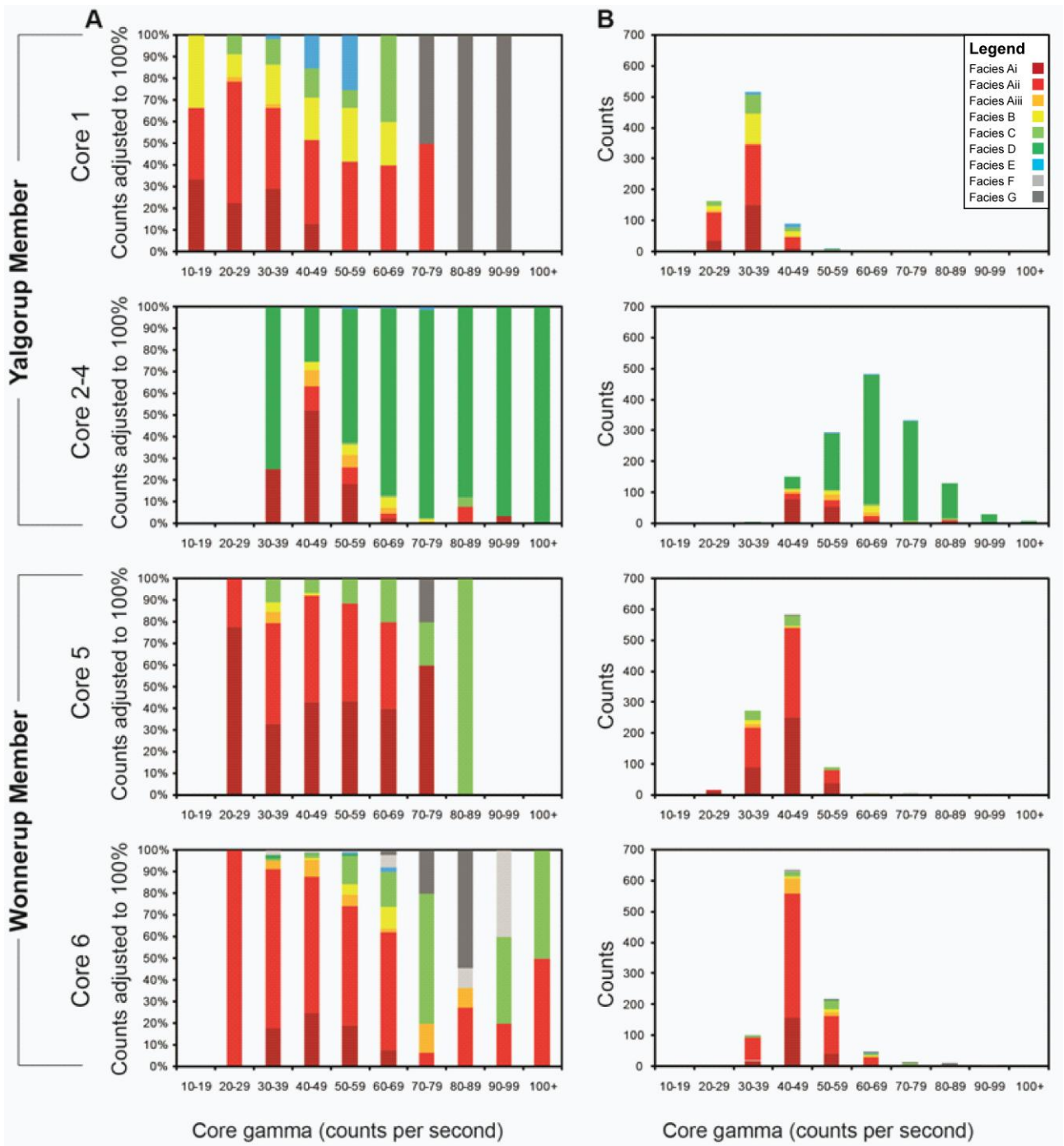


Figure 1.9. Comparison of core gamma ray with lithofacies for each cored interval. (A) 100% stacked chart showing relative proportions of each lithofacies. (B) Stacked chart showing abundances of core gamma per core, measured in counts per second. Core gamma was taken approximately every 5 cm.

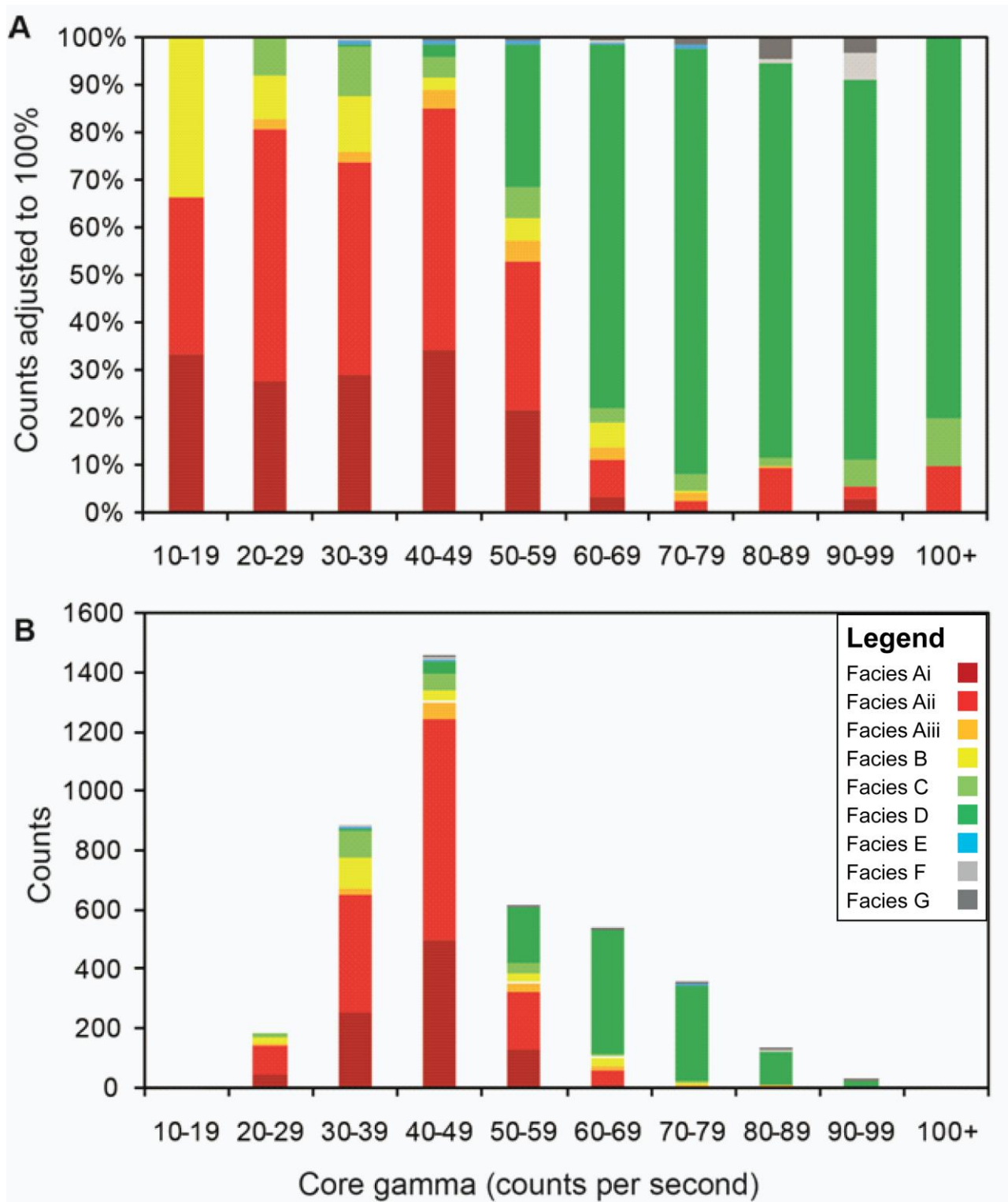


Figure 1.10. Comparison of core gamma ray with lithofacies for all cored intervals. (A) 100% stacked chart showing relative proportions of each lithofacies. (B) Stacked chart showing abundances of core gamma, measured in counts per second. Core gamma was taken approximately every 5 cm.



## 1.6 Discussion

### 1.6.1 DEPOSITIONAL ENVIRONMENT

Analysis of the cored sections of Harvey-1 allows for interpretation of the depositional environments. All 6 cores exhibit lithofacies that are typical of braided fluvial environments (Fig. 1.2) (Miall, 1996).

Core 1 comprises mixed high energy fluvial channel fill, barforms and fluidized barforms, with moderate to low energy fluvial barforms and stacked rippleforms. These are punctuated by thin swampy/overbank deposits. These depositional environments are characteristic of a migrating braided fluvial system (Miall, 1996; Bhattacharyya and Morad, 1993) (Fig. 1.2).

Cores 2 to 4 comprise palaeosols, intercalated with high energy fluvial channel fill and high to moderate energy barforms, with rare swampy/overbank deposits. The setting for these depositional environments is characteristic of vertisols, which are soils with high expanding clay content, particularly smectite (Fig. 1.11A) (Blokhuys, 1982; Spaargaren, 1994). High smectite content is confirmed in core 2-4 by HyLogger data (see module 2, Fig. 2.7 G). Smectite in these soils could be derived from the original rock or form as a result of genesis from primary minerals, requiring a high pH and high mobile Si and Mg (Blokhuys, 1982). In ephemeral fluvial systems, expanding clay minerals expand during wet winter seasons, and contract during dry, summer seasons (Fig. 1.11B). This causes vertical desiccation cracks during the drying of clay minerals. During the dry season, surface sediment or mulch fills these cracks through channel flow by flash flooding of poorly sorted, medium-grained to gravelly sands. On rewetting, smectite rehydrates and expands. During expansion, the desiccation cracks re-seal, but due to additional material now present, a greater volume is required. The expanding material presses and slides the sand against each other, creating slickensides and developing a 'vertic' structure (Fig. 1.11B).

Cores 5 and 6 are comprised predominantly of high energy fluvial channel fill and barforms. These are punctuated by moderate to low energy channel barforms and stacked rippleforms, and swampy/lagoonal deposits and crevasse splays. These depositional environments are characteristic of a continually operating fluvial channel system, with variations in energy correlating to grain size variations (Miall, 1996; Hjellbakk, 1997).

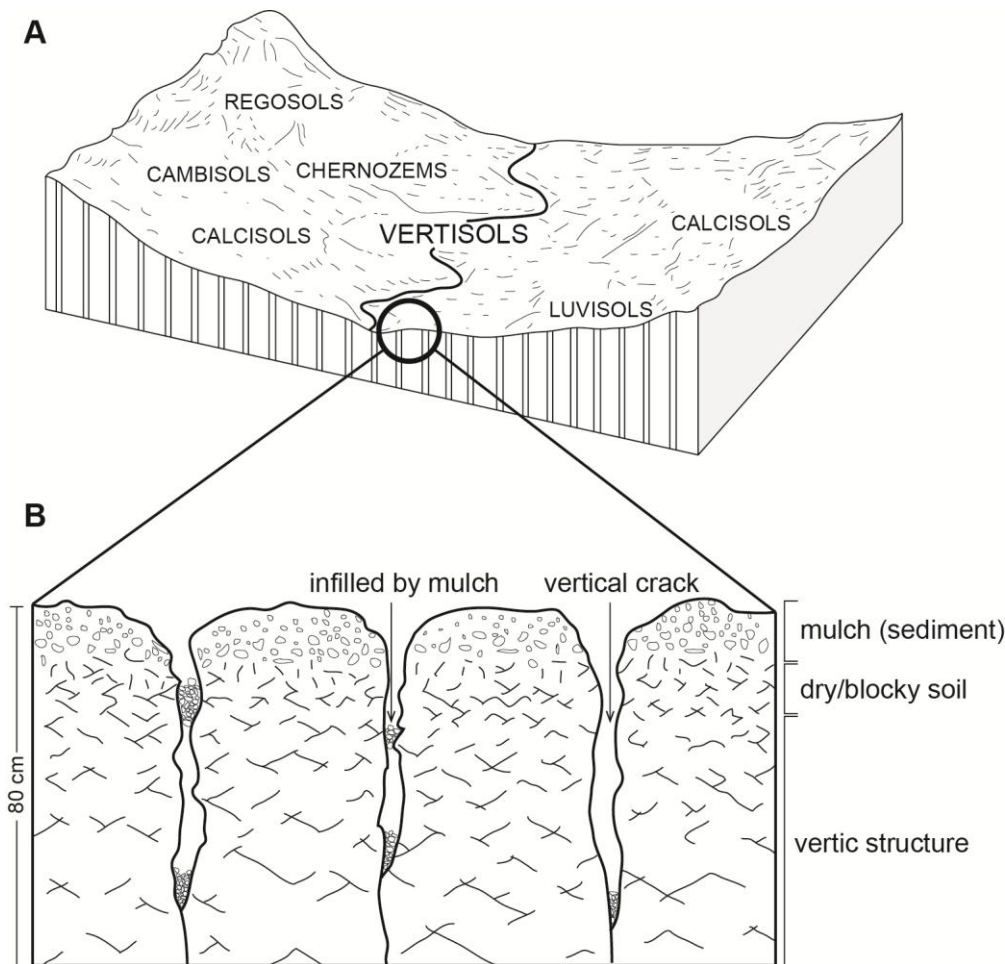


**Figure 1.11. Vertisol development as floodplain palaeosols. (A) Schematic diagram showing vertisols among other soil types, developing in fluvial floodplains. (B) Schematic diagram showing components of vertisol development.**

### 1.6.2 CUMULATIVE AND CONTINUOUS THICKNESS CHARACTERISTICS OF FACIES

Cumulative and continuous thicknesses of facies provide a statistical overview of the geology of the cored intervals of the Yalgorup and Wonnerup Members of the Lesueur Sandstone. Combined with petrophysical properties, such as porosity and permeability, these statistics provide an overview of the proportions of each lithofacies per cored interval and the rate of facies switching.

The Lesueur Sandstone can be divided into its two Members, the Yalgorup and Wonnerup, based on its distinct lithofacies distribution. The Yalgorup consists of a rapidly-switching, on the order of 1m, mixed lithofacies, with the exception of extensive floodplain palaeosols in the lower Yalgorup. However, even within this soil profile there is rapid switching in the sandstone dykes, between high energy channel fill and moderate energy channel barforms, indicated by the variation in grain size. The Wonnerup Member is more homogeneous in terms of lithofacies development. However, within a lithofacies unit, there is still rapid-switching between crossbeds and foresets, indicated by 1-10cm beds of alternating grain-size sandstones. These are primarily high energy channel fill and barforms, with rare lower energy rippleforms and swampy/lagoonal deposits.

### 1.6.3 COMPARISON WITH THE SEDIMENTOLOGY OF THE LESUEUR SANDSTONE IN PINJARRA-1

The Lesueur Sandstone was analyzed as part of a geothermal exploration project by the WA Geothermal Centre of Excellence (Timms et al., 2012). It is the most proximal deep exploration hole to Harvey-1 and contains the same facies as found in Harvey-1. It consists of 16 short (1-10 m) cored intervals. The

thicknesses of continuous facies are not considered here, because facies were often thicker than the scale of the cored sections in Pinjarra-1.

The downhole facies distribution of Pinjarra-1 is comparable to that of Harvey-1 (Fig. 1.6 and Fig. 1.12). If we assume that the Yalgorup Member in Pinjarra-1 is the same thickness as in Harvey-1, then that makes the Yalgorup Member mixed-facies, and the Wonnerup Member dominant in facies Ai to Aii (Fig. 1.12). This is similar to the distribution of Harvey-1. Since the two Members of the Lesueur Sandstone were not differentiated during core logging of Pinjarra-1, only the total cumulative facies for the Lesueur Sandstone is compared. This is similar to the cumulative thickness of Harvey-1, with the exception of floodplain palaeosols (facies D), which is significantly more frequent in Harvey-1.

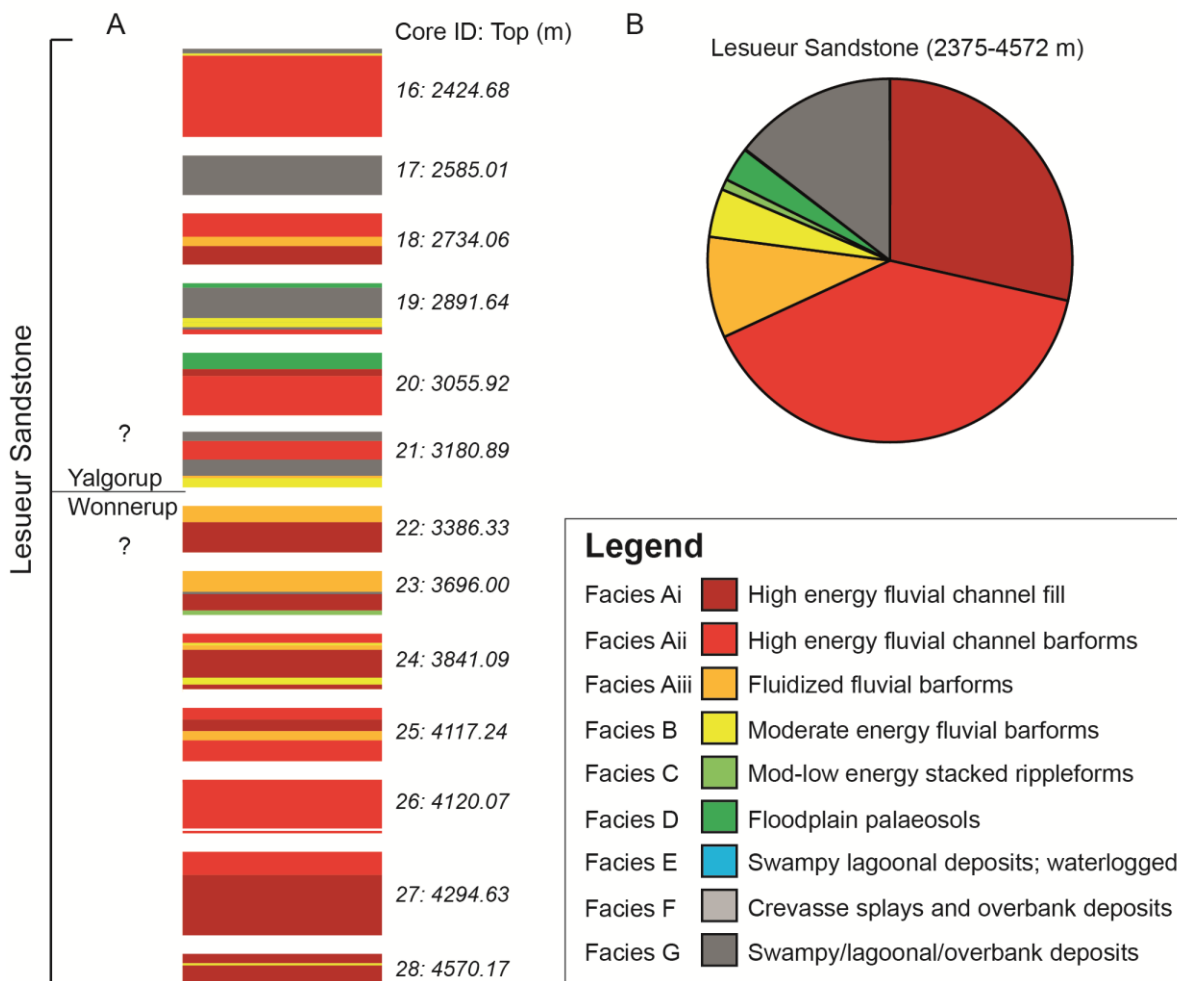


**Figure 1.12. Facies analysis of the Lesueur Sandstone from Pinjarra-1. (A) Downhole distribution of facies. The Yalgorup/Wonnerup Members boundary is interpreted based the thickness of the Yalgorup Member in Harvey-1. (B) Cumulative facies thicknesses, showing relative proportions of facies in cored intervals (modified from Timms et al. submitted).**

### 1.6.4 CORE GAMMA AND LITHOFACIES

The frequency of lithofacies types have been plotted against core gamma values to investigate whether lithofacies can be inferred from gamma response. The correlation between core gamma radiation and lithofacies is moderate to good. The core gamma, in counts per seconds, for facies Ai-Aiii, B-D and E-G are typically 10-50, 50-90 and 70-90, respectively. There are some overlaps between the gamma responses for different facies. The data show that the probability of a particular gamma response being linked to a particular lithofacies varies (Fig. 1.9 and Fig. 1.10). The probability of a facies having a core gamma in these

ranges is between 50-90% (Fig. 1.10). There are between 10-50% exceptions to this correlation. i.e., using gamma alone to infer lithofacies type in non-cored intervals leads to a reasonable 'rule-of-thumb', but not a unique interpretation.

The exceptions could be the result of: (a) proximity shadow effects, particularly where low gamma sandstone and high gamma mudstone are juxtaposed; (b) geological responses in sandstones, including: (i) K in clay-rich sandstone; (ii) K in feldspar-rich sandstone; (iii) U/Th in heavy mineral-rich layers; or (c) ingress of KCl-rich drilling mud.

### **1.6.5 PRELIMINARY FEASIBILITY STUDIES**

This study aimed at providing a first geological description of the units crossed by the Harvey-1 well. The Wonnerup Member represents the targeted storage reservoir, whereas the Yalgorup Member and the Basal Eneabba Shale (not cored) correspond to the targeted seals. The Wonnerup Member (cores 5 and 6) has thick continuous intervals of clean, coarse-grained sediments with very little mudstone intervals. This is an ideal lithology for a CO<sub>2</sub> reservoir. There were 46 core plugs taken to test the reservoir potential by measuring porosity and permeability.

The Yalgorup Member has strongly interbedded facies, with relatively thin continuous thicknesses. The shale/mudstone in cores 2-4 are significantly intruded by sandstone dykes. Due to the poor sorting of the sandstone dykes, these are likely to be of low permeability, and therefore still baffles to fluid flow. There are 19 samples targeted from cores 2-4, primarily in sandstone, because the integrity of shale samples will likely fail when plugged. These core plugs are used to characterize the permeability of the sandstones intervals in the Yalgorup Member. Lastly, there are 25 samples assigned to core 1, to test the upper Yalgorup Member. Unfortunately, the Basal Eneabba Shale was not cored.

## **1.7 Conclusions**

The cored sections of Harvey-1 intersected the Yalgorup Member (cores 1-4) and the Wonnerup Member (cores 5-6) of the Lesueur Sandstone. Nine lithofacies were identified from core logging. The Yalgorup Member consists of mixed-thickness, interbedded high to low energy channel-fill facies, and swampy/overbank deposits and palaeosols. The Wonnerup Member consists of thick, continuous, high energy channel-fill facies, with minor intercalations of moderate to low energy channel-fill/stacked rippleforms and rare swampy deposits. The stratigraphy in Harvey-1 is comparable to that of Pinjarra-1, when the same facies scheme is applied.

Core gamma response was compared to lithofacies interpreted from core logging. There was a moderate correlation between low core gamma (high energy channel fill and barforms, facies Ai-Aiii), moderate core gamma (low to moderate energy barforms, rippleforms and palaeosols, facies B-D) and high core gamma (swampy/overbank deposits and crevasse splays, facies E-G). There is a 50-90% probability that the core gamma, in counts per seconds, for facies Ai-Aiii, B-C and E-G are 10-50, 50-70 and 70-100+, respectively. However, facies D (palaeosols) have two components in Harvey-1. The sandstone component exhibits a low core gamma response and the silty mudstone exhibits a high core gamma response. The total core gamma varies depending on the proportion of each of these lithotypes.

Preliminary feasibility studies indicated that the reservoir in the Wonnerup Member is, at least vertically, continuous and thick while the Yalgorup Member may act as a baffle to vertical fluid migration due to the presence of interlayered shaly and sandy intervals. The Basal Eneabba Shale was not cored and could not be analyzed in detail; nevertheless it could potentially be an additional effective seal.

## **2 Module 2: Petrographic and mineralogical analysis**

## 2.1 Summary

The Perth Basin consists of rocks that form aquifers (reservoirs) and aquitards (seals) and these have recently been studied for CO<sub>2</sub> geosequestration potential. Determining the mineralogy of these rocks allows better prediction of any reactions (either dissolution or precipitation) that carbon dioxide may have during long-term storage. This is best characterized using thin section and scanning electron microscopy of selected thin sections. A selection of 27 samples from existing core plug offcuts was prepared for thin section analysis to establish the petrography, microstructure and mineralogy. The same samples were analysed for quantitative mineralogy using X-ray diffraction by Geotechnical Services PTY LTD (work commissioned by WADMP) and for multiphysics laboratory characterization (see results in the next modules).

The mineralogy is comprised primarily of monocrystalline quartz, with rare polycrystalline quartz, K-feldspar, albite in low-porosity rocks, kaolinite, illite and smectite with minor opaque minerals, micas, garnet, organic carbon and carbonates. Diagenesis is primarily characterized by the weathering and replacement of K-feldspar and albite to kaolinite, smectite and minor illite. Minor authigenic quartz overgrowth and iron-rich chlorite was also present, particularly in deeper samples.

Of particular importance to CO<sub>2</sub>-brine-rock interactions in the potential reservoir sandstone is the proportions of reactive minerals. Among the rock forming minerals identified in the potential storage levels of Harvey-1, K-feldspar is a potential reactor in presence of carbonic acid (formed by hydration of CO<sub>2</sub>). The slow reaction, occurring in a time frame of hundreds to thousands of years, forms colloidal kaolinite, which may clog up permeable pathways between framework grains, thereby reducing the mobility of CO<sub>2</sub>-rich fluids.

## 2.2 Introduction

Carbon dioxide geo-sequestration is different from other industrial operations that extract fluids, such as petroleum and groundwater production. The injection of CO<sub>2</sub> into saline formation waters, such as those found in the SW- Hub, may allow the CO<sub>2</sub> to be stored hydrodynamically for tens of thousands of years (Janda and Morrison, 2001). Furthermore, a series of reactions between the formation mineralogy and CO<sub>2</sub>-enriched formation waters can produce immobile mineral forms that allow storage for millions to hundreds of millions of years (Janda and Morrison, 2001). An understanding of the mineralogy is one component that needs to be established to characterize any reactions that carbon dioxide may have during long-term storage. This is best characterized using thin section and scanning electron microscopy of selected thin sections. This method also allows micro-textures to be resolved, which can aid in establishing any fluid pathway anisotropy.

Analysis of the cored sections and of the wireline logs was done for Harvey-1, a stratigraphic data well drilled proximal to Harvey in the SW-Hub. Detailed sedimentary core logging was undertaken to provide an overview of the cored sections in Harvey-1 (module 1, Fig. 1.4 and Fig. 1.5). Core sample selection and subsequent thin section preparation allowed for characterization of the mineralogy, microstructure and petrography. Mineralogy and textural data from Harvey-1 will be used to assess the potential of carbon storage at the SW-Hub.

## 2.3 Analytical Techniques/Approach

### 2.3.1 THIN SECTION PREPARATION

Polished thin sections were made from 27 core samples. These samples also underwent 3-D porosity-permeability measurement by Helium-injection (module 4). A list of samples may be found in Appendix B. Sampling was heavily biased towards medium to coarse sandstone intervals and the sandstone dyke

components of floodplain palaeosols. In siltstone, claystone and shale, the integrity of rocks were unlikely to be cohesive enough for strength testing.

Selected core plug offcuts were initially impregnated with a blue dye to highlight porosity. The impregnated samples were then mounted on short (27 mm by 46 mm) thin sections and ground and polished down to a thickness of 30 microns. The prepared sections were examined and digitally imaged at low magnification using a Zeiss Axio Imager II under plane-polarized and cross-polarized transmitted light, and plane-polarized reflected light. Three stitched images of the entire thin section were collected for each section. These stitched images are located in Appendix C.

### **2.3.2 PETROGRAPHY**

Basic petrography of thin sections included examining the lithology, sedimentary micro-structure, grain size distribution and textural maturity. These data are objective to a certain extent; grain size was measured against a scale bar for a limited number of grains. Textural maturity (sorting, rounding and sphericity) was assessed semi-objectively against sand folders. Together with mineralogy point counts, these data were then used to classify the samples into different facies, using a fluvial-dominated scheme (see module 1, Fig. 1.2) (Miall, 1996)

Point counting was done on whole-thin-section images using JMicroVision<sup>®</sup>. A rectangular area was selected for each thin section for 250 or 400 counts, dependent on the thin section size, with a random grid. The list of minerals comprise mono-crystalline quartz, poly-crystalline quartz, feldspar, clay minerals, opaque minerals, organic carbon, micas, carbonates, other minerals (chlorite, zircon, Ti-oxides), occluded porosity (filled with clay minerals and carbonates) and clear porosity. Clear and occluded porosity were distinguished in thin section based on how similar the blue resin colour (on the edge of the thin section) was to a porosity point count. Occluded porosity tends to be green-blue, whereas clear porosity is a primary-colour blue. The advantages of using this thin section petrography are: (a) the ability to distinguish phases of similar chemistry (e.g. illite and muscovite); (b) distinction between mono- and poly-crystalline quartz; (c) identifying the texture of framework and matrix minerals, and; (d) 2-D visualization of porosity size, shape and if porosity is occluded.

### **2.3.3 MINERALOGY: X-RAY DIFFRACTION**

Offcuts of 28 core plugs were submitted to Geotechnical Services PTY LTD by GSWA for quantitative phase analysis by X-ray diffraction (XRD). General limitations of XRD analysis are:

- Detection limit of 1-2% on most crystalline phases,
- Peak overlay may occur in the presence of multiple phases resulting in non-unique interpretation, and
- Phase identification is based on a comparison of the acquired data to a standard reference file of inorganic compounds.

### **2.3.4 HYLOGGING™ DATA INTERPRETATION**

Hyperspectral logging technologies provide a method for rapid and objective mineralogical logging of geological drill core. The Hylogger™, developed by CSIRO, employs reflectance spectroscopy to determine diagnostic spectral features indicative of mineralogy, mineral chemistry and physical characteristics of geological samples (Ndlovu et al., 2011; Summers et al., 2011). Core is fed through a machine which measures continuous visible and infrared spectra and collects digital imaging without destroying the core in the process, with sample spacing between 1 and 5 cm. For the Harvey-1 cores, this provided 40,000 data points. Although the data relies on interpretation of wavelength bands, CSIRO has developed The Spectral Geologist™ (TSG), which automatically analyses samples based on characteristic wavelengths. Further correction and interpretation of data was undertaken by the Department of Mines and Petroleum.

Minerals can be identified through characteristic reflection of visible and infrared light by their molecular components. When exposed to light, these molecular bonds begin to vibrate. The vibrations, combined with electronic changes at the molecular and atomic level, results in the selective absorption of light. The partially-reflected light is measured and characterised by spectrometers. Particular mineral compositions have specific and unique wavelengths defining their spectral signature. Minerals that can be analysed include those containing an OH<sup>-</sup> group (clay minerals, chlorite), silicates, carbonates, iron oxides and others. Of particular interest to Harvey-1 was the distribution of clay minerals and chlorite, which required an understanding of only the short wavelength infrared (SWIR) spectrum. These are of particular importance to rock-fluid interactions, including reactions with carbon dioxide.

### 2.3.5 QUANTITATIVE GRAIN SIZE ANALYSIS

The grain size of a sedimentary rock is typically taken to be the coarsest grains, with the exception of a few outliers. Gauging of grain size purely by the use of a sand folder in hand samples or by measurement against a scale bar in thin section does not provide a full description of the finer-grained components of a sedimentary rock sample. JMicroVision<sup>®</sup> has an in-built area measurement tool, which measures the length, width and area, among other 2-D statistical properties, of all the grains in a selected area. Depending on the mean grain size, this can be in the order of 10<sup>2</sup> to 10<sup>5</sup> grains in an analysed sample. This provides a robust quantitative grain size analysis including the size distribution of individual framework grains. Furthermore, the analyses are rapid and can be processed in under a day.

There are several steps involved in preparation and processing of a particular grain size analysis (Fig. 2.1). Firstly, it requires an image of a 2-D surface; a full thin-section photomicrograph is ideal (Appendix C). Processing of quantitative grain sizes requires a binary image, where, for example, all white areas are framework grains, and all black areas are porosity. This is best achieved by using plane-polarized, reflected light images. An image is firstly imported into ImageJ<sup>®</sup> software. This image is then converted into 8-bit (greyscale) and then a binary of the image is taken. This makes all grains black and porosity white. The image is subsequently inverted, which allows an algorithm 'fill holes' to be used to remove any erratic holes within grains. 'Fill holes' is not used in two of the very fine to fine grained, matrix-supported sandstone samples (sample 38 – facies E and sample 44 – facies D), because the algorithm cannot differentiate between holes and boundaries between very fine grains. It is also not used in the majority of samples from deeper intervals (cores 5 and 6). These exhibit compaction-related sub-grain textures, which show up as elongate 'holes' when converted to binary and therefore cannot be resolved by the algorithm. The last remaining problem is that grains touching each other need to be separated. An algorithm 'watershed' is applied, which creates boundaries between such grains. This assumes that all grains adhere to an elliptical form, such that a straight line can be made at the concave impositions between two grains. This is a reasonable assumption in fluvial river systems, where quartz and feldspar grains are typically sub-angular to sub-rounded. 'Watershed' occasionally gives poor results, which can be attributed to two factors: (1) compaction-related sub-grain fractures are often distinguished, making grain sizes smaller, and; (2) in some samples, the fluvial-derived sediments are angular, where 'watershed' divides at any concave incursions into grains. The final binary image is then imported into JMicroVision<sup>®</sup>.

JMicroVision<sup>®</sup> can perform a grey threshold object extraction. This allows all distinct grains to be measured at a known scale. For this, the scale must first be defined, either by knowing how many millimetres are in a pixel or by drawing a straight line across the image and defining its length. The latter is easier as a scale bar is already present in each image. The object extraction is then set up. An area which encompasses as many grains as possible is selected, with a minimum surface filter of 10 pixels, an "all borders" filter and a threshold colour that selects the colour of the grains. After processing, statistics can be exported, including grain length/width, orientation, eccentricity and angularity. From this, further statistics may be calculated, such as grain size, sorting and roundness/sphericity. The only artefact that is introduced with JMicroVision<sup>®</sup> is the large proportion of very small grains that may skew the grains size statistics towards counting up more fine grained materials. This is attributed to: (1) very small particles in the matrix, such as clay minerals, which show up as speckled, partially-occluded porosity; (2) partially-dissolved feldspars, and; (3)



smaller particles due to watershed effect. However, even with these artefacts, this method still provides a statistically robust approach to characterizing the grain size of sedimentary rocks.

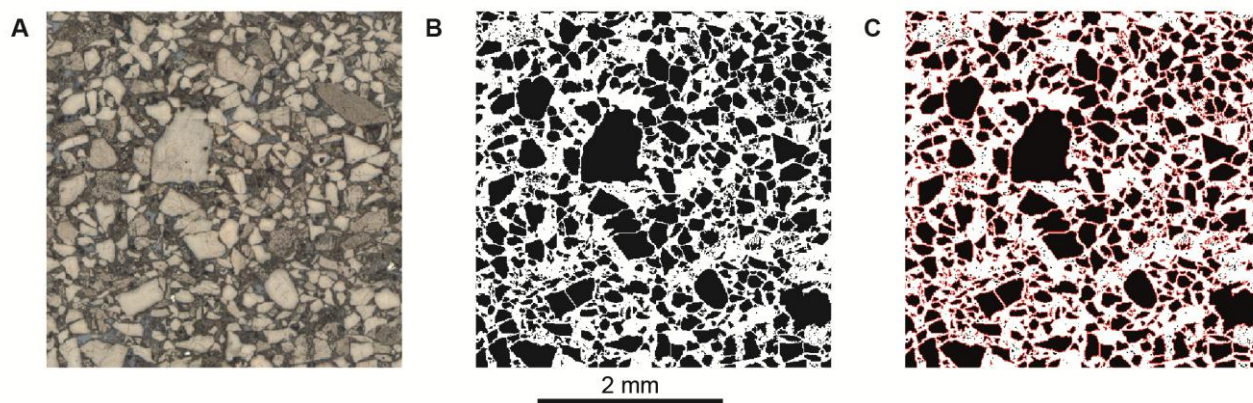


**Figure 2.1. Quantitative grain size analysis procedure. (A) Reflected, plane polarized light image of polished thin section. (B) 8-bit, binary, Fill Holes- and Watershed-applied image, made in ImageJ. (C) Grains have been statistically analysed in JMicroVision; grain boundaries are shown by red lines.**

## 2.4 Results

### 2.4.1 PETROGRAPHY AND MINERALOGY

Mineralogy and sedimentary structure analysis was undertaken for each thin section. Subsequently, these were assigned facies and compared to the facies assigned to the core logging regions. The lithofacies scheme that was used for the core logging, from Timms et al. (2012), was accurate at the thin section scale (Fig. 2.2, Fig. 1.2 and 1.3). Occasionally there was some discrepancy between thin section and core facies assignment, but these were updated to reflect the thin section facies. X-ray diffraction (XRD) results are used in conjunction with thin section analyses to aid in establishing the exact mineralogy.

Thin section analysis shows that the four samples in core 1, in the upper Yalgorup Member, contain primarily quartz, K-feldspar and kaolinite, with minor framework carbonates, rare opaque minerals, micas and heavy minerals (Fig. 2.3). Quartz is primarily monocrystalline and 5-10% of total quartz is polycrystalline. Polycrystalline quartz is typically composed of two to three quartz sub-grains, but occasional large clasts in the coarsest of sandstones (facies Ai) exhibit up to 30 sub-grains (Fig. 2.4). Quartz is also commonly deformed, shown by undulose extinction, particularly near the edges of grains. There seems to be no systematic orientation to the undulose extinctions. Feldspars are predominantly microcline with minor orthoclase. Orthoclase, in particular, is severely weathered and interfingered with kaolinite. Kaolinite is mainly localized in pore spaces that are of a similar size and adjacent to framework grains, but also as coatings on quartz grains. Carbonates in core 1 are identified as High-Mg calcite from XRD (Fig. 2.5 and 2.6).

Cores 2 to 4 in the lower Yalgorup Member, which are nearly continuous, show a different mineralogy to that of core 1 (Fig. 2.3). Thin sections in cores 2 to 4 are primarily composed of quartz, feldspars, clay minerals and rare framework calcite and dolomite. Quartz is predominantly monocrystalline, but as high as 30% of quartz is polycrystalline in samples from a low-energy depositional environment (facies D and E) (Fig. 2.4). Feldspar in cores 2-4 are mixed plagioclase (albite) and K-feldspar (microcline and orthoclase) (Fig. 2.5). Similarly to core 1, these are heavily weathered and mixed with interstitial clay minerals. Clay minerals consist of mixed kaolinite, smectite and illite. Kaolinite and smectite tend to form in pore spaces that are of a similar size to adjacent framework grains, whereas illite tends to form as variable-thickness coatings on quartz and feldspar framework grains. Porosity, as a result, is partially occluded by clay minerals.

Samples from cores 5 and 6, from the Wonnerup Member, are typically clean, variably-bedded medium to very coarse grained sandstones. The mineralogy comprises mainly monocrystalline quartz, with rare polycrystalline quartz, K-feldspar, clay minerals, rare organic carbon, opaque minerals, micas and carbonates (Fig. 2.3). Framework grains, particularly quartz, are more rounded than in the Yalgorup Member. K-feldspar is still heavily weathered, and interlaced with clay minerals. Clay minerals in cores 5 and 6 comprise mainly kaolinite and berthierine, a high Fe-bearing kaolin-serpentine mineral identified from XRD results (Fig. 2.5). They are difficult to distinguish, but both form as interstitial clays in pores similar in size to adjacent framework grains. Rare illite is present in 2 samples. Ankerite, calcite and dolomite, identified from XRD, are present in four samples in total and form as framework grains (Fig. 2.5). Organic carbon is present in two samples, exclusive to laminated migrating rippleforms (facies C) (Fig. 2.4). Organic carbon tends to define laminae in facies C. There is also rare garnet present in samples from core 5 and 6, particularly in variable medium to high energy fluvial depositional environments (facies Aii).

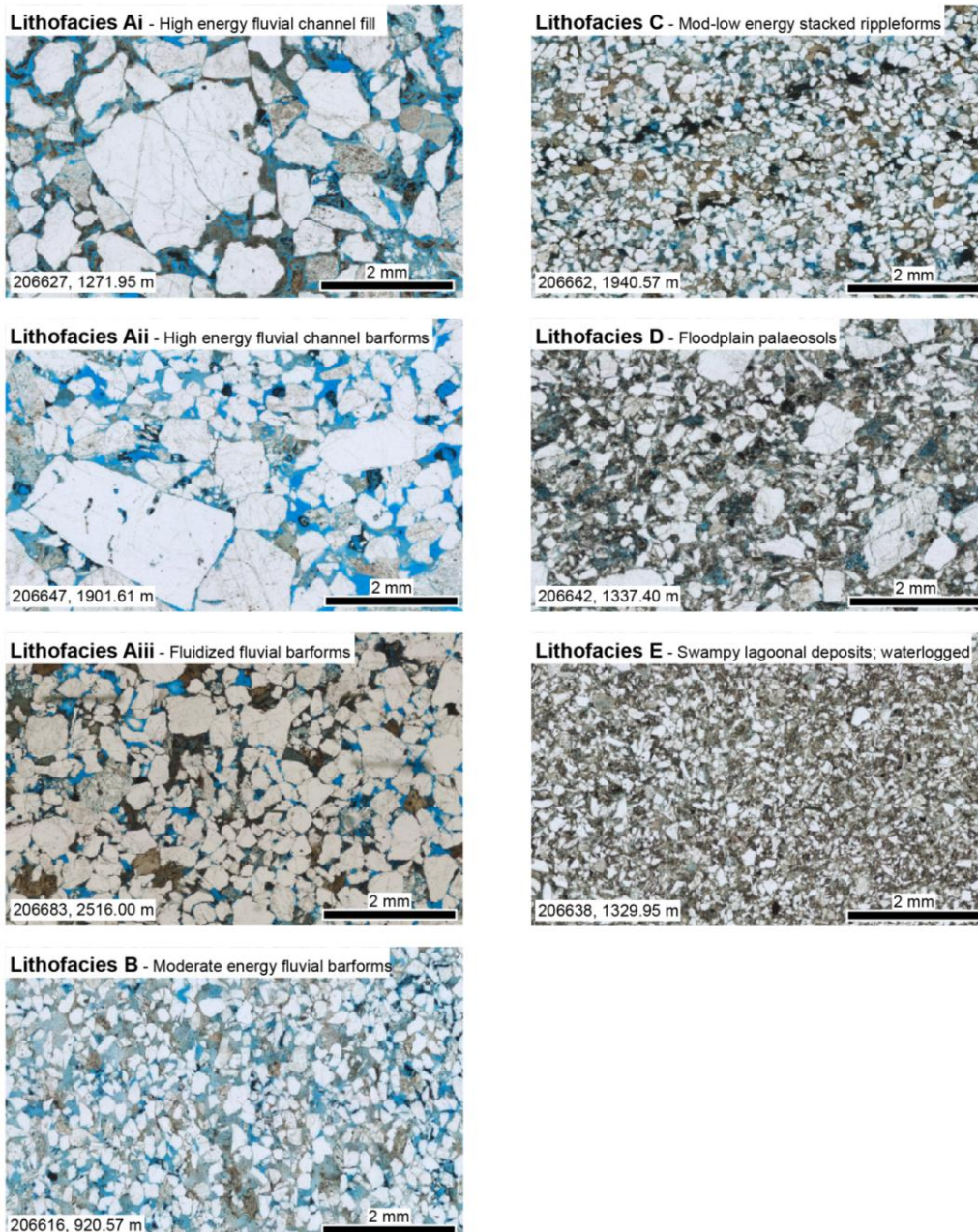


Figure 2.2. Optical photomicrographs, in transmitted plane polarized light, of representative samples from each lithofacies. Note that no samples were taken of facies F and G. Samples have been impregnated with blue resin to show porosity. Sample number and depth of recovery is indicated in the lower left-hand corner of each figure. Samples from depth greater than 1380m belong to the Wonnerup Member; those from shallower depth are from the Yalgorup Member.

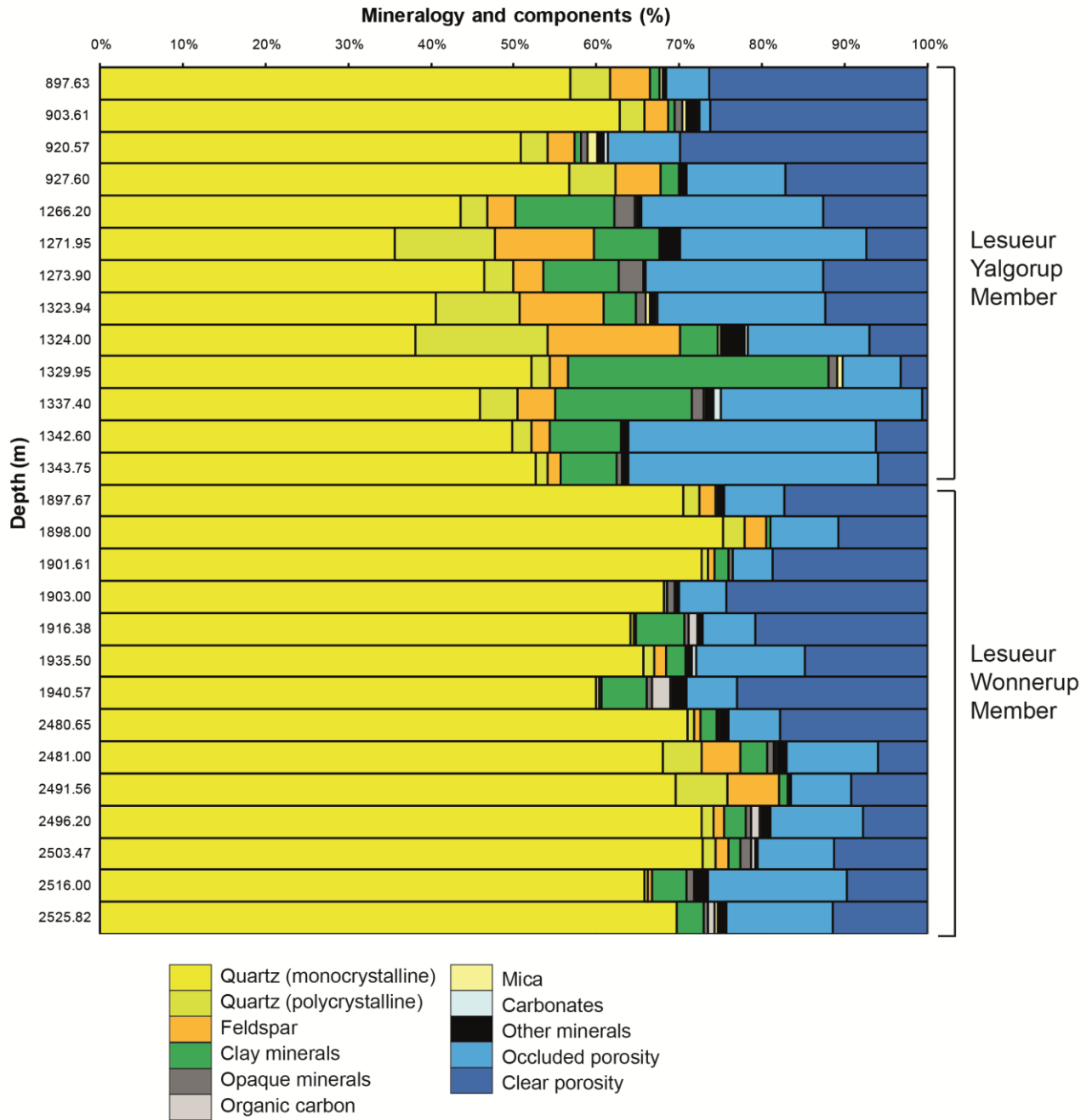


Figure 2.3. Bar charts to show modal mineralogy from point count data, sorted by depth.

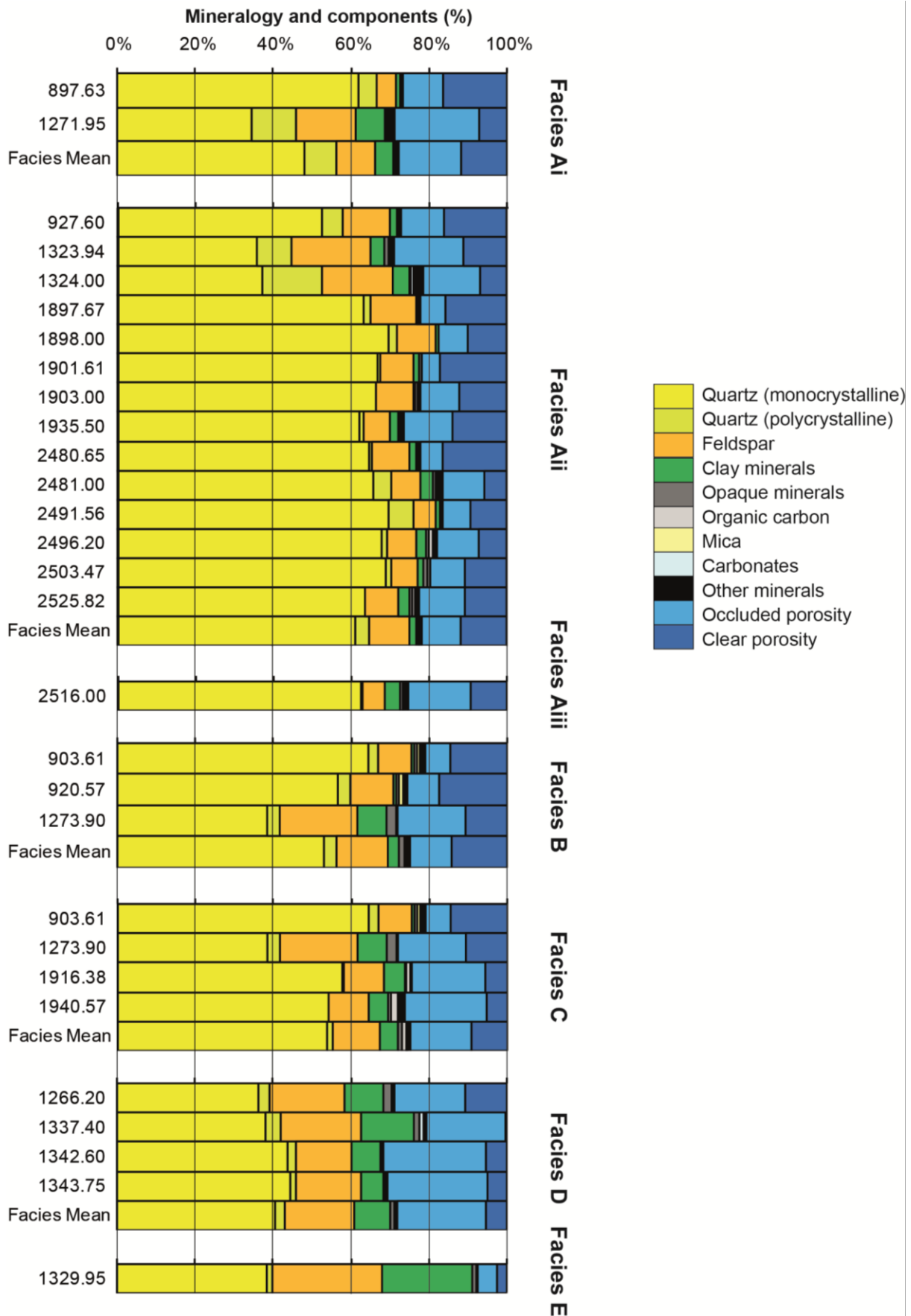


Figure 2.4. Bar charts to show modal mineralogy from point count data, sorted by lithofacies. Vertical axis expresses depth in meters.

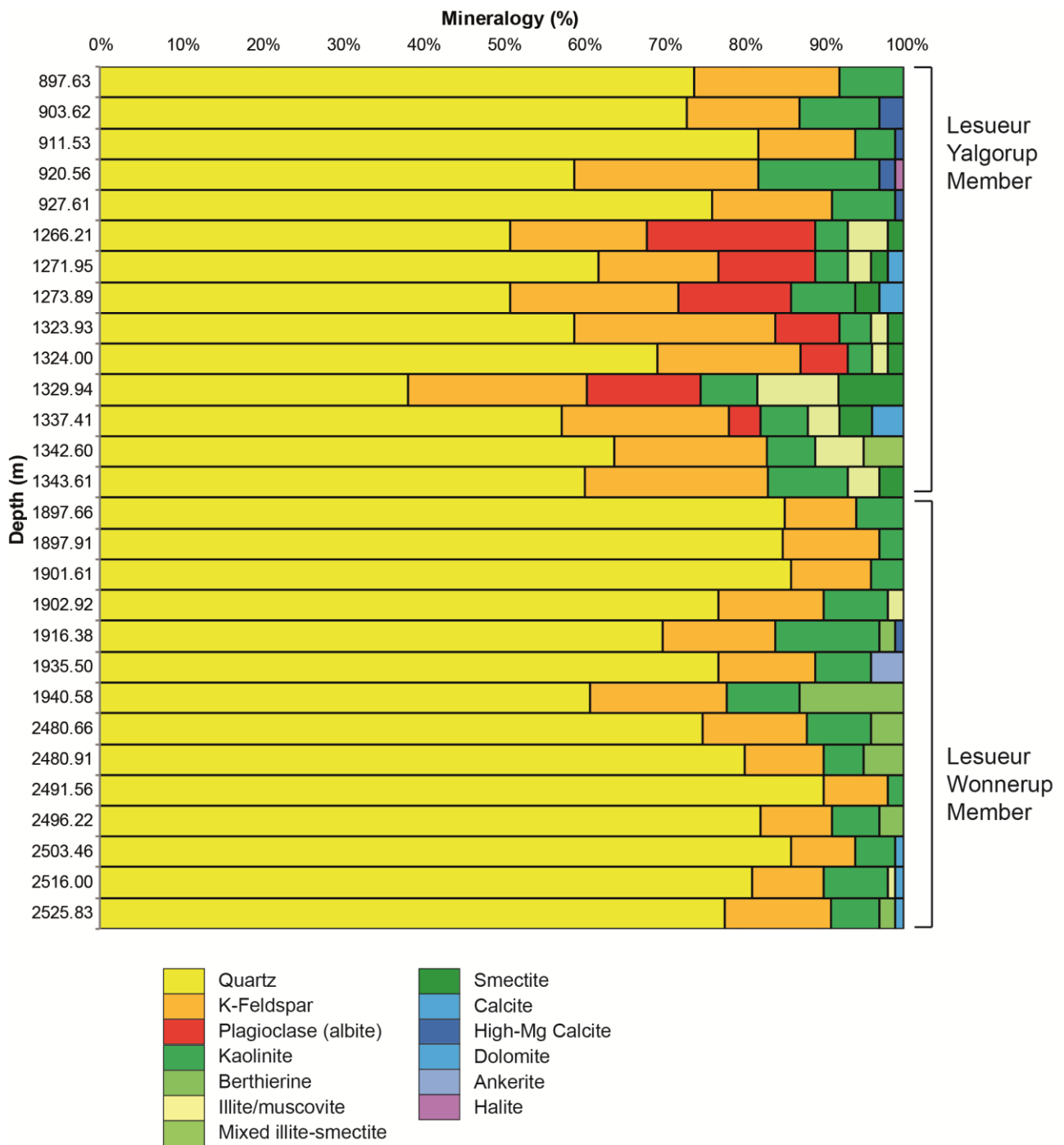


Figure 2.5. Bar charts to show modal mineralogy from x-ray diffraction data, sorted by depth.

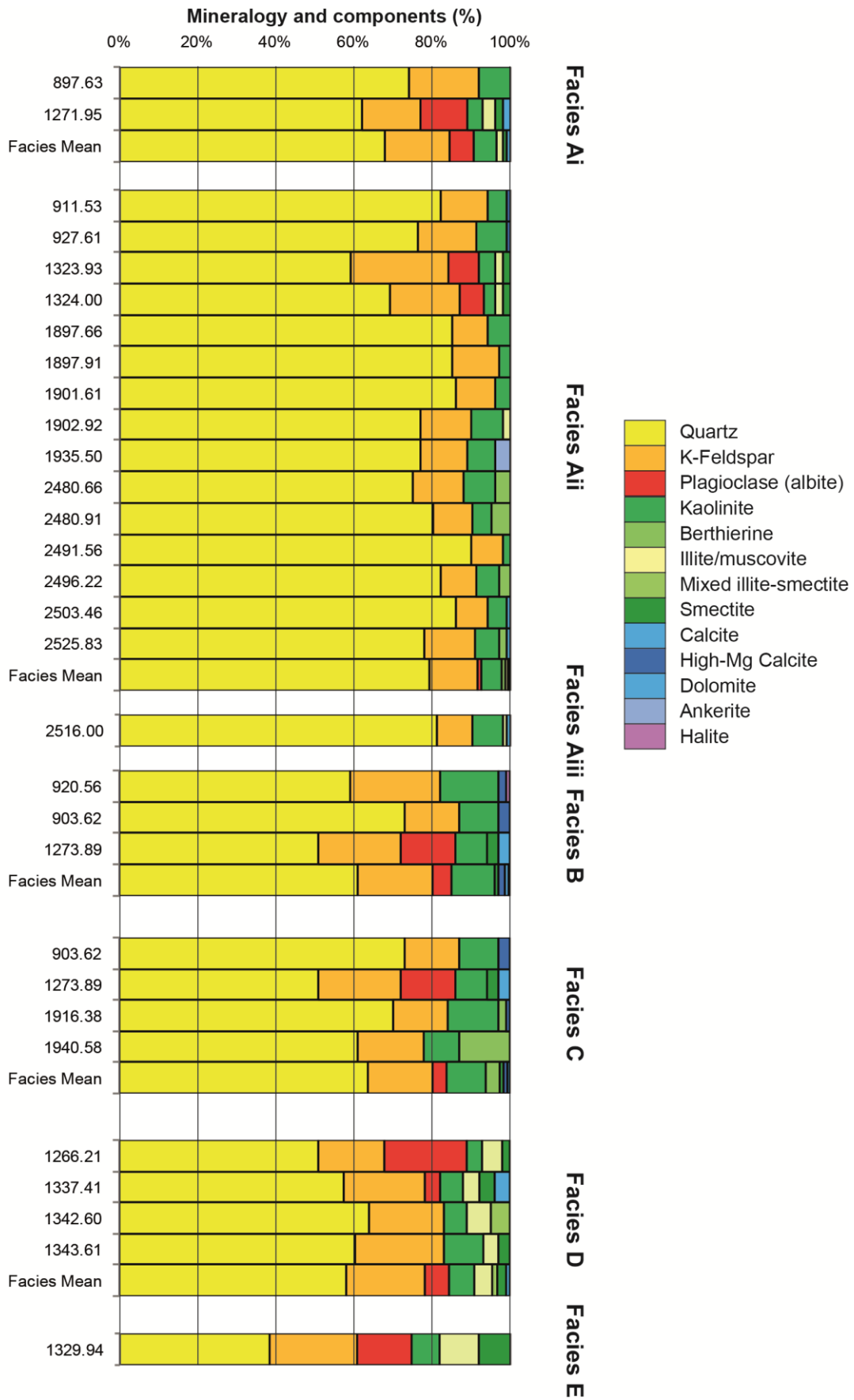
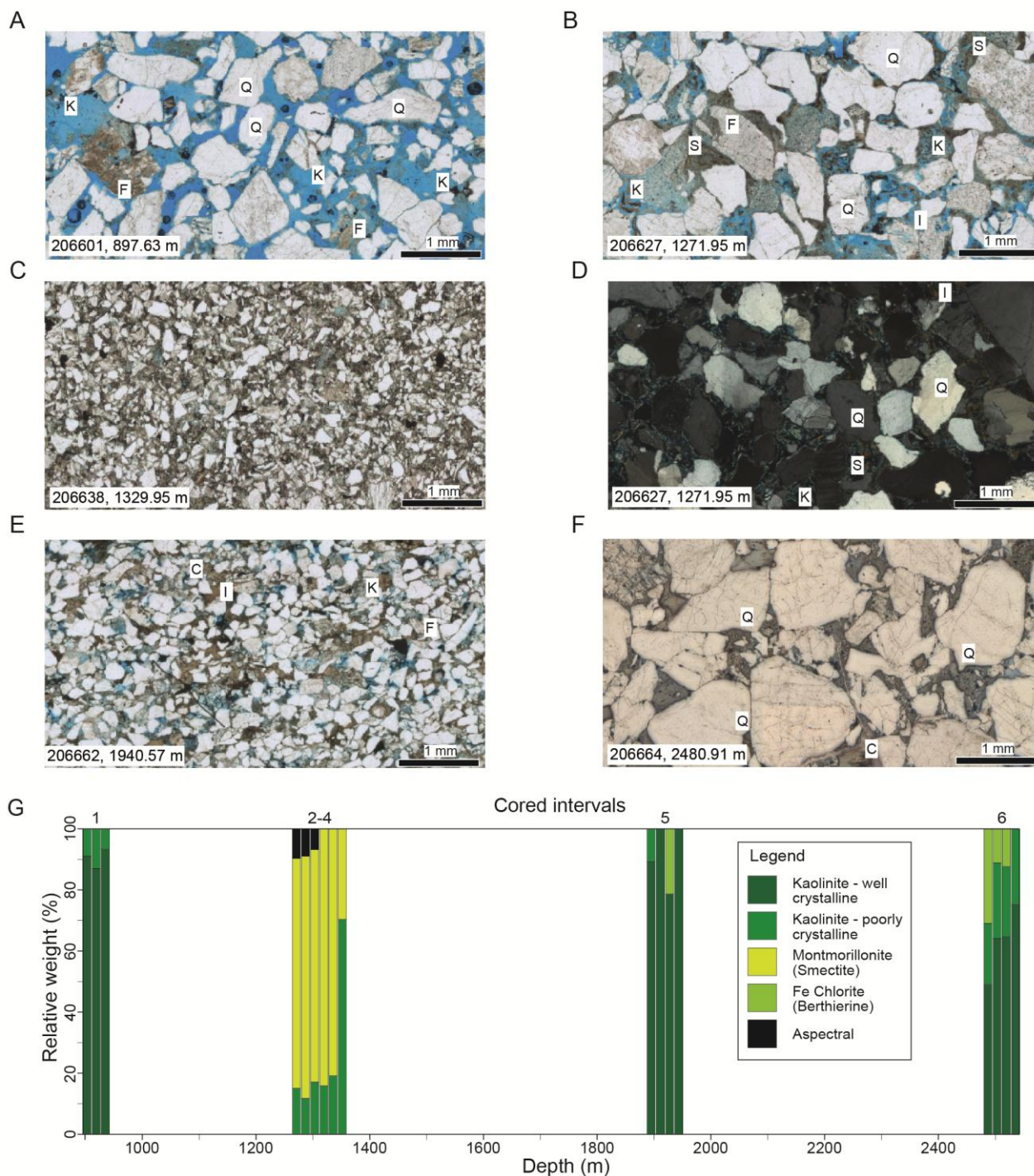


Figure 2.6. Bar charts to show modal mineralogy from x-ray diffraction data, sorted by lithofacies. Vertical axis expresses depth in meters.



**Figure 2.7. Diagenetic phases, textures and distribution in Harvey-1. (A) Patchy authigenic kaolinite cementation. (B) Pervasive kaolinite cement mixed with illite and smectite cement. (C-D) Mixed proportions of kaolinite, illite and smectite cement. (E) Kaolinite and chlorite cement, with minor illite. (F) Fractured grains typical in coarse grained rocks from deeper intervals, with elongate chlorite (berthierine) between quartz grains. Q=quartz, F=feldspar, K=kaolinite, I=illite, S=smectite, C=chlorite. (G) Distribution of OH- group-bearing minerals (except illite), including kaolinite, smectite and Fe-chlorite.**

## 2.4.2 DIAGENETIC CEMENTS AND DISTRIBUTION

Quartz overgrowth cements are very weakly developed in cores 1 to 4, but are more common in cores 5 to 6. They are identified by dust rims on detrital quartz grains, and marked by long and concavo-convex

boundaries (Fig. 2.7F). The proportions of quartz overgrowths to detrital overgrowths have not been measured.

Kaolinite is the main diagenetic clay mineral, which typically occurs as microcrystalline coatings on detrital grains and as heterogeneously distributed pore-occluding clots (Fig. 2.7A-E). Illite is a secondary diagenetic mineral, which typically occurs as pore-occluding clots (Fig. 2.7B-E). Smectite forms are inter-grown with illite in pore-occluding clots. This is restricted to cores 2-4 in floodplain palaeosols (facies D) (Fig. 2.7B-D). Berthierine, an iron-rich chlorite, is found in the Wonnerup Member, particularly in finely laminated and bedded sandstone (facies C and Aii, respectively). Clay-rich laminae found in these facies comprise primarily organic carbon, berthierine and minor kaolinite (Fig. 2.7E-F). Data collected from the Hylogger shows that these minerals, which are most likely diagenetic, are distributed unevenly downhole (Fig.2.7G). Core 1, at the top of the Yalgorup Member, comprises primarily well-formed kaolinite, with minor poorly-formed kaolinite. Core 2 comprises poorly-formed kaolinite and montmorillonite (smectite). Core 5 and 6 comprises poorly- and well-formed kaolinite and berthierine, an iron-rich chlorite, with core 6 exhibiting more chlorite. The distribution of illite is unknown, due to its composition being indistinguishable from muscovite.

Compaction-related textures such as elongate grain boundaries and reduced primary porosity, increase with depth. Bedding-parallel intragrain fractures, however, are not pervasive and do not propagate across multiple grains. Randomly oriented fractures are common, but show no increased frequency with depth, suggesting they were inherited prior to deposition. These internal fractures do not propagate across grains.

Solution features, such as stylolites, were not observed in Harvey-1.

### **2.4.3 QUANTITATIVE GRAIN SIZE DISTRIBUTION**

Lithofacies are primarily characterized by their grain size, sorting, colour and sedimentary structures. Quantitative grain size analysis of framework grains in each thin section samples allows for further characterization of these facies.

All samples exhibit a pronounced positively skewed tail, which indicates that the sorting in the majority of facies is moderate to poor (Fig. 2.8). This is less pronounced in facies D and E, where grain sizes are much smaller, and the very fine grains (<0.01 mm) are screened out because they are smaller than the resolution of the image. When these data are sorted by facies, there is a trend of reducing mean and median grain size from facies Ai to facies E (Fig. 2.9). The maximum grain size tends to decrease from facies Ai to E. However, facies Aii and facies D have some very large grains (> 2 mm). These do not exceed more than 20 and 5 grains for facies Aii and D, respectively, and therefore do not significantly alter the mean. Facies Aiii, B and C are relatively similar, with an insignificant grain size and sorting differences between samples of these facies. The differentiation of these three facies cannot be measured by grain size and sorting alone, and therefore their identification depends heavily on their sedimentary structures and colour.

## **2.5 Discussion**

### **2.5.1 PROVENANCE**

Mineralogical analyses are able to identify the possible provenance for samples. Harvey-1 samples consist of predominantly single-crystal quartz, with some polycrystalline quartz, particularly in facies Ai, and extremely rare lithic fragments. With moderate feldspars and clay minerals, these would typically classify as subarkose (Folk, 1965) and orthoquartzite (Selley, 1988). In conjunction with the presence of minor garnet, their provenance is likely to be from granites and granitic gneisses. Quartz-feldspar-lithic fragments proportions suggest that the origin of sedimentary clasts is from stable cratons and transitional continents. This can be potentially derived from the Yilgarn craton, Greater India (Gondwana breakup), the Leeuwin complex, the Albany-Fraser orogen or any combination of these source regions which cannot be distinguished based on the analysis of clast types alone. The exact provenance of the infill of the basin is



still an open question; however, studies of detrital zircons indicate a relatively minor Yilgarn component (Cawood & Nemchin, 2000; Sircombe & Freeman, 1990), while the presence of non-altered feldspar in the Triassic sediments intersected by Harvey-1 and Pinjarra-1 may suggest that a non-negligible component of the infill originated from a relatively close source (the Yilgarn) as also postulated in the stratigraphic forward modelling of Griffiths et al., (2012).

## 2.5.2 DIAGENESIS

An understanding of diagenetic minerals is important to understand the reactions that may take place upon introduction of carbon dioxide into the rock system. In the Harvey-1 rock samples, framework grains consist primarily of quartz and K-feldspar, the latter of which can have slow reactions with carbon dioxide (Janda and Morrison, 2001). Clay minerals typically do not react with carbon dioxide, however, they do have a good potential for slowing the movement of CO<sub>2</sub> through in partially-occluded pores (Janda and Morrison, 2001).

Authigenic quartz, identified as rims on quartz grains, is low (estimated at <5 %). This is thought to be the result of early kaolinite formation, coating quartz grains and therefore inhibiting quartz precipitation (Tada and Siever, 1989). However, in the Wonnerup Member (cores 5 and 6), the lower abundance of clay minerals to form a coating around framework grains allows authigenic quartz overgrowths to develop. The dissolution and re-precipitation of quartz thereby forms long and sutured contacts.

Kaolinite pores are sub-hedral and similar in size to that of adjacent framework grains. This may suggest that kaolinite is formed through dissolution of other framework grains. Point counting has shown that plagioclase (albite) is rare, except in clay-rich floodplain palaeosols and swampy deposits. The dissolution of albite provides the aluminium and silicon for kaolinite formation, whereas sodium and potassium have probably been leached out by formation waters. Furthermore, many potassium feldspar clasts appear partially dissolved, probably as a result of preferential removal into solution from sodium feldspar lamellae in originally perthitic grains. Illite formed after kaolinite, probably from the dissolution of potassium feldspar and albite in the absence of formation waters becoming saturated. This may have allowed for potassium to remain out of solution and bond with the liberated aluminium and silicon. Since the majority of illite is formed in lower energy and lower porosity facies, this may have prevented the liberated potassium and sodium to dissolve.

The volume gained when K-feldspar breaks down to kaolinite is negligible because their specific gravities are almost equivalent. This suggests that primary pore space was approximately 20% prior to K-feldspar weathering to kaolinite.

Samples in Harvey-1 are weakly deformed. Undulose extinction and internal fractures in quartz grains do not propagate across grains. They are not preferentially orientated at grain-grain contacts, suggesting that deformation was inherited prior to deposition.

Further investigations may reveal more quantitative information on the maximum temperature witnessed by the rocks and on the degree of total pore space alteration during burial and diagenesis.

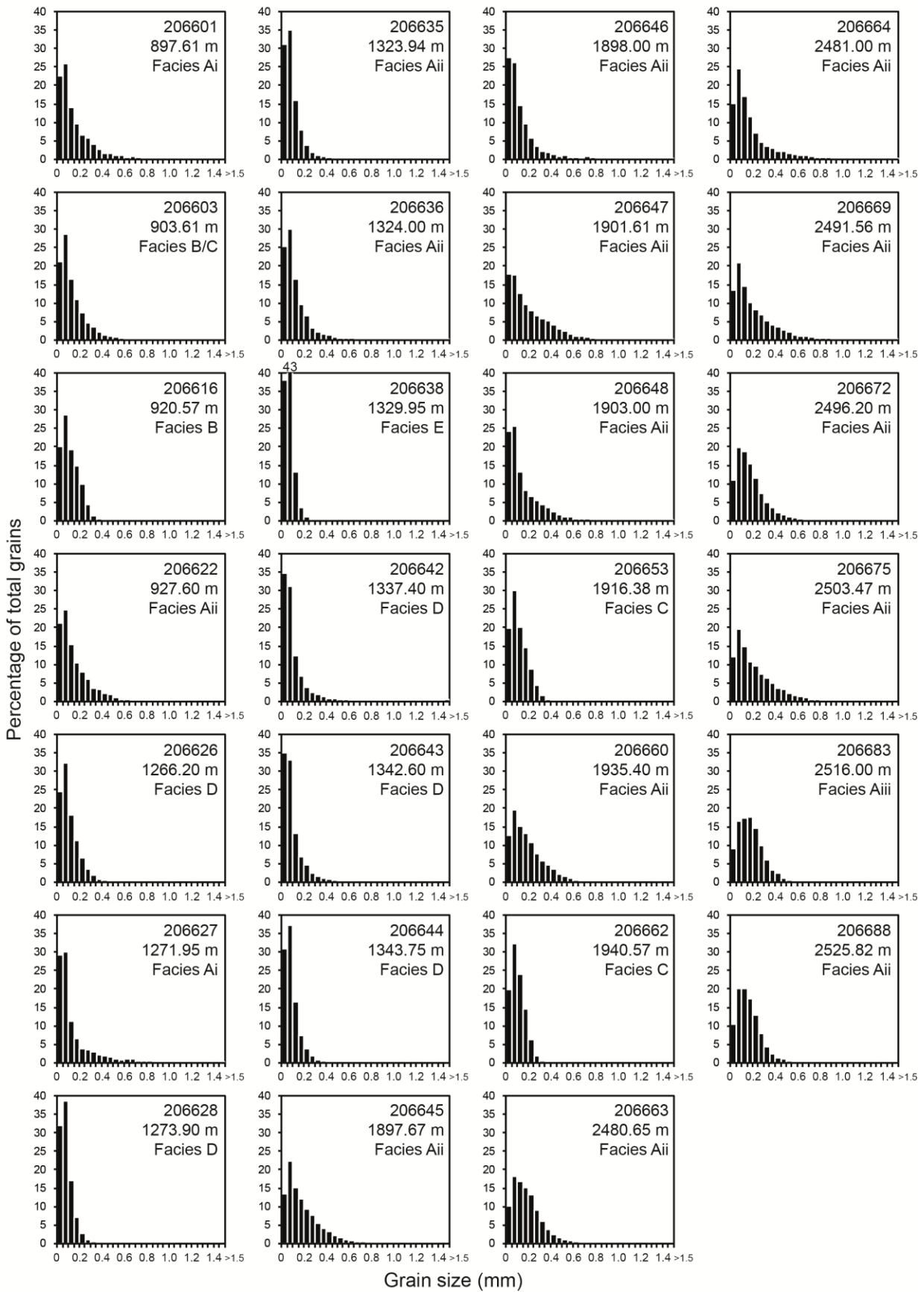
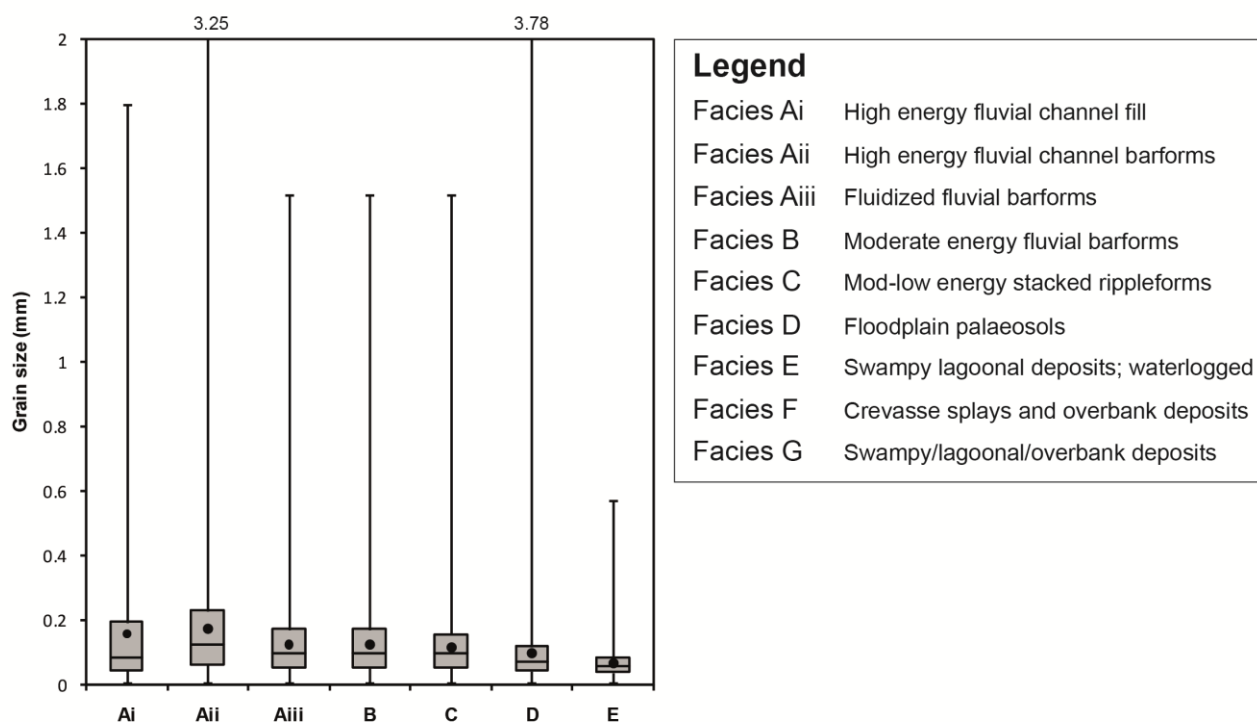


Figure 2.8. Quantitative grain size distribution outputs per sample, sorted by depth.



**Figure 2.9.** Quantitative box-and-whisker plots to show the distribution of grain sizes per facies. The graph shows the minimum (base of error bar), first quartile (base of rectangle), median (in rectangle), third quartile (top of rectangle), maximum (top of error bar) and mean (dot).

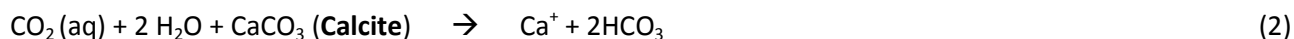
### 2.5.3 MINERAL REACTIONS

There are a number of geochemical reactions that can be expected when introducing carbon dioxide into a saline aquifer (Fisher et al., 2011; Shao et al., 2010; Wilkinson et al., 2009). These reactions include the interaction of CO<sub>2</sub>-enriched formation waters and the following minerals: (1) calcium carbonates (including calcite, dolomite and ankerite); (2) Plagioclase feldspar, and; (3) K-feldspar. The primary reactive mineral constituent is K-feldspar, which reacts as per below:



The products of the reaction include solid kaolinite and silicon dioxide (quartz or amorphous), with potassium ions and carbonic acid dissolved in solution. Kaolinite tends to precipitate as colloidal clays on grain surfaces, which do not significantly alter the porosity or permeability of the storage reservoir (Wilkinson et al., 2009). The Wonnerup Member, which acts as the potential reservoir for carbon dioxide storage, contains 8-13% K-feldspar in high energy channel fill and barforms. These facies are the primary constituent, with over 85% comprising of facies Ai-Aiii.

A secondary mineralogical reaction occurs between CO<sub>2</sub>-enriched formation water and carbonates. In the equation below, calcite is used as an example, but similar reactions occur with dolomite and ankerite:



In three samples examined 1% calcite and dolomite is present in three samples, and 4% ankerite is present in one sample. This provides another mechanism for mineral trapping of CO<sub>2</sub>, albeit significantly smaller than K-feldspar interaction. Dolomite and calcite cement dissolves without any precipitates, increasing the storage capacity, permeability and injectivity (Fisher et al., 2011). This can be advantageous, but could be undesired due to increased mobility of CO<sub>2</sub>. The results of the geochemical analysis from the project *Geochemical characterisation of gases, fluids and rocks in the Harvey-1 data well* (Stalker et al. 2013) will provide additional information on the reactivity of the SW-Hub reservoir unit to acidic brine and supercritical CO<sub>2</sub>.

## 2.6 Conclusions

Thin section samples were taken from the Yalgorup and Wonnerup Members of the Lesueur Sandstone. Single-crystal quartz is the dominant form of quartz. Small garnet inclusions and minor polycrystalline quartz suggests the provenance is from granites or granitic gneisses. Previous radiometric studies have indicated that this is most likely from the Yilgarn craton, Greater India (Gondwana breakup), the Leeuwin complex, the Albany-Fraser orogen or any combination of these (Cawood and Nemchin, 2000).

There is significant compaction and cementation (primarily kaolinite, and to a lesser extent illite, smectite and chlorite cement) in all samples, increasing with depth. The sub-hedral nature and size (reflecting the size of adjacent grains) of clay-occluded pores suggests that secondary porosity was created through weathering of feldspars. Authigenic quartz cement is rare and is thought to have been transported out of the system by formation waters.

Upon introduction of CO<sub>2</sub> into the Wonnerup Member, two mineral reactions may occur. The primary reaction is that of K-feldspar with CO<sub>2</sub>-enriched formation waters, producing harmless soluble products and kaolinite. This reaction is relatively slow, with significant dissolution of K-feldspar grains happening on the order of hundreds to thousands of years. A secondary reaction is that of carbonates with CO<sub>2</sub>-enriched formation waters, which may partially dissolve the solid minerals. These may increase the porosity and permeability of samples in the short terms (years to tens of years), increasing the mobility of injected CO<sub>2</sub>.

# 3 Module 3: Wireline log analysis of Harvey 1

### 3.1 Summary

This study is part of the ANLEC R&D project to evaluate the suitability of the lower Lesueur Sandstone, in the Southern Perth Basin, to store carbon dioxide (CO<sub>2</sub>) emitted by various industrial sources in the SW of Western Australia.

Well log data from Harvey 1 are interpreted to obtain rock properties required for carbon storage site evaluation. A complete suite of log data was used to evaluate petrophysical properties of the Lesueur sandstone. The shale volume interpretation highlighted shale intervals of varying thickness (maximum 30m) in the Yalgorup Member. The Wonnerup Member on the other hand is composed from thick sand intervals lacking major shale breaks. Total porosity reduces with depth from 26% to less than 10% and permeability reduces from more than 4000mD to less than 10mD within the Wonnerup Member. Permeability of sand intervals for the Yalgorup Member ranges from more than 10,000mD to about 4mD.

Applying a shale volume cutoff of less than 20% and effective porosity larger than 8%, net to gross (NTG) values of 78% and 48% were computed for Wonnerup and Yalgorup Members respectively.

There is a slight water salinity difference between the Yalgorup and Wonnerup Members. The Yalgorup Member shows higher pore water salinity. The higher salinity of this Member when compared to the Wonnerup Member may indicate that shaly intervals in the lower part of the Yalgorup Member constitute a barrier or baffle and may inhibit fluid communications between the upper and lower Members of the Lesueur Sandstone. This observation may be relevant for the qualitative estimation of the containment potential of the proposed geosequestration site.

## 3.2 Introduction

The fluvial Lesueur Sandstone of Middle – Late Triassic age has been subdivided into an upper Member (Yalgorup Member) and a lower sandstone Member (Wonnerup Member). The Yalgorup Member includes sandstone with subordinate interbeds of finer clastic rocks whereas, the Wonnerup Member comprises mostly of sandstone beds. In the Wonnerup Member, the sandstone is feldspathic, poorly sorted, coarse- to very coarse-grained and light grey to colourless, in contrast to the Yalgorup Member, which is dark grey.

The objective of the petrophysical study was to evaluate the potential of the Lesueur Sandstone as a carbon dioxide geological sequestration site in the region of south western Western Australia. This study is part of an integrated study that investigates the rock facies and wireline log analysis for the petrophysical evaluation of the Lesueur Sandstone.

## 3.3 Data Collection

Wireline log data from Harvey 1 was provided by the Western Australia Department of Mines and Petroleum (WA DMP) for petrophysical evaluation. The log data available included gamma-ray, gamma ray spectrometry, density logs, neutron porosity, sonic log measurement, array resistivity and nuclear magnetic resonance. Fig. 3.1 displays the composite log data for Harvey-1.

A total of 82 routine core analysis data were available at the time this study was conducted. The core data included grain density, porosity and permeability, measured at 5.5 and 30MPa of confining pressure by Geotechnical Services PTY LTD (work commissioned by WADMP).

## 3.4 Data Quality Control

Editing and quality control of the raw wireline well logs were carried out before petrophysical evaluation. There is a major problem with the log data for the upper part of the Lesueur Sandstone (Yalgorup Member). Borehole size enlargement is pervasive from depths between 955m to 1376m. Borehole caving appears to occur for most of the shaly intervals. For the enlarged intervals the calliper data shows significant deviation from the bit size (BS=8.5 in.) and density correction values are quite large.

Core gamma scan was used to align core and log depth for the purpose of the core-log calibration and comparison.

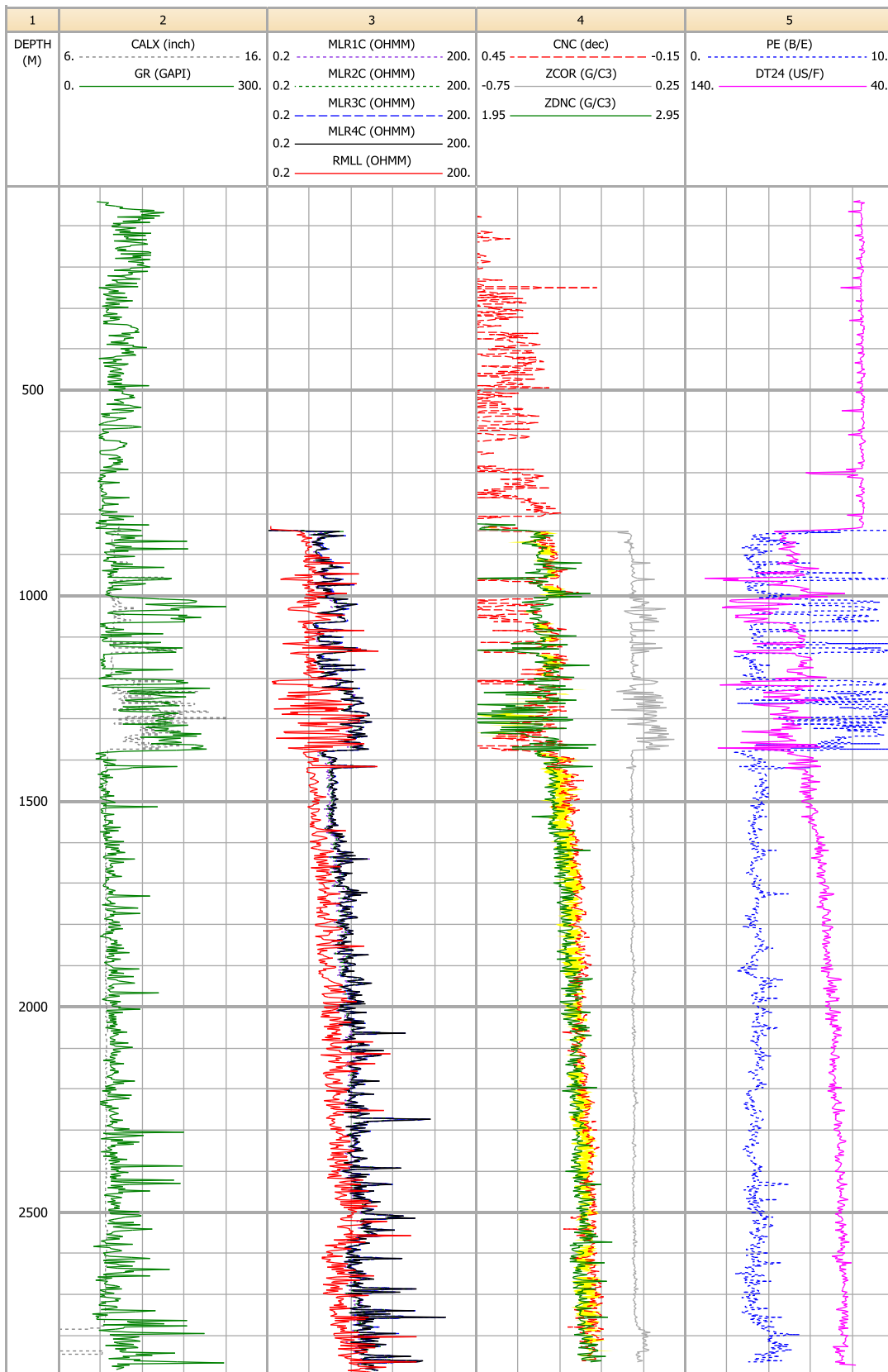


Figure 3.1. Log data for Harvey-1



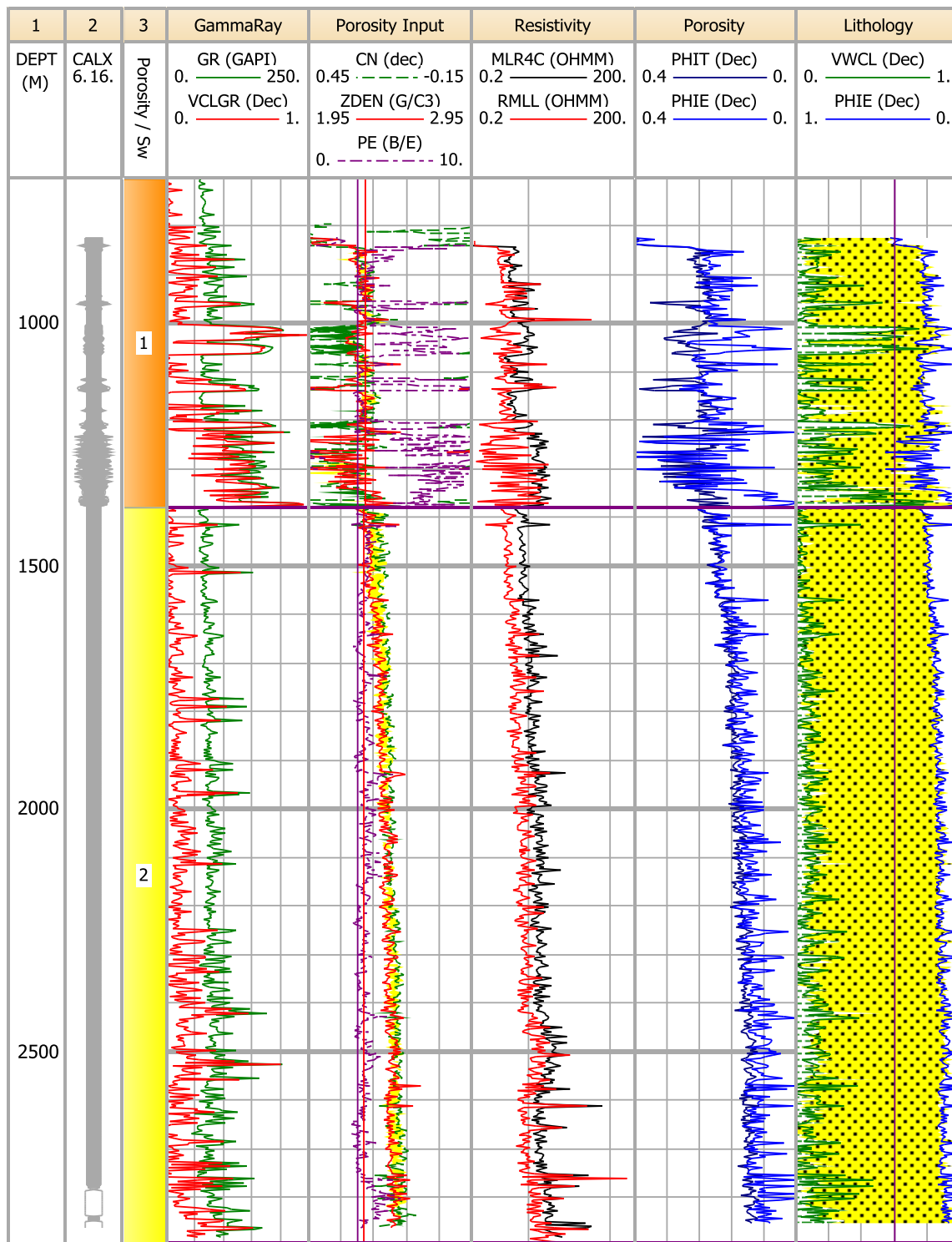


Figure 3.2. Log interpretation for Harvey-1

### 3.5 Petrophysical Evaluation

In this study the petrophysical evaluation defines shale volume, total porosity, effective porosity, permeability and net to gross ratio (NTG) of the Upper Lesueur Sandstone (named here as the Yalgorup Member) and Lower Lesueur Sandstone (Wonnerup Member). Figure 3.2 illustrates the log interpretation results for Harvey 1. The following sections describe the results of the log interpretations in detail.

### 3.5.1 VOLUME OF SHALE (VSH)

Mud log data indicates that the Yalgorup Member (from 704m to 1380m) includes sandstone with subordinate interbeds of shale and siltstone. The Wonnerup Member comprises mostly feldspathic, poorly sorted, coarse to very coarse grained sandstone with minor subordinates of shales and siltstone. The quantitative shale volume interpretation was based on the gamma ray and neutron-density log responses. The interpretation was also checked against mud log data and the core description report. The shale volume evaluation indicated that shale intervals of up to 30m in thickness exist within the Yalgorup Member, whereas the Wonnerup Member has only a few thin shale intervals. Total shale thickness for the Yalgorup Member is about 145m, based on a shale cutoff value of 50%. This thickness of shale is about 21% of the total thickness of the Yalgorup Member, which is about 676m. Whereas for the Wonnerup Member, with a total thickness of 1501m, the shale thickness is approximately 25m, less than 2% of the total thickness of this Member (Fig. 3.3).

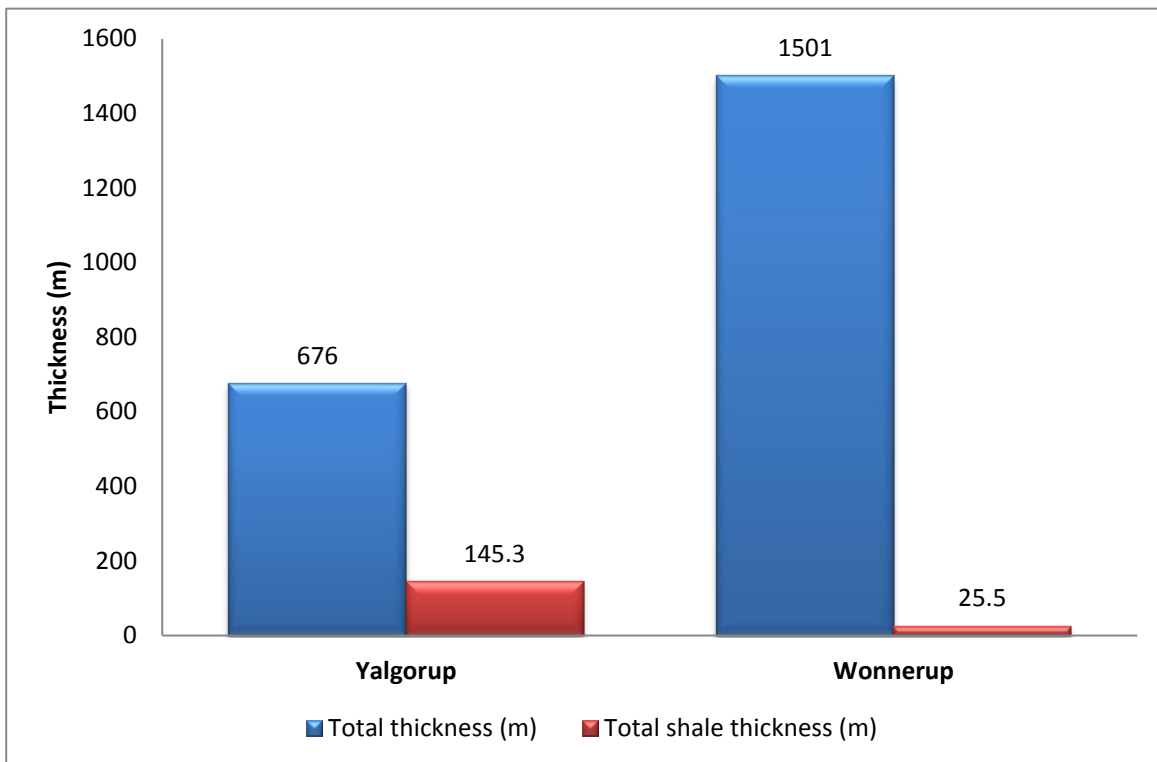


Figure 3.3. A comparison of the shale thickness with the total thickness of the Lesueur Sandstone Members

### 3.5.2 POROSITY

Neutron, density and sonic log data were used to estimate total, effective and secondary porosities. The following basic equations were used for porosity calculations:

$$\phi = \frac{\rho_{ma} - \rho_b}{\rho_{ma} - \rho_f}$$

Equation 3.1

Where:  $\rho_b$  = the bulk density of the formation  
 $\rho_m$  = the density of the rock matrix

$\rho_f$  = the density of the fluids occupying the pore space

$\phi$  = the porosity of the rock

$$\phi = \frac{\Delta T_{log} - \Delta T_{ma}}{\Delta T_f - \Delta T_{ma}} \quad \text{Equation 3.2}$$

where,  $\Delta T_{log}$  is the reading on the sonic log

$\Delta T_{ma}$  is the transit time of matrix material

$\Delta T_f$  is the transit time of the saturating fluid (189  $\mu$ s/ft for freshwater)

The effective porosity in shaly formations is calculated by including a correction for the contribution of shale to the log measurements according to:

$$\phi_{Dshc} \approx \phi_e = \frac{\rho_{ma} - \rho_b}{\rho_{ma} - \rho_f} - V_{sh} \frac{\rho_{ma} - \rho_{sh}}{\rho_{ma} - \rho_f} \quad \text{Equation 3.3}$$

Where:

$\rho_b$ : bulk density (gm/cc);  $\rho_f$ : fluid density (gm/cc);  $\rho_{ma}$ : matrix density (gm/cc);  $\phi_D$ : density derived porosity;  $V_{sh}$ : volumetric fraction of shale;  $\rho_{sh}$ : shale bulk density (gm/cc);  $\phi_{Dshc}$ : shale corrected density porosity and  $\phi_e$ : effective porosity.

$$\phi_{Nshc} \approx \phi_e = \phi_{Nc} - (\phi_{Nc-sh} \times V_{sh}) \quad \text{Equation 3.4}$$

Where:

DT: sonic log reading (msec/ft);  $DT_f$ : transit time for the fluid (msec/ft);  $DT_{ma}$ : transit time for matrix (msec/ft);  $DT_{sh}$ : shale transit time (msec/ft);  $\phi_s$ : sonic derived porosity and  $\phi_{Sshc}$ : shale corrected sonic porosity.

A porosity-depth trend is observed, with total porosity varying from 26% to 10% decreasing with depth (Fig. 3.4). In the Yalgorup Member average total porosity is 23%. This reduces to 14% for the Wonnerup (Fig. 3.5).

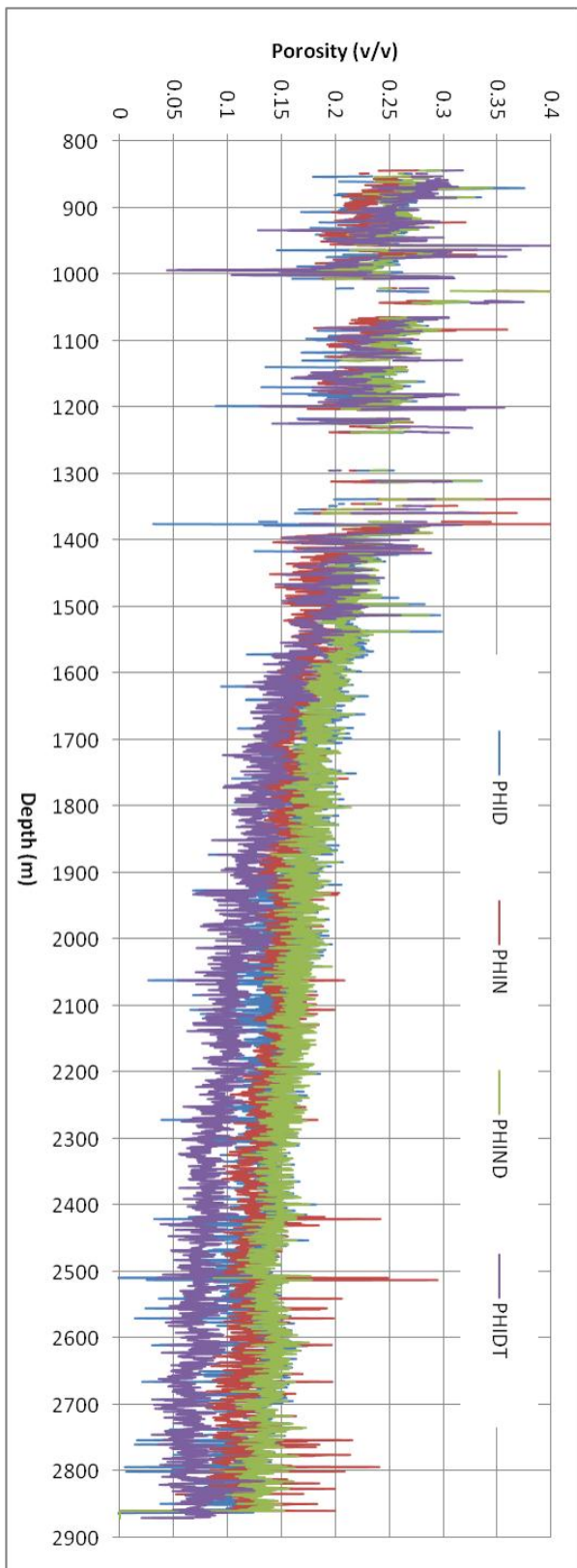


**Figure 3.4. Porosity-depth trend for the Lesueur Sandstone. Density porosity (PHID), neutron porosity (PHIN) and average neutron-density porosity (PHIND) show slightly higher porosity values than that of the sonic porosity (PHIDT). This difference in porosity can be due to the development of dissolution porosity with increased depth.**

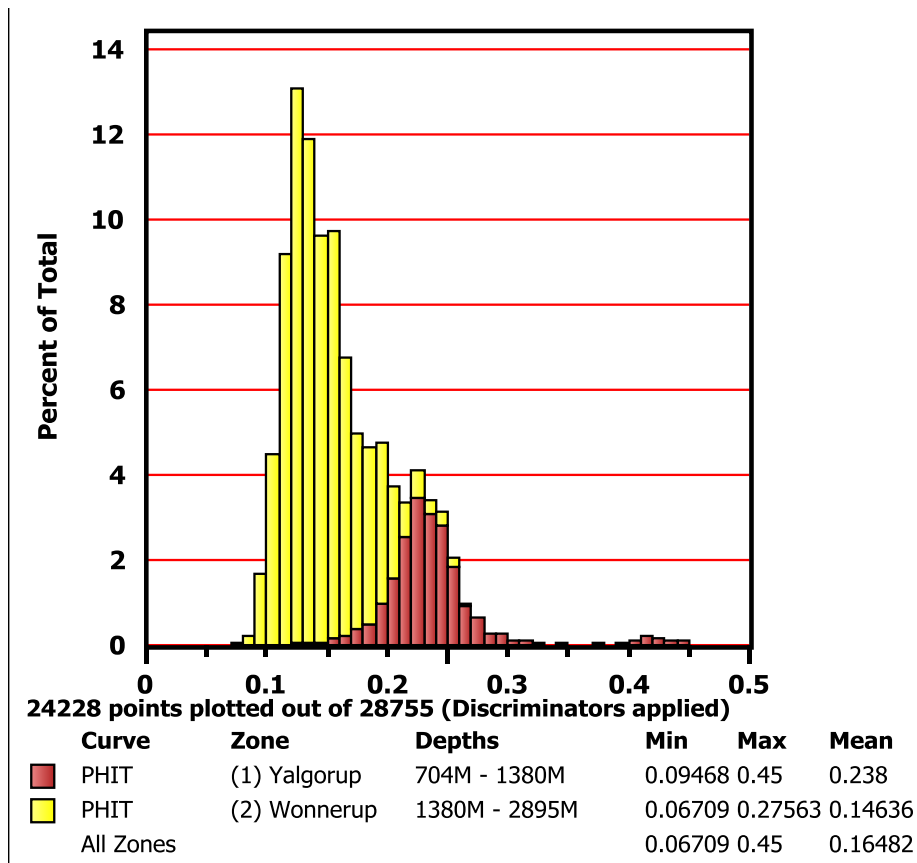


Figure 3.5. A histogram showing the fractional porosity distribution for the Yalgorup and Wonnerup Members. Horizontal axis represents fractional porosity values.

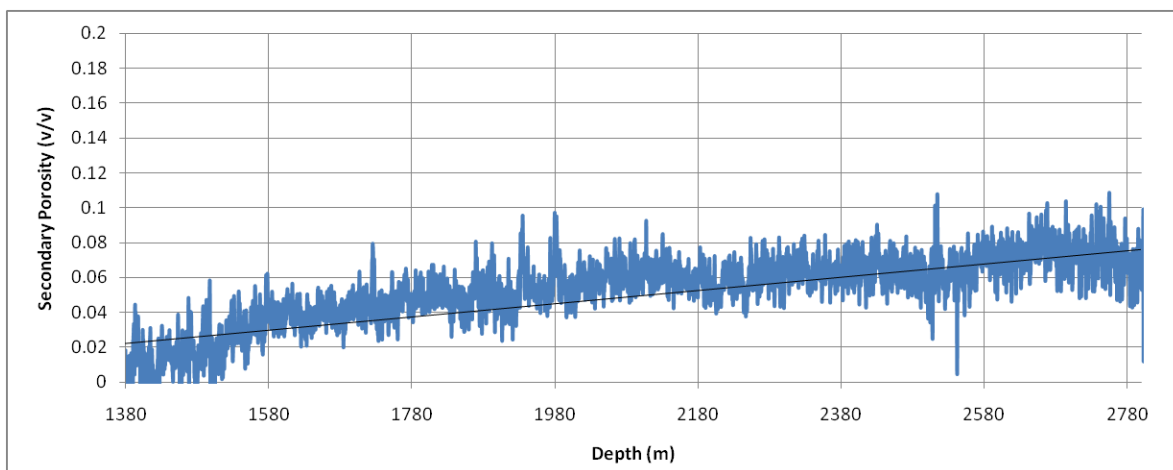


Figure 3.6. Secondary porosity, calculated from the difference between the total and sonic porosity, increases with increasing depth.

Secondary porosity is calculated from the difference between neutron-density porosity and sonic porosity. Secondary porosity that may result from feldspar dissolution and other lithic grains, increases with increasing depth from near to zero to about 8% (Fig. 3.6). Secondary porosity in the sandstone may develop through feldspar dissolution during deep burial.

A comparison between core and log porosity shows an acceptable match. The best correlation is between the effective density porosity and core porosity with a coefficient of determination of about 72% (Fig. 3.7).

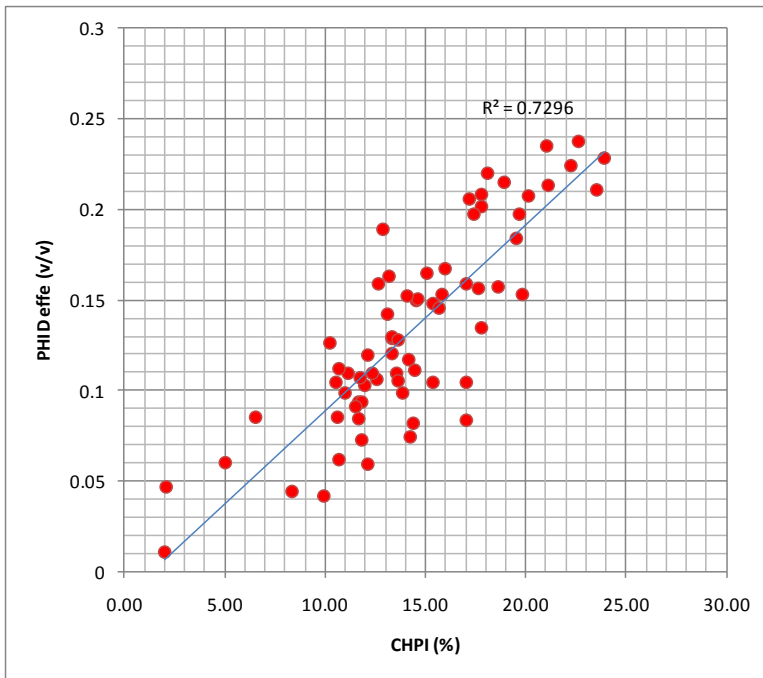


Figure 3.7. A plot of core porosity (CPHI) versus the effective density porosity (PHIDeffe).

### 3.5.3 WATER SATURATION

Mud log data, the well completion report and resistivity logs all indicate a fully water saturated sandstone for the whole drilled section.

### 3.5.4 PORE WATER RESISTIVITY (RW)

The Archie equation was used to estimate the resistivity of the formation water. When brine saturation ( $S_w$ ) = 1, and tortuosity factor ( $a$ ) = 1, then,

$$R_{wa} = R_t \times \phi^m \quad \text{Equation 3.5}$$

Cementation exponent ( $m$ ) is necessary to estimate apparent pore water resistivity ( $R_{wa}$ ) for the Archie method. The Picket plot indicates  $m=1.65$  for the Lesueur Sandstone (Fig. 3.8).

$R_{wa}$  from the Archie method (considering  $m=1.65$  and  $a=1$ ) indicates a value of approximately 0.1 ohm-m and 0.14 ohm-m for the Yalgorup Member and the upper part of the Wonnerup Member respectively (Fig. 3.9). These values can be translated to 40,000ppm NaCl equivalent salinity for the Yalgorup Member and 30,000ppm NaCl equivalent salinity for the Wonnerup Member at a temperature of 50°C.

In general the pore water resistivity for the Yalgorup Member appears to be less than the Wonnerup pore water resistivity, if we consider the general increasing trend of  $R_w$  with depth (green line in Fig. 3.9). This may indicate that these two rock units are not hydraulically in communications and that the shaly intervals in the lower part of the Yalgorup Member can be considered as intra-formational barriers to the upward migration of the CO<sub>2</sub> plume.

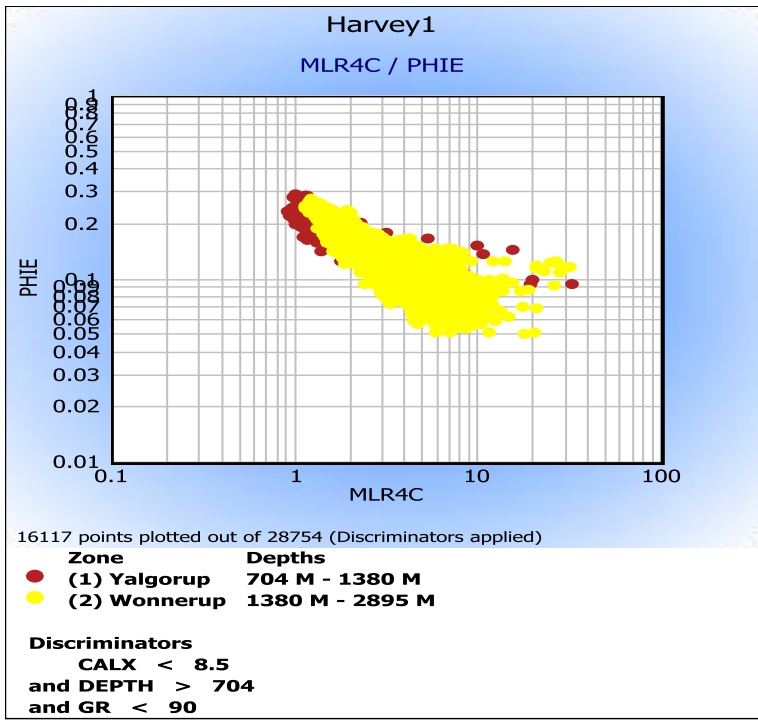


Figure 3.8. Picket plot of deep resistivity versus porosity. This plot suggests a value of 1.65 for the cementation exponent and a  $R_w$  of about 0.1 ohm-m and 0.14 ohm-m for the Yalgorup Member and the upper part of the Wonnerup Member respectively.

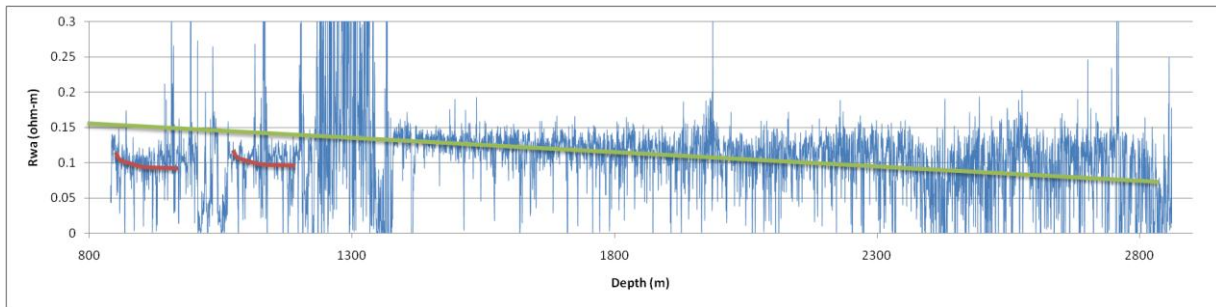


Figure 3.9. Pore water resistivity for the Lesueur Sandstone. The green line shows the general salinity trend with depth for the Wonnerup Member. Sand intervals in the Yalgorup Member show a lower resistivity (Red lines) trend when compared with the general trend.

### 3.5.5 PERMEABILITY

Nuclear magnetic resonance (NMR) tools are able to provide a measurement of the amount of both effective and capillary pores, and thus they can be used to estimate permeability. NMR measurements have been conducted over seven depth intervals in the Wonnerup Member. Figure 3.10 shows the different porosity types measured by the NMR tool for Harvey 1.

The relaxation time ( $T_2$ ) cutoffs of 3.4ms and 33ms are used to define clay-bound water from free fluid index porosity respectively. As it can be seen in Figure 3.10, the clay-bound water is not the major porosity type since the clay content of the Wonnerup Member is very low. In general total NMR porosity reduces from 25% to about 12% with depth.

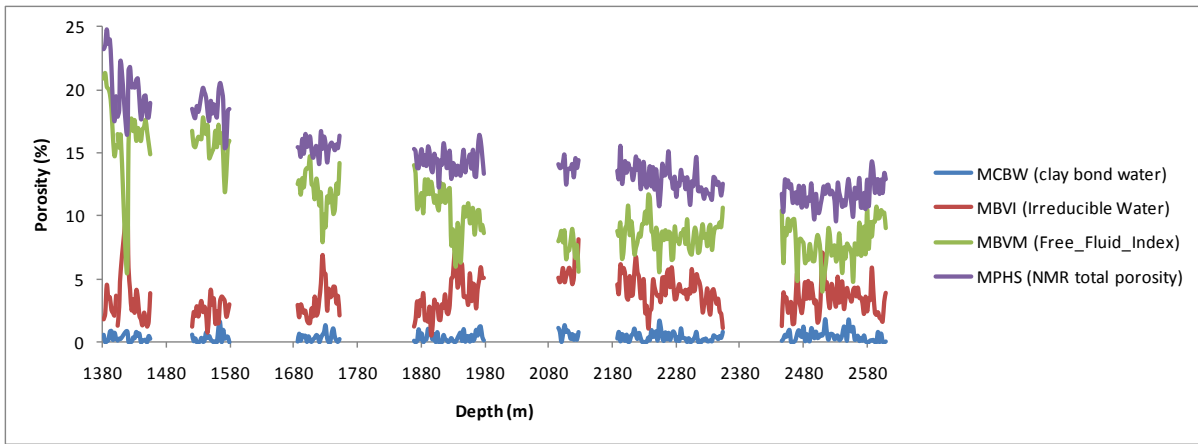


Figure 3.10. Clay-bound water, irreducible water, free fluid index and total NMR porosity for the Wonnerup Member.

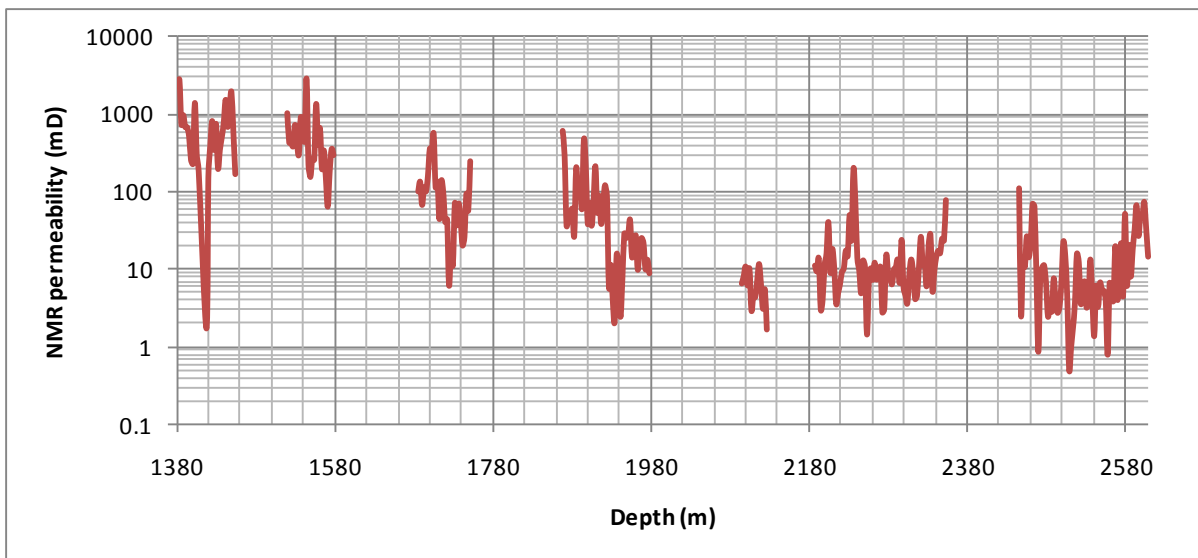


Figure 3.11. Permeability variation with depth for the Wonnerup Member. Permeability reduces significantly with depth.

Nuclear Magnetic Resonance data was used for permeability estimation. For this purpose the Coates model was utilized to estimate permeability:

$$k = \left[ \left( \frac{\phi}{C} \right)^2 \left( \frac{FFI}{BVI} \right) \right]^2 \quad \text{Equation 3.6}$$

Where,  $k$  = permeability (in mD);  $\phi$  = NMR total porosity (in %);  $C$  = a constant that reflects the correlation between the rock's pore throat and pore size and is a function of pore geometry;  $FFI$  = the free fluid index, and  $BVI$  = the bound volume of irreducible water.

A value of 10 was considered representative for  $C$ .

Figure 3.11 shows the permeability variation with depth for the Wonnerup Member.

Using multi-regression analysis, relationships to transform the well log data into permeability were developed in this study. Table 3.1 lists equations that can be used to estimate permeability for un-cored intervals. There is a strong relation between the bulk density and the permeability. The other log data appear to have less correlation with the permeability (Fig. 3.12). The equations introduced in Table 3.1 are



valid for clean sands since they are based on the NMR permeability that has been run in the sandstone part of the Lesueur Sandstone.

Equation	R-Sq
$\log k = 27.8 - 10.9 \text{ ZDNC}$	71.6%
$\log k = 31.2 - 12.1 \text{ ZDNC} - 3.38 \text{ CNC}$	72.3%
$\log k = 29.1 - 11.0 \text{ ZDNC} - 1.17 \text{ CNC} - 0.285 \text{ PE}$	73.6%
$\log k = 19.6 - 8.64 \text{ ZDNC} - 7.69 \text{ CNC} + 0.0536 \text{ DT}$	73.5%
$\log k = 18.2 - 7.73 \text{ ZDNC} - 5.39 \text{ CNC} + 0.0511 \text{ DT} - 0.272 \text{ PE}$	74.7%
$\log k = 23.9 - 10.3 \text{ ZDNC} - 8.83 \text{ CNC} + 0.0504 \text{ DT} + 0.0313 \text{ MLR4C}$	74.0%
$\log k = 22.4 - 9.36 \text{ ZDNC} - 6.52 \text{ CNC} + 0.0481 \text{ DT} - 0.270 \text{ PE} + 0.0307 \text{ MLR4C}$	75.1%

**Table 3.1. Relationships between different log data and permeability.** k is permeability (mD), ZDNC is bulk density (g/cc), CNC is neutron porosity (v/v), PE is photoelectric factor (barn/e), DT is sonic transit time (us/ft) and MLR4C is deep resistivity (ohm-m).

Figure 3.13 shows the correlation between the NMR-Coates permeability and calculated permeability using the last equation in Table 3.1. This equation was used to calculate permeability over the whole thickness of the Wonnerup and Yalgorup Members (Figs 3.14 and 3.15). This shows a clear trend in the permeability reduction with depth. Permeability reduces from more than 4000mD to less than 10mD for the Wonnerup Member. For the Yalgorup Member bad hole flag intervals and shale layers were removed before conducting the permeability calculation. For this Member, the permeability of sand intervals range from more than 10,000mD to less than 4mD.

There is a good correlation between the core permeability and the calculated permeability. Figure 3.16 shows the relation between these two permeabilities for the Yalgorup and Wonnerup Members.

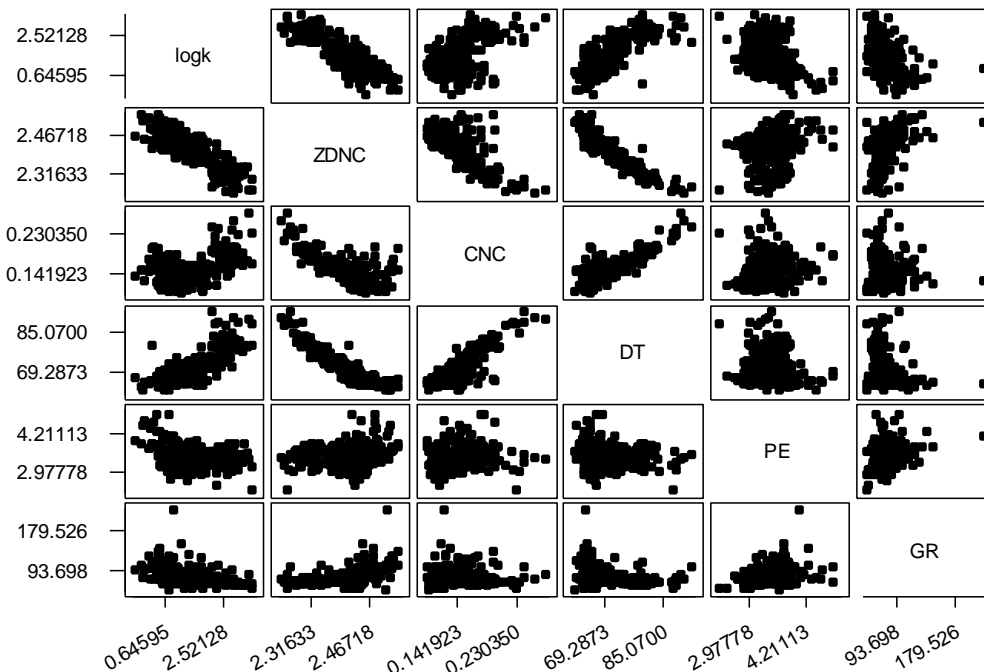


**Figure 3.12. Matrix plot of the NMR permeability versus the log data.**

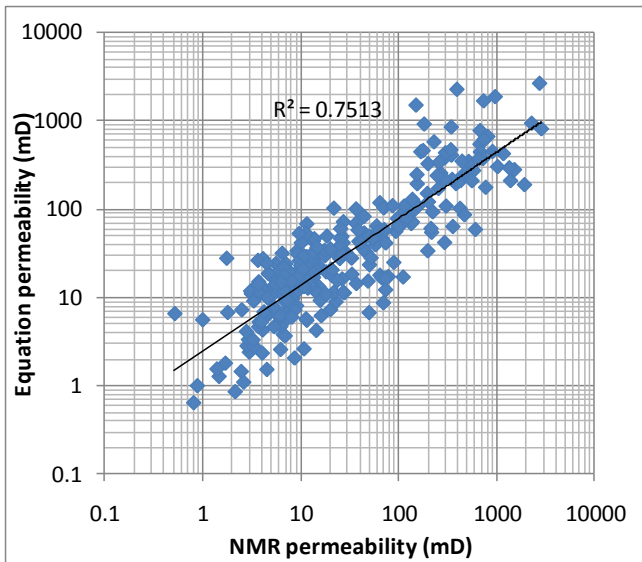


Figure 3.13. The correlation between the NMR permeability and calculated permeability from the last equation in Table 3.1.

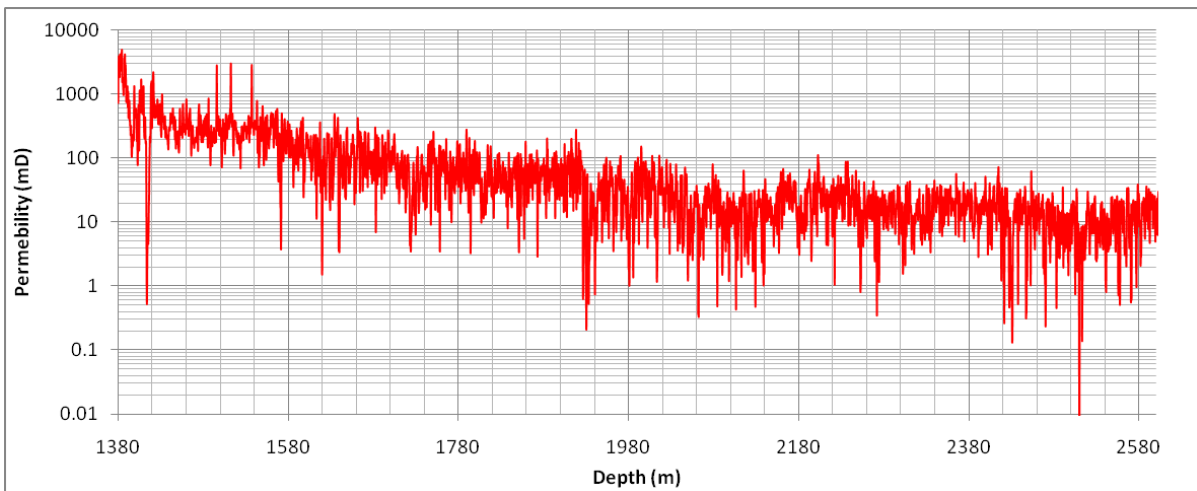


Figure 3.14. Calculated permeability versus depth for the Wonnerup Member.

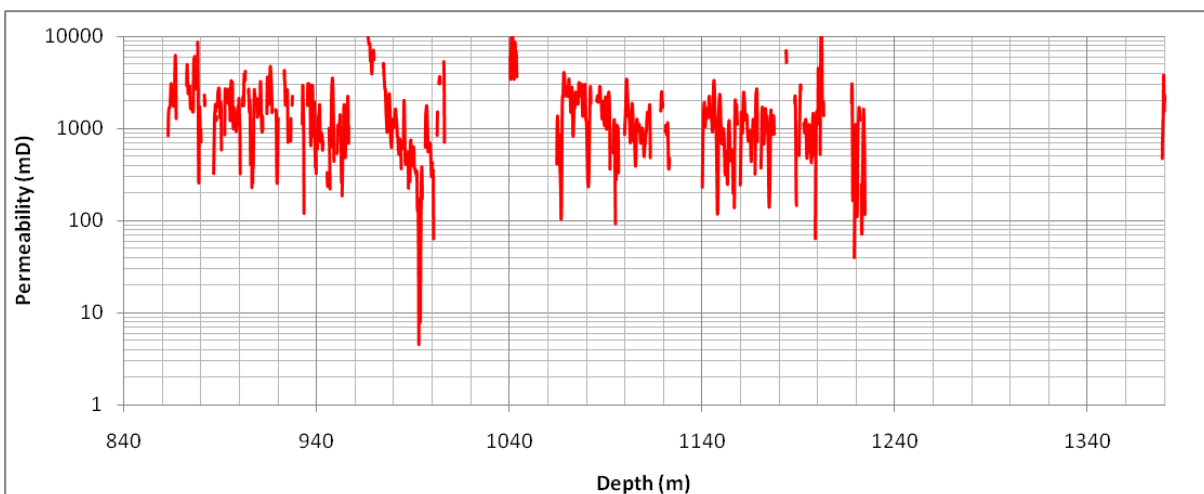


Figure 3.15. Calculated permeability versus depth for the Yalgorup Member. Bad hole data are removed.

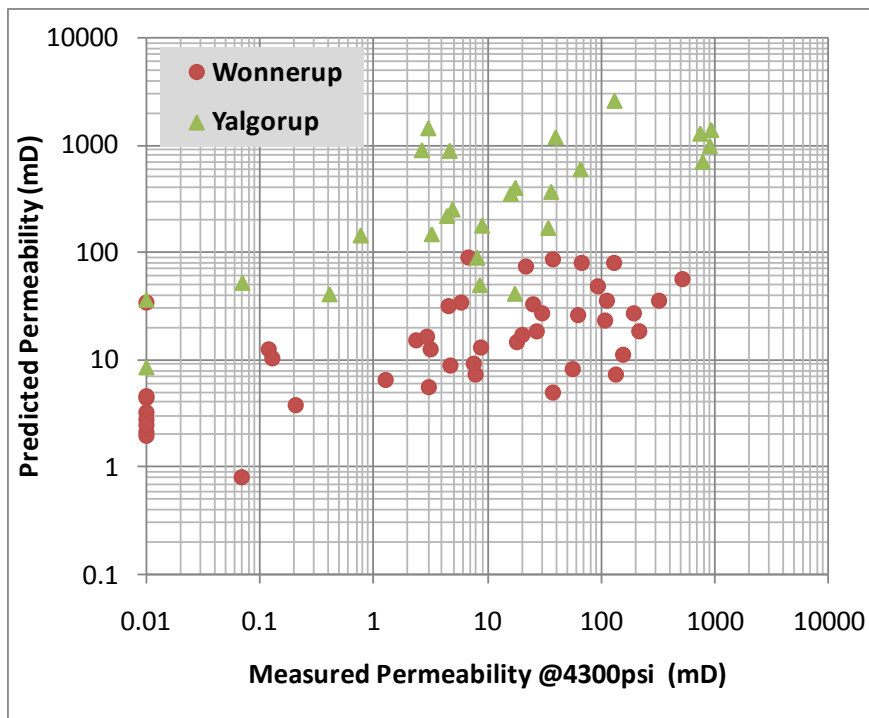


Figure 3.16. Measured permeability versus calculated permeability for the Yalgorup and Wonnerup Members.

Nevertheless, differences in the measured and predicted permeabilities are inevitable considering that the two techniques investigate different rock volumes and that the samples tested in the laboratory may have been affected by some sort of modifications with respect to their in – situ state, including stress relief, drying and machining. Finally, it should be noted that the laboratory permeability is based on the measurements of pore pressure decay in a gas saturated sample, while NMR permeability is inverted from a relaxation time signal of hydrogen nuclei subject to a magnetic field. As such any correlation between laboratory and log measurements should be used as a qualitative guide, but care should be taken when inferring quantitative relationships.

### 3.5.6 POROSITY AND PERMEABILITY RELATION

There is a good match between core porosity and core permeability. This match improves when the samples are plotted separately for each Member or for each facies (Fig. 3.17, see also detailed analysis in module 4).

Log porosity shows relatively less correlation with the core permeability as indicated by the r-squared value of about 38% (Fig. 3.18). There is however a non-linear correlation between these two variables in the form of the following equation:

$$k \text{ (mD)} = 0.039e^{37.339\phi}$$

Since the coefficient of determination value for this regression equation is low, there would be a large uncertainty if this equation was to be used to calculate permeability.

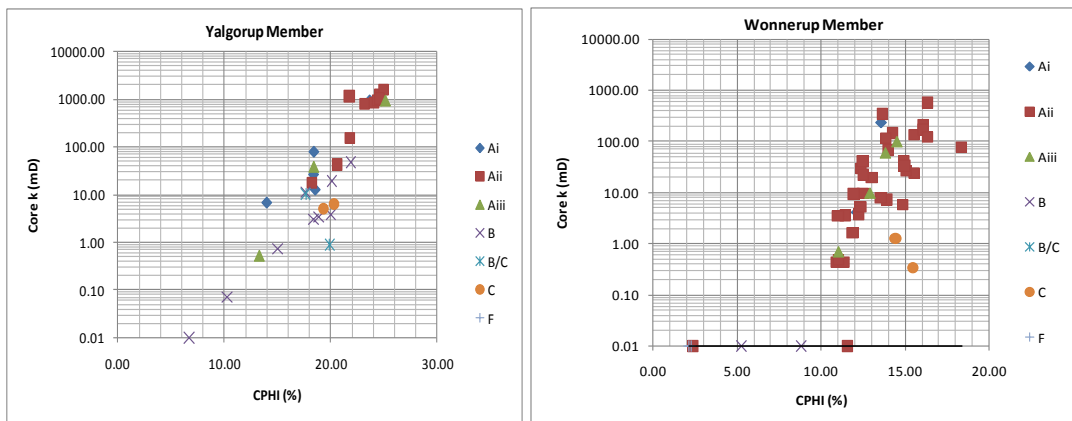


Figure 3.17. Core porosity versus core permeability for the Wonnerup and Yalgorup Members.

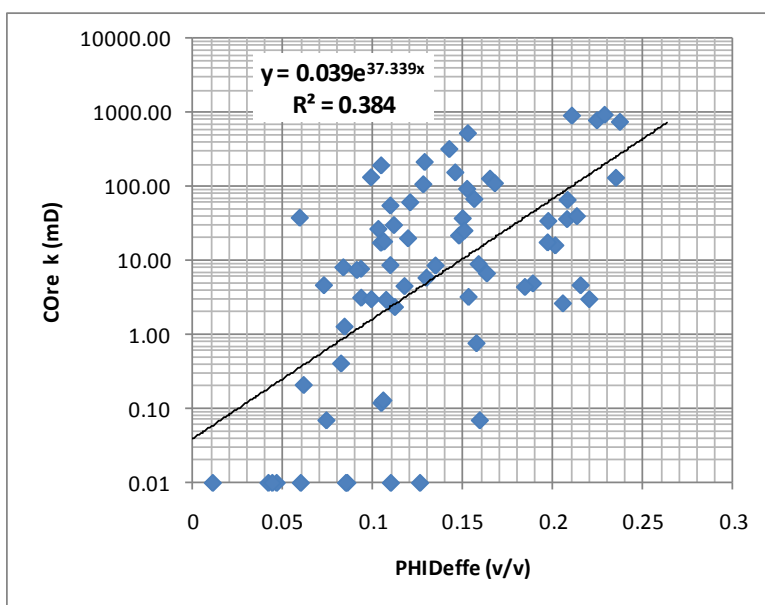


Figure 3.18. A plot of log porosity versus core permeability.

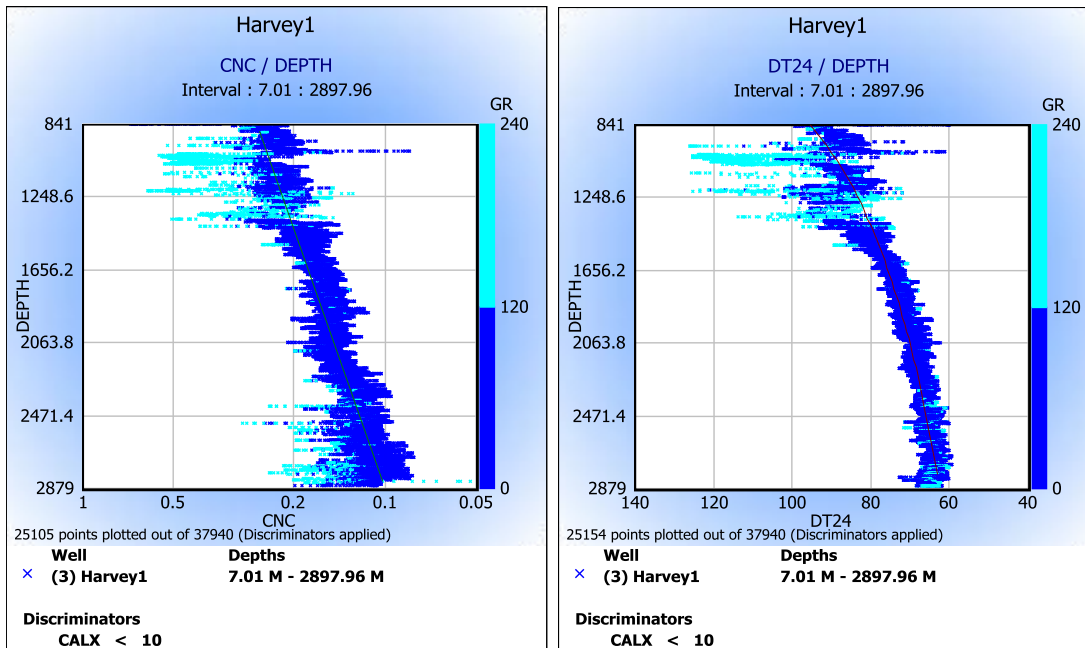
### 3.6 Summary of Petrophysical Evaluation Results

Table 3.2 summarizes the petrophysical properties evaluated in this study. These petrophysical properties are computed separately for the Yalgorup and Wonnerup Members.

Member	Top (MDRT)	Base (MDRT)	Thickness (m)	Net sand thickness (m)	N/G	Effective porosity (%)	Permeability (mD)
Yalgorup	704	1380	676	259	0.48*	16	1705
Wonnerup	1380	2895	1515	1188	0.78	13	95

Table 3.2. A summary of the average estimated petrophysical properties for the Lesueur Sandstone, Harvey-1. \*This NG value is for the part of the Yalgorup that has a complete suite of log data.

The Yalgorup Member shows significant log pattern differences when compared with the Wonnerup Member. In the Yalgorup Member there are many washouts in the shale intervals. Very high acoustic transit time and high neutron porosity values for the shale intervals of the Yalgorup having good borehole conditions suggest possible over-pressuring conditions (Fig. 3.19).



**Figure 3.19. Sonic transit time (left) and neutron porosity (right) versus depth. The upper part of the Lesueur Sandstone (Yalgorup Member) shows a high DT and high hydrogen index for the shaly intervals indicating possible over-pressure conditions. Bad hole intervals are removed.**

Sand intervals of the Yalgorup Member are also very different from the sands of the Wonnerup. They show very different log responses as indicated in Table 3.3 comparing the petrophysical values recorded on a clean sandstone in the Yalgorup Member (depth 1069.5m) with a clean sandstone in the Wonnerup Member (depth 1663m).

Member	Depth (m)	GR (API)	MLR4C (ohm m)	RMLL (ohm m)	CNC	ZDNC (g/cm <sup>3</sup> )	DT (μs/F)	Pe (B/E)	PHINDeffe	RWa
Yalgorup	1069.5	58	0.9	0.64	0.229	2.22	89.8	3.93	0.23	0.1
Wonnerup	1663	67	1.98	1.05	0.174	2.33	75.8	3.44	0.17	0.14

**Table 3.3. Comparative table summarising the wireline log characteristics of clean sandstone intervals from the Yalgorup and Wonnerup Members.**

It appears that the Yalgorup Member is lithologically different from the Wonnerup Member. Based on the core analysis report, the Yalgorup samples are very friable (that is more likely due to lack of cementation), and show a different composition (high content of feldspar and plagioclase; and presence of smectite and calcite) when compared with the Wonnerup Member. These differences may suggest that these two rock units may have formed in different environments.

### 3.7 Conclusions

A complete suite of log data including GR, density, neutron, PE, sonic, array resistivity and NMR were used to evaluate petrophysical properties of the Lesueur sandstone in Harvey 1. All computations were conducted separately for the upper Member, the Yalgorup, and the lower Member, the Wonnerup, of the Lesueur Sandstone. The data quality for the Yalgorup Member is not good due to extensive washout, whereas for the Wonnerup has good borehole quality.

The Lesueur Sandstone has the potential to be the target reservoir for CO<sub>2</sub> sequestration. The formation has reasonable porosity and permeability based on a petrophysical evaluation. The petrophysical evaluation estimated shale volume, porosity, effective porosity and permeability and net to gross ratio. The shale volume interpretation highlighted shale intervals of varying thickness (maximum 30m) in the Yalgorup Member. The Wonnerup Member on the other hand is composed of thick sand intervals with a lack of major shale breaks. In general both Members show a distinct porosity and permeability depth trend. Total porosity reduces from 26% to less 10% and permeability reduces from more than 4000mD to less than 10mD within the Wonnerup. Permeability of sand intervals for the Yalgorup Member ranges from more than 10,000mD to 4mD.

Applying a shale volume cutoff of less than 20% and effective porosity larger than 8%, net to gross (NTG) values of 78% and 48% were computed for the Wonnerup and Yalgorup Members respectively.

# 4 Module 4a: Petrophysical core plug characterization

## 4.1 Summary

This module is concerned with a series of laboratory measurements performed on core plugs extracted from the Harvey-1 well. The aim was to experimentally determine their porosity, permeability and pore size characteristics before using four selected samples in core flooding tests.

Porosity and permeability tests resulted in mean values of 20% and 344mD, and 12% and 60mD for the Yalgorup and Wonnerup Members respectively.

The measurements detail the flow properties of the rocks intersected by Harvey-1 and help elucidate their distribution with lithology (facies) and depth. This, in turn, may prove useful in identifying possible injection targets at depth.

## 4.2 Introduction

The fluvial Lesueur Sandstone of Middle – Late Triassic age has been subdivided into an upper Member (Yalgorup Member) and a lower sandstone Member (Wonnerup Member). Core plugs selected from the cored sections of the Harvey-1 well were submitted to a series of laboratory measurements aimed at characterizing their porosity, permeability and pore size distribution.

In interpreting the results the samples were sorted by depth and subdivided according to the Member of the Formation they were assigned to; moreover they were classified according to the facies scheme described in modules 1 and 2. Using this approach discriminating trends of porosity, permeability, depth emerge.

## 4.3 Analytical Techniques/Approach

### 4.3.1 X-RAY COMPUTER TOMOGRAPHY

X-ray CT (computer tomography) is a radiological imaging system first developed by Hounsfield (1973). The non-destructive technique uses x-rays to create a three-dimensional data set of a sample by stacking contiguous cross-sectional two-dimensional images. The principles of imaging have been extensively described elsewhere (e.g. Wellington and Vinegar, 1987) and will not be repeated here. In brief, CT-scan imagery corresponds to a 2-D or 3-D linear X-ray attenuation pixel matrix, where the attenuation is a function of the density, atomic number and thickness of the sample being analysed.

In geomaterials studies, the applications of CT scanning include viewing full-diameter core sections contained in an opaque barrel to determine orientation relative to bedding, presence of fractures and nodules. Applications also include identifying non-damaged, full diameter sections of core to facilitate sampling site selection and detailed density studies for highly interbedded intervals. Additionally, the CT systems can be used for quality assessment of prepared plug samples prior to specialized core testing. This technique is generally suitable for visualization from metre to millimetre scale.

The three-dimensional data of the core plugs tested at CSIRO was acquired using a Toshiba Xspeed medical imager operating at 120 kV. The images were used to evaluate the integrity of the samples prior to further experimental testing.

### 4.3.2 CORE POROSITY AND PERMEABILITY

#### Helium porosity and permeability

A total of 90 right cylindrical core plugs were submitted to Geotechnical Services PTY LTD by GSWA for Helium porosity and permeability measurements.



A sub set of 28 samples were subsequently received by CSIRO, trimmed to achieve the correct geometry and tested again using an automated AP 608 Helium Permeameter-Porosimeter (Coretest Inc.) located in the CSIRO Petrophysics laboratory.

In a standard test a sample is loaded into the core holder and flooded with inert Helium gas. Helium expansion is monitored and the pore volume (i.e. porosity) of the rock sample is calculated following Boyle's law:

$$V_1 = \frac{P_2 \cdot V_2}{P_1}$$

Where  $V_1$  is the volume of Helium permeating the rock sample;  $P_2$  and  $V_2$  are the pressure and the calibrated volume of Helium before being released into the sample; and  $P_1$  is the pressure of gas after sample infiltration.

Permeability was measured using the unsteady state pulse decay method (Jones, 1972) which consists of recording the differential pressure at the edge of a core plug when the inlet of this plug is connected to a gas tank initially set at a given pressure. The technique has been widely used in core evaluation and returns the equivalent liquid permeability measurement (i.e. Klinkenberg corrected) which can then be readily used to estimate water flow behaviour under the assumption of no interaction between fluid phase and solid rock framework.

Porosity and permeability of each of the 28 core plugs were measured at pressures of 3.4, 13.8 and 34.5 MPa. Three measurements were taken at each step of pressure to assess the statistical error of the analysis.

### **Mercury injection porosimetry**

For the evaluation of pore size distribution within the tested specimens, quarter inch offcuts of 28 core plugs were submitted to Geotechnical Services PTY LTD by GSWA for mercury injection capillary pressure measurements. The samples were tested in a Micrometrics Autopore IV porosimeter by injecting mercury at increasing capillary pressure steps up to a maximum pressure of 413 MPa.

### **Nuclear magnetic resonance (NMR)**

Nuclear magnetic resonance (NMR) relaxation time measurements can provide critical information about the physico-chemical properties of fluids in porous materials from both wireline logging and laboratory tools (Gruenwald and Knight, 2011; Walbrecker et al., 2011). Applications of NMR in petroleum well logging over the past several decades have demonstrated robust links between measured relaxation times and important formation properties, including pore size distribution and permeability (Clennell et al., 2006; Coates et al., 1991; Josh et al., 2012). During NMR measurement, proton nuclei are first aligned according to the direction of an applied magnetic field  $B_0$ , and then perturbed from their equilibrium state by a pulse characterized by the proton resonance frequency. In an NMR test the magnetization and transverse relaxation time ( $T_2$ ) of hydrogen nuclei contained in the pore fluid is measured. Different pore sizes in fluid saturated rocks will produce characteristic  $T_2$  distributions as the amplitude of transverse magnetization is proportional to the number of hydrogen nuclei. As a consequence, the observed  $T_2$  distribution of a saturated core sample represents the pore size distribution of the rock.

Low field NMR measurements have been collected on 27 core plugs (sample 206643 extracted from the Yalgorup Member at depth 1342.6m, lost cohesion during water saturation and could not be tested) using a Maran-Ultra spectrometer at 2 MHz (Oxford Instruments Ltd.) to investigate water content, its relation with pore size and mobility, as well as deriving permeability from empirical equations. Before NMR measurements were taken, the dry samples were brine saturated under vacuum for 24-48 hours using the brine salinity estimated from the resistivity log (see module 3). The difference in mass between the dry and brine saturated core plugs was used to calculate porosity and compared to the helium gas porosity results to check for full saturation. Once saturated, the samples were wrapped in cling film to avoid water evaporation, stored in a plastic jar that fit the sample holder and tested in the NMR spectrometer using the Carr–Purcell–Meiboom–Gill (CPMG) pulse sequence. This spin-echo method calculates the pore size

distribution using the distribution of transverse magnetic relaxation time ( $T_2$ ). The principle and details of this analysis are described elsewhere (Kleinberg et al., 2003a; Kleinberg et al., 2003b; Jorand et al., 2011); our experimental protocol ensures a resolution of pore body size >10nm and calculates the pore radius (in micrometers) from the  $T_2$  values as indicated by Dunn et al. (2002).

Module 3 illustrated how NMR logs from borehole logging can be used to estimate porosity and permeability of the underground rock units; in this module a comparison is made between laboratory measurements of porosity and permeability using the NMR method and the helium method described above. This analysis is used as verification of the NMR results at the lab scale to infer the validity of the NMR log data.

## 4.4 Results





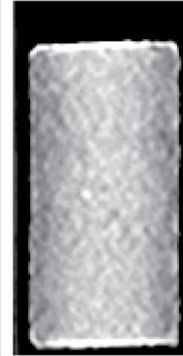
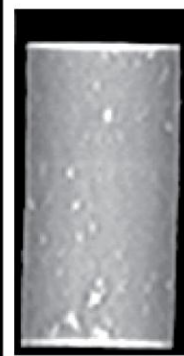
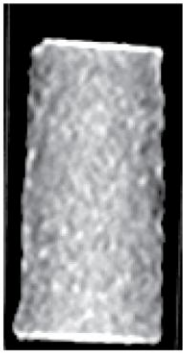




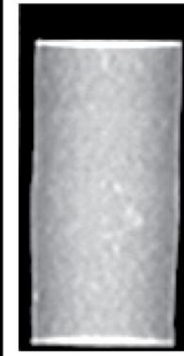




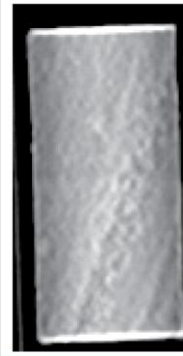

### 4.4.1 X-RAY CT

CT images of the core plugs are reported in Fig. 4.1. Most of the samples are somewhat irregular in their shape and show some degree of heterogeneity due to the presence of bedding planes occurring with cm scale thickness. Four of the samples (206601; 206609; 206622, and 206627 all from the Yalgorup Member, see Fig. 4.1 for depth) are composed of very coarse, poorly cemented grains (Facies Ai and Aii, see Figure 4.1) which precluded the machining of a properly shaped cylinder for petrophysical analysis.

### 4.4.2 HELIUM POROSITY AND PERMEABILITY

The results of the porosity and permeability measurements on the 28 core plugs are tabulated in Appendix E. There is an excellent agreement between the measurements performed by Geotech and those repeated at CSIRO on the same plugs using the same methodology. The mercury injection method always returns slightly different values from the helium porosity, but a systematic trend could not be identified. It should be noted that the mercury injection method determines porosity from a small offcut of sample; on the other hand helium porosity is determined on a full size plug, the same plug later used for other petrophysical and geomechanical tests. In the following paragraphs the reference porosity is the one measured by the helium method unless otherwise stated.

Figure 4.2 shows the results of the measurements performed on the complete Harvey-1 plug collections plotted against depth of each sample. Porosity shows an inverse trend dependency, while permeability seems to be scattered in a non-depth dependent way. Finally when the samples are sorted according to the facies scheme described in module 1 some clustering can be observed indicating that the facies classification is able to capture some of the petrophysical characteristic of the sediments.

$\rho_b = 2.02 \text{ g/cc}$ $\phi = 23.60 \%$ $k = 918.17 \text{ mD}$ $Z = 9897.63 \text{ m}$	$\rho_b = 2.11 \text{ g/cc}$ $\phi = 17.97 \%$ $k = 9.59 \text{ mD}$ $Z = 903.62 \text{ m}$	$\rho_b = 2.00 \text{ g/cc}$ $\phi = 24.6 \%^*$ $k = 242.78 \text{ mD}$ $Z = 911.53 \text{ m}$	$\rho_b = 2.12 \text{ g/cc}$ $\phi^* = 18.29 \%$ $k^* = 5.21 \text{ mD}$ $Z = 920.56 \text{ m}$	$\rho_b = 2.06 \text{ g/cc}$ $\phi = 22.24 \%$ $k = 789.52 \text{ mD}$ $Z = 927.61 \text{ m}$	$\rho_b = 2.12 \text{ g/cc}$ $\phi = 15.45 \%$ $k = 5.57 \text{ mD}$ $Z = 1266.21 \text{ m}$
					
206601	206603	206609	206616	206622	206626
$\rho_b = 2.08 \text{ g/cc}$ $\phi^* = 21.54 \%$ $k^* = 242.78 \text{ mD}$ $Z = 1271.95 \text{ m}$	$\rho_b = 2.20 \text{ g/cc}$ $\phi = 12.77 \%$ $k = 0.48 \text{ mD}$ $Z = 1273.89 \text{ m}$	$\rho_b = 2.11 \text{ g/cc}$ $\phi = 15.93 \%$ $k = 5.94 \text{ mD}$ $Z = 1323.93 \text{ m}$	$\rho_b = 2.11 \text{ g/cc}$ $\phi = 15.61 \%$ $k = 10.86 \text{ mD}$ $Z = 1324 \text{ m}$	$\rho_b = 2.33 \text{ g/cc}$ $\phi = 6.14 \%$ $k = 0.03 \text{ mD}$ $Z = 1329.94 \text{ m}$	$\rho_b = 2.32 \text{ g/cc}$ $\phi = 9.08 \%$ $k = 0.17 \text{ mD}$ $Z = 1337.41 \text{ m}$
					
206627	206628	206635	206636	206638	206642
$\rho_b = 2.30 \text{ g/cc}$ $\phi = 7.47 \%$ $k = 0.07 \text{ mD}$ $Z = 1342.6 \text{ m}$	$\rho_b = 2.26 \text{ g/cc}$ $\phi = 11.95 \%$ $k = 0.35 \text{ mD}$ $Z = 1343.61 \text{ m}$	$\rho_b = 2.24 \text{ g/cc}$ $\phi = 14.24 \%$ $k = 143 \text{ mD}$ $Z = 1897.66 \text{ m}$	$\rho_b = 2.20 \text{ g/cc}$ $\phi = 15.55 \%$ $k = 199 \text{ mD}$ $Z = 1897.91 \text{ m}$	$\rho_b = 2.19 \text{ g/cc}$ $\phi = 15.39 \%$ $k = 525 \text{ mD}$ $Z = 1901.61 \text{ m}$	$\rho_b = 2.27 \text{ g/cc}$ $\phi = 12.86 \%$ $k = 6 \text{ mD}$ $Z = 1902.62 \text{ m}$
					
206643	206644	206645	206646	206647	206648

\* = estimated from NMR

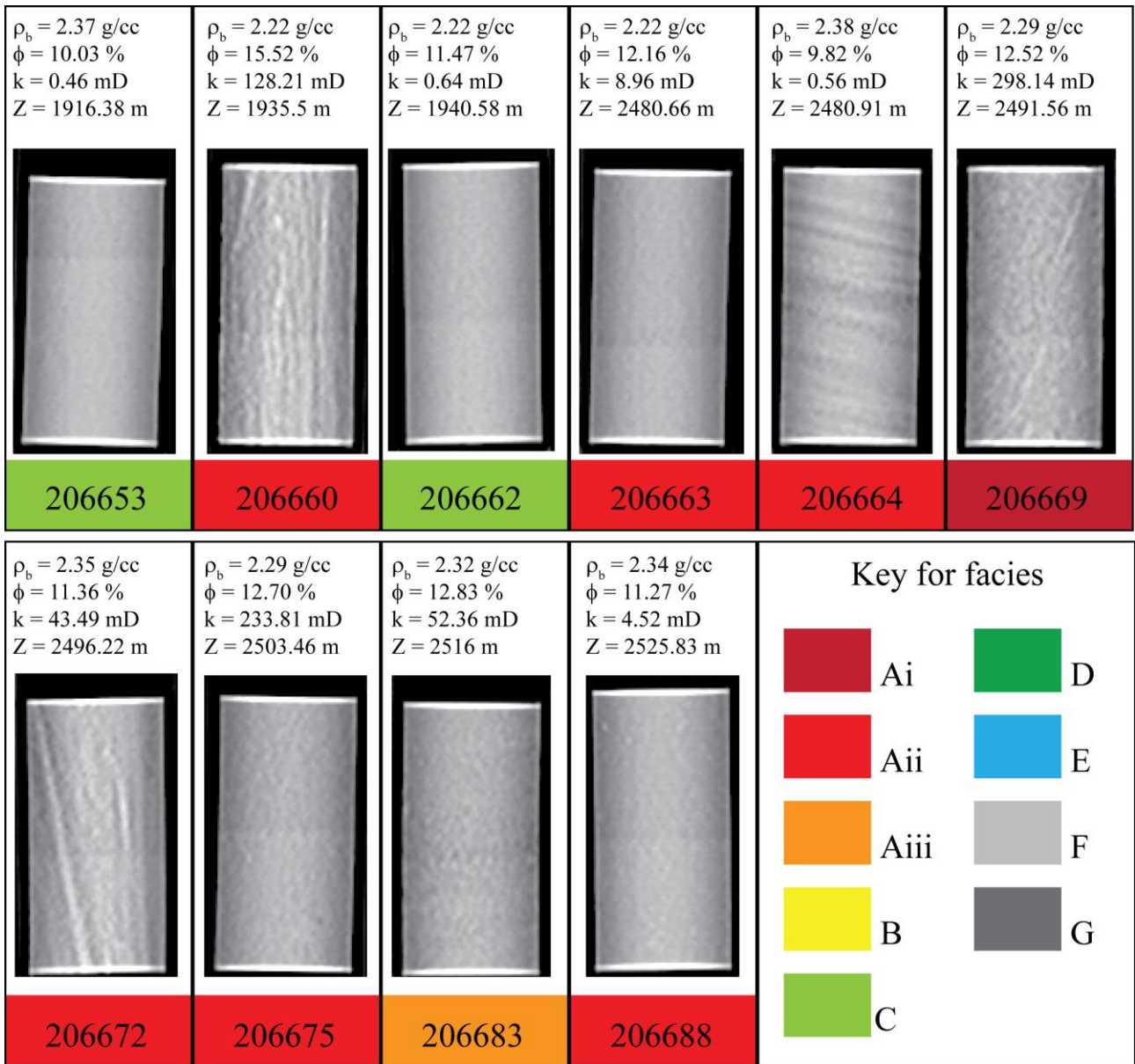
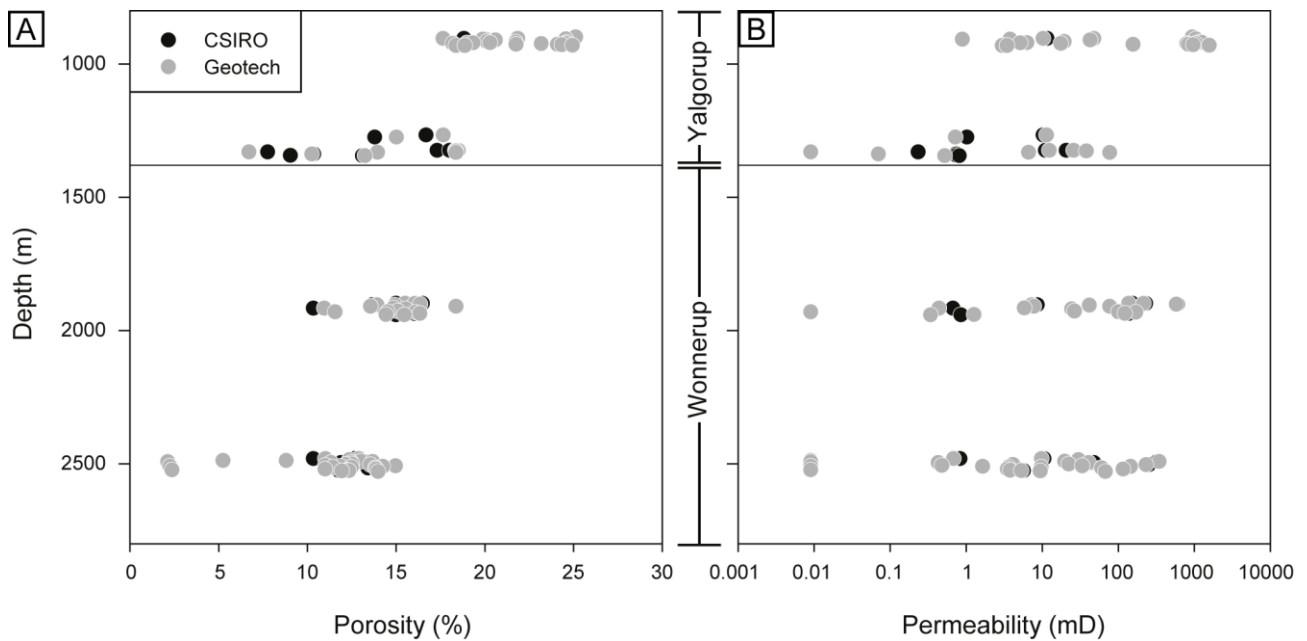


Figure 4.1. X-Ray CT scans of the cylindrical core plugs used in this study; each plugs is 38mm across. The grey level of the scan is associated with the atomic number and density of the analyzed material: brighter levels correspond to denser phases.  $\rho_b$  = bulk density;  $\phi$  = porosity,  $k$  = permeability;  $Z$  = depth.



**Figure 4.2. Relationships between porosity, permeability and depth, determined from helium-injection at Geotech and CSIRO on Harvey-1 core plugs. (A) Porosity versus depth (the results from the two labs have a  $R^2$  coefficient of 0.964). (B) Permeability versus depth (results from the two labs have a  $R^2$  coefficient of 0.997).**

Helium porosity and permeability results have been graphed and colour coded for facies (Fig. 4.3). This shows that high energy channel fills and barforms (facies Ai-Aiii) have the highest porosity and permeability; moderate to low energy barforms, migrating rippleforms and palaeosols (facies B-D) have intermediate porosity and permeability, and; Swampy/overbank deposits and crevasse splays have the lowest porosity and permeability (facies E-G). There are still overlaps between facies that are attributed to depth variation. To analyze purely the lithofacies control on petrophysical properties, porosity and permeability has been graphed for each facies, colored for depth (Fig. 4.3 B-G). These graphs show a strong trend of reducing porosity and permeability with depth. When comparing the lithofacies with each other, there is a significant reduction in porosity from facies Ai-Aiii to B-D to E-G. Facies E, F and G were not individually graphed because of their limited sample numbers but can be referred to in Fig. 4.3A.

#### 4.4.3 MERCURY INJECTION POROSIMETRY

Pore throat sizes were analyzed via mercury-injection capillary pressure and nuclear magnetic resonance (Fig. 4.4, and Fig. 4.5). Mercury-injection capillary pressure shows that modal pore throat sizes decrease is relatively uniformly from facies Ai to E (Fig. 4.4A). The modal pore throat size for facies Ai and Aii is typically around 10  $\mu\text{m}$ , whereas the modal pore throat for facies B to E is between 0.8 and 2  $\mu\text{m}$ . To further assess the distribution of macro- and micro-pore throats, box-and-whisker plots were made that show the relative abundances of pore throats larger than 3  $\mu\text{m}$  (Fig. 4.4B) and smaller than 0.1  $\mu\text{m}$  (Fig. 4.4C). These show that macro-pore throats are typically limited to facies Ai and Aii, with rare occurrences in facies B and C. Conversely, micro-pore throats are most prevalent in facies B to E and are rare in facies Ai to Aii.

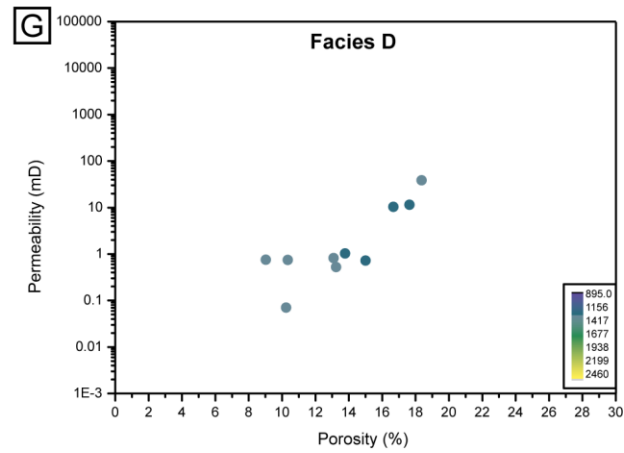
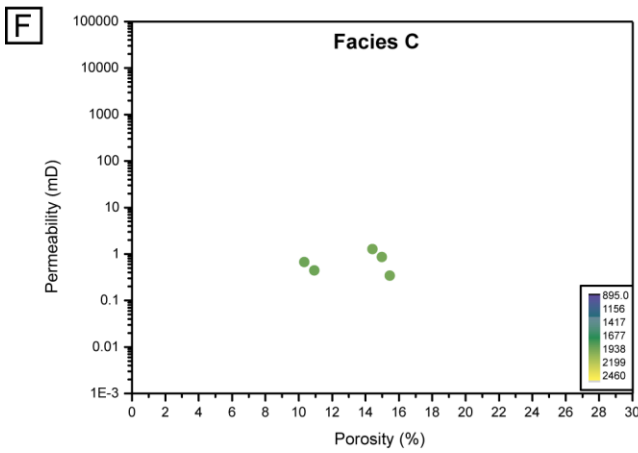
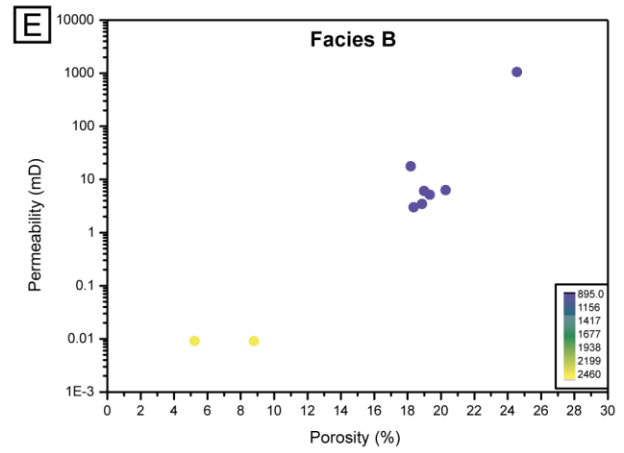
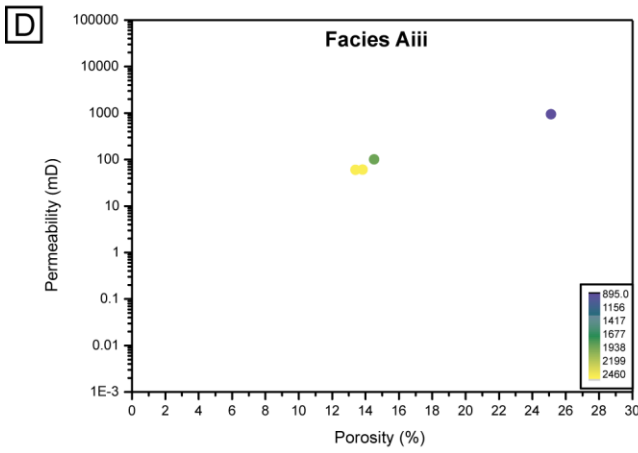
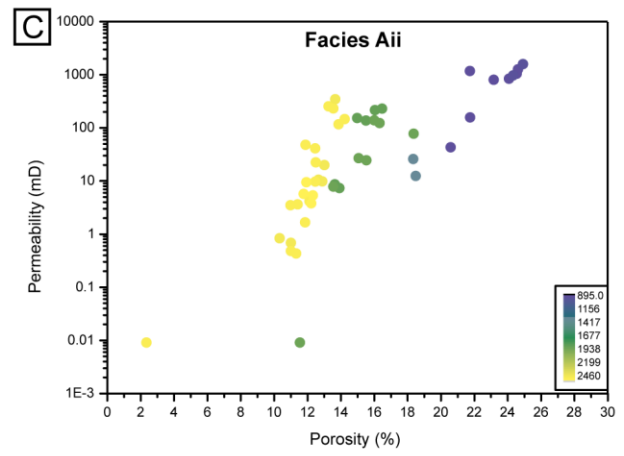
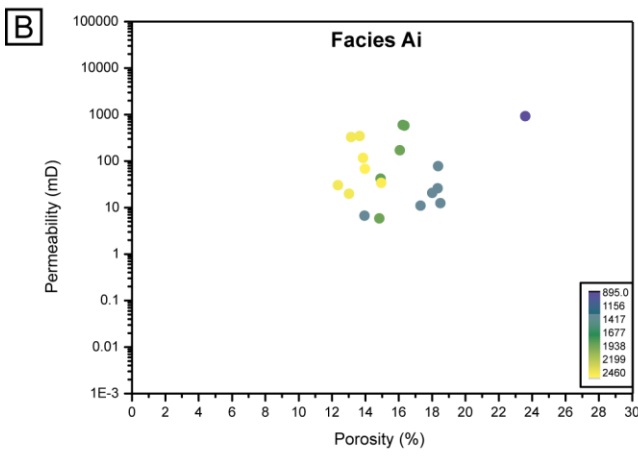
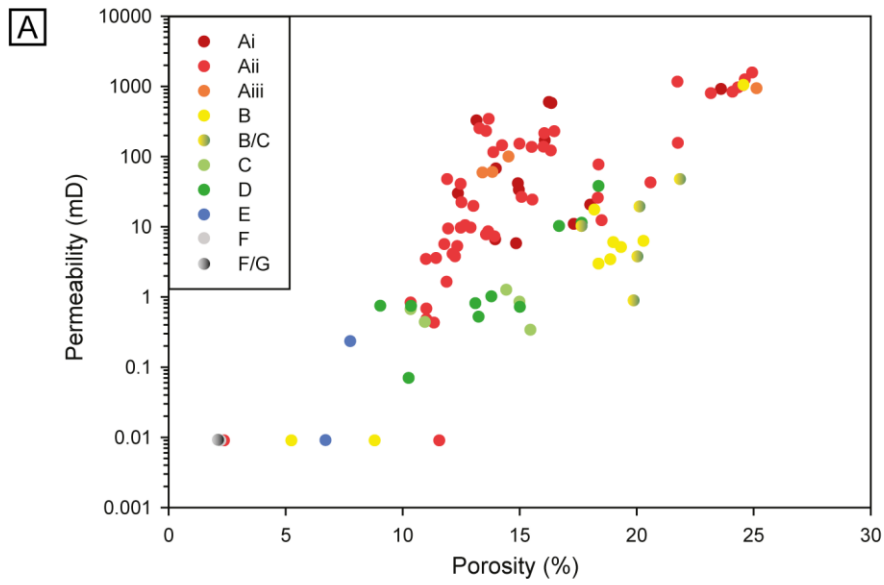


Figure 4.3. Lithofacies and depth control on porosity and permeability, determined from helium-injection at Geotech and CSIRO into core plugs from Harvey-1. (A) Porosity versus permeability, colour coded for facies type. (B-G) Porosity versus permeability colour coded for depth where: (B) Facies Ai; (C) Facies Aii; (D) Facies Aiii; (E) Facies B; (F) Facies C, and; (G) Facies D.

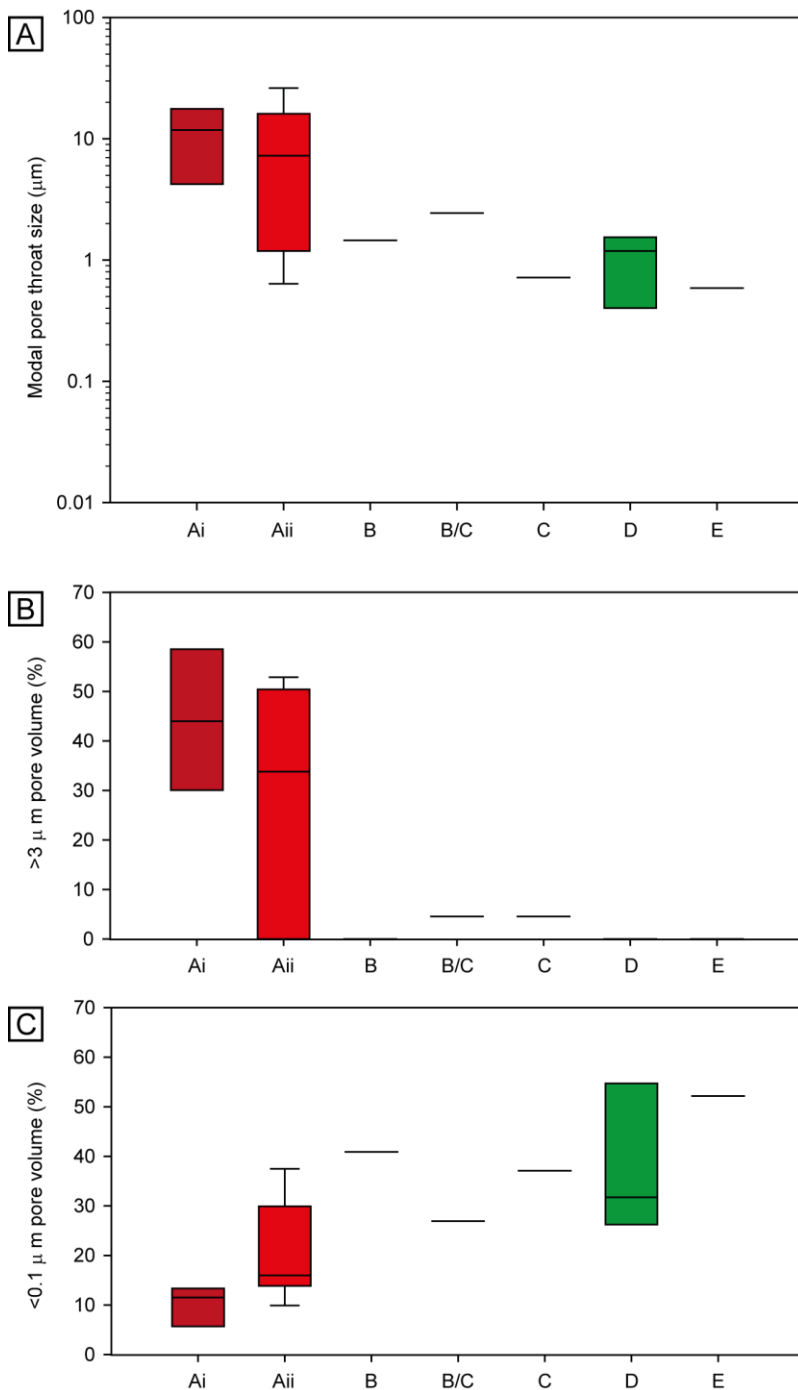
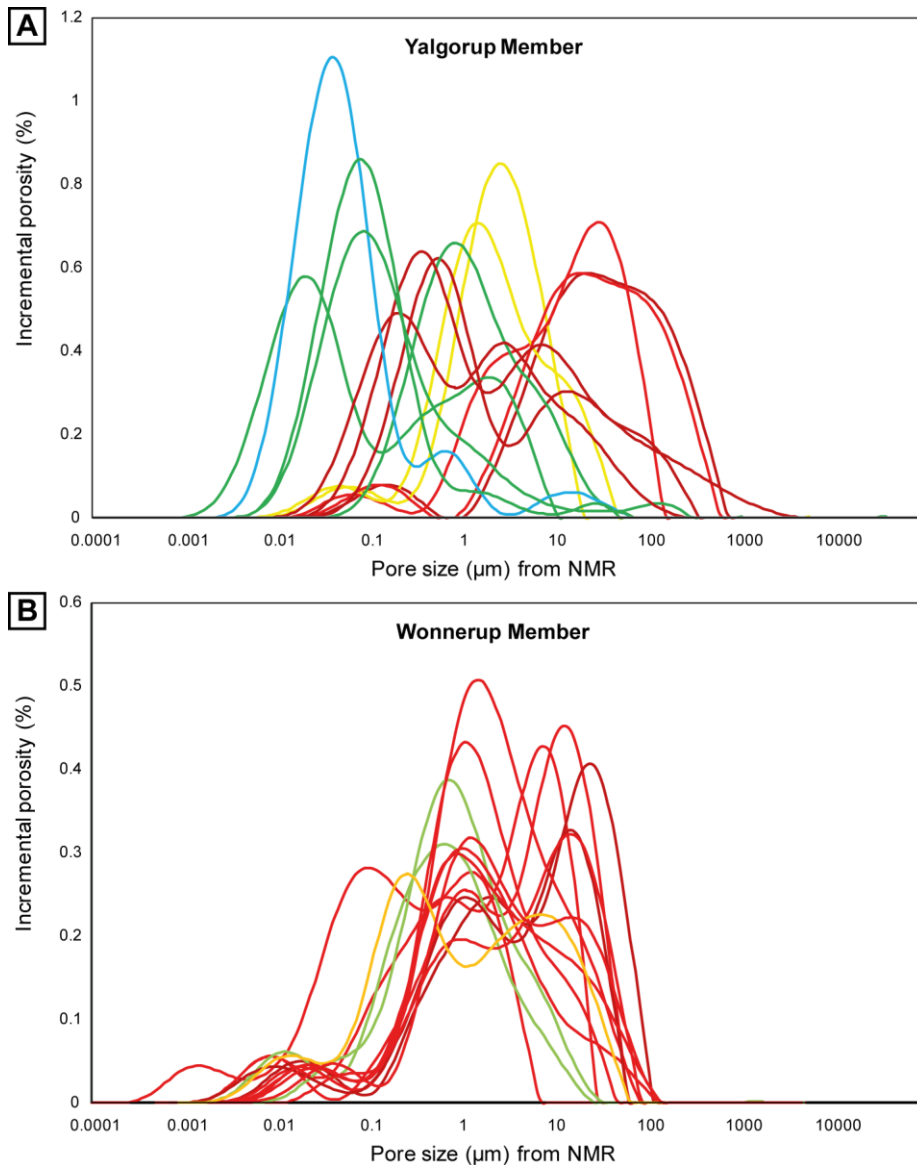


Figure 4.4. Pore throat sizes determined from mercury-injection capillary pressure. (A) Modal pore throat size versus facies. (B) Percentage of pore throat sizes larger than  $3 \mu\text{m}$  versus facies. (C) Percentage of pore throat sizes smaller than  $0.1 \mu\text{m}$  versus facies.

#### 4.4.4 NMR

Nuclear magnetic resonance results have been divided into the Wonnerup and Yalgorup Members (Fig. 4.5 A, Fig. 4.5B). In the Yalgorup Member, facies Ai and Aii typically have bimodally-distributed pore throat

sizes, between 0.1-1  $\mu\text{m}$  and 10-100  $\mu\text{m}$ . Facies B is unimodally distributed, with pore sizes averaging 3  $\mu\text{m}$ . Facies C is unimodally distributed, with varying means per sample of 0.1-1  $\mu\text{m}$ . Facies D is unimodally distributed, with means between 0.02 and 1  $\mu\text{m}$ , but the majority of samples are positively skewed. Facies E is unimodally distributed, with a mean of 0.03  $\mu\text{m}$ . In the Wonnerup Member, pore throat sizes are typically smaller for the same facies as in the Yalgorup Member, which may be attributed to compaction and hence reduction in pore throat sizes. Facies Ai and Aii typically have bimodally-distributed pore throat sizes, averaging 1  $\mu\text{m}$  and 10-100  $\mu\text{m}$  respectively. Facies Aiii is bimodally-distributed, with peaks at 0.2 and 7  $\mu\text{m}$ . Facies C is unimodally distributed, with a mode of 1  $\mu\text{m}$ .



**Figure 4.5. Pore throat size distribution determined from nuclear magnetic resonance, colour coded according to the facies assigned to the tested sample (see Fig. 4.2 for legend). (A) Yalgorup Member. (B) Wonnerup Member.**

#### 4.4.5 NMR POROSITY AND PERMEABILITY

The porosity and permeability results from helium and NMR methods are summarised in Fig. 4.6. It is evident that samples from the Wonnerup Member show an excellent correlation between the porosity measured by the two methods. The slope of the linear regression is <1 indicating that He porosity (typically used as the reference measurement) slightly overestimates NMR porosity. The Yalgorup samples show very



poor correlation between NMR and Helium porosity and the former is always seen to overestimate the latter; this could be due to the sensitivity of NMR to the clay bound water present in the samples.

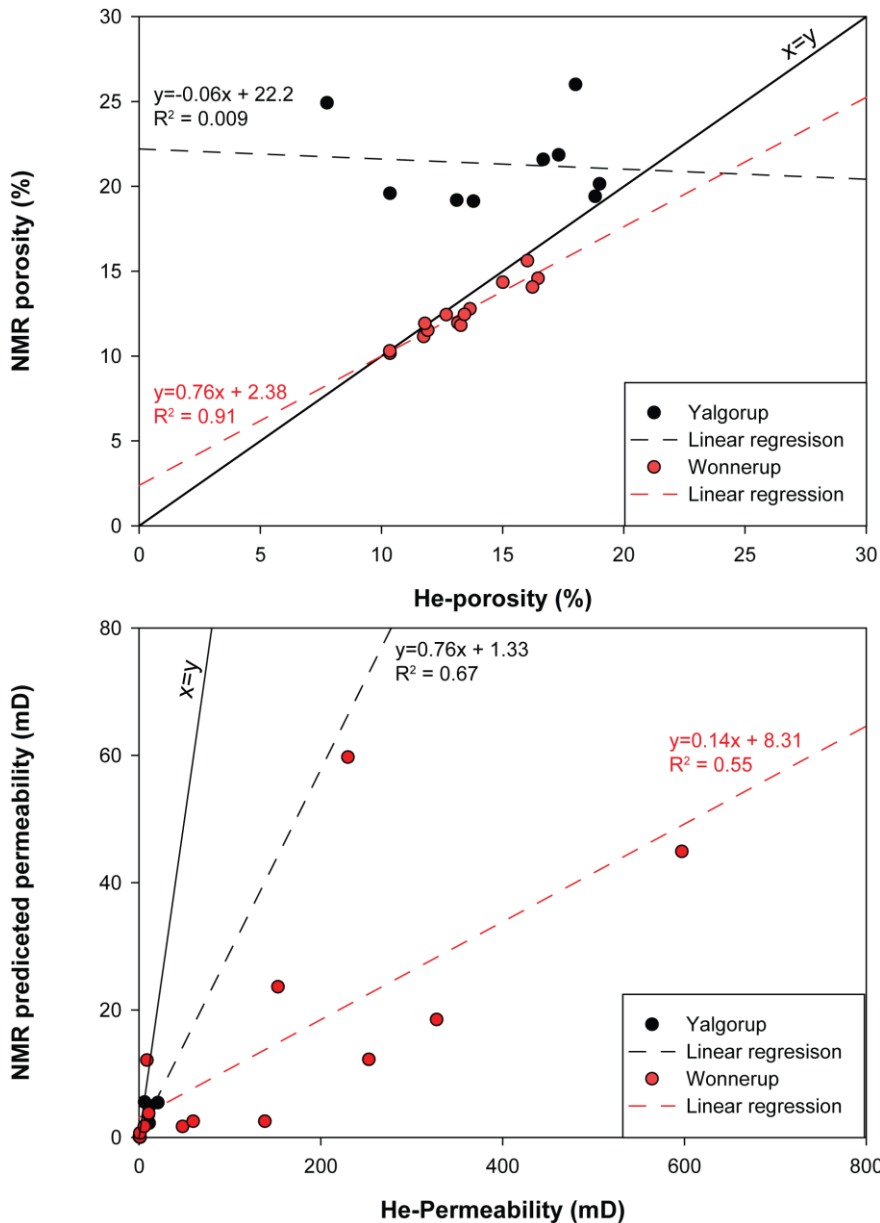


Figure 4.6. Comparison between porosity (above) and permeability (below) measured by NMR and Helium methods for samples of the Yalgorup and Wonnerup Members of the Lesueur Sandstone.

Permeability estimated using Coates model (see module 3 equation 3.6) correlates reasonably well with the helium permeability ( $0.55 < R^2 < 0.67$ ), but underestimates it in samples from both the Yalgorup and Wonnerup Members; the correlation between the two methods is however superior in the shallower Yalgorup specimen lending support to the permeability estimated from the wireline log tool presented in module 3.

## 4.5 Discussion and conclusions

Petrophysical properties, such as porosity and permeability, are inversely correlated with depth for Wonnerup and Yalgorup members in Harvey-1 (Fig. 4.3). Within a cored section, however, helium core plug

porosities show a porosity variation up to 12% and a permeability variation by up to four orders of magnitude. Similarly, continuous porosity and permeability derived from density and NMR logs respectively, recorded over a larger depth interval than that covered by the cored sections, show a porosity variation of 28% and a permeability variation up to six orders of magnitude giving a feeling for the heterogeneity of the rocks. This variation of porosity and permeability is likely controlled by lithofacies.

It should be noted however that while porosity is a scalar property, permeability is a symmetric tensor of second rank, reducing to a scalar only in the case of isotropic rocks (see review by Bernabe, 1992). It is therefore of interest to evaluate the anisotropy of permeability imparted by the layered nature of the sediments intersected by Harvey-1, as this could have important implications for vertical and horizontal fluid movement in the sub-surface. This assessment was completed by studying 15 pairs of core plugs cored in mutually perpendicular directions: parallel and normal to the macroscopic sedimentary planes identified during logging. Horizontal and vertical samples are defined by the cylindrical axis being parallel or perpendicular to the bedding respectively. The samples were selected to be in close vicinity, generally within a distance of a few centimetres from one another (see Appendix for sample locations) and tested following the same protocol described above.

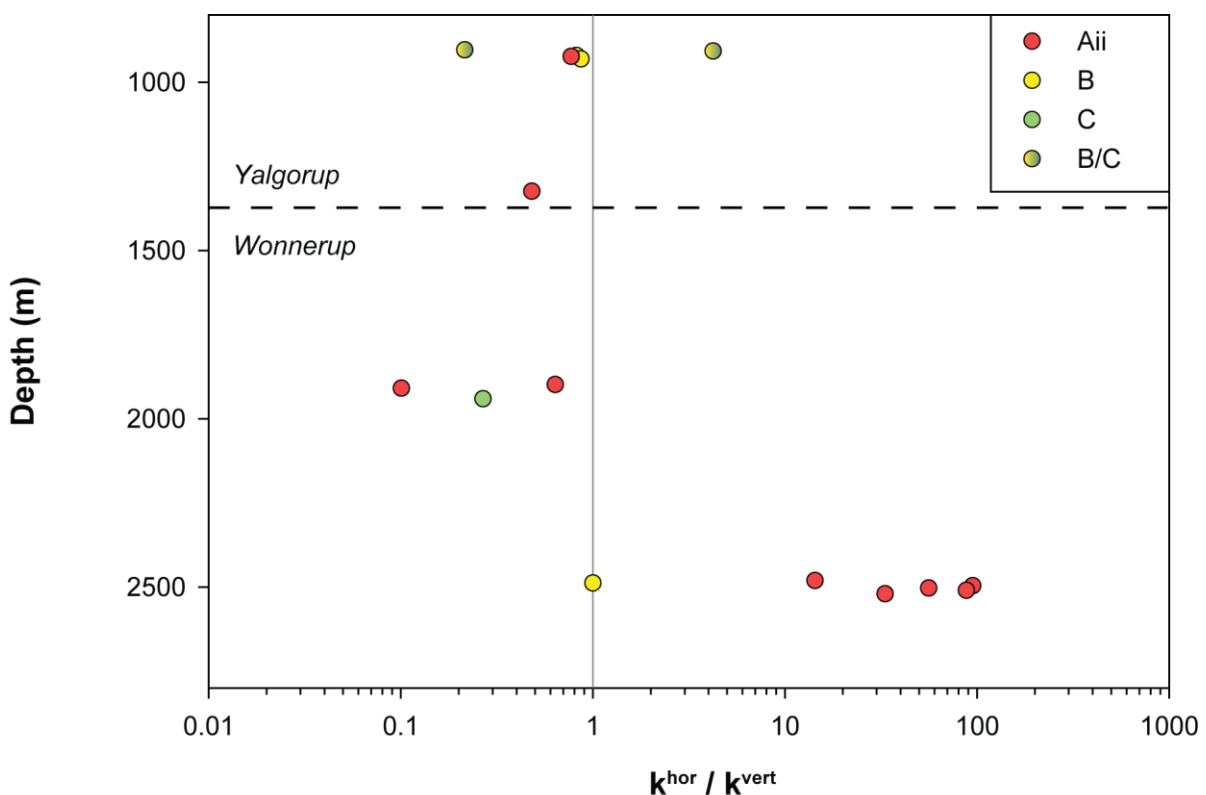


**Figure 4.7. Permeability anisotropy versus depth for pairs of samples extracted from Harvey-1. The vertical line represents the isotropic case where  $k^{hor} = k^{vert}$ . Permeability measurements were performed by Geotechnical Services PTY LTD at a confining pressure of 5.5 MPa.**

Test results are summarised in Fig. 4.7 where permeability anisotropy is defined as the ratio of permeability along the bedding ( $k^{hor}$ ) over permeability across the bedding ( $k^{vert}$ ) and plotted versus depth of recovery of the sample. Samples belonging to lithofacies Aii show nearly isotropic permeability at shallow depths in the Yalgorup Member while showing a remarkable anisotropy at depth in the Wonnerup Member, displaying up to two orders of magnitude greater permeability along the bedding than across it. Samples identified as belonging to Facies B show approximately isotropic behaviour independently of their depth; this in agreement with their lithological description as massive sandstone. Only one pair of samples from Facies C was tested and indicates slightly higher vertical permeability than horizontal which may reflect the heterogeneity of fine cross laminated sandstone. Finally, two pairs of core plugs identified as mixed Facies B/C show contrasting behavior at similar depth with one pair displaying  $k^{hor}/k^{vert} > 1$  and the other

$k^{hor}/k^{vert} < 1$ . The most evident observation from the above analysis is the marked anisotropy in permeability showed in the deeper samples of Facies Aii (the possible injection target). This is likely a result of the cross bedded nature of the sandstone, occurring with significant grain size variation between beds therefore increasing the tortuosity of the pore network across the beds. It is also possible that the effect of bedding is enhanced by compaction at depth acting mainly normal to the sedimentary planes.

Assuming a laterally continuous and homogeneous reservoir the observed anisotropy may have beneficial effects in terms CO<sub>2</sub> injection as the fluid will move laterally with ease while its vertical displacement would be hindered by the structure of the sediments. A more systematic approach to permeability anisotropy measurements as a function of depth and facies coupled with detailed microstructural analysis of the pore network and grain arrangement may reveal important information on the possible fluid migration pathways in the rocks encountered in Harvey-1



## 5 Module 4b: Core Flooding

## 5.1 Summary

This module presents core flooding experiments on core plugs extracted from the Harvey-1 well performed at reservoir condition. Samples were flooded with CO<sub>2</sub> saturated brine and brine equilibrated CO<sub>2</sub>, the obtained residual scCO<sub>2</sub> saturations were ranging between 22.9% and 42.7% and are inversely proportional to the samples' absolute permeabilities. The samples showed a 25%-51% reduction in permeability after undergoing the scCO<sub>2</sub>-brine flooding while the changes in their porosity values were negligible; such observation has been interpreted as due to fines migration.

The results of this module should assist in the evaluation of the storage capacity and injectivity potential of the predicted storage units of the SW-Hub.

## 5.2 Introduction

This report presents the results of the reservoir condition core-flooding experiments conducted on a selected number of core-plugs drilled from the core material recovered from well Harvey-1. All the core samples tested were from the Wonnerup Member within the Lesueur Formation. The core samples were selected in a way that they would cover most of the identified facies within the Wonnerup formation.

The main objectives of the core flooding experiments are:

- To measure water, CO<sub>2</sub> relative permeability under in-situ reservoir conditions.
- To measure the achievable levels of scCO<sub>2</sub> capillary residual trapping.
- To investigate the occurrence of chemical reactions between the injected fluids and in-situ created solute and the host rock within the experimental timeframe.
- To evaluate the scCO<sub>2</sub> seal efficiency through measurement of capillary entry pressure.
- To evaluate the difference in porosity and permeability of the samples before and after core flooding

In order to achieve the above listed objectives, five core-flooding experiments were performed. Three of the experiments were of conventional unsteady-state tests with the main aim of measuring the relative permeabilities and end-point residual saturations. The fourth experiment was conducted with the main objective of taking time-lapse effluent brine samples which could be analysed for changes in chemical species and verify any chemical reactions which may have occurred between the fluids and a core plug during a typical core-flooding experiment (results reported in project *Geochemical characterisation of gases, fluids and rocks in the Harvey-1 data well*, by Stalker et al., 2013). The last experiment was conducted on a shale disk prepared from the shale material drilled from well Harvey-1. The purpose of this experiment was to measure the capillary entry pressure of the shale to scCO<sub>2</sub> under in-situ reservoir conditions. The difference in transport properties of the samples before and after core flooding tests was assessed in all cases by repeating the He-porosity-permeability and NMR measurements illustrated in module 4a.

This module has been divided in two main sections. The first part of module 4b presents comprehensive details on the equipment and materials used as well as the experimental procedure followed while carrying out the experiments. In the second part, provides the results of the above mentioned experiments and are presented and discussed in details.

## 5.3 Experimental Techniques

### 5.3.1 MATERIAL

#### Fluids

In total three different types of fluids were used during the various stages of the experimental work conducted. These fluids included:

- *Dead brine*: brine with no dissolved gas content,
- *CO<sub>2</sub>-saturated brine*: brine saturated with CO<sub>2</sub> at in-situ reservoir conditions,
- *vapour-saturated scCO<sub>2</sub>*: scCO<sub>2</sub> saturated with water vapour at in-situ reservoir conditions.

The CO<sub>2</sub> gas used was of at least 99.9% (mol%) purity. The brine was prepared in the lab using distilled water and appropriate amounts of analytical grade sodium chloride (NaCl).

### Core plugs

In total four different core-plugs were tested (Table 5.1). Three core plugs were selected from sandy facies of the Wonnerup Member (likely representing the targeted storage formation) while the fourth sample was a thin shale disk representing the shale interval within the Wonnerup Member. The petrophysical characteristics of these core plugs are presented in Table 5.1. The porosity and helium permeability values listed in Table 5.1 were measured using an automated helium poro-permeameter under the net effective pressure of the reservoir. The brine permeabilities reported in this table were also measured at the beginning of each core-flooding experiment under in-situ reservoir conditions using a synthetic formation brine composition of 30,000 ppm NaCl.

It is worth noting that all the core plugs tested were horizontal samples (i.e. drilled parallel to the geological bedding). X-ray diffraction (XRD) mineralogy analyses were conducted by Geotechnical Services PTY LTD, on offcuts of the core-plugs tested. The results of the XRD analysis show that apart from quartz and k-feldspar which are the main constituents of sandstone rocks, all three samples contain kaolinite with sample 206660 having the highest percentage (7%). Furthermore, sample 206660 contains 4% of ankerite which is a type of carbonate mineral (calcium, iron, magnesium, manganese carbonate).

Sample ID	Depth, m	Length, cm	Diameter, cm	Lithology	Porosity, %	Klinkenberg corrected Helium permeability, mD	In-situ Brine Permeability, mD
206647	1901.6	7.4	3.63	Sandstone	15.47	532	48.0
206660	1935.5	7.52	3.76	Sandstone	15.56	129	16.5
206669	2491.6	7.5	3.77	Sandstone	12.57	299	238
Shale Disk 1	1318.6	1.5	3.8	Shale	---	----	----

**Table 5.1. Characteristics of the core samples used for the core flooding experiments.**

All three samples are recovered from depths relevant to the expected injection levels in the proposed SW-Hub (1800-3000 meters see <http://www.globalccsinstitute.com/publications/western-australia-greenhouse-gas-capture-and-storage-tale-two-projects>); moreover the samples are described as lithofacies Ai and Aii, i.e. the most abundant lithofacies types in the Wonnerup Member of the Lesueur Sandstone and should therefore well represent the potential CO<sub>2</sub> storage reservoir.

X-ray CT images and characteristics of the pore space of the samples, as measured by mercury injection, are illustrated in Fig. 5.1.

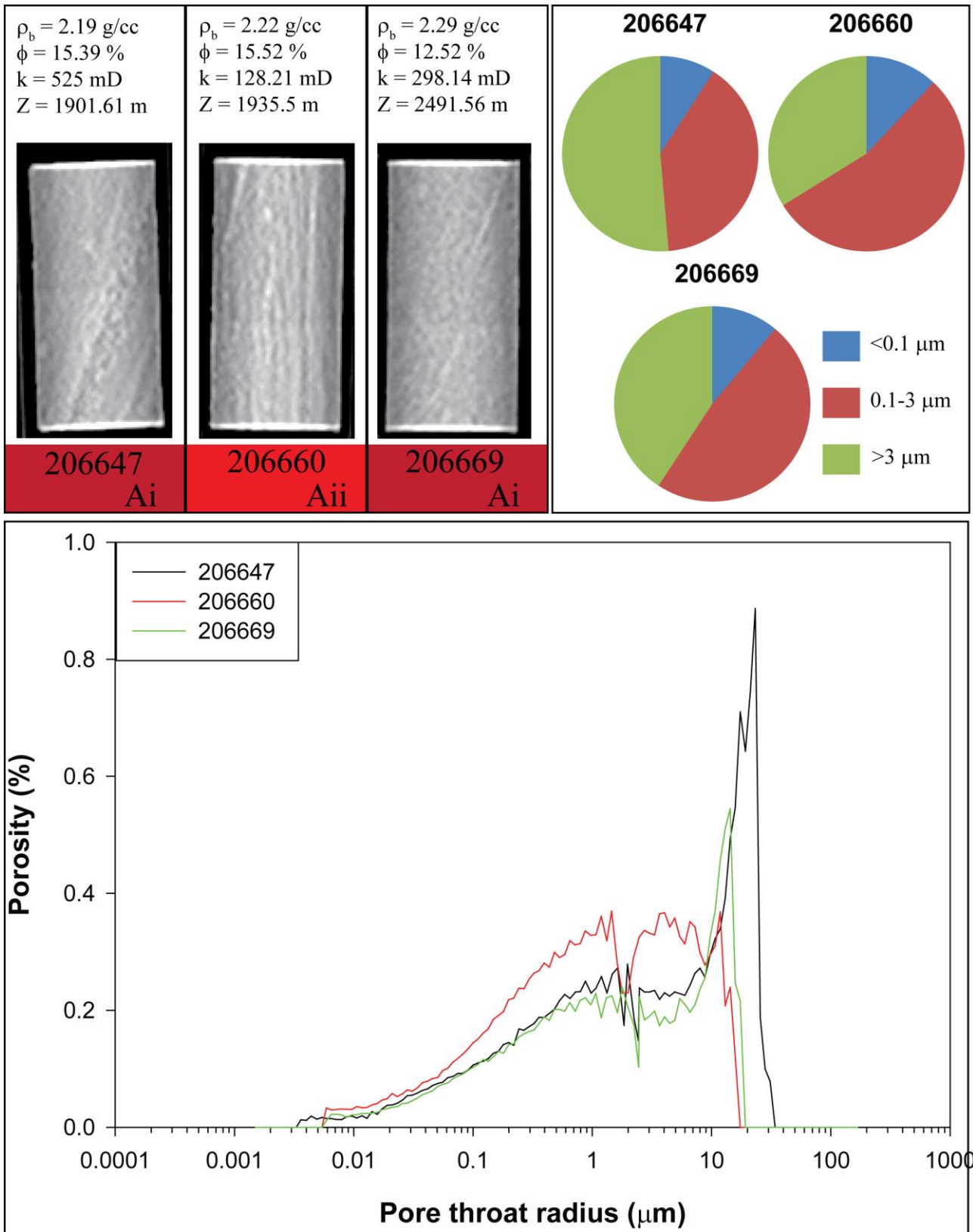


Figure 5.1. Top left: X-ray CT images of the samples prior to core flooding tests. Top right: pie charts representing the relative percentage of pore space subdivided in three size classes. Bottom: pore size distribution as measured by mercury injection porosimetry on offcuts of the three samples tested.



### 5.3.2 EXPERIMENTAL CONDITIONS

For all four core samples, Table 5.2 lists the values of the in-situ reservoir condition parameters used during the experiments. The pore pressure and temperature values were calculated for each depth using the data gathered during pressure and temperature surveys run in the Harvey-1 well. Overburden pressure, on the other hand, was calculated using an overburden pressure gradient of 6.9 KPa/m (1 psi/ft), as a typical value suggested in the literature (Lyons and Plisga, 2005; Tiab and Donaldson, 2004). The salinity values were calculated from the well logs run in well Harvey-1.

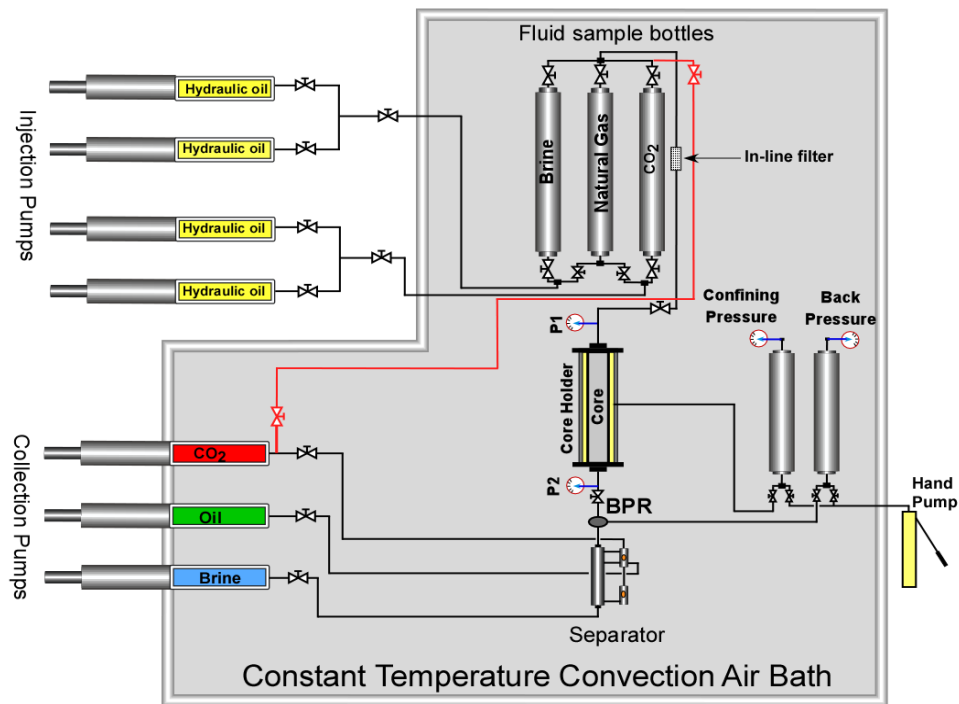
Reservoir parameter	Sample ID			
	206647	206660	206669	Shale disk
Depth, m	1,901.6	1,935.5	2,491.6	1,318.6
Pore pressure, MPa	19.05	19.39	24.95	13.22
Overburden pressure, MPa	43.02	43.78	56.36	29.83
Reservoir temperature, °C ( $\pm 0.5^\circ$ C)	60.7	61.2	69.2	52.2
Formation water salinity, ppm NaCl	30,000	30,000	30,000	40,000

Table 5.2. Reservoir P-T conditions during the experiment.

### 5.3.3 EXPERIMENTAL APPARATUS

The core-flooding experiments were carried out using the high pressure-high temperature, three-phase steady-state core-flooding apparatus located within the Department of Petroleum Engineering at Curtin University. A schematic of the core-flooding rig is presented in Fig. 5.2. The apparatus is capable of handling experiments with pressures up to 103.5 MPa (15,000 psi) and temperatures up to 200° C. Most of the critical wetted metal parts of the apparatus are made of highly corrosion resistant materials (e.g. hastelloy, titanium or duplex and super duplex stainless steel) which make the equipment corrosion resistant even under high temperature environments with high salt concentrations. All the components carrying fluids during experiments are placed inside a large constant temperature convection oven (Fig. 5.2). The temperature inside the oven is controlled using a PID (proportional–integral–derivative) controller module which can regulate the temperature with an accuracy of 0.5° C.

The core-flooding apparatus utilises four injection pumps (Fig. 5.2) which could be run either independently or in synchronised pairs. All four pumps are of pulsation-free, positive-displacement pump type. The injection pumps can have the pressure, volume and flow-rate values set and recorded with accuracies of 35 KPa (5 psi), 0.05 cc and 0.05 cc/hr, respectively. All the pressure sensors utilised within the core-flooding rig have the same 35 KPa (5 psi) measurement accuracy.



**Figure 5.2. The schematic diagram of the experimental apparatus used to run the core-flooding.**

The core-holder used in this research was a standard biaxial core-holder (Fig. 5.3). Standard biaxial or hydrostatic type core-holders are defined as core-holders that have common radial and axial pressure applied to the core-sample. A specially designed spider-web-type groove pattern (Fig. 5.3) is utilised on the end-faces of the core-holder's distribution plugs which comes in contact with end-faces of the core sample. This is to make sure that the fluids, before entering or on exiting the core-sample, are evenly distributed on the whole face of the core-sample. This type of groove pattern is very effective in making the capillary inlet and outlet effects, which are commonly experienced during the displacement experiments, less pronounced. All core-holder out-flow fluids are passed through a dome-type back-pressure regulator (BPR) which keeps the pressure inside the sample constant and equal to reservoir in-situ pore pressure and, furthermore, prevents any back-flow of the produced fluids into the core sample from the high pressure separator.

The separation and collection system is comprised of a high pressure-high temperature three-phase vertical separator, three collection pumps and associated sensors. The separation occurs due to gravity inside the specially designed separator, which can operate at the same pressure and temperature as reservoir in-situ conditions (i.e. P-T conditions inside the core sample). This is highly beneficial, especially for the material balance calculations, since there is no need to back-convert the produced volumes to reservoir conditions, which would be necessary if the fluids were being flushed into ambient conditions. Furthermore, for the experiments performed here, the high pressure inside the separator eliminated the liberation of the CO<sub>2</sub> already dissolved in the CO<sub>2</sub>-saturated injection brine or the evaporation of the hot water coming out of the core-sample, both of which could cause serious errors during the material balance calculations. With regards to technical specifications, the three collection pumps are identical to the injection pumps previously described.

All of the sensors and electronic interfaces of the apparatus are connected to two computers with appropriate data logging and monitoring software installed. The whole system including the sensors, the PID controllers and the injection and collection pumps are monitored and controlled using these two computers. The data logging can be done with time-steps as short as one second.

For the core-flooding experiments conducted, a special multilayered combination sleeve was used. This combination sleeve was necessary due to the tendency of scCO<sub>2</sub> to diffuse and penetrate through most

flexible rubber sleeves, which could cause the sleeve to lose its integrity and fail. Also, material balance calculations necessary to derive fluid saturations inside the core sample can be erroneous due to loss of scCO<sub>2</sub> through diffusion. This combination sleeve was made of three layers including one layer of heat-shrink Teflon, one layer of aluminium foil and one layer of conventional Viton. The heat-shrink Teflon sleeve has an extremely low permeability to CO<sub>2</sub>, but, to make sure that the CO<sub>2</sub> would not escape to the overburden annular space, a layer of aluminium foil was also placed between the Teflon and Viton sleeves.

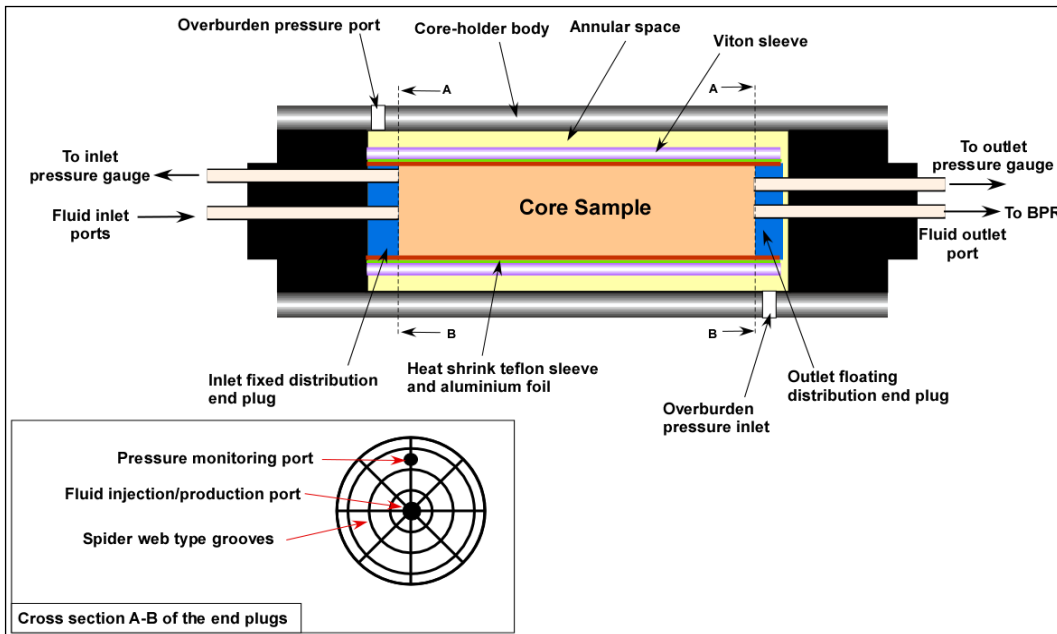


Figure 5.3: Schematic cross-section illustration of the core-holder assembly used during core-flooding.

### 5.3.4 EXPERIMENTAL PROCEDURE

#### Mutual presaturation of brine and CO<sub>2</sub>

In order to have immiscible displacement, before the start of a core-flooding experiment, the brine and scCO<sub>2</sub> had to become mutually saturated with each other under in-situ reservoir conditions. Below is an outline of the procedure followed to achieve this mutual saturation:

1. Two of the three fluid sample bottles within the experimental apparatus were cleaned, evacuated and filled, one with CO<sub>2</sub> and the other with de-aerated brine and they were brought to reservoir in-situ P-T conditions.

After isolating the bottles, CO<sub>2</sub> was brought in contact with the brine by opening the relevant valves and using the lines connecting the two bottles together (Fig. 5.4).

While the two bottles were connected, using one of the injection pumps, about 200 cc of the brine was injected into the CO<sub>2</sub> bottle. After waiting for 10-15 minutes for the brine to settle at the bottom of the CO<sub>2</sub> bottle, about 200 cc CO<sub>2</sub> was injected into the brine bottle. Due to gravity, this volume of CO<sub>2</sub> would stay like a gas cushion on top of the brine bottle.

Then the system was brought to reservoir conditions and left for about 5 days for the CO<sub>2</sub> cushion to diffuse into the brine and for the brine at the bottom of the CO<sub>2</sub> bottle to evaporate into the CO<sub>2</sub>. The convective mixing (Ennis-King and Paterson, 2007; Ennis-King et al., 2003) phenomenon was expected to enhance the diffusion of CO<sub>2</sub> into the brine in order to create a more homogenous mixture. During this time one of the injection pumps shown in (Fig. 5.4) was left connected directly to the CO<sub>2</sub> bottle while operating under the constant pressure (equal to reservoir pressure). During this process, the two bottles and connecting lines were inside a constant temperature (equal to reservoir temperature) convection oven. The

CO<sub>2</sub> being dissolved into the brine could be detected through monitoring the small changes in the volume of the pump which kept the pressure of the CO<sub>2</sub> bottle constant.

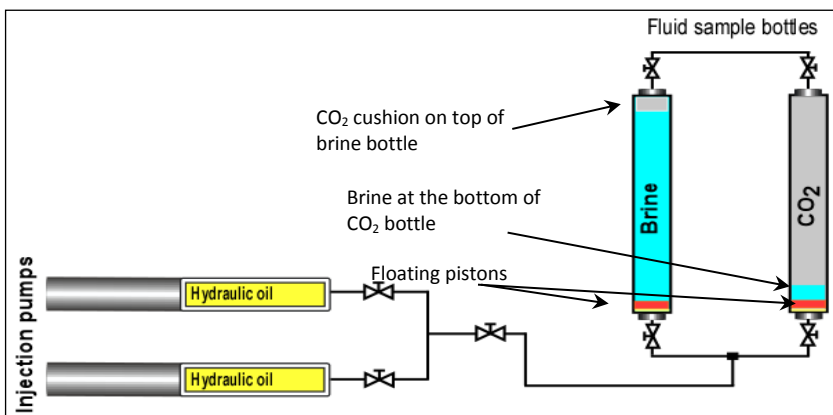


Figure 5.4: Schematic diagram of the configuration used to bring CO<sub>2</sub> and brine in contact with each other.

After the above-mentioned time, a small volume of the brine which had been in contact with CO<sub>2</sub> was produced into the separator. At the same time the CO<sub>2</sub> collection pump, connected to the separator was used to keep the pressure inside the separator equal to reservoir pressure. With the injection of brine into the separator, if the volume of the existing CO<sub>2</sub> inside the CO<sub>2</sub> collection pump kept decreasing, it indicates that further CO<sub>2</sub> was being dissolved into the brine produced into the separator. In other words, the brine had not become fully saturated with CO<sub>2</sub> and needed to be left in contact with CO<sub>2</sub> for a few more days. But if the volume of CO<sub>2</sub> inside the CO<sub>2</sub> collection pump did not change it indicates that the brine was fully saturated with CO<sub>2</sub>.

Steps 3, 4 and 5 were repeated until it was felt that the brine had become fully saturated with CO<sub>2</sub>. It is worth noting that, during the flooding experiments, any produced CO<sub>2</sub> could be recycled through recycling lines shown in red in Fig. 5.2. The CO<sub>2</sub> inside the CO<sub>2</sub> bottle was expected to become saturated with water vapour much faster after the 200 cc water was placed at the bottom of the bottle.

### Core flooding procedure

Below is an outline of the steps involved in carrying out any of the earlier mentioned conventional unsteady-state core-flooding experiments. This procedure has been designed based on the standard procedures and protocols available in the literature (Bennion and Bachu, 2005; Izgec et al., 2008; Perrin and Benson, 2010; Saedi et al., 2011).

1. A sample was wrapped in the previously described multi-layered sleeve before being inserted into the core-holder. In order to eliminate the effect of gravity segregation (underrun or override of the injected fluids) within the sample tested while undergoing the core-flooding experiment, the core-holder containing the sample was placed vertically so the injection would be performed from base to the top. In order to apply overburden pressure to the sample, after loading the wrapped sample into the core-holder, the overburden fluid was pumped (using a hand pump) slowly into the annular space of the core holder.
2. After gradually increasing the overburden pressure to the full reservoir net effective pressure, all the inlet and outlet ports of the core-holder were capped or connected to appropriate flow-lines and pressure gauges. Then low pressure CO<sub>2</sub> gas was passed through the sample for at least 20 minutes. Due to its high diffusivity, CO<sub>2</sub> would displace and replace much of the air present in the sample's pore space. Compared to air, the CO<sub>2</sub> which replaced the air could be evacuated from the sample more effectively when required. Furthermore, any CO<sub>2</sub> remaining after evacuation would readily dissolve in the saturating dead brine and be removed from the sample during the later in-situ saturation and initial brine permeability measurement process.
3. After flushing the sample with CO<sub>2</sub>, all the flow-lines and the sample inside the core-holder were evacuated using a vacuum pump for at least 24 hours. Then the back pressure was brought to full

in-situ reservoir pressure, and the air bath temperature was raised to reservoir temperature. Then the core sample was displaced and saturated using dead formation brine while the confining pressure was increased and then maintained equal to its in-situ reservoir value. The sample was left under reservoir conditions in contact with brine for another 48 hours to become completely saturated with dead brine and to establish adsorption equilibrium.

4. In the next step the CO<sub>2</sub>-saturated brine was injected into the core sample at constant flow-rate to displace the dead formation brine. The CO<sub>2</sub>-saturated brine injection continued until steady-state conditions were achieved (i.e. constant and steady differential pressure across the sample and production flow-rate was equal to injection flow-rate).
5. Then, the injection of the vapour-saturated scCO<sub>2</sub> began at constant flow-rate (primary drainage flood). The displacement continued until steady-state conditions were reached (i.e. no more brine production and constant and steady differential pressure across the sample). At the conclusion of this drainage process there was a so called "bump flow" (i.e. a short period of high injection flow-rate) performed to examine and quantify the existence of any capillary end-effect (Grigg and Svec, 2006; Heaviside and Balck, 1983; Rapoport and Leas, 1953).
6. After the conclusion of the primary drainage, the core-sample was subjected to the primary imbibition flood. CO<sub>2</sub>-saturated brine was injected into the sample at constant flow-rate. The brine injection continued until steady-state conditions were achieved. Like before, steady-state conditions meant no more CO<sub>2</sub> production from the sample and having stable and constant differential pressure across the sample.
7. In the next step, for two of the experiments, the sample underwent another cycle of drainage-imbibition floods (secondary drainage and imbibition). For this purpose, steps number 5 and 6 were repeated.
8. At the conclusion of the experiment, the core-holder was depressurised and the core sample was removed.

As mentioned before, in addition to the three conventional core-flooding experiments performed using the above described procedure, a fourth experiment was also conducted with the main aim of collecting brine samples for geochemical analyses from the outflow of the core-plug. For this experiment, the same procedure outlined above was followed, however, in this experiment the produced brine during each stage of the flooding procedure, instead of going through to the separator, was collected in small volumes of 10-20 cc in plastic vials which were then capped and refrigerated before being sent off to a geochemical laboratory for analysis.

### Capillary Entry Pressure Measurement Procedure

As mentioned before, the last core-flooding experiment was conducted on a thin shale disk representing the shale intervals in the Yalgorup Member of the Lesueur Sandstone. The objective of this experiment was to measure the shale's capillary entry pressure to scCO<sub>2</sub> under in-situ reservoir conditions. Unfortunately even the best available shale sample was too friable and a full intact disk could not be recovered (Fig. 5.5). In order to preserve the shale sample, it was immersed in silicon oil immediately after cutting the disk from a whole core section.



**Figure 5.5** Cross-sectional view of the shale disk showing the fractures induced during sample preparation (sample diameter=3.8 cm)

In order to make the cracked disk (Fig. 5.5) usable for the test it was placed between two Teflon disks (Fig. 5.6) and then the assembly was wrapped in Teflon tape, a heat-shrink FEP sleeve and two layers of aluminium foil before being loaded into the core-holder. Then a small hole (diameter of approximately 3mm) was drilled into the Teflon disks placed on either sides of the shale disk to direct the injected scCO<sub>2</sub> onto an intact (crack-free) part of the sample's face. If scCO<sub>2</sub> was being injected onto the whole face of the sample, it could easily escape through the pre-existing fractures, which would result in capillary entry pressure being significantly underestimated.

As mentioned earlier, the shale disk was preserved in silicon oil and, as a result, the sample required some sort of cleaning before it could be used for the experiment. Any leftover oil residues were removed from the surface of the shale disk using a very fine sandpaper. Then the sample was washed in formation brine to clean the sample from any fines released during the sanding process. The process of sample preparation and loading into the core-holder was carried out as fast as possible to prevent the vaporisation of the brine within the preserved shale disk.

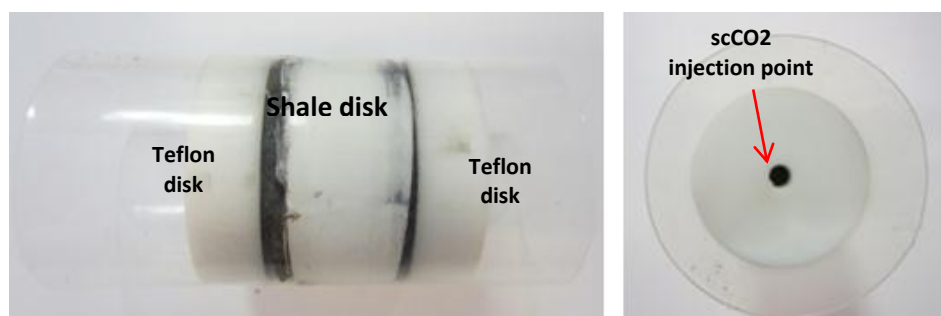


**Figure 5.6 Shale disk sample assembly (sample dimensions: D=3.8 cm, L=1.5 cm).**

After loading the sample assembly into the core holder, overburden pressure was raised to full in-situ net effective pressure. Then, the downstream side of the sample was evacuated by vacuum to remove any air. After that, low pressure formation brine and CO<sub>2</sub> were introduced into the downstream and upstream sides of the shale disk, respectively. Then, brine, CO<sub>2</sub> and overburden pressures were increased at the same rate until all reached that of in-situ reservoir values. Increasing the pressure of the fluids at the same pace eliminated the possibility of applying any differential pressure across the sample which could possibly allow the CO<sub>2</sub> invade the pore space of the shale before full in-situ pore pressure could be achieved.

In the next step the core sample was left in contact with the fluids for about 2 hours while all the pressures were kept constant. This was necessary to eliminate any pressure disturbances which may have been created during the setup process. Then, while the brine pressure in the downstream side of the disk was kept constant, scCO<sub>2</sub> injection was commenced to increase the pressure in the upstream side of the disk in a stepwise fashion. In each step the scCO<sub>2</sub> pressure was raised by 345 KPa (50 psi) and subsequently kept constant for 2 hours. During this time the pressure gauge connected to the production side of the sample was monitored for any possible increase in the brine pressure. If no change in brine pressure was detected then it was thought that scCO<sub>2</sub> had not invaded the pore space of the shale disk. Then scCO<sub>2</sub> pressure was raised by another 345 KPa (50 psi) and maintained for another 2 hours while monitoring the brine pressure. This stepwise increase in pressure would be continued until an increase in the brine pressure in the production side of the sample would be detected. The differential pressure applied across the sample at that moment would be very close to the capillary entry pressure of the shale to scCO<sub>2</sub> under reservoir conditions.

## 5.4 Results and discussion

The main data generated as part of this experimental work includes the relative permeabilities and the end-point residual saturations. The capillary entry pressure of the shale could also be an important data

generated here but due to the poor condition of the available shale sample, meaningful data could not be generated. The relative permeability data generated includes the full curve for the drainage floods and the end-points for the imbibition floods.

Presented in the following part of this report are the above mentioned data for each individual core sample tested, along with a discussion of the results obtained.

### 5.4.1 SAMPLE 206647

Sample 206647 consisted of, to some extent, poorly sorted sandstone (Fig. 5.7). This feature was expected to influence the results of the core-flooding experiment.



Figure 5.7 Sample 47H (L=7.4cm, D=3.63cm).

Two drainage (primary and secondary) floods were conducted on this core sample using the core-flooding procedure outlined earlier. One imbibition flood was also conducted in between the two drainage floods. The end-point residual saturations obtained at the end of the drainage and imbibition floods are presented in Table 5.3 along with the corresponding end-point relative permeabilities for the displacing fluids.

Sample ID	End-point Residual Saturation of the Displaced Fluid, %			End-point Relative permeabilities for the Displacing Fluid, fraction (fraction)		
	Primary Drainage	Primary Imbibition	Secondary Drainage	Primary Drainage	Primary Imbibition	Secondary Drainage
206647	45.00	22.87	44.22	0.223	0.353	0.230

Table 5.3 End-point residual saturations and relative permeabilities for the floods conducted on sample 206647.

Presented in Fig. 5.8 is the brine production versus pore volumes of scCO<sub>2</sub> injected through the sample for the primary drainage flood conducted on sample 206647. The relative permeability curves corresponding to this brine production profile are also shown in Fig. 5.9. The data using these curves have been plotted are presented in Appendix F. It is worth noting that the relative permeability data provided in this report were calculated using a history matching technique. For this purpose, Sendra software from Weatherford Petroleum Consultants, which is based upon a two-phase, 1D black-oil simulation model together with an automated history matching routine, was used to reconcile time and spatially dependent experimental data and generate the relative permeabilities.

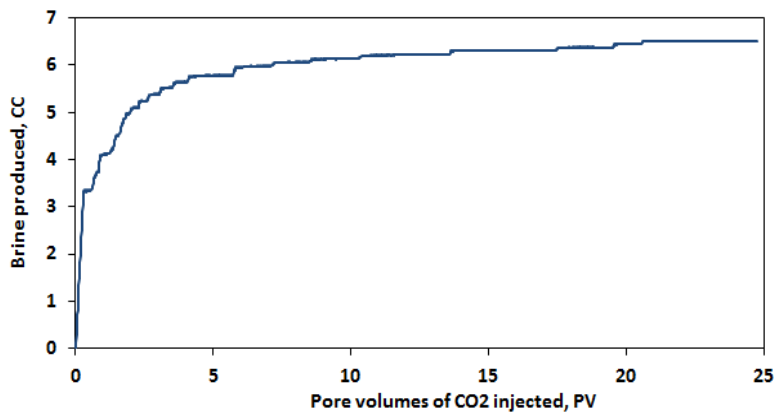


Figure 5.8 Brine production profile for the primary drainage conducted on sample 206647.

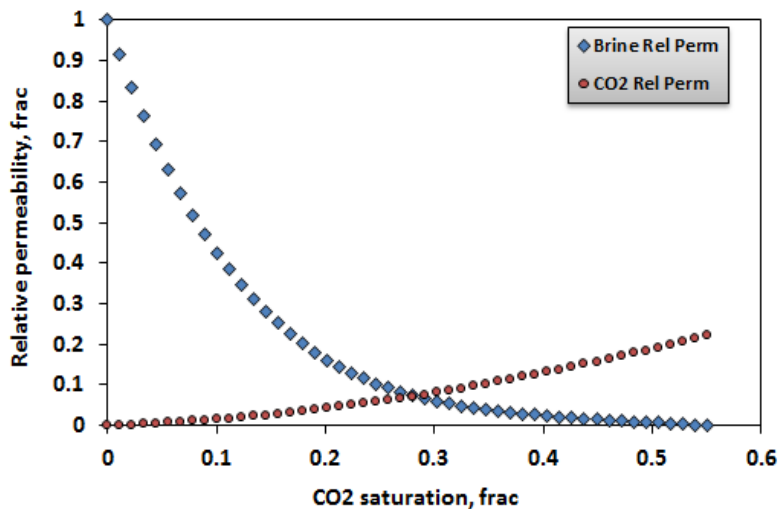


Figure 5.9 Relative permeability curves for the primary drainage conducted on sample 206647.

The sample's absolute permeability measured under in-situ reservoir conditions (Table 5.2) at the beginning of the core-flooding experiment using 30,000 ppm NaCl formation brine was considerably (more than 11 times) less than the permeability measured on the dry sample using helium (Table 5.1). Furthermore, the helium permeability measurement conducted on the post-flood dry sample showed a reduction of almost 25% compared to that of the pre-flood conditions. The difference between the helium and brine and the pre- and post-flood permeabilities may be mainly attributed to any damages (e.g. fines migration) caused by presence of clay minerals in the sample's pore space. As mentioned before, the results of the XRD analysis showed that sample 206647 contained 4% (wt%) kaolinite. The role of fines migration in the permeability reduction of the post-flood sample is further reaffirmed by the fact that while permeability of the sample was reduced after undergoing the flooding procedure, the change in its porosity was not appreciable. This is in line with what has been reported in the literature by other researchers (Hayatdavoudi and Ghalambor, 1996; Morris and Shepperd, 1982; Musharova et al., 2012; Priisholm et al., 1987).

Furthermore, the end-point relative permeability to brine measured at the end of the primary imbibition is unusually low. This again could be attributed to the earlier mentioned fines migration phenomenon which may have occurred during the flooding procedure. It is worth noting that the migration of any fines which may result in the plugging or blockage of the sample's pore throats may intensify the snap-off trapping mechanism and consequently cause the residual  $\text{scCO}_2$  saturations to be abnormally high.



### 5.4.2 SAMPLE 206660

The primary focus of the core-flooding experiment conducted initially on sample 206660 was to investigate the occurrence of any geochemical reactions between the fluids and the rock while undergoing the flooding procedure. Therefore, about 55 brine samples of each about 10-20cc were collected during the multistage core-flooding experiment conducted on this sample. After this initial core-flooding experiment, a second experiment was conducted on this sample focusing on the measurement of residual saturations and relative permeabilities. The results of this experiment are presented and discussed here while the results of the chemical analysis conducted on the brine samples taken during the first experiment are included elsewhere (Stalker et al., 2013).

As part of the second core-flooding experiment, sample 206660 underwent a primary drainage flood followed by a primary imbibition flood. The end-point residual saturations obtained at the end of the drainage and imbibition floods are reported in Table 5.4 along with the corresponding end-point relative permeabilities for the displacing fluids.

Fig. 5.10 shows the brine production versus pore volumes of scCO<sub>2</sub> injected through the sample for the primary drainage flood. The relative permeability curves corresponding to this brine production profile are presented in Fig. 5.11. The data from which these curves have been plotted are presented in Appendix F.

Sample ID	End-point Residual Saturation of the Displaced Fluid, %		End-point Relative permeabilities for the Displacing Fluid (fraction)	
	Primary Drainage	Primary Imbibition	Primary Drainage	Primary Imbibition
206660	40.12	42.71	0.206	0.125

Table 5.4 End-point residual saturations and relative permeabilities for the floods conducted on sample 206660.

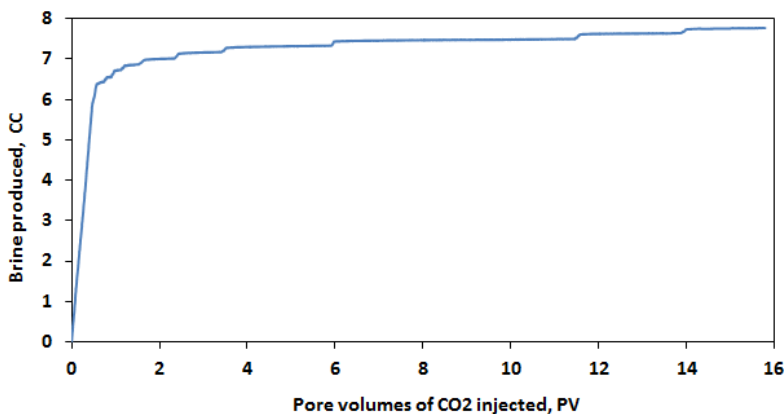


Figure 5.10. Brine production profile for the primary drainage flood conducted on sample 206660.

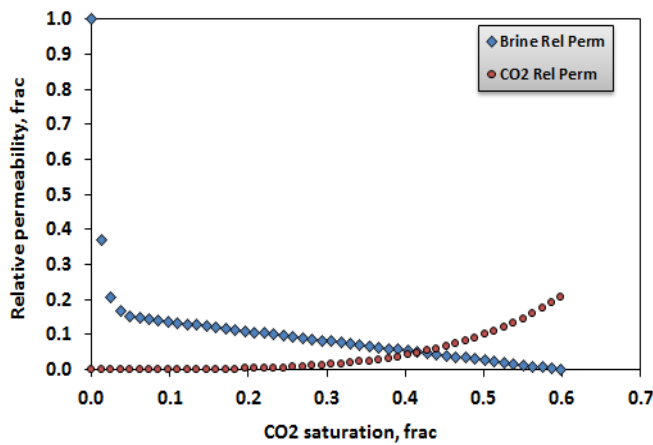


Figure 5.11 Relative permeability curves for the primary drainage conducted on sample 206660H.

Similar to sample 206647, the in-situ brine permeability of sample 206660 was considerably less than its helium permeability (by almost a factor of 8) (Table 5.1). Also, the post-flood dry sample showed 51% reduction in permeability to helium. With the lack of any evidence proving otherwise, it may be concluded the most likely cause of the permeability reduction and the difference between the brine and helium permeabilities is due to fines migration. The results of the XRD analysis support this claim as the data show that the sample contained 7% (wt%) kaolinite. Similar to the previous sample, the porosity of this sample also did not change considerably after undergoing the flooding procedure.

While the measured end-point CO<sub>2</sub> relative permeability is within the expected range, the end-point brine relative permeability is extremely low. Furthermore, the corresponding residual scCO<sub>2</sub> saturation is very high. As mentioned earlier when discussing the results for sample 206647, the very low end-point relative permeability to brine and very high residual scCO<sub>2</sub> saturation may have been caused by blockage or plugging of the pore-throats by the clay (kaolinite) fines mainly during the imbibition flood. The fines movement could also be responsible for the unusual shape of the brine relative permeability curve seen in Fig. 5.11.

### 5.4.3 SAMPLE 206669

The last core-flooding experiment was conducted on sample 206669. Similar to sample 206647, two drainage floods (primary and secondary) and an imbibition flood (primary) were conducted in turn on this sample.

The end-point residual saturations obtained at the end of the drainage and imbibition floods are presented in Table 5.5 along with the corresponding end-point relative permeabilities for the displacing fluids.

Sample ID	End-point Residual Saturation of the Displaced Fluid, %			End-point Relative permeabilities for the Displacing Fluid (fraction)		
	Primary Drainage	Primary Imbibition	Secondary Drainage	Primary Drainage	Primary Imbibition	Secondary Drainage
206669	41.65	34.47	41.84	0.172	0.096	0.15

Table 5.5 End-point residual saturations and relative permeabilities for the floods conducted on sample 206669.

Presented in Fig. 5.12 is the brine production versus pore volumes of scCO<sub>2</sub> injected through the sample for the primary drainage flood conducted on sample 206647. The corresponding relative permeability curves are also plotted in Fig. 5.13. The data using which these curves have been plotted are presented in Appendix F.

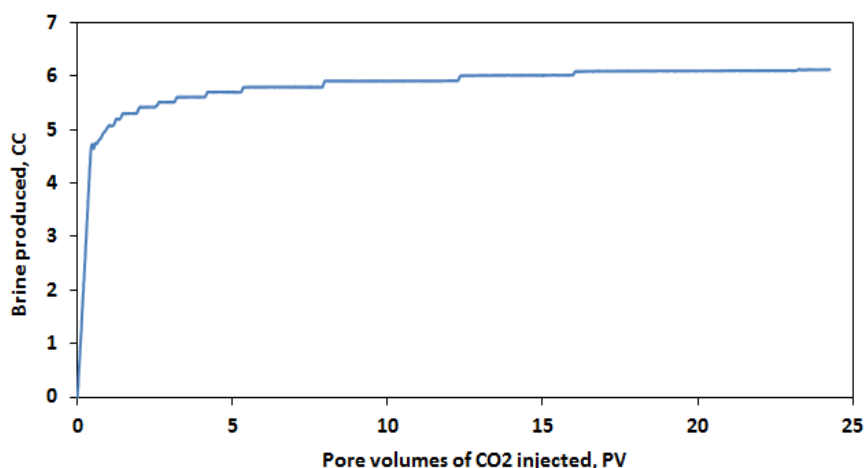


Figure 5.12 Brine production profile for the primary drainage conducted on sample 206669.

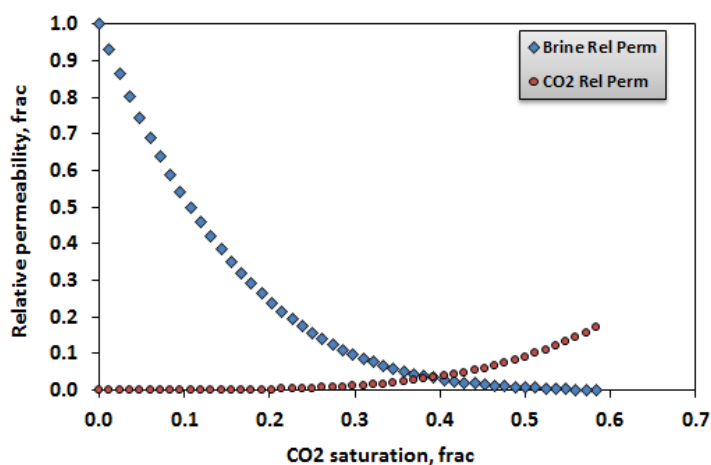


Figure 5.13 Relative permeability curves for the primary drainage conducted on sample 206669.

Sample 206669 exhibited features similar to those observed for sample 206647 and 206660. Again here, there was a considerable difference between the in-situ brine permeability and the one measured using helium (Table 5.1). Also, the post-flood sample showed about 44% reduction in its permeability compared to its initial pre-flood value. One more time, the existing evidence (thin sections, XRD data, pre-flood SEM images) all point towards potential reactions which may have had occurred between the injected fluids and the clay minerals present in the core sample's pore space. Also, once again, the difference between the pre- and post-flood porosities of sample 206669 were negligible.

Like before, the extremely low end-point relative permeability to brine and very high residual  $\text{scCO}_2$  saturation may have been caused by the damage done to the pore space of the core sample by the potential movement of clay fines.

#### 5.4.4 SHALE DISK 1

As mentioned earlier, a small shale disk (Table 5.1) was prepared from the shale material recovered from the Harvey-1 core samples. The aim was to use this shale disk to measure its capillary entry pressure to  $\text{scCO}_2$  under in-situ reservoir pressure and temperature. As indicated before, due to the shale material being very friable, a fully intact disk could not be recovered for this experiment (Fig. 5.5).

While using a special sample assembly (Fig. 5.6) it was attempted to make the sample usable for the experiment, unfortunately, no meaningful results could be generated from the test. Using the earlier described procedure, the  $\text{scCO}_2$  pressure in the upstream side of the sample was raised through a stepwise fashion to about 17.25 MPa (2500 psi) in excess of the downstream brine pressure but after waiting for

almost 15 hours no pressure increase was detected in downstream side of the sample. One likely reason for  $\text{scCO}_2$  not to invade the sample, or for any possible invasion to be so slow that could not be detected, could be the fact that  $\text{scCO}_2$  was exposed to the sample through a very small portion of the sample's face (an area of about 3 mm in diameter) instead of the whole face of the sample which could help eliminate the effect of any small scale localised heterogeneity in the shale sample.

## 5.5 Summary and Conclusions

In total three conventional core-flooding experiments were conducted on three different core-plugs from the Wonnerup Member of the Lesueur Formation. The main data generated by the experiments included residual  $\text{scCO}_2$  saturations and relative permeabilities for the drainage floods. While the residual  $\text{scCO}_2$  saturations obtained were relatively high, as one may expect, they are inversely proportional to the samples' absolute permeabilities (Fig. 5.16).

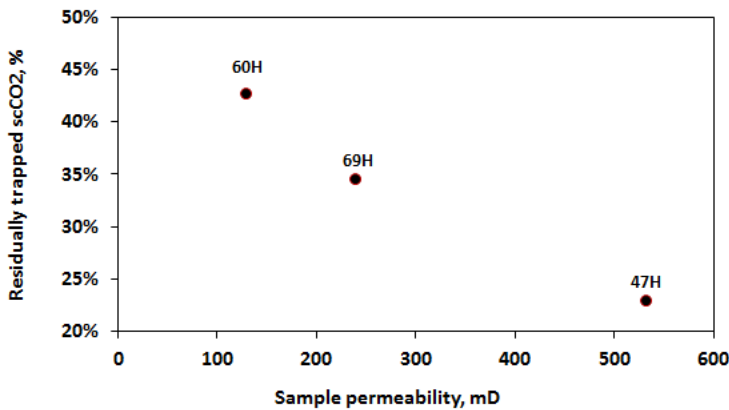


Figure 5.14 Residual  $\text{scCO}_2$  saturation versus sample permeability

As pointed out earlier, the results of the XRD analysis performed on the offcuts of the samples tested here indicated that all three samples contained 2%-7% (wt%) of kaolinite. Kaolinite is a type of clay mineral which is known to cause severe formation damage associated with migration of fines within the pore space of the porous media (Hayatdavoudi and Ghalambor, 1996; Musharova et al., 2012; Priisholm et al., 1987). Presence of kaolinite in the pore space could cause moderate to significant reduction in the permeability of a core sample once flooded. While permeability could be considerably affected by the fines migration phenomenon, porosity, on the other hand, is not expected to change considerably.

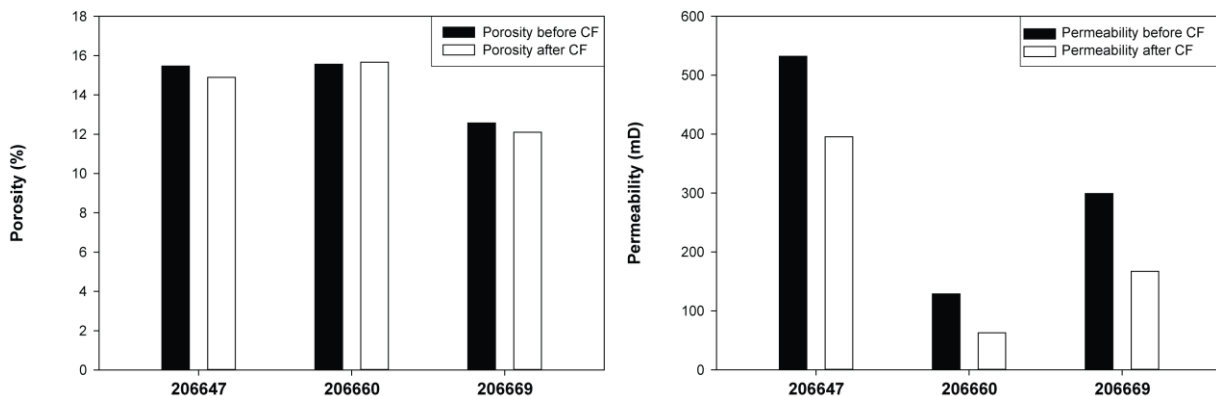


Figure 5.15. Porosity (left) and permeability (right) measured using the Helium methods on the three core plugs before and after core flooding experiments (CF). Note that while the variation in porosity is minimal, there is a significant decrease of permeability of all three sample tested.

The samples tested here showed a 25%-51% reduction in permeability after undergoing the scCO<sub>2</sub>-brine flooding while the changes in their porosity values were negligible (Fig. 5.16). In the absence of any alternative evidence, the results of all the analysis performed point towards fines migration to be the main cause of issues encountered while flooding the samples tested here.

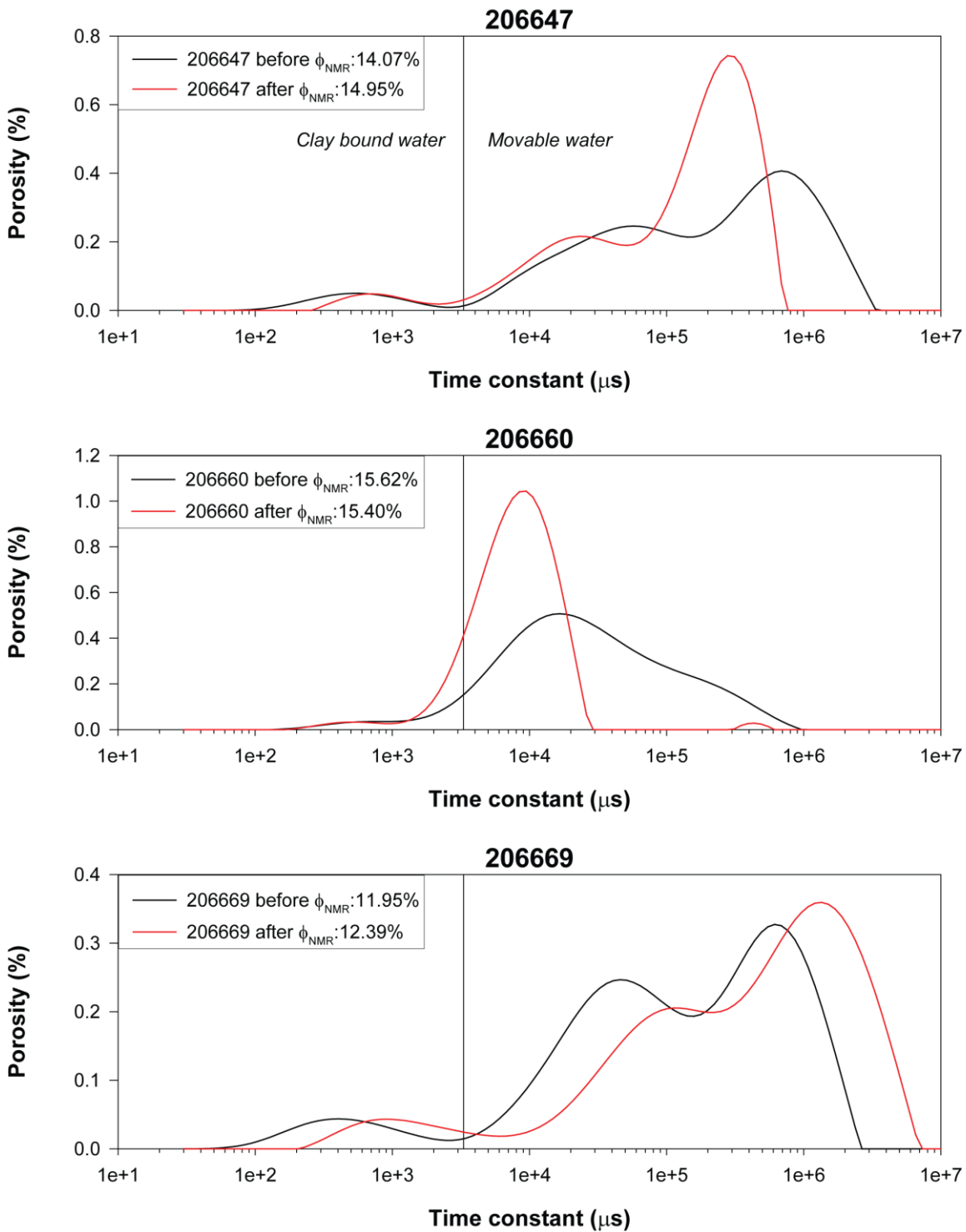


Figure 5.16. NMR inverted porosity for the three core samples before and after core flooding experiments. The total porosity is non significantly affected by the flooding tests but the relaxation time curve for the same specimen is significantly different.

The fines migration hypothesis is supported by observations in finds support in the NMR measurements performed on the specimens before and after core flooding experiments (Fig. 5.15) indicating a negligible variation of total porosity (as also indicated by the Helium measurements) but a significant difference in the distribution of pore sizes. In general the larger pores (the right end of the spectrum) seem to disappear in favour of a higher proportion of medium size pores, an observation compatible with the occlusion of larger pores by the fine material dislodged by the fluids flowing through the pore space.

Any formation damaged caused by fines migration may have introduced some degree of uncertainty in the results obtained. As pointed out earlier, the measured end-point residual  $\text{scCO}_2$  saturations are higher than usual and the brine end-point relative permeability values measured for all the samples are very low. Both of these observations could have been due to fines migration caused by dislodgement of kaolinite particles during the flooding procedure (Fig. 5.17).

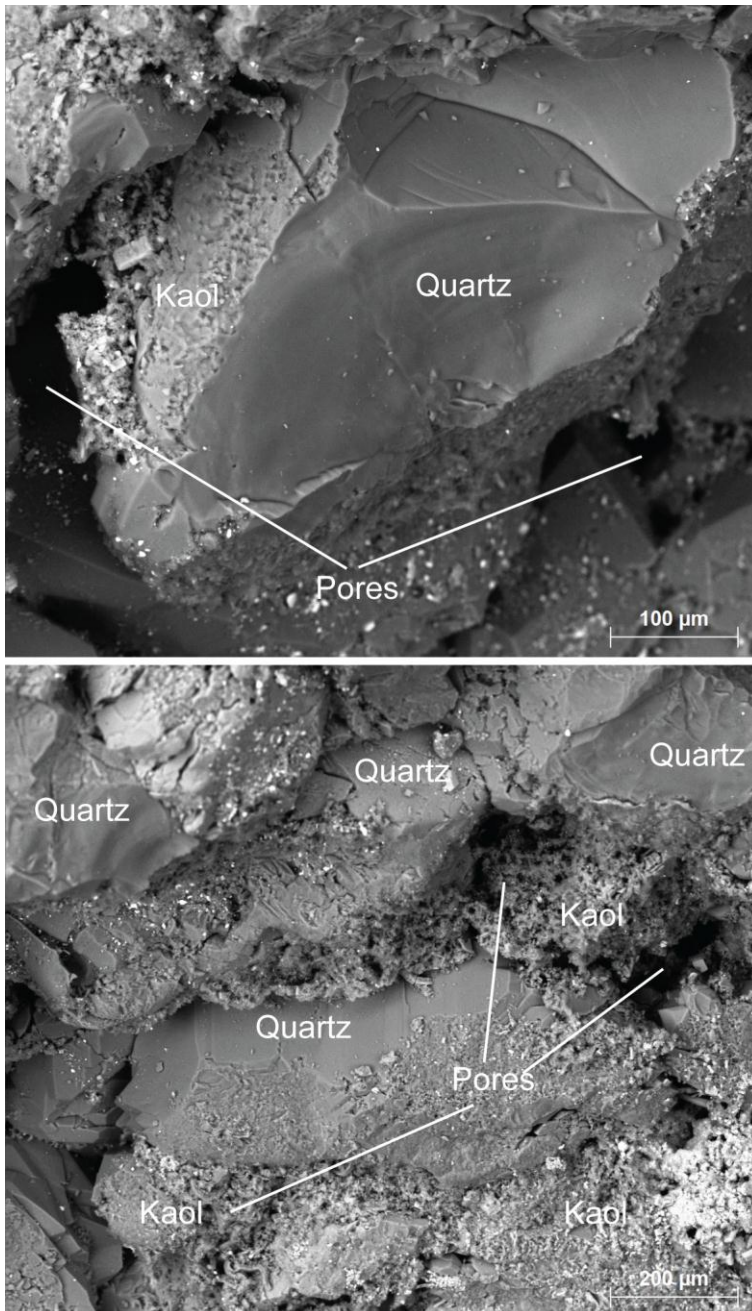


Figure 5.17. Scanning electron microscopy images of sample 206669 showing the occurrence of diagenetic, fine grained kaolinite (Kaol in the figure) partially occluding the pores between detrital quartz grains

Furthermore, as usual with any scCO<sub>2</sub>-brine flooding experiment, the injection fluids (i.e. scCO<sub>2</sub> and carbonated brine) may have had chemical interactions with the matrix of the rock samples tested. This may not be fully compatible with some of the assumptions made in deriving the Darcy's Law which is the basis for the relative permeability measurements and interpretation techniques applied.





# 6 Module 5a Geomechanical-ultrasonic core plug characterization

## 6.1 Summary

This module summarizes the geomechanical and rock physics high pressure experiments performed on core plugs from the Yalgorup and Wonnerup Members of the Triassic Lesueur Formation. The specimens were tested at conditions simulating the in situ pressure and fluid content.

The tests indicate that the members behave significantly differently from the mechanical and elastic points of view: the Yalgorup is relatively weak while the Wonnerup show stronger and stiffer responses.

The results of this module have been used in the fault reactivation evaluation of the area (Langhi et al., 2013) and can be feed into reservoir simulations to estimate, for example, the safe maximum injection pressure in the reservoir to avoid fracturing of the rocks and consequent fluid escape.

## 6.2 Introduction

This module presents the results of high pressure experiments performed on core plugs extracted from Harvey-1. The experimental characterisation of the core material followed two directions: i) geomechanical tests, aimed at obtaining the mechanical response and contemporaneously measuring ultrasonic wave velocity on saturated samples as a function of the applied stress; and ii) high pressure ultrasonic tests aimed at measuring the ultrasonic wave velocities as a function of fluid content and stress state.

The experimental results are discussed in terms of available literature values and, where possible, empirical correlations are established among measured rock properties. These could be of use, for instance, for estimation of rock strength parameters from wireline logs.

## 6.3 Analytical Techniques/Approach

The experimental protocols and testing equipment adopted in this study are illustrated in the following paragraphs.

### 6.3.1 GEOMECHANICAL TESTS

Consolidated undrained multi stage triaxial tests (Fjaer et al., 1992) were performed on saturated samples using a Terratek testing machine (Fig 6.1). The equipment comprises a high stiffness load frame, a pressure vessel, and three independent stepping motor pumps for cell and pore pressure control, as well as for axial load. The operational limits of the rig are 70 MPa confining pressure (oil used as a confining medium), 70 MPa pore pressure and 400 MPa axial stress on a 38mm diameter sample (Delle Piane et al., 2011; Dewhurst and Siggins, 2006). All experiments were conducted at room temperature; data logging and pump control is based on a LabVIEW program. The sample assembly includes:

1. A cylindrical sample mounted between top and base platens;
2. An impermeable Viton membrane (0.75 mm thick), isolating the specimen from the confining fluid and housing the radial and off-axis ultrasonic P-wave and S-wave transducers;
3. Two steel platens housing ultrasonic P- and S- transducers with provision for pore pressure measurements placed at both ends of the specimen;
4. Two diametrically opposed linear variable differential transformers (LVDT) clamped on the top and bottom platens to measure axial displacements;
5. A radial strain cantilever device composed of two measuring arms;
6. A load cell placed underneath the bottom platen.

Multi stage triaxial tests were performed at 6 levels of confining stress ranging between 10 and 60MPa using brine saturated sample listed in Table 6.1. Samples were chosen to be representative of the various lithofacies identified for the Yalgorup and Wonnerup Members of the Lesueur Sandstone. The brine salinity used during the tests is derived from the resistivity log analysis (cfr. module 3). Samples were saturated by immersion in a brine bath under forced vacuum for >24hours. Three Yalgorup samples failed during this process (Fig. 6.2); their failure is thought to be a result of the interaction between the brine and the rock forming swelling clay minerals (smectite).

To ensure drained behaviour, axial loading was conducted in axial displacement control at a nominal axial strain rate of less than 20 ms/hour, and excess pore pressures generated during loading are allowed to drain via fluid ports in the loading platens (i.e. top and bottom pore taps kept open with pore pressure = 0). At each stage of confining pressure the samples were axially loaded up to approximately 90% of peak strength. Subsequent loading stages were carried out after isotropic pressurisation and a suitable stabilisation period; during the final stage at the highest confining pressure the sample was loaded until failure (Fig. 6.1).

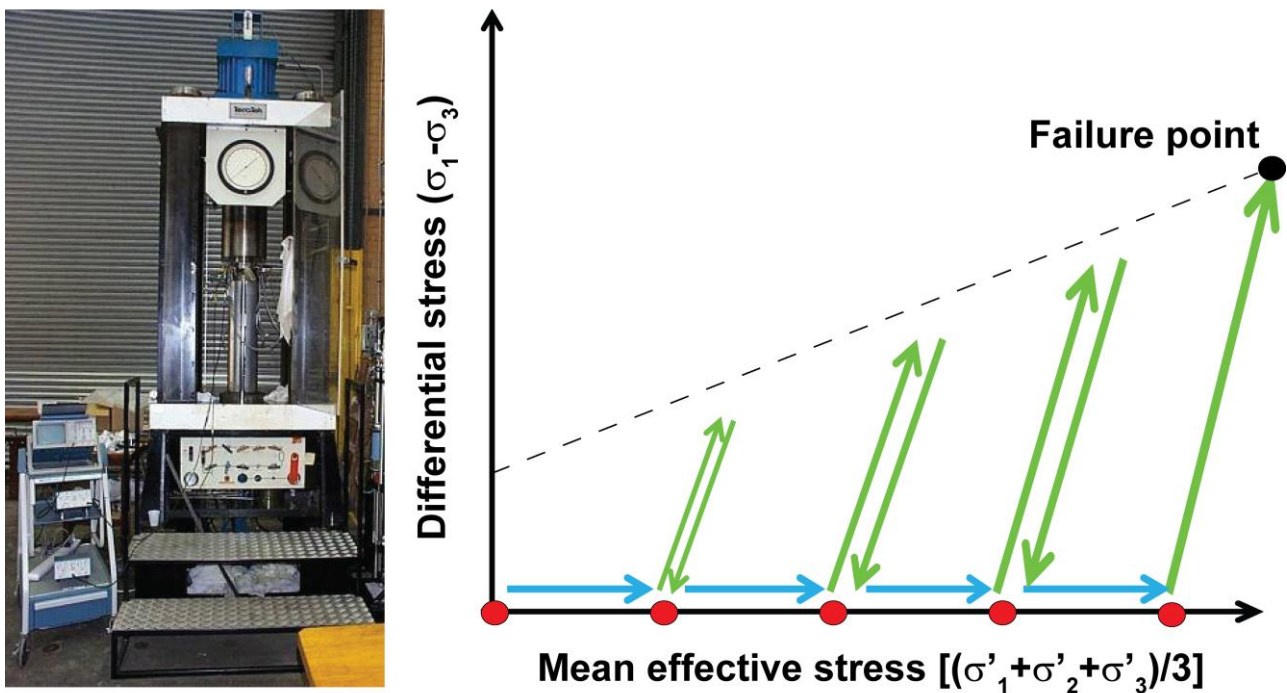


Figure 6.1. Left: Terratek triaxial testing machine equipped with ultrasonic system for measurement of P- and S-wave velocity. Right: Diagram illustrating the stress evolution during a multistage triaxial test.

The main reason for using this type of testing is to avoid heterogeneity in properties between core plugs. The downside of multi-stage testing is potentially fatiguing samples from repeated cycling above the elastic yield point of the material therefore achieving a lower bound of the mechanical properties characteristic of the tested rock.

In describing the experimental protocol the following nomenclature is used:

- Confining pressure ( $Cp$ ): isotropic pressure applied to the sample using hydraulic oil
- Pore pressure ( $Pp$ ): pressure of the fluids saturating the pore network of the sample
- Effective pressure:  $Cp - Pp$

- Differential stress: Difference between the maximum principal stress and minimum principal stress ( $\sigma_1 - \sigma_3$ )

Mean effective stress: mean of the effective principal stresses acting on the sample:  $(\sigma_1' + \sigma_2' + \sigma_3')/3$ <sup>1</sup>

The stress-strain data from multi-stage triaxial tests were used to determine the specimen's Mohr-Coulomb failure envelope. The failure envelope can be determined from the stress ( $\sigma_1, \sigma_3$ , pore pressure) conditions at the time of failure following the equations:

$$\sigma_n' = 0.5(\sigma_1' + \sigma_3') - 0.5(\sigma_1' - \sigma_3') \cos 2\theta \quad \text{Equation 6.1}$$

$$\tau = 0.5(\sigma_1' - \sigma_3') \sin 2\theta \quad \text{Equation 6.2}$$

where  $\sigma_n$  = normal stress;  $\tau$  = shear stress, the prime indicates effective stress values and  $\theta$  is the angle between  $\sigma_1$  and the failure plane. The linear failure envelope is defined as:

$$\tau = C + \mu\sigma \quad \text{Equation 6.3}$$

Where  $\tau$  and  $\sigma$  as the shear and normal stress at failure,  $C$  = cohesion of the rock and  $\mu$  the coefficient of internal friction. Unconfined compressive strength ( $UCS$ ) was estimated as:

$$UCS = 2C \tan \beta; \beta = \frac{\pi}{4} + \frac{\Phi}{2}; \tan \Phi = \mu \quad \text{Equation 6.4}$$

The Young's modulus ( $E$ ) and Poisson's ratio ( $\nu$ ) were determined as the tangential slope of the curve of differential stress versus average axial strain and the tangential slope of the curve of average radial strain versus average axial strain at between 40% and 60% of the maximum differential stress.

Knowing  $E$  and  $\nu$ , the static bulk ( $K$ ) and shear ( $G$ ) moduli were calculated as:

$$K = \frac{E}{3(1 - 2\nu)} \quad \text{Equation 6.5}$$

$$G = \frac{E}{2(1 + \nu)} \quad \text{Equation 6.6}$$

Compressional ( $V_p$ ) and shear ( $V_s$ ) wave velocities were recorded along the core axis, at isotropic confining stress conditions and during axial loading at doubling load levels (e.g. 1kN, 2kN, 4kN, 8kN etc.) following the pulse transmission technique described by Birch, (1960). The method consists of measuring the travel time of an elastic pulse through a rock sample of known length. The nominal excitation frequencies used in this study were 0.5 MHz for P- and S-waves. The ultrasonic propagation system consists of a pulser-receiver and a digital oscilloscope recording the signals. Considering the uncertainties in the arrival times and those related to the dimension of the samples and the positioning of the transducers, the corresponding ultrasonic velocity errors could be estimated to sum up to approximately  $\pm 1\%$  for P-waves and  $\pm 2\%$  for S-waves.

---

<sup>1</sup> The symbol ' indicates the effective stress component i.e. subtracted of pore pressure

<i>Sample ID</i>	<i>Depth (m)</i>	<i>Brine (NaCl ppm)</i>	<i>Orientation</i>	<i>Formation Member</i>	<i>Facies</i>
206616	920.56	40,000	H	Yalgorup	B
206628	1273.89	40,000	H	Yalgorup	D
206635	1323.93	40,000	H	Yalgorup	Aii
206636*	1324	40,000	V	Yalgorup	Aii
206638*	1329.94	40,000	H	Yalgorup	E
206643*	1342.6	40,000	H	Yalgorup	D
206644	1343.61	40,000	H	Yalgorup	D
206645	1897.66	30,000	H	Wonnerup	Aii
206646	1897.91	30,000	V	Wonnerup	Aii
206648	1902.92	30,000	V	Wonnerup	Aii
206662	1940.58	30,000	H	Wonnerup	C
206672	2496.22	30,000	H	Wonnerup	Aii
206675	2503.46	30,000	H	Wonnerup	Aii
206683	2516.00	30,000	V	Wonnerup	Aiii

**Table 6.1.** List of sample tested for determination of geomechanical properties. H and V are core plugs drilled parallel and orthogonal to the macroscopic bedding respectively. \*Sample failed while saturating with brine, no data acquisition possible.

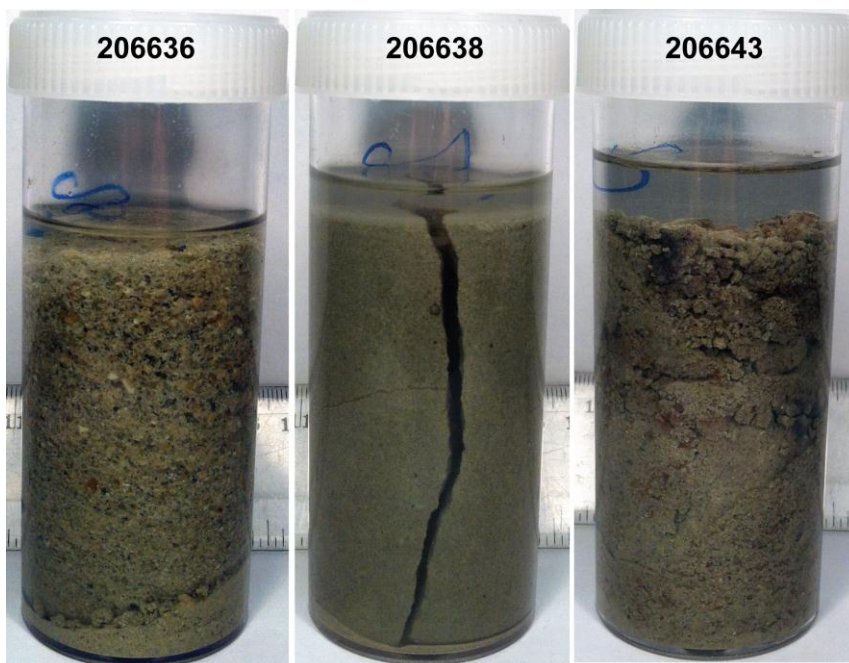


**Figure 6.2.** Samples selected for use in geomechanical tests but failed during saturation possibly due to interaction between brine and swelling clays.

### 6.3.2 ULTRASONIC TESTS

Multi stage isotropic tests were performed on the samples listed in Table 6.2 using an instrumented Hoek cell (Fig. 6.3). The equipment comprises a high stiffness load frame, a pressure vessel with an internal moulded impermeable membrane and three independent stepping motor pumps for cell and pore pressure control, as well as for axial load. The operational limits of the rig are 70 MPa confining pressure (oil used as a confining medium), 70 MPa pore pressure and 50 tons of axial load. All experiments were conducted at room temperature; data logging and pump control is based on a LabVIEW program. The sample assembly includes:

1. A cylindrical (38mm in diameter) sample mounted between top and base platens;
2. Two steel platens housing ultrasonic P- and S- transducers with provision for pore pressure measurements placed at both ends of the specimen;
3. Two diametrically opposed linear variable differential transformers (LVDT) clamped on the top and bottom platens to measure axial displacements;
4. A load cell.

For each test a dry sample was initially installed in the cell and step wise brought to increasing levels of confining pressure (values listed in Table 6.3). Between each increment sufficient time was allowed for sample equilibration, before further increasing pressure. Ultrasonic velocities ( $V_p$  and  $V_s$ ) travelling along the axis of the cylinder were measured at each confining stress step after sample equilibration (Fig. 6.2). After reaching the maximum confining pressure the sample was unloaded and saturated using the brine composition indicated in Table 6.2. After sample saturation the pressure cycle and ultrasonic measurements were repeated at the same effective stress conditions used during the dry pressure cycle and with a constant pore pressure of 1MPa (Table 6.3).

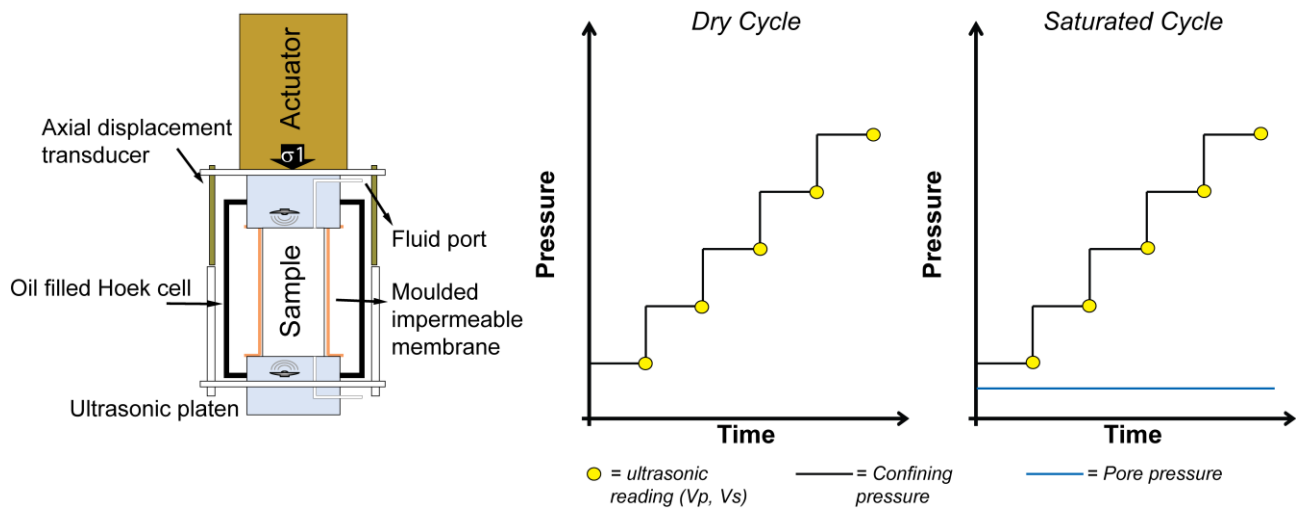


**Figure 6.3. Left: Hoek cell equipped with an ultrasonic system for measurement of P- and S-wave velocity. Right: Diagrams illustrating the stress evolution during the dry and brine-saturated rock physics tests.**

Under the assumption of homogeneity and isotropy the measured density ( $\rho$ ),  $V_p$  and  $V_s$  were used to estimate the dynamic elastic moduli of the rock according to the established elasticity relationships (e.g. Mavko et al., (2009)

$$E = \frac{\rho V_s^2 (3V_p^2 - 4V_s^2)}{V_p^2 - V_s^2}$$

**Equation 6.7**

$$\nu = \frac{V_p^2 - 2V_s^2}{2(V_p^2 - V_s^2)}$$

Equation 6.8

$$K = \frac{E}{3(1-2\nu)}$$

Equation 6.9

$$G = \frac{E}{2(1+\nu)}$$

Equation 6.10

Where  $E$  is the Young's modulus;  $\nu$  is the Poisson's ratio,  $K$  is the bulk and  $G$  the shear modulus.

Sample ID	Depth (m)	Brine (NaCl ppm)	Orientation	Member	Facies
206622	927.61	40,000	H	Yalgorup	Aii
206626	1266.21	40,000	H	Yalgorup	D
206653	1916.38	30,000	H	Wonnerup	C
206688	2525.83	30,000	H	Wonnerup	Aii

Table 6.2. List of samples tested for determination of ultrasonic elastic properties. H = sample cored parallel to the macroscopic orientation of bedding. Brine salinity is derived from the resistivity wireline logs (cfr. module 3).

Dry cycle CP (MPa)	Saturated cycle	
	CP (MPa)	PP (MPa)
1	2	1
2	3	1
5	6	1
10	11	1
30	31	1
60	61	1

Table 6.3. Experimental conditions used during ultrasonic testing of the Harvey-1 samples. CP = confining pressure; PP = pore pressure.

## 6.4 Results

### 6.4.1 MECHANICAL DATA

Images of the tested specimens are collected in Appendix G; almost all the samples failed by shear fracturing and developed a distinct and localized fracture plane oriented at an acute angle with respect to the cylinder axis. Sample 206644 is the exception as it does not show any evident strain localization but rather a pervasive deformation resulting in a barrel shaped specimen.

The mechanical properties derived from the experimental program are summarized in Table 6.4.

Sample ID	Z (m)	$\phi$ (%)	$\kappa$ (md)	UCS (MPa)	C (MPa)	$\mu$	E (Gpa)	$\nu$	G (Gpa)	K (Gpa)	Facies
206616	920.56	N/A	N/A	20.08	7.79	0.26	10.2	0.17	4.36	5.15	B
206628	1273.89	12.77	0.48	N/A	N/A	N/A	2.20	N/A	N/A	N/A	D
206635	1323.93	15.93	5.94	N/A	N/A	N/A	1.80	0.25	0.72	1.20	Aii
206644	1343.61	11.95	0.35	14.18	5.82	0.19	7.90	0.23	3.21	4.88	D
206645	1897.66	14.24	143.05	50.25	15.47	0.50	16.10	0.21	6.65	9.25	Aii
206646	1897.91	15.55	198.79	28.88	7.93	0.71	21.60	0.18	9.15	11.25	Aii
206648	1902.92	12.86	6.04	72.59	20.58	0.60	19.30	0.21	7.98	11.09	Aii
206662	1940.58	11.47	0.64	37.63	10.60	0.61	20.00	0.19	8.40	10.75	C
206672	2496.22	11.36	43.49	69.19	18.84	0.65	20.30	0.22	8.32	12.08	Aii
206675	2503.46	12.70	233.81	55.27	14.17	0.72	23.30	0.17	9.96	11.77	Aii

**Table 6.4. Summary of geomechanical properties measured on core plugs from Harvey 1. Z= depth;  $\phi$ =Helium porosity at 3.5 MPa;  $\kappa$ =Klinkenberg corrected Helium permeability at 3.5 MPa; UCS= unconfined compressive strength; C=cohesion;  $\mu$ = friction coefficient; E=Young's modulus  $\nu$ = Poisson's ratio; G=Shear modulus; K= bulk modulus. E,  $\nu$ , G and K are static elastic moduli at 40 MPa of effective pressure.**

Most of the samples can be well described by a linear Mohr-Coulomb failure envelope (Fig. 6.4-6.5) and the derived geomechanical and elastic parameters show a positive correlation with depth (Fig. 6.6). It should be noted however that the conditions of the recovered cores imposed a constraint on the sampling strategy so that while the Wonnerup Member of the Lesueur Sandstone is reasonably well characterized due to its homogeneity in lithofacies distribution with depth, only 4 samples from the Yalgorup Member could be tested. As seen in module 1 of this report, the Yalgorup Member consists of mixed-thickness, interbedded high to low energy channel-fill facies, and swampy /overbank deposits and palaeosols and is significantly more heterogeneous than the Wonnerup Member, as such, the four samples tested are hardly representative of the general behaviour of the stratigraphic unit.



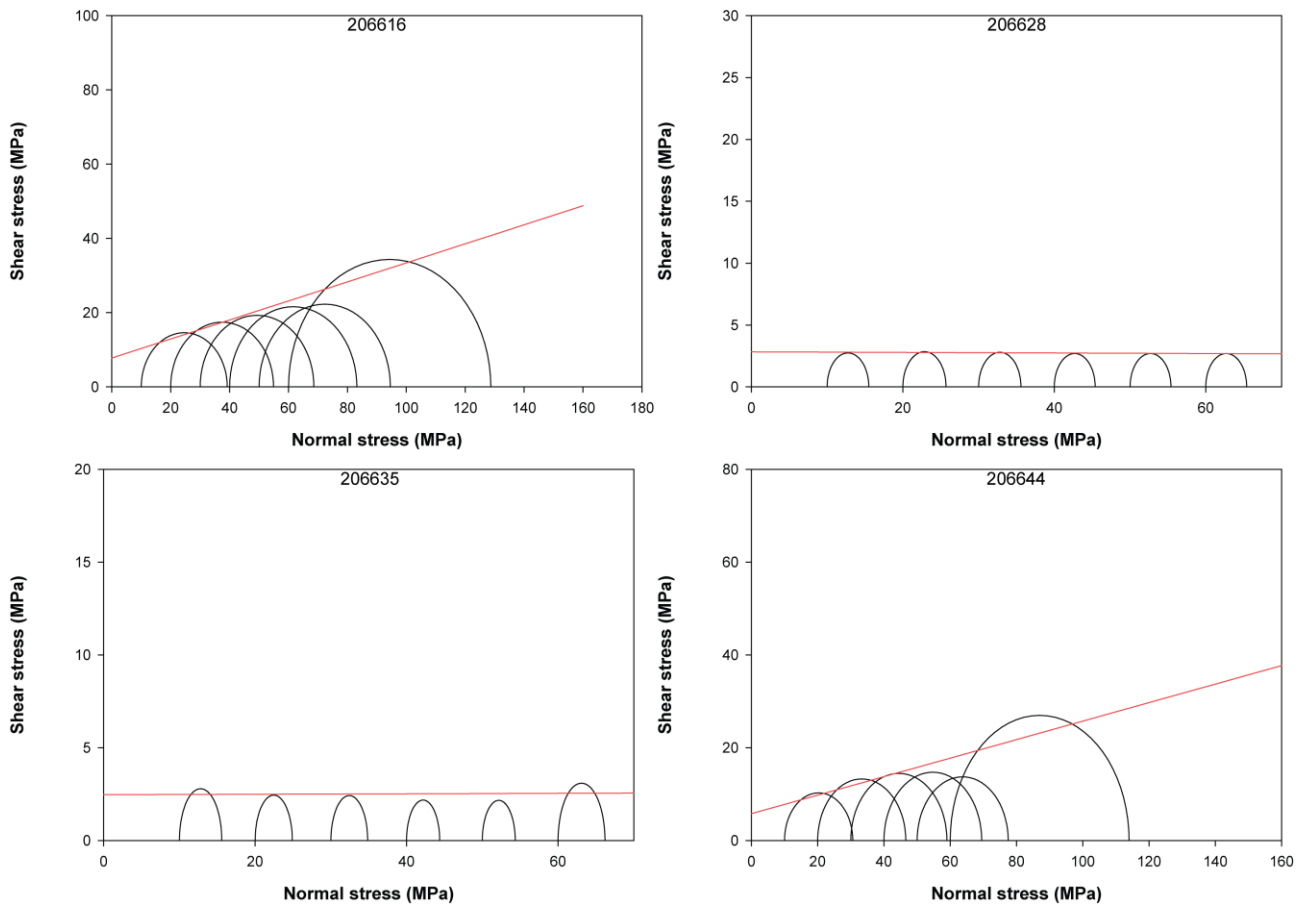


**Figure 6.4. Mohr circles and associated failure envelopes (red lines) for Yalgorup specimens extracted from Harvey-1.**

Additionally, among the four Yalgorup samples, two displayed a mechanical behaviour not compatible with a linear Mohr failure criterion. Samples 206628 and 206635 showed a very similar and unusual response: their strength did not show any pressure sensitivity (Mohr circles maintain the same size during the multi stage test) and failed at very low (<5MPa) differential stress at the highest confining pressure reached during the tests. This sort of mechanical response is not normally observed in consolidated sandstones and is more characteristic of an unconsolidated granular material; nevertheless the samples were indeed well consolidated and free of pre-existing damage as indicated by the CT scans reported in module 4. Moreover the specimens failed via the generation of a localized shear fracture. It is therefore difficult to explain such mechanical response in view of the available information on the samples. Additional tests on Yalgorup specimens may reveal whether the observed behaviour is representative of the sedimentary units' mechanical properties or it can be disregarded as an experimental oddity.

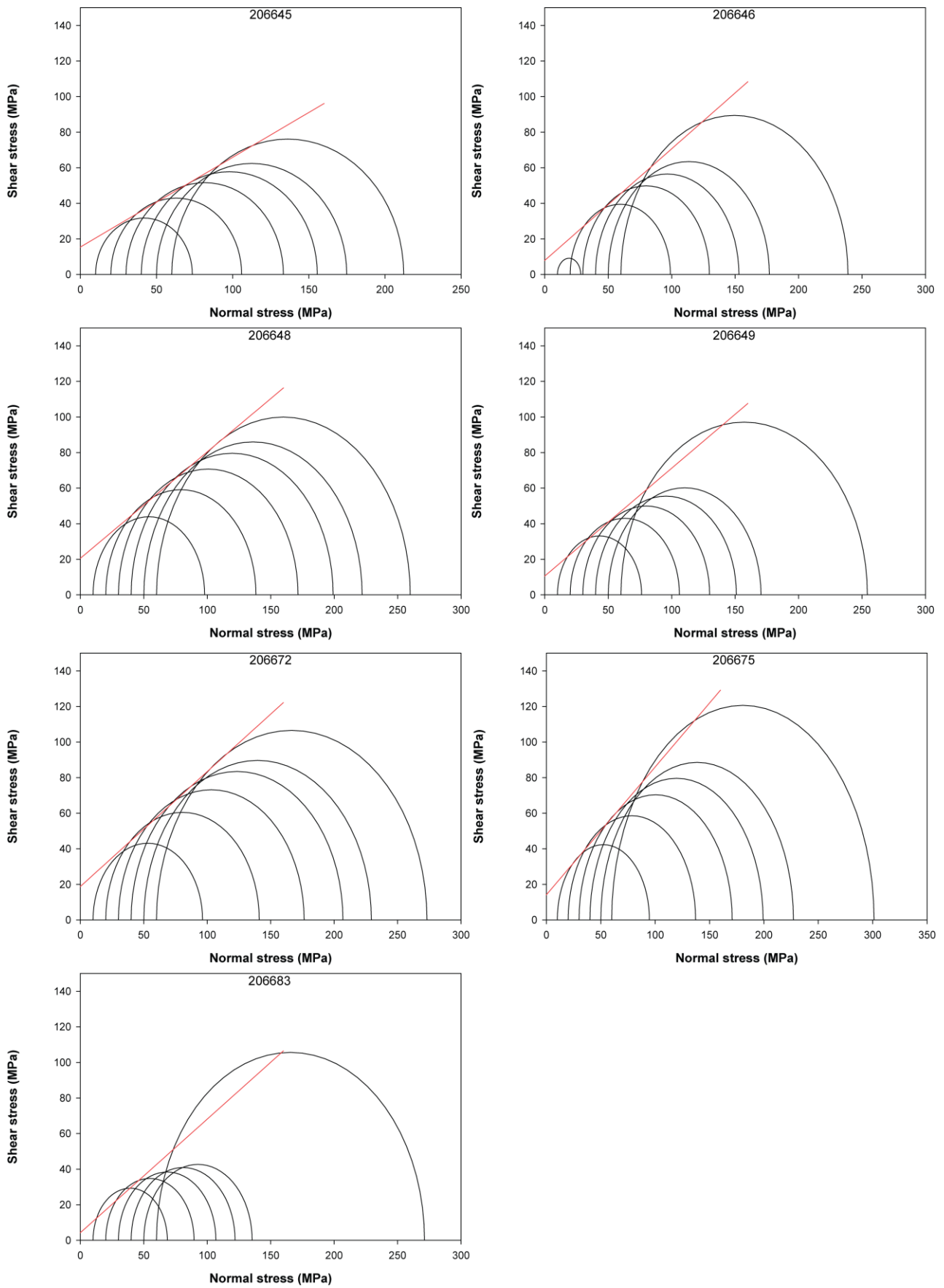


Figure 6.5. Mohr circles and associated failure envelopes (red lines) for Wonnerup specimens extracted from Harvey-1.

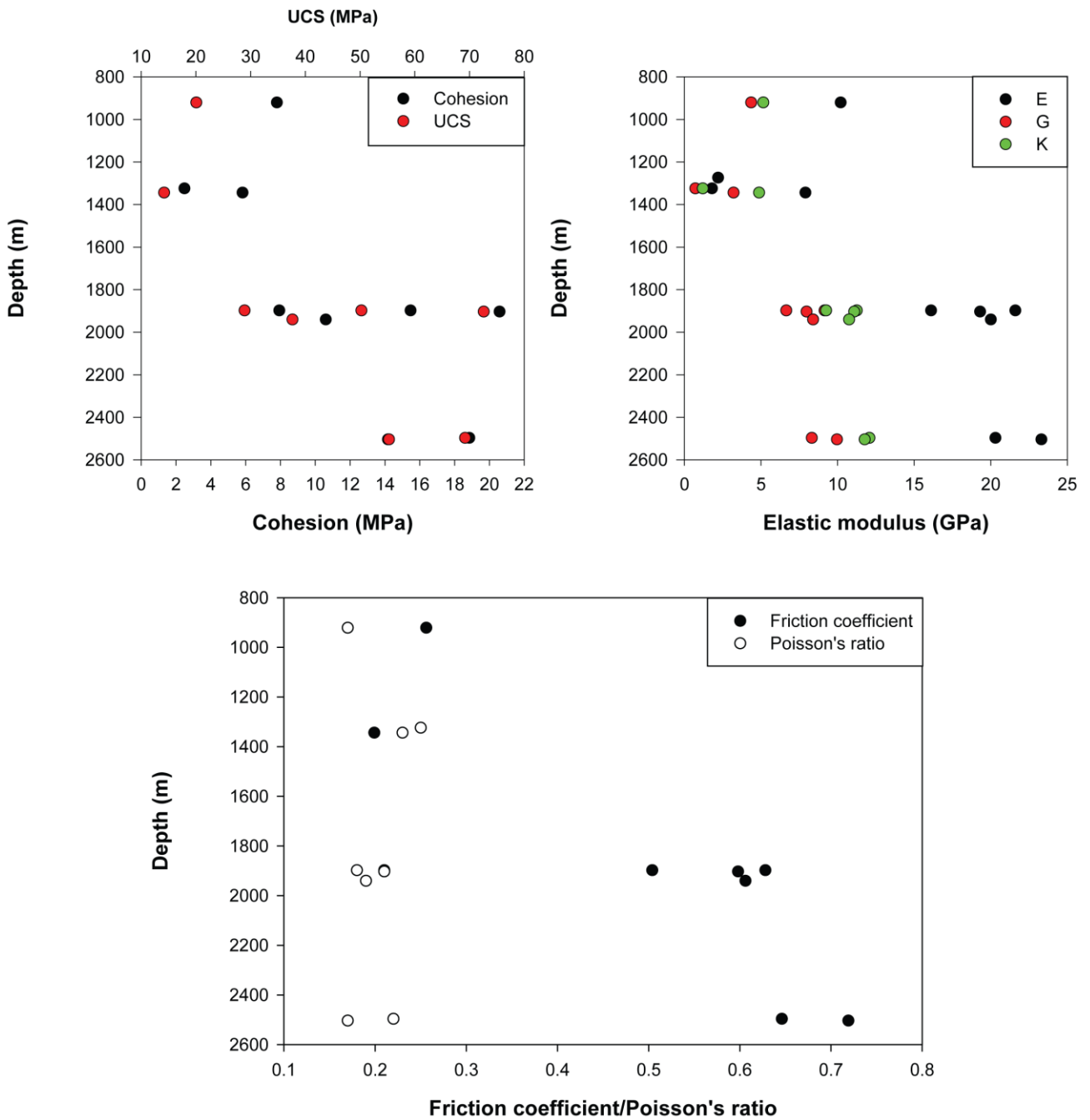


Figure 6.6. Geomechanical and static elastic moduli derived from multistage triaxial tests on core plugs, plotted as a function of sample depth. The static elastic moduli E, G and K are those measured at 40MPa of effective confining pressure

## 6.4.2 ROCK PHYSICS DATA

### Multistage triaxial tests

The experimentally measured ultrasonic data is presented in Fig. 6.7 (Yalgorup samples) and Fig. 6.8 (Wonnerup samples) as plots of velocities and  $V_p$ - $V_s$  ratio versus mean effective stress.

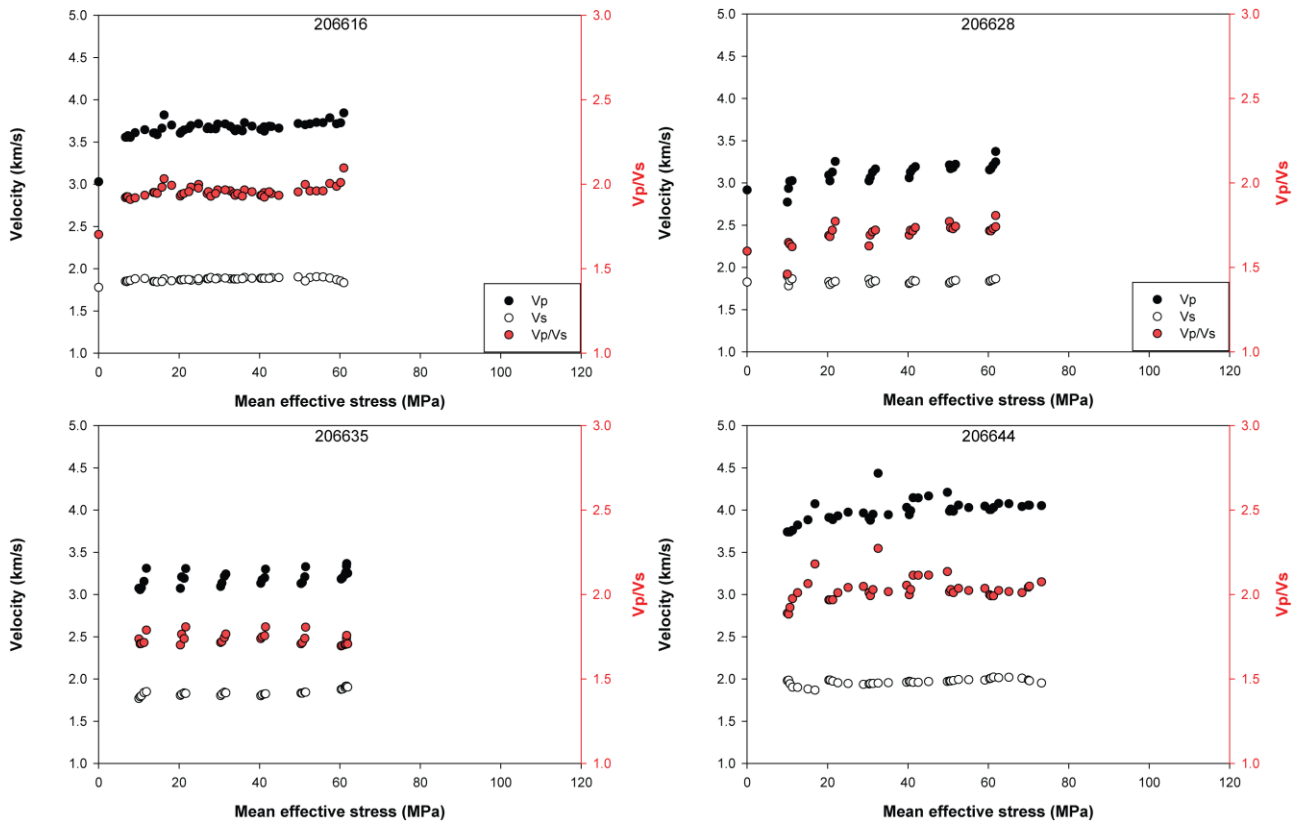
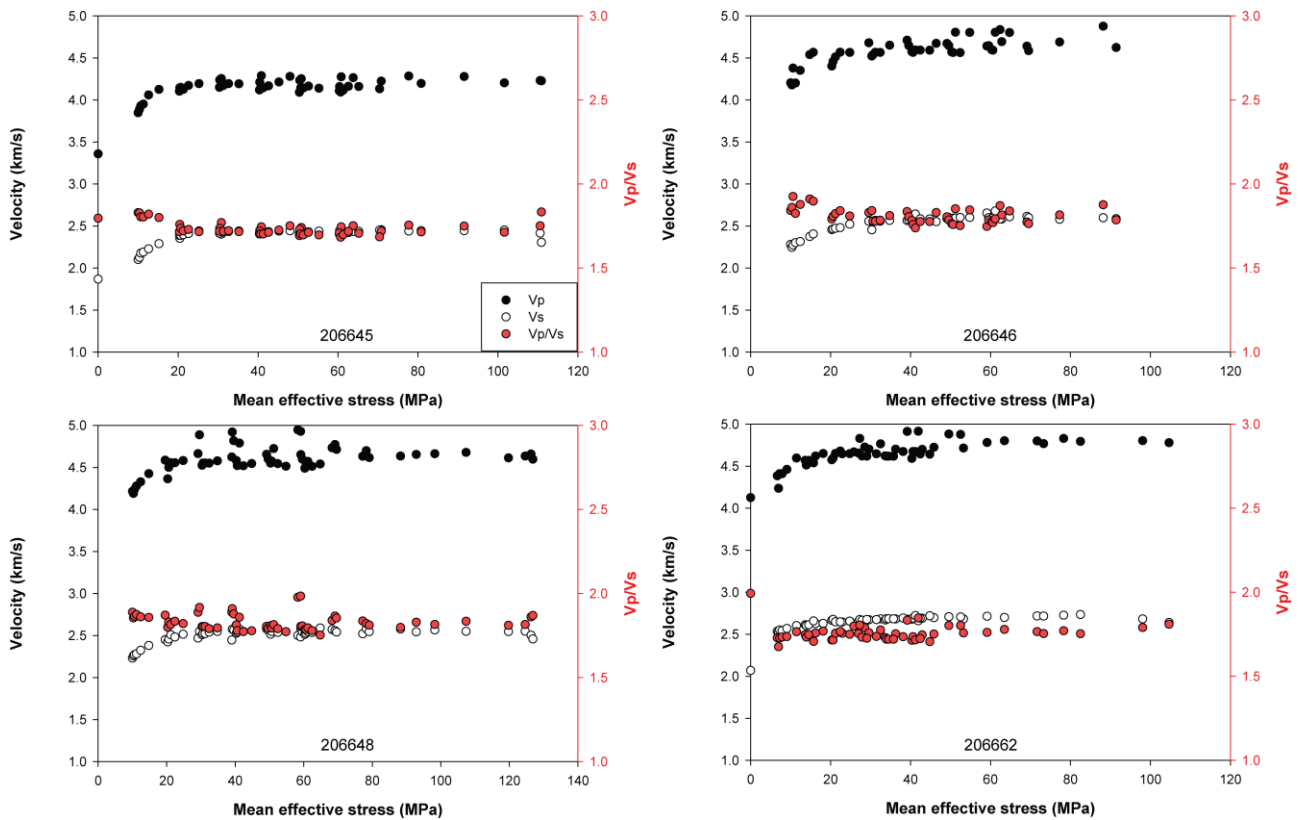
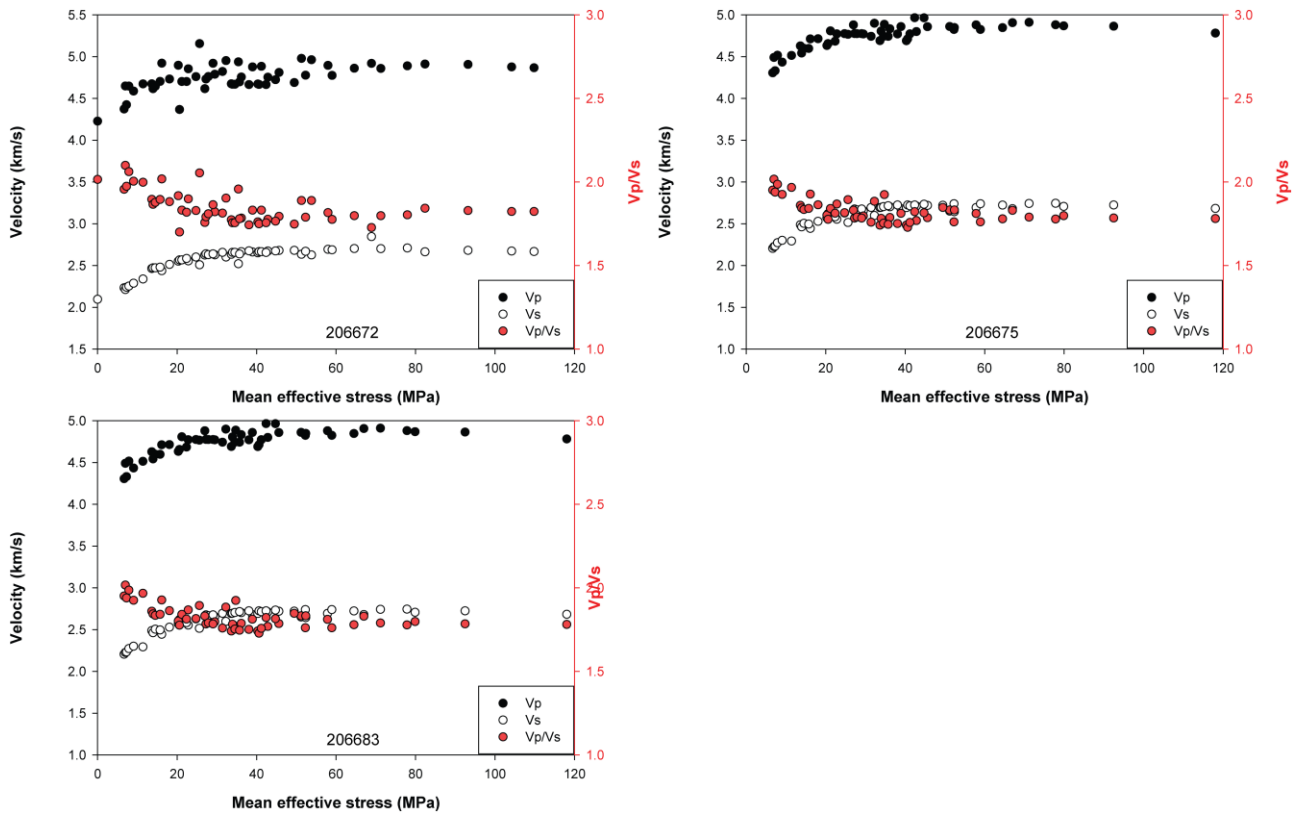


Figure 6.7. Ultrasonic velocities measured during multistage triaxial tests plotted as a function of mean effective stress for the Yalgorup samples.





**Figure 6.8. Ultrasonic velocities measured during multistage triaxial tests plotted as a function of mean effective stress for the Wonnerup samples.**

The elastic wave velocities recorded on the Yalgorup samples show moderate stress sensitivity and after an initial increment stabilize at mean effective stress of approximately 10MPa. Absolute values of Vp and Vs range between 3-4 and 1.6-2 km/s respectively (Fig. 6.7).

The velocities collected on the Wonnerup are generally higher than those on the Yalgorup samples and display pronounced stress sensitivity: both Vp and Vs increase with mean effective stress and stabilize at values 30-40MPa (Fig.6.8), a response that is normally attributed to the closure of compliant pores at the contact between solid grains (i.e. Sayers, 1990). The Wonnerup samples indicate Vp to be as high as 5km/s and Vs to be around 2.5km/s.

### Multistage isotropic tests

Elastic wave velocities measured during isotropic pressure cycles of dry and brine saturated samples are presented in Fig. 6.9 as plots of ultrasonic velocity against effective stress. The four tested specimens show similar response to that of the samples described above, where velocities increase with effective stress and stabilize at value of approximately 30MPa. The highest velocities are recorded on samples recovered from the Wonnerup Member. The main difference in elastic wave velocities between dry and brine saturated conditions is an increase in Vp, while Vs does not seem to be affected by the presence of brine in the pore space (Fig. 6.9).

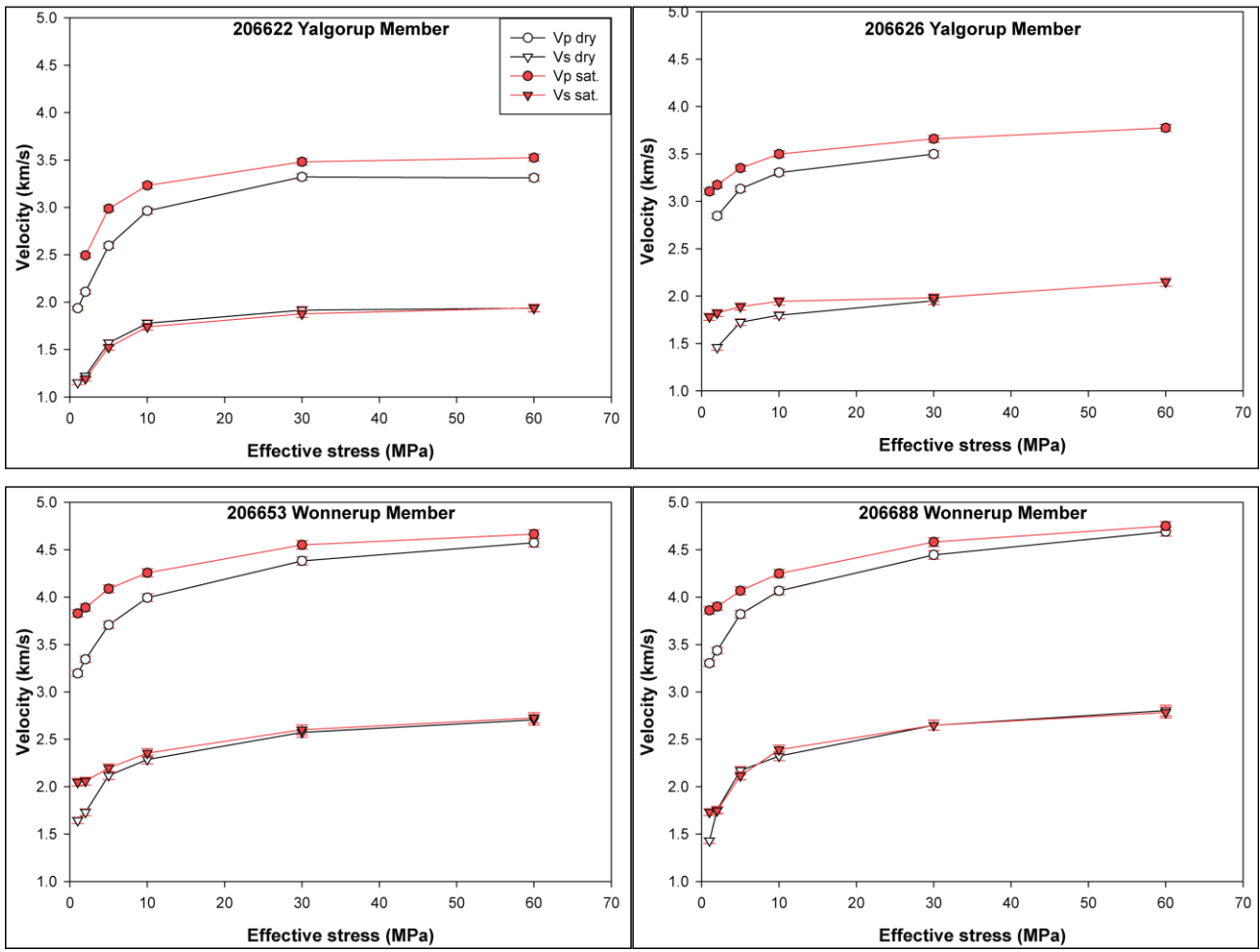


Figure 6.9. Ultrasonic velocities measured during multistage isotropic tests plotted as a function of effective stress.

## 6.5 Discussion

### 6.5.1 MECHANICAL BEHAVIOR

The mechanical response of the Harvey-1 samples can be compared with literature data: Table 6.5 summarizes a compilation of properties for sediments ranging from poorly consolidated sandstones to highly consolidated shale. Based on the results of the geomechanical tests on the Harvey-1 rock samples, they can be classified as poorly consolidated to consolidated sandstones.

Many geomechanical problems encountered during drilling have to be addressed even when core samples are not available for laboratory testing; to overcome this, several empirical relations have been proposed that relate rock strength to parameters measurable with wireline logs (Zoback 2010). Below, a comparison is made between the data collected on the Harvey-1 samples and some commonly used relations from the literature. Fig. 6.10 shows the relations between UCS and porosity as obtained in this work and compared with those of Plumb (1994) and Lashkaripour and Dusseault (1993). Plumb's relation ( $UCS=357(1-2.8\phi)^2$ ) is considered to be an upper bound as it is derived from very clean sandstones while Lashkaripour and Dusseault (1993) proposed a relation based on a set of shale data with porosity below 20% ( $UCS=193\phi^{-1.14}$ ). The experimental data falls in between the two predictions and shows a poor regression coefficient. A better correlation is obtained between  $V_p$  and UCS even though the experimental data shows much lower values than those obtained using the relation proposed by Freyburg in 1972 ( $UCS= 35V_p - 31.5$ ) (Fig. 6.10).

Rock type	UCS (MPa)	E (GPa)	$\nu$
Poorly consolidated sandstone	<10	<1	0.4
Poorly cemented sandstone	10-50	5-10	0.3-0.35
Consolidated sandstone	50-250	10-30	0.1-0.35
Highly consolidated sandstone	>100	30-50	0.15-0.25
Soft shale	0.5-5	1-5	0.3-0.4
Highly consolidated shale	5-100	5-70	0.2-0.3

**Table 6.5. Compilation of mechanical properties of sedimentary rock modified from Nauroy (2011).**

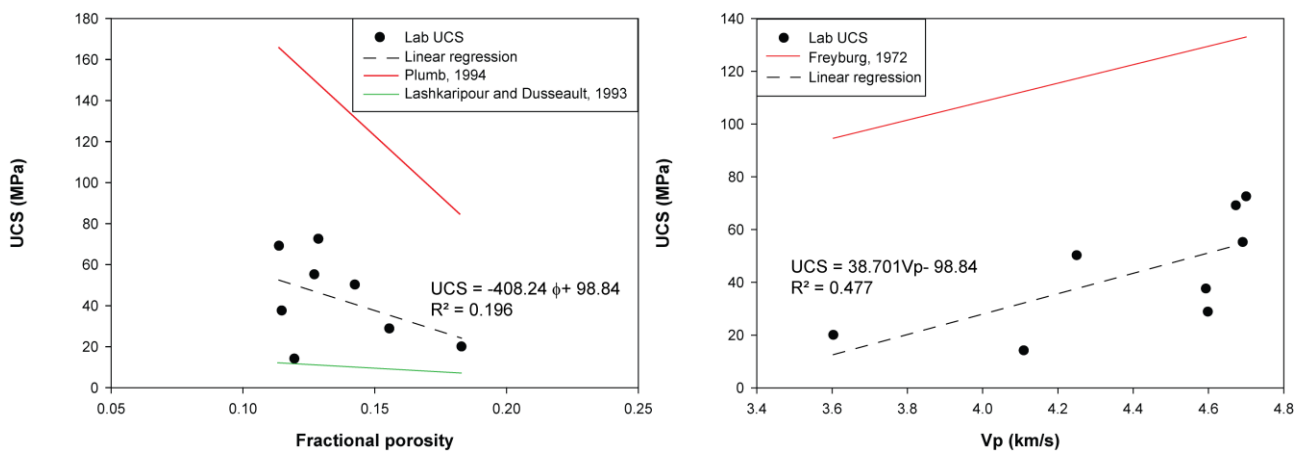


**Figure 6.10. Empirical relations from the literature between UCS and porosity (left) and UCS and Vp (right) compared with laboratory data.**

### 6.5.2 VP VS RELATIONSHIPS FROM THE LABORATORY COMPARED WITH EMPIRICAL REGRESSION LINES

Literature derived Vp-Vs relations are often used for lithology discrimination from seismic or sonic log data and for the estimation of the sediments' Poisson's ratio (Mavko et al., 2009; Zoback, 2010 and references therein). The wireline log data collected in Harvey-1 only comprised Vp, therefore the only Vs measurements available on the units crossed by the well are those performed in the laboratory at ultrasonic frequencies.

Below, a comparison is made between some popular empirical Vp-Vs relations found in the literature (Castagna et al., 1986; Han et al., 1986; Castagna et al., 1993) and that derived from the measurements on the Harvey-1 core plugs. The data indicate a very strong correlation between Vp and Vs with an R<sup>2</sup> of 0.967, though the regression line displays a lower slope than those reported in the literature (Table 6.6, Fig. 6.9). As no Vs was collected during wireline logging, the laboratory estimates can be used in support of Vs prediction from downhole sonic Vp data.

Regression	Equation	Reference
Castagna	$V_s = 0.8042V_p - 0.8559$	Castagna et al. (1993)
Han	$V_s = 0.7936 V_p - 0.7868$	Han et al., (1986)
Mudrock line	$V_s = 0.8621 V_p - 1.1724$	Castagna et al. (1985)
Laboratory data	$V_s = 0.5986 V_p - 0.1082$	This study

Table 6.6. Vp-Vs relations from the literature and from the data collected on Harvey 1 core plugs.

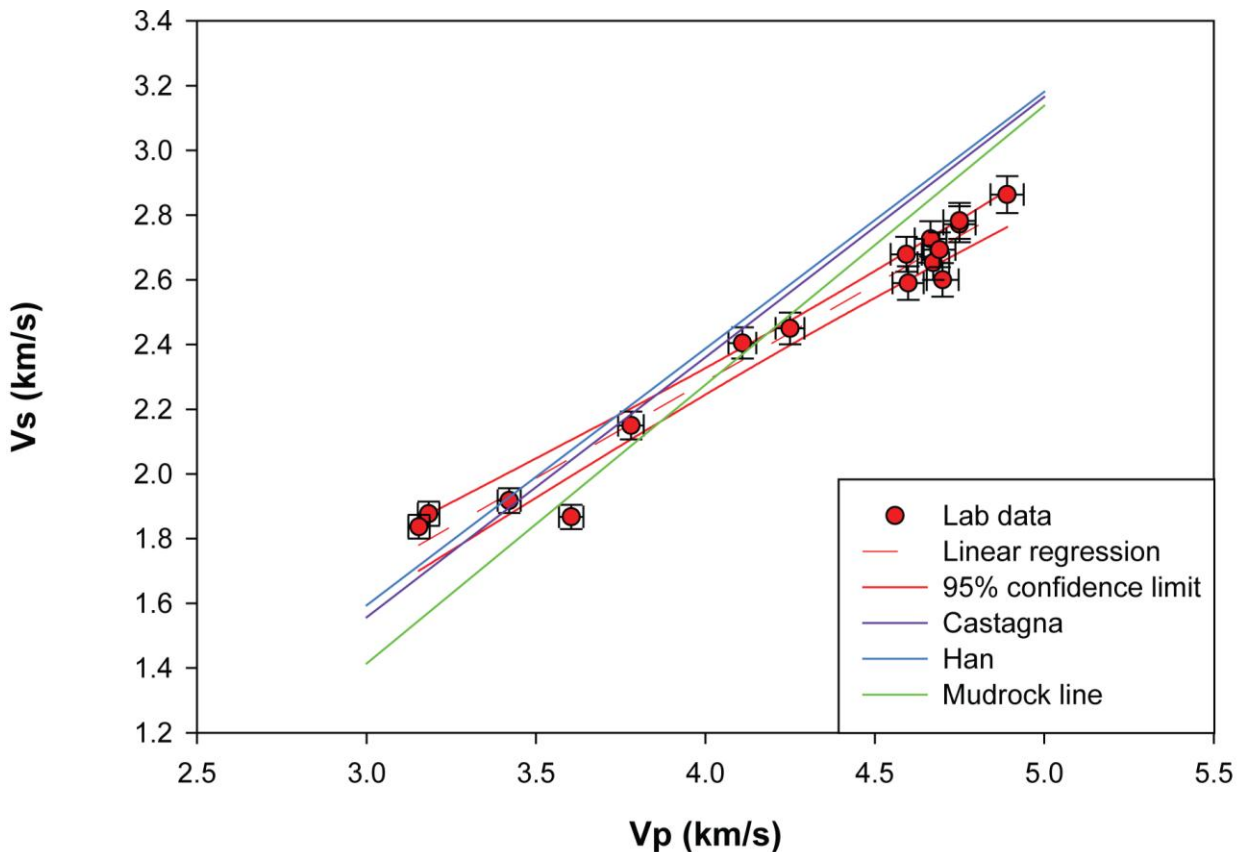


Figure 6.11. Vp-Vs cross plot for ultrasonic velocities collected on Harvey-1 core plugs and regression lines from published works.

### 6.5.3 ELASTIC WAVE VELOCITIES: LOG AND LAB

Figure 6.12 illustrates a comparison between the wireline acoustic measurements collected along the Harvey-1 borehole and the ultrasonic values measured on core plugs at ultrasonic frequency. Despite the large difference in frequency of the probing elastic wave and investigated rock volume, the two methods give comparable results in terms of Vp. As a first order approximation, one can assume the laboratory measured Vs to be a realistic estimate of the shear wave velocities down the well (not available for comparison at the time this study was conducted).



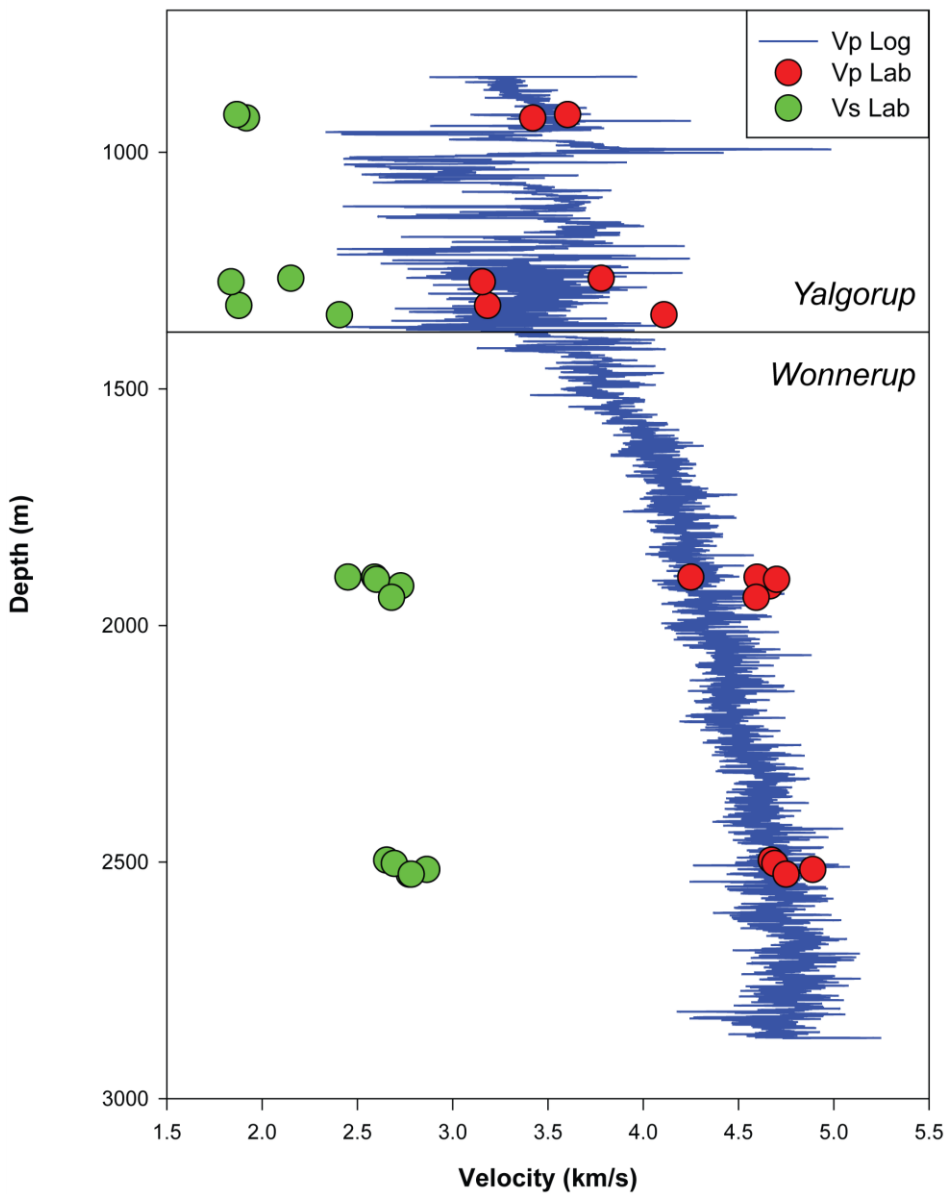


Figure 6.12. Comparison between acoustic wireline log (Vp Log) and ultrasonic laboratory measurement (Vp Lab , Vs Lab) as function of depth in Harvey-1.

#### 6.5.4 GASSMANN FLUID SUBSTITUTION

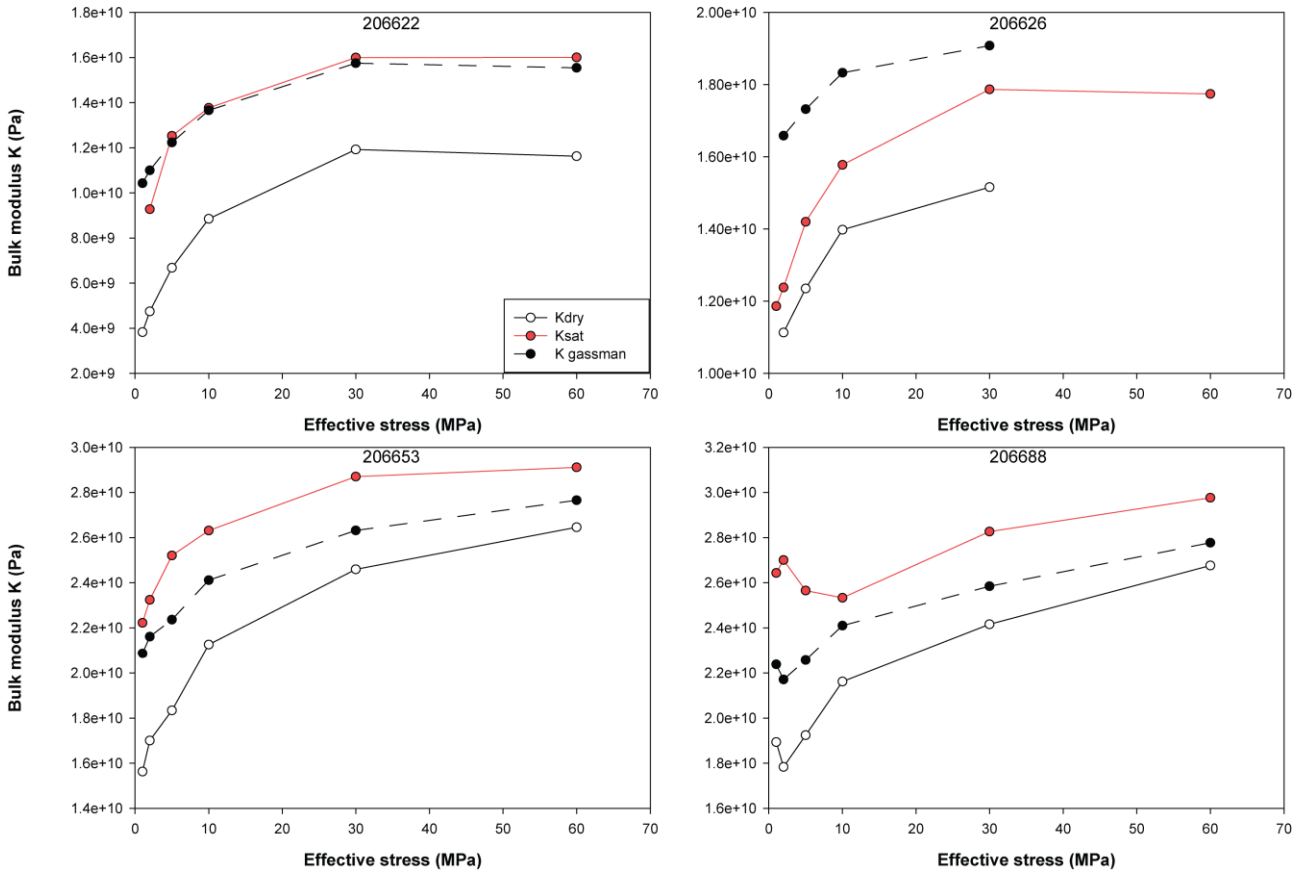
The theoretical effect of fluid on rocks' elastic properties is estimated using Gassmann's (Gassmann, 1951) theory, which allows the comparison between the theoretical effects of fluids and the actual measured effects of fluid saturation on the seismic velocity.

Gassmann's theory can be used to calculate the saturated bulk modulus from an elastic wave velocity measurement on a dry sample by:

$$K_{sat} = K_{dry} + \frac{\left(1 - \frac{K_{dry}}{K_{min}}\right)^2}{\frac{\phi}{K_{fluid}} + \frac{1-\phi}{K_{min}} - \frac{K_{dry}}{(K_{min})^2}}$$

Equation 6.11

Where  $K_{sat}$  is the saturated bulk modulus;  $K_{dry}$  is the modulus calculated from the laboratory velocity measurements,  $\phi$  is the fractional porosity;  $K_{min}$  is the effective modulus of the solid grains; and  $K_{fluid}$  is the modulus of the saturating fluid. Gassmann's theory implies that the shear modulus does not change between the dry and saturated case. For the above calculation, the bulk modulus of water is  $K_{fluid}$  (2.2 GPa), and an arbitrary value of  $K_{min}$  of 35GPa is assumed to be representative of a typical sandstone (see for example Wang, 2000).



Equation 6.12. Results of Gassmann's fluid substitution on four samples from Harvey-1.

It should be noted that Gassmann's derivation is based on the following assumptions for a porous system:

- Pore pressure is in equilibrium between pores (i.e. the pore fluid has enough time to reach equilibrium after the compression induced by the passage of the elastic wave);
- The solid, porous frame consists of a single solid material (i.e. the rock is mono-mineralic);
- Pores are hydraulically connected and are homogeneously and fully filled with a non-viscous fluid;
- The system is closed (i.e. the fluid volume does not change);
- The pore fluid does not chemically interact with the solid frame.

In the four samples tested, the S wave velocity remains largely independent of brine saturation while P wave velocity increases from the dry to the brine conditions in the same sample (Fig 6.9): an observation compatible with Gassmann's approach.

Fig. 6.12 summarizes the results of Gassmann predicted and the experimentally derived dynamic bulk modulus for the dry and saturated case on the four samples discussed above. It is evident that sample 206622 shows an excellent agreement between measured and predicted bulk modulus in brine saturated conditions. The other three samples show contrasting behaviour and the theoretical prediction either overestimates (sample 206628) or underestimates (samples 206653, 206688) the measured saturated bulk modulus. The reason for the observed discrepancy can be related to any one of the assumptions of Gassmann's theory not being satisfied by the natural system, further study would be needed to identify to dominant source of inconsistency.

## 6.6 Conclusions

From the measurements of the Harvey-1 samples, it is possible to conclude that the mechanical and elastic properties of the Yalgorup and Wonnerup samples are significantly different. The Yalgorup is relatively weak ( $14 < UCS < 20 \text{ MPa}$ ;  $2 < E < 10 \text{ GPa}$ ) while the Wonnerup show stronger and stiffer responses ( $29 < UCS < 72 \text{ MPa}$ ;  $16 < E < 23 \text{ GPa}$ ). Generally the samples' responses are consistent with a linear Mohr-Coulomb failure criterion.

Elastic wave velocities measured in the laboratory show little stress sensitivity in the Yalgorup while they increase with effective stress and stabilize at an effective stress of 30-40 MPa in the Wonnerup samples. At simulated "in-situ" conditions the P- and S- wave velocities display values of approximately 3.6 and 2 km/s in the Yalgorup and 4.7 and 2.8 km/s in the Wonnerup respectively.

Fluid effects on the rocks' elastic properties were tested by comparing the results obtained on the same samples under dry and brine saturated conditions. Brine saturation causes an increase in compressional wave velocity while shear wave velocities do not change with the presence of fluids. The experimental values were compared with theoretical predictions using Gassmann's fluid substitution theory. This gave contrasting results; further research should be focused on the comparison between measurements and predictions under  $\text{CO}_2$  saturated conditions not explored in this work.

There is good agreement between the laboratory velocities and those measured in the well via wireline acoustic logging; this gives confidence regarding the relevance of the laboratory study and application of finding to the field scenario where core samples are unavailable.



## **7 Module 5b Low-frequency laboratory measurements of samples from Harvey 1.**

## 7.1 Summary

Low-frequency measurements of elastic properties were conducted on three sandstone samples obtained from the Harvey-1 well drilled in the Harvey region, Western Australia.

In this report we present the data obtained with a low-frequency laboratory apparatus designed for measurements of complex Young's moduli and extensional attenuation of rocks at seismic (1-120 Hz) and teleseismic (0.1-1Hz) wave frequencies and at strain amplitudes of  $10^{-8}$  –  $10^{-6}$  (Mikhailsevitch et al. 2011).

The experiments included two stages of measurements: on the dry samples and on the same samples saturated with brine. The measurements with the dry samples were performed at confining pressures of 9 MPa (sample 206603 from the Yalgorup Member) and 24 MPa (samples 206663 and 206664 from the Wonnerup Member) to replicate the "in situ" pressure conditions. The measurements with brine saturated sandstones were conducted at 14 MPa (sample 206603) and 29 MPa (samples 206663 and 206664), the pore pressure was 5 MPa, therefore the effective pressure acting on the samples was the same as in the dry case. Due to unusual behavior of the attenuation measured in sample 206603, the measurements for this sample were repeated with higher confining (29 Mpa) and pore (6 MPa) pressures. The fourth sample 20664 failed during the initial stages of the measurements and could not be used for data collection.

The mineralogy of the samples was retrieved from X-ray diffraction analysis (see module 2), while a synthetic brine was constituted to represent the salinity of formation water interpreted from the resistivity wireline logs (cfr. module 3).

The tests consistently indicate negligible frequency dependence of the elastic moduli in the dry samples, while significant attenuation and dispersion are observed at low frequencies in the brine saturated samples. The results, though preliminary in nature and only limited to a small sample population, may indicate that a significant difference in seismic response can be expected when pore fluids are substituted in the pore space of the sedimentary rocks intersected by Harve-1, as such geophysical remote sensing by seismic imaging could provide important information of the movement of CO<sub>2</sub> on the subsurface reservoir.

## 7.2 Apparatus

The mechanical assembly of the apparatus used in the low frequency measurements is presented in Fig. 7.1. The assembly comprises two large steel platforms and a number of components between them, which includes a hydraulic actuator, a Hoek triaxial core holder, a piezoelectric stack actuator PSt 1000/35/60 (APC International Ltd) with the limit of maximum load of 70,000 N and with the frequency of its mechanical resonance >20 kHz, an aluminium calibration standard, and two aluminium plugs having ports for a fluid injection. The main purpose of using the platforms is to reduce the spurious mechanical resonances in the mechanical assembly.

A rock sample to be tested with two semiconductor strain gauges KSP-1-350-E4 (Kyowa Electronic Instruments Co., Ltd.) glued to its surface (see Fig. 7.2) is placed inside an elastomer sleeve, which is mounted within the triaxial cell. The fluid ports in the aluminium plugs attached to the sample enable the flow of fluids through the sample and provide the means for pore pressure control (see Fig. 7.3). The cell and the hydraulic actuator (model RCS201, Enerpac) are connected via fluid lines with two manual hydraulic pumps (model P392, Enerpac) providing lateral and longitudinal static forces applied to the rock.

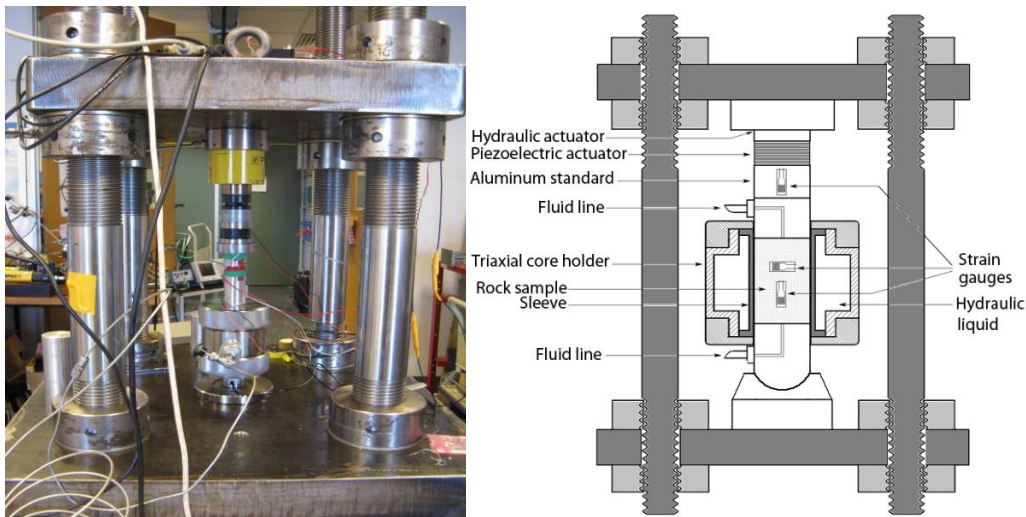
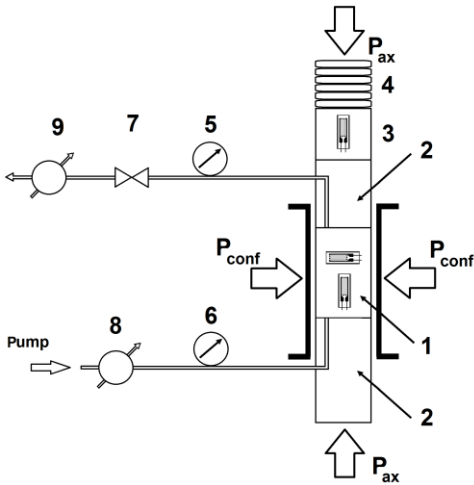


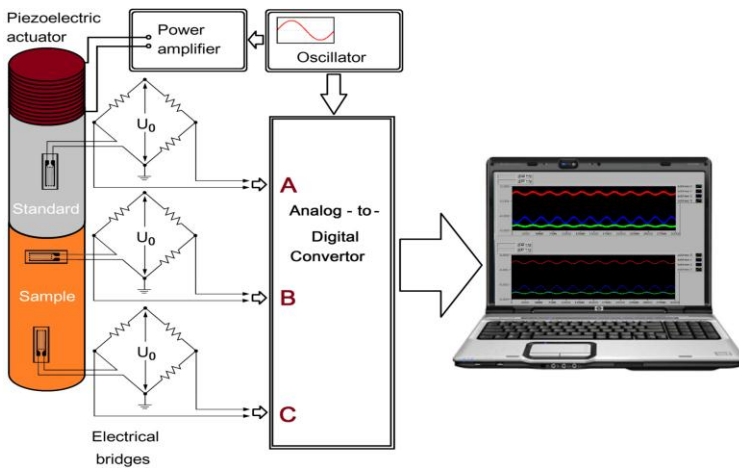
Figure 7.1. The mechanical assembly of the low-frequency laboratory apparatus.



Figure 7.2. Sandstone sample 206603 with radial and axial strain gauges glued to its surface.



**Figure 7.3.** The diagram of fluid ports: 1 – sample with two orthogonal strain gauges, 2 –two aluminium plugs with fluid ports, 3 – aluminium standard with a strain gauge, 4 – piezoelectric adaptor, 5 and 6 – pressure gauges, 7 – relief valve, 8 and 9 – flow meters.



**Figure 7.4.** The electrical schematics of the low-frequency laboratory apparatus.

The electrical schematics of the apparatus is presented in Fig. 7.4. The multilayer piezoelectric actuator transforms the periodic voltage, applied by an oscillator, into mechanical stress, which causes displacements in the aluminium standard and tested sample mounted in series. The displacements modulate the conductivity of the strain gauges. A set of electric bridges (BCM-1 Wheatstone Bridge, Omega Engineering Ltd) transforms the modulated conductivity into electric signals, which, after digitizing by an analogue-digital converter (model 100, InstruNet, Omega Engineering Ltd), are received by an acquisition computer, where the signals are averaged and processed. The value of extensional attenuation is derived from the phase delay between the stress applied to the sample and the strain in the rock. The resulting signals corresponding to the strains in the aluminium standard and rock sample presented in Fig. 7.5.



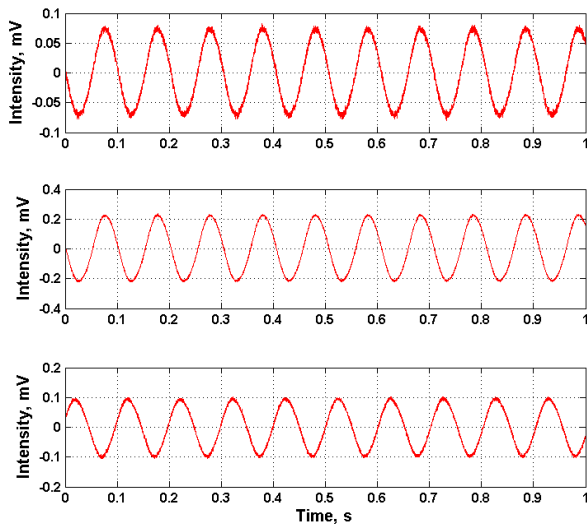


**Figure 7.5.** Signals obtained from the brine saturated sandstone sample 206663 at the frequency of the periodical stress oscillations 10 Hz and at confining and pore pressures 29 and 5 MPa correspondingly. The top signal was obtained from the gauge attached to the aluminium standard, the middle and bottom signals were obtained from the axial and radial gauges attached to the rock sample. The number of averages is 100.

### 7.3 Method and operation

For low frequency measurements we modified a version of the stress-strain technique employed by Spencer (1981), Paffenholz and Burkhardt (1989), and Batzle et al. (1999). Here we describe our approach in more detail.

The signals corresponding to the axial and radial components of the strain in the rock sample are detected by the strain gages, one of which is aligned with longitudinal direction and the second is orthogonal to the first one (see Fig. 7.2). These signals (Fig. 7.5) are used to calculate the Young's modulus and Poisson's ratio.

We assume that periodical stress is applied along z-axis, then from Hooke's law:

$$\sigma_{zz} = E\varepsilon_{zz} \quad \text{Equation 7.1}$$

Where  $\varepsilon_{zz}$  and  $\sigma_{zz}$  are the specimen strain and stress along z-axis .

The Young's modulus of the specimen  $E$  is

$$E = \frac{\sigma_{zz}}{\varepsilon_{zz}} \quad \text{Equation 7.2}$$

The stress  $\sigma_{zz}$  can be expressed through the parameters of the aluminium standard as  $E_{al}\varepsilon_{zz}^{al}$ , where  $E_{al}$  is the known Young's modulus and  $\varepsilon_{zz}^{al}$  is a measured amplitude of axial strain. So, the Young's modulus of the specimen is:

$$E = E_{al} \frac{\varepsilon_{zz}^{al}}{\varepsilon_{zz}} \quad \text{Equation 7.3}$$

Using the Young's modulus determined by Eq. (6.2), we can find bulk  $K$  and shear  $\mu$  moduli, compressional  $V_p$  and shear  $V_s$  velocities:

$$K = \frac{E}{3(1-2\nu)}, \quad \mu = \frac{E}{2(1+\nu)} \quad \text{Equation 7.4}$$

$$V_p = \sqrt{\frac{K + \frac{4}{3}\mu}{\rho}}, \quad V_s = \sqrt{\frac{\mu}{\rho}} \quad \text{Equation 7.5}$$

Here  $\rho$  is the density of the sample,  $\nu = -\varepsilon_{xx}/\varepsilon_{zz}$  is the Poisson's ratio. Strains  $\varepsilon_{xx}$  and  $\varepsilon_{zz}$  are detected in radial and axial (longitudinal) directions correspondingly by two mutually perpendicular strain gauges glued to the sample (Fig. 7.2).

The extensional attenuation  $Q_E^{-1}$  in the sample is estimated as the phase shift  $\Delta\varphi$  of the signals obtained from the axial strain gauges coupled with the rock sample and the aluminium standard (see Figure 6.6):

$$Q_E^{-1} = \tan(\Delta\varphi) \approx \Delta\varphi \quad \text{Equation 7.6}$$

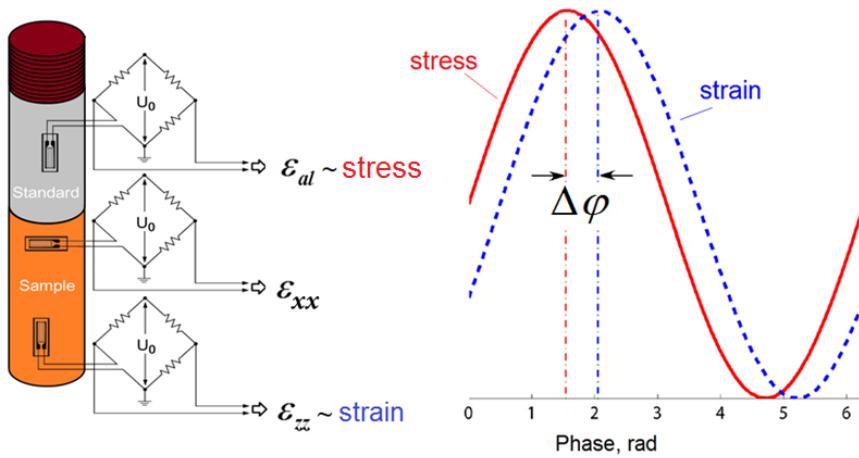


**Figure 7.6.** The extensional attenuation is measured as a phase shift between two sinusoidal signals detected by the strain gauges attached in longitudinal direction to the aluminium standard (red line) and rock sample (blue dash line).

The measurements presented below were conducted using oscillating frequencies ranging between 0.1 and 120 Hz. At each frequency the stress-strain readings of 100 oscillations were averaged to improve the signal-to-noise ratio of the signals obtained from strain gauges.

Each sample was first tested dry at a given confining pressure replicating the in-situ lithostatic stress assuming a stress gradient of 10MPa/km. Subsequently the sample was brine saturated and tested again using a differential pressure ( $P_{diff} = \text{Confining Pressure} - \text{Pore pressure}$ ) equivalent to the confining pressure of the dry cycle.

Samples 206603, 206663 and 206664 were saturated at a confining pressure of 30 Mpa. To ensure the full saturation of the sample at least 10 pore volumes of brine were pumped through the samples under a constant pressure of 6 MPa. Due to low permeability of the samples the flow rate of brine during saturation did not exceed 0.005 cm<sup>3</sup>/s (0.3 cm<sup>3</sup>/min).

## 7.4 Measurement Results

### 7.4.1 DESCRIPTION OF SAMPLES

Low-frequency measurements were conducted on four sandstone samples obtained from Harvey-1 well. The samples characteristics are presented in Table 7.1. X-ray tomographic images of the samples obtained prior to testing are reported in Fig. 7.7.

<b>GSWA sample #</b>	<b>206603</b>	<b>206642</b>	<b>206663</b>	<b>206664</b>
<b>Depth (m)</b>	903.62	1337.41	2480.66	2480.91
<b>Bulk density (g/cc)</b>	2.11	2.32	2.31	2.38
<b>Porosity (%) @ 35MPa</b>	17.97	9.08	12.16	9.82
<b>Permeability (mD) @ 35MPa</b>	9.59	0.17	8.96	0.56
<b>Orientation</b>	Par.	Par.	Par.	Norm
<b>Quartz (%)</b>	73	58	75	81
<b>Albite(%)</b>		4		
<b>K-feldspar (%)</b>	14	21	13	10
<b>Calcite (%)</b>		4		
<b>High-Mg calcite (%)</b>	3			
<b>Kaolinite (%)</b>	10	6	8	5
<b>Berthierine (%)</b>			4	5
<b>Illite/Muscovite (%)</b>		4		
<b>Smectite (%)</b>		4		
<b>Brine salinity (NaCl ppm)</b>	40000	40000	30000	30000
<b>Member</b>	Yalgorup	Yalgorup	Wonnerup	Wonnerup

**Table 7.1. Characteristics of tested samples. Orientation refers to the the way the cylinder was cut with respect to the macroscopic bedding: par.=parallel; norm. = normal. Mineralogy is from XRD as described in module 2.**

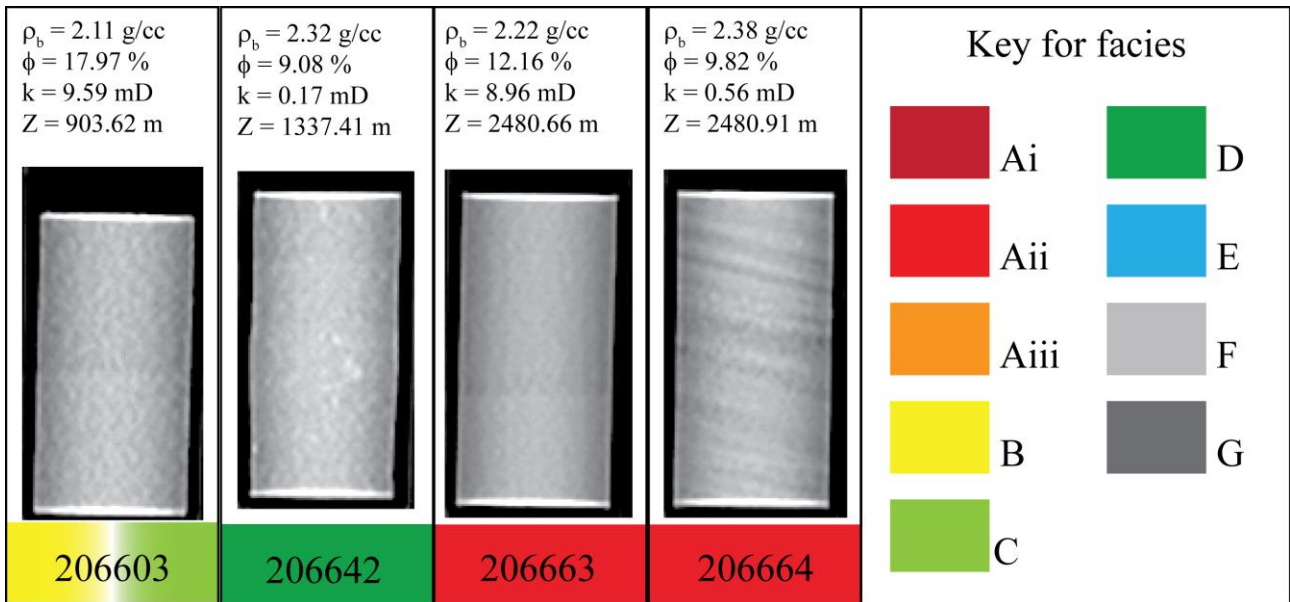


Figure 7.7. X-ray tomographic images of the core plugs prior to the low frequency measurements.  $\rho_b$  = bulk density;  $\phi$ = porosity;  $k$  = permeability;  $Z$  = depth.

Samples were selected to represent both the Yalgorup (206603 and 206642) and Wonnerup (206663 and 206664) Members of the Leuseur Sandstone. The sample selection rationale was motivated by the choice of lithofacies representing the Members under investigation. In this light, samples 206603 and 206642 are described as moderate to low energy rippleforms and paleosols respectively. The two samples from the Wonnerup member are both described as high energy fluvial channel barforms. Samples 206663 and 206664 were collected from approximately the same depth but are cored in orthogonal orientations with respect to the macroscopic bedding: the former being parallel and the latter being normal to bedding (Fig. 7.7).

#### 7.4.2 SAMPLE 206603 (YALGORUP MEMBER)

The results obtained from testing sample 206603 are presented in Figs. 6.8 -6.10. The experimental data are given in Tables 7.2 – 7.5.

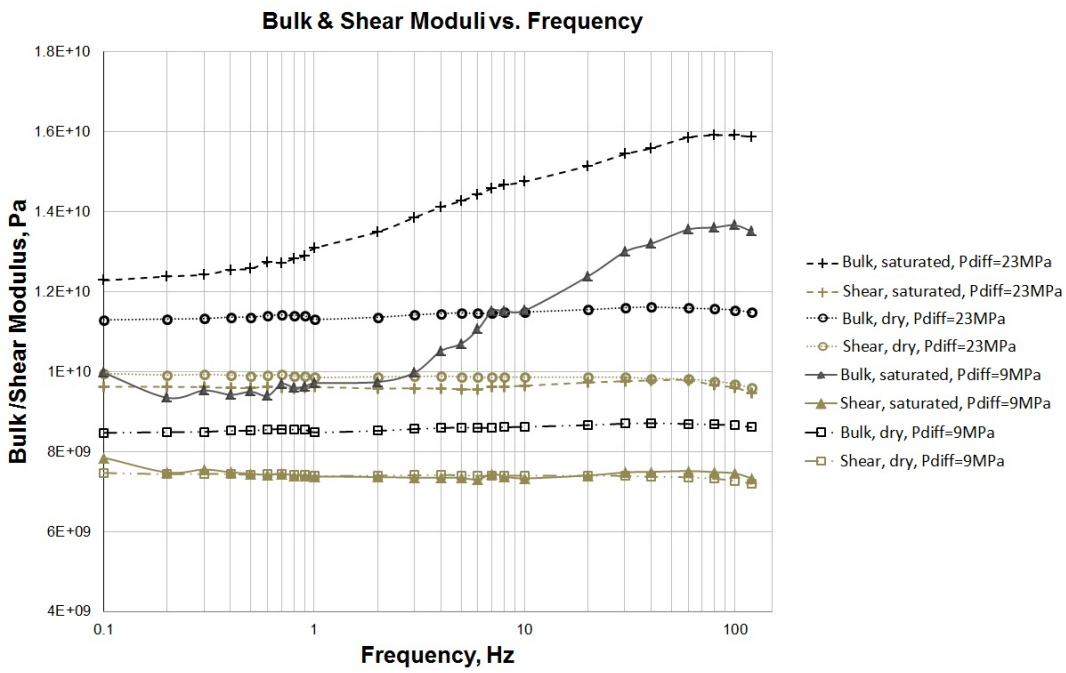


Figure 7.8. Bulk and shear moduli measured for dry and brine saturated sandstone sample 206603. The measurements with the dry sandstone are conducted at confining pressures of 9 and 23 MPa and a pore pressure of 0.1 MPa; the confining pressures for the brine saturated sample are 15 and 29 MPa, and the pore pressure is 6 MPa.

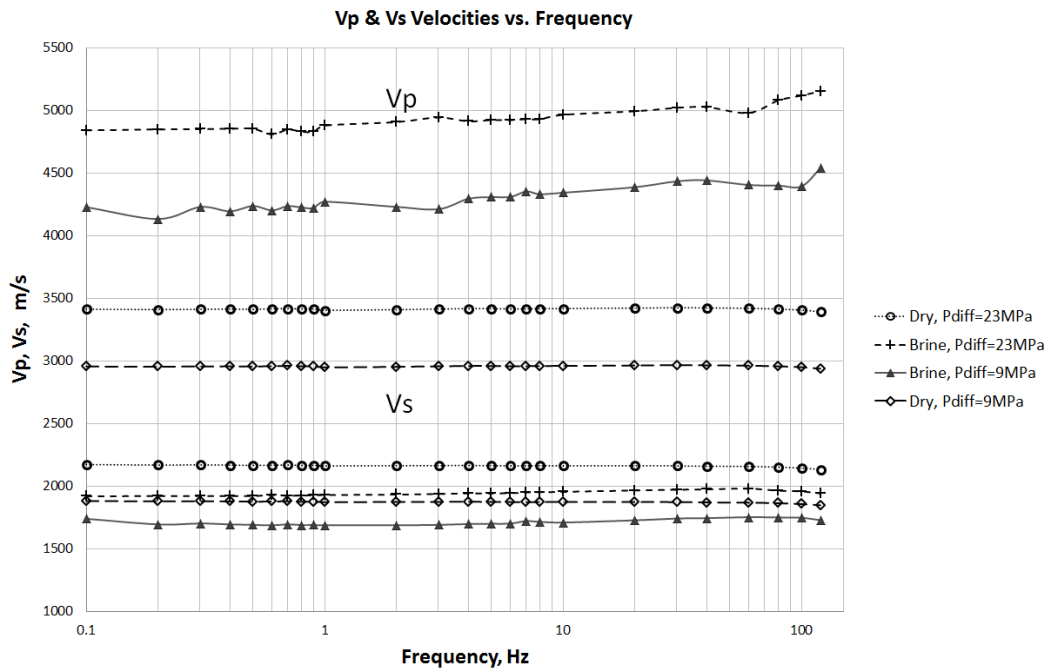


Figure 7.9.  $V_p$  and  $V_s$  velocities obtained for dry and brine saturated sandstone sample 206603. All pressure parameters are the same as in Figure 6.7.

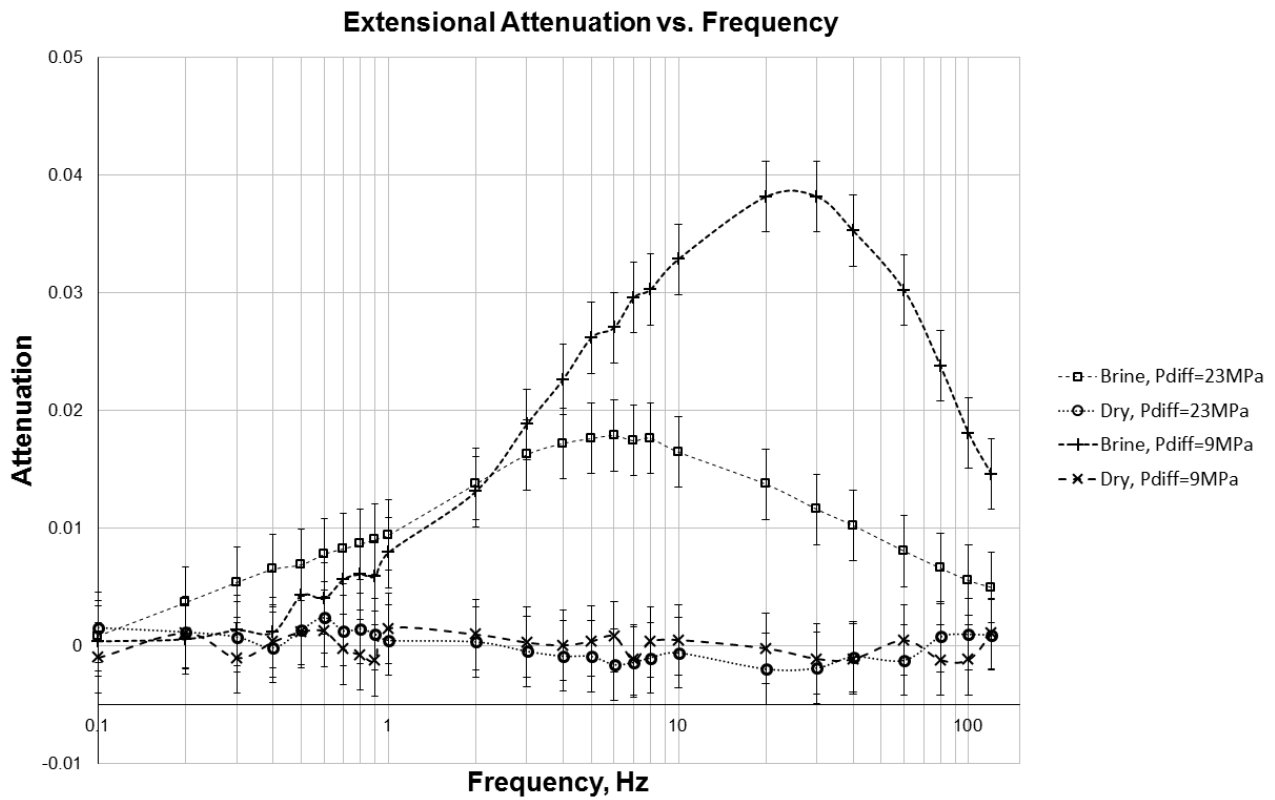


Figure 7.10. Extensional attenuation measured for dry and brine saturated sandstone sample 206603. All pressure parameters are the same as in Figure 6.7.

### 7.4.3 SAMPLE 206642 (YALGORUP MEMBER)

Sample 206642 crushed at the very beginning of the measurements (see Fig. 7.11), as such no data were collected.



Figure 7.11. Top and bottom of sample 206642 broken in the Hoek's cell under a confining pressure of  $\sim 10$  MPa.

#### 7.4.4 SAMPLE 206663 (WONNERUP MEMBER)

The results obtained from testing sample 206663 are presented in Figs. 6.12 – 6.14. The data from the measurements are presented in Tables 7.6 – 7.7.

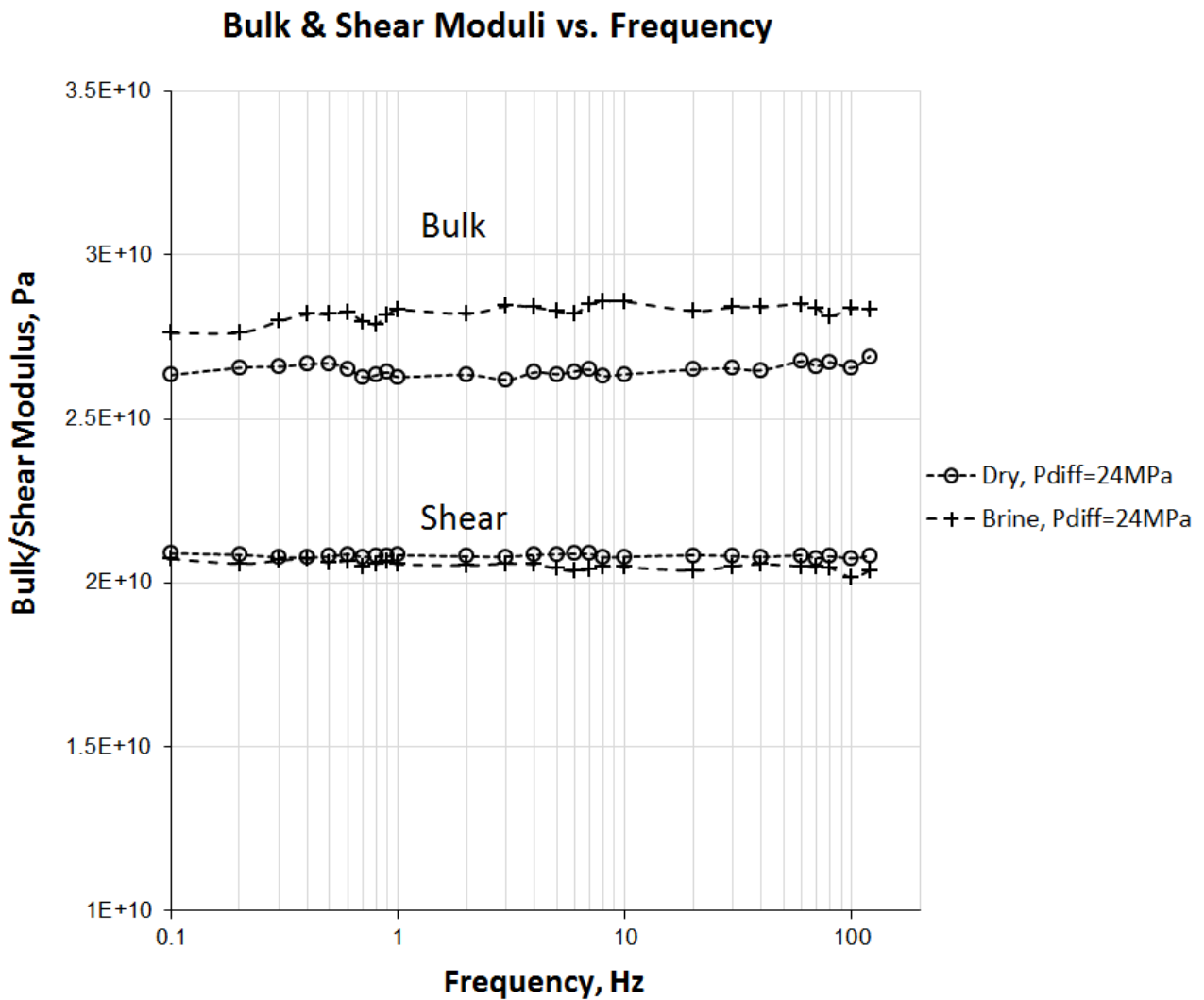


Figure 7.12. Bulk and shear moduli measured for dry and brine saturated sandstone sample 206663. The measurements with the dry sandstone are conducted at a confining pressure of 24 MPa and a pore pressure of 0.1 MPa; the confining and pore pressures for brine saturated sandstone are 29 MPa and 5 MPa correspondingly.

### V<sub>p</sub> & V<sub>s</sub> Velocities vs. Frequency

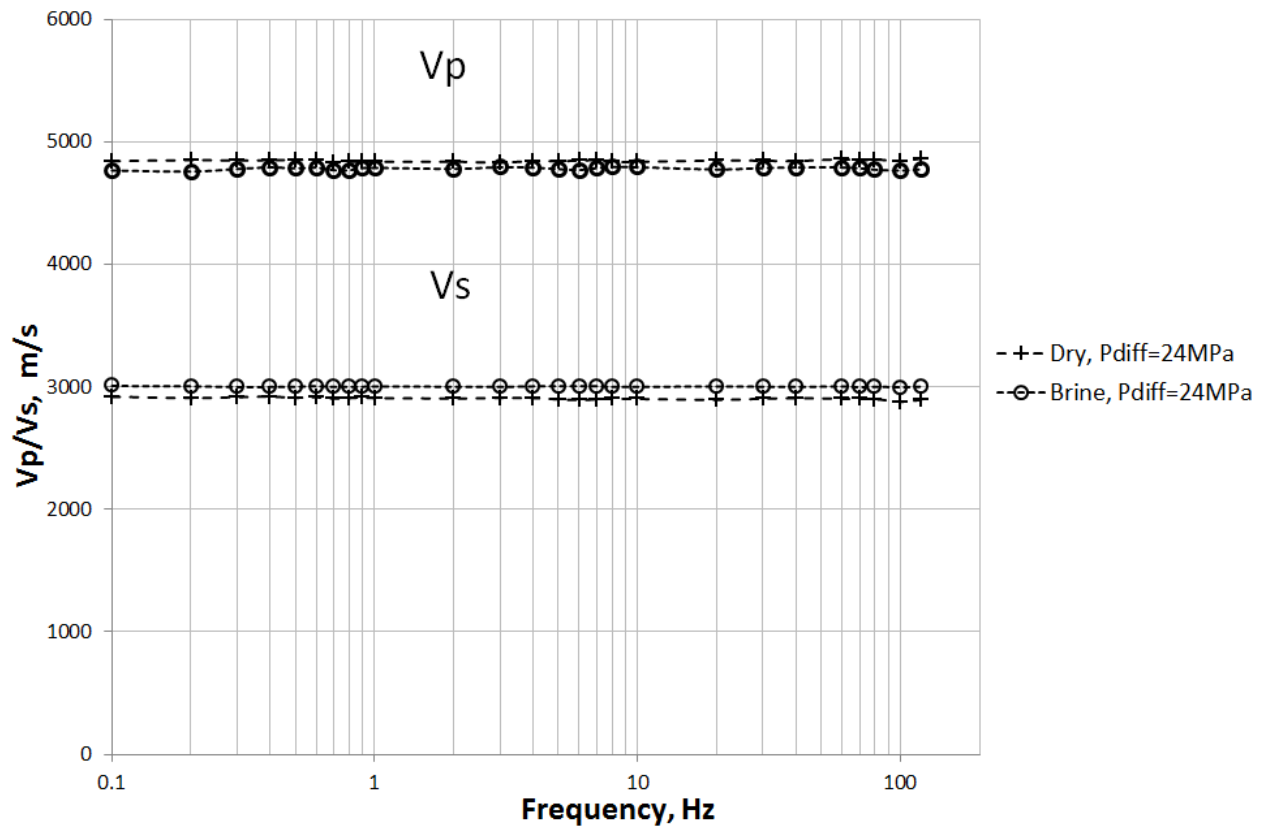


Figure 7.13. V<sub>p</sub> and V<sub>s</sub> velocities obtained for dry and brine saturated sandstone sample 206663. All pressure parameters are the same as in Figure 6.11.



### Extensional Attenuation vs. Frequency

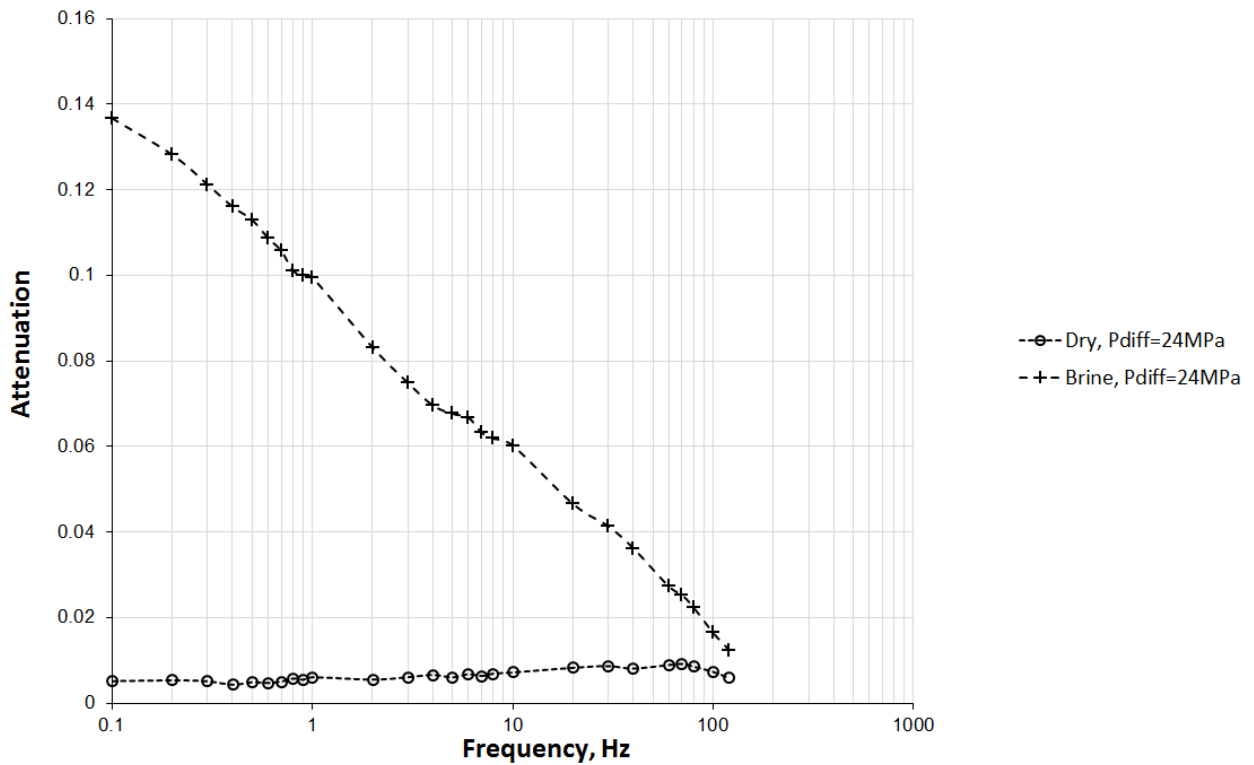


Figure 7.14. Extensional attenuation measured for dry and brine saturated sandstone sample 206663. All pressure parameters are the same as in Figure 6.11.

#### 7.4.5 SAMPLE 206664 (WONNERUP MEMBER)

The results from the measurements on sample 206664 are presented in Figs 6.15 -17. The experimental data are given in Tables 7.8 – 7.9.

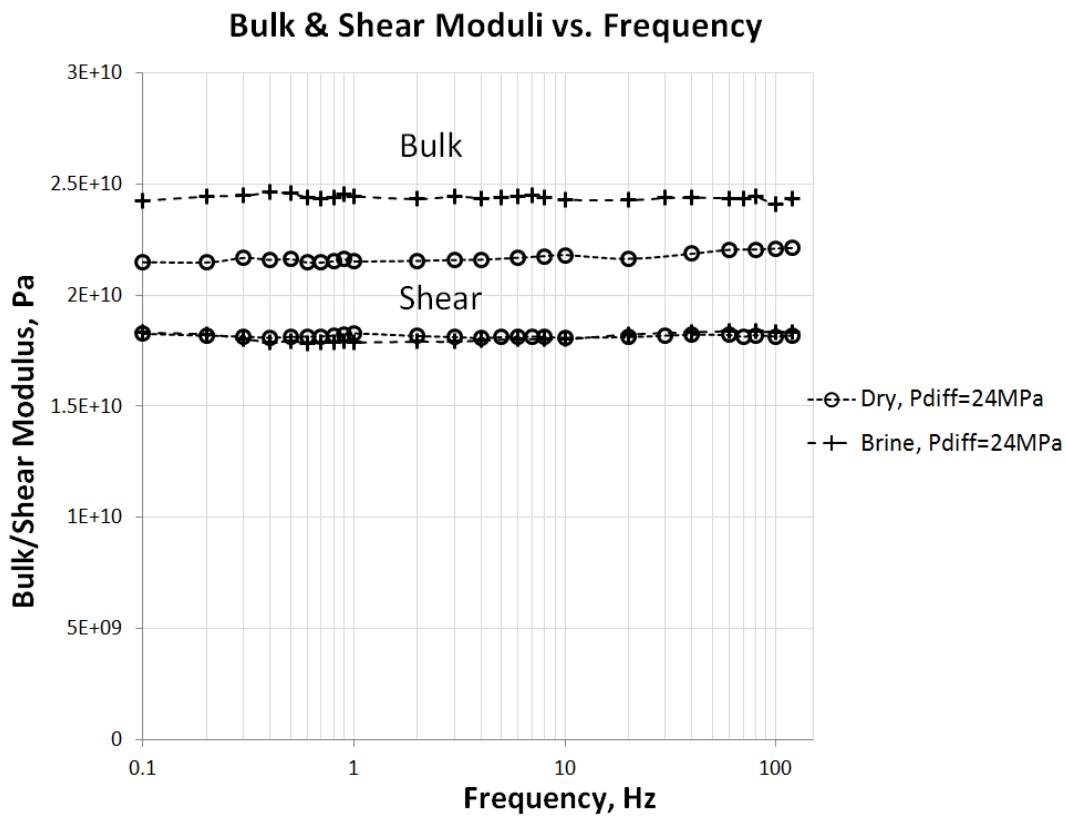


Figure 7.15. Bulk and shear moduli measured for dry and brine saturated sandstone sample 206664. The measurements with the dry sandstone are conducted at a confining pressure of 24 MPa and a pore pressure of 0.1 MPa; the confining and pore pressures for brine saturated sandstone are 29 MPa and 5 MPa correspondingly.

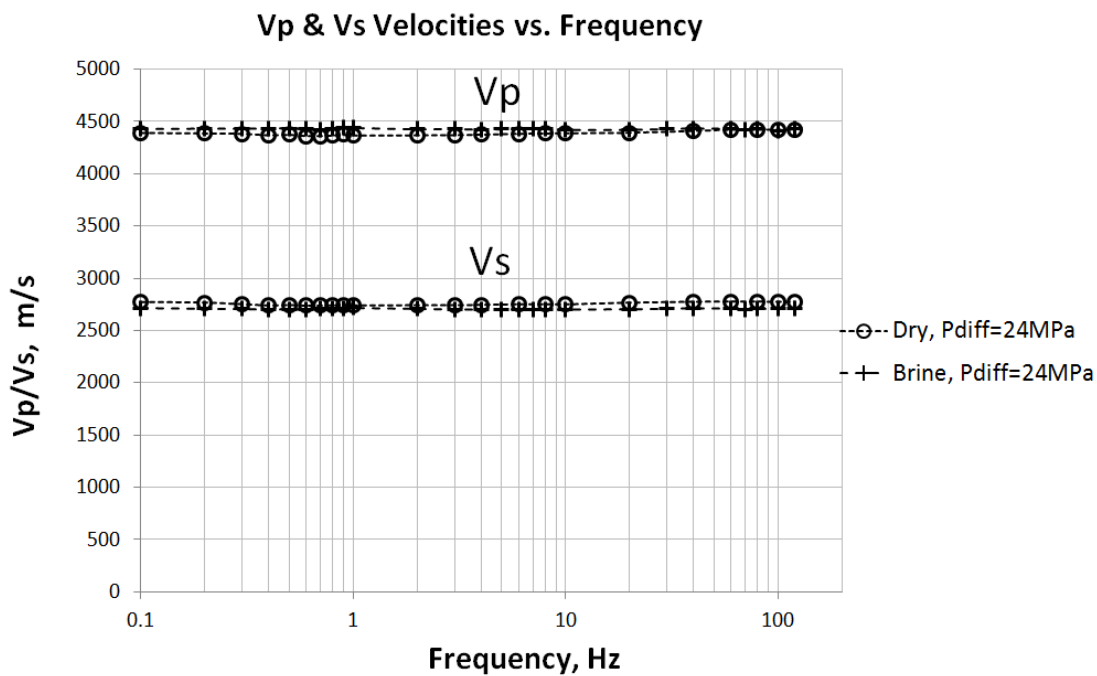


Figure 7.16.  $V_p$  and  $V_s$  velocities obtained for dry and brine saturated sandstone sample 206664. All pressure parameters are the same as in Figure 6.14.

## Extensional Attenuation vs. Frequency

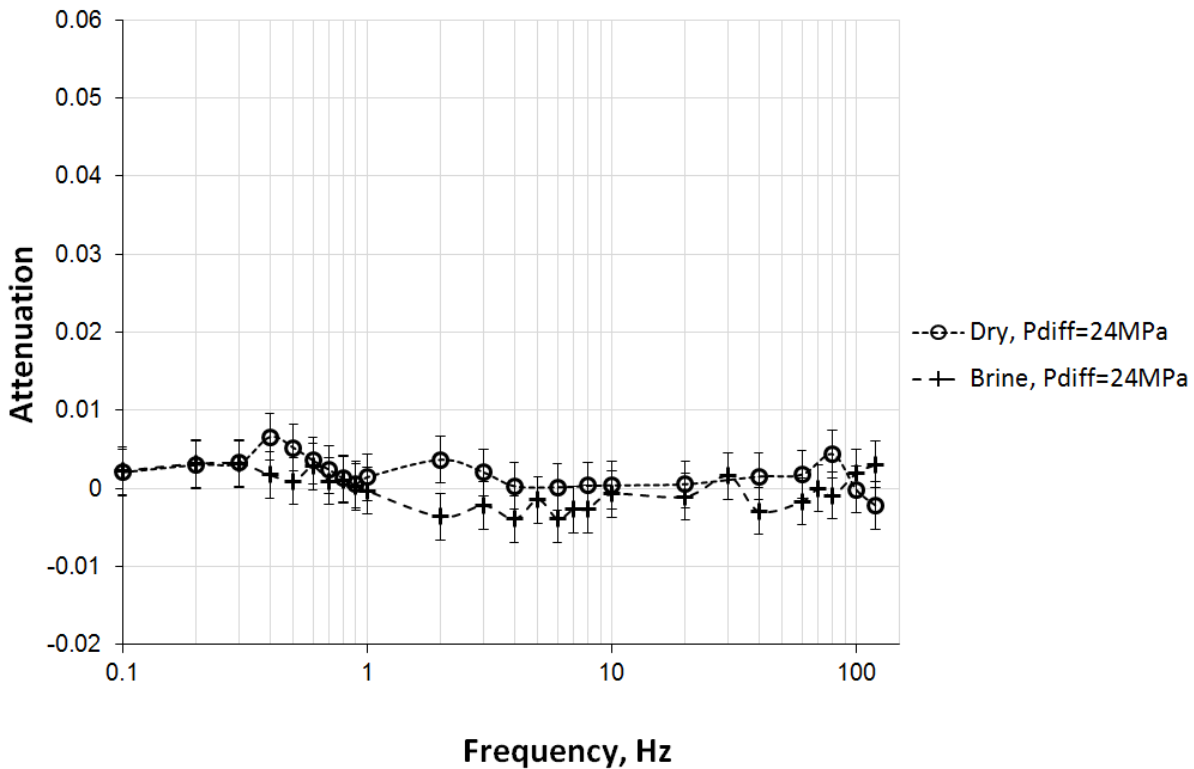


Figure 7.17. Extensional attenuation measured for dry and brine saturated sandstone sample 206664. All pressure parameters are the same as in Figure 6.14.

## 7.5 Discussion and conclusions

The results measured for two samples 206603 (Yalgorup Member) and 206663 (Wonnerup Member) require some additional analysis. The measurements in brine saturated sample 206603 revealed a prominent peak of extensional attenuation at frequency  $\sim 25$  Hz and effective pressure  $P_{eff} = 9$  MPa. The increase of the effective pressure to 23 MPa caused decrease in the attenuation and shift in frequency of the peak. A significant dispersion of the bulk modulus of the water saturated sandstone in the frequency range from 0.1 to 120 Hz was also observed. The dispersion of the bulk modulus of dry sandstone was within the accuracy of our measurements. These results can be interpreted as the evidence of the presence of squirt flow (Mavko and Nur, 1975) as mechanism of dispersion in the sample at the frequencies of measurements.

It should be noted that high attenuation and Young's modulus dispersion at seismic frequencies is a well known phenomena. Spencer (1981) observed significant Young's modulus dispersion and attenuation at frequencies of a few hundreds of Hertz in water saturated Navajo sandstone. Paffenholz and Burkhardt (1989) found substantial attenuation in fully water saturated Mittelrhaet and Obemkirchner sandstones with peaks of attenuation at a few tens of Hertz, and also in limestone and dolomite, where the peaks of attenuation were observed at  $\sim 0.1$  and  $\sim 20$  Hz respectively. Batzle et al. (1999) conducted low frequency (5 – 2500 Hz) measurements on brine and distilled water saturated low-permeability sandstone and also concluded that a peak of attenuation in the brine saturated sandstone can be observed at seismic frequency or even at frequency below the seismic band. Mikhaltsevitch et al. (2012) observed a peak of attenuation in distilled water saturated Donnybrook sandstone with low permeability ( $\sim 7.8$  mD) at a frequency of  $\sim 0.8$  Hz and effective pressures  $P_{eff} = 2.5, 7$  and 15 MPa.

The bulk modulus measured for sample 206603 (Yalgorup Member) does not increase considerably when saturated with brine as compared with the bulk modulus under dry conditions, which is in agreement with the corresponding results of Spencer (1981) and Paffenholz and Burkhardt (1989).

The results obtained for the extensional attenuation in sample 206663 (Wonnerup Member) presented in Fig. 7.14 were re-measured three times (the last experiments with this sample were undertaken two months after the first ones). All measurements demonstrate significant attenuation in the sample increasing at lower frequencies. We speculate the unusual attenuation can be caused by compliant porosity in the sample (microfractures).

The results consistently indicate negligible frequency dependence of the elastic moduli in the dry samples, but seem to highlight a strong effect of the pore fluid (synthetic brine in the testes above) in inducing attenuation and dispersion at low frequencies. While the limited amount of tested samples does not allow for a generalization of the results, one can speculate that these observations may have important consequences on the seismic monitoring of the CO<sub>2</sub> in the reservoir (i.e. when gas-like supercritical CO<sub>2</sub> partially replaces water as interstitial pore fluid in the storage rocks). A more systematic study performed on a larger sample population and utilizing different saturating fluids may provide a more robust quantification of these effects.

Frequency	Axial	Radial	Axial	Phase	Phase	Extensional	Poisson	Young	Bulk	Shear	Vp	Vs
Hz	signal standard, $\mu V$	signal rock, $\mu V$	signal rock, $\mu V$	axial standard, rad	axial rock, rad	attenuation	ratio rock	modulus, Pa	modulus, Pa	modulus, Pa	m/s	m/s
0.1	65.12	41.96	263.3	-1.7124	-1.7097	-0.001	0.159	1.73E+10	8.47E+09	7.47E+09	2955	1881
0.2	64.46	42.01	261.2	-1.7407	-1.7383	0.00109	0.161	1.73E+10	8.49E+09	7.44E+09	2954	1878
0.3	64.23	41.82	260	-1.7659	-1.7639	-0.00103	0.161	1.73E+10	8.5E+09	7.45E+09	2955	1879
0.4	64.01	42.02	259.2	-1.5757	-1.5747	0.00035	0.162	1.73E+10	8.52E+09	7.44E+09	2956	1877
0.5	63.8	42.03	258.7	-1.7729	-1.7704	0.00118	0.162	1.73E+10	8.52E+09	7.42E+09	2955	1876
0.6	63.63	42.02	257.6	-1.6525	-1.649	0.00124	0.163	1.73E+10	8.55E+09	7.43E+09	2958	1877
0.7	62.61	41.28	253.1	-1.7435	-1.741	-0.00027	0.163	1.73E+10	8.57E+09	7.44E+09	2960	1878
0.8	62.37	41.33	252.8	-1.7432	-1.7406	-0.00074	0.163	1.73E+10	8.55E+09	7.42E+09	2957	1876
0.9	62.9	41.68	254.9	-1.694	-1.6919	-0.00124	0.164	1.73E+10	8.56E+09	7.42E+09	2958	1876
1	62.35	41.23	253.9	-1.5469	-1.5453	0.00147	0.162	1.72E+10	8.48E+09	7.39E+09	2948	1872
2	62.58	41.49	254.3	-1.478	-1.4767	0.00097	0.163	1.72E+10	8.52E+09	7.4E+09	2953	1873
3	62.35	41.56	252.9	-1.4769	-1.4765	0.00029	0.164	1.73E+10	8.57E+09	7.41E+09	2957	1874
4	62.38	41.63	252.7	-1.5526	-1.5527	5.26E-05	0.165	1.73E+10	8.59E+09	7.42E+09	2959	1875
5	62.17	41.72	252	-1.5391	-1.5394	0.00039	0.166	1.73E+10	8.6E+09	7.41E+09	2959	1874
6	61.96	41.62	251.5	-1.5428	-1.5439	0.00081	0.166	1.72E+10	8.59E+09	7.4E+09	2958	1873
7	61.81	41.62	251	-1.5423	-1.5434	-0.00118	0.166	1.72E+10	8.6E+09	7.39E+09	2958	1872
8	61.73	41.57	250.4	-1.5333	-1.5341	0.00035	0.166	1.73E+10	8.61E+09	7.4E+09	2959	1873
10	61.61	41.57	249.9	-1.5579	-1.5585	0.00051	0.166	1.73E+10	8.62E+09	7.4E+09	2960	1872
20	61.14	41.53	247.7	-1.5141	-1.5173	-0.00021	0.168	1.73E+10	8.66E+09	7.4E+09	2963	1873
30	60.56	41.4	245.2	-1.6151	-1.6195	-0.0011	0.169	1.73E+10	8.7E+09	7.39E+09	2966	1872
40	60.51	41.72	245.5	-1.5959	-1.6005	-0.00111	0.17	1.73E+10	8.71E+09	7.37E+09	2965	1869
60	59.68	41.21	242.6	-1.5652	-1.5726	0.00049	0.17	1.72E+10	8.69E+09	7.36E+09	2961	1868
80	59.08	41.17	241.2	-1.5365	-1.5443	-0.00119	0.171	1.71E+10	8.68E+09	7.32E+09	2956	1863
100	58.64	41.4	240.8	-1.6972	-1.7073	-0.00117	0.172	1.7E+10	8.66E+09	7.27E+09	2949	1856
120	57.97	41.61	240.3	-1.6626	-1.6753	0.00105	0.173	1.69E+10	8.61E+09	7.2E+09	2938	1847

**Table 7.2. Results of low-frequency measurements for sample 206603 (Yalgorup Member) under dry conditions. Confining pressure – 9 MPa, pore pressure – 0.1 MPa.**

Frequency	Axial	Radial	Axial	Phase	Phase	Extensional	Poisson	Young	Bulk	Shear	Vp	Vs
Hz	signal standard, $\mu V$	signal rock, $\mu V$	signal rock, $\mu V$	axial standard, rad	axial rock, rad	attenuation	ratio rock	modulus, Pa	modulus, Pa	modulus, Pa	m/s	m/s
0.1	86.83	41.96	263.3	-1.7124	-1.7097	0.0016	0.159	2.31E+10	1.13E+10	9.96E+09	3412	2172
0.2	85.95	42.01	261.2	-1.7407	-1.7383	0.0012	0.161	2.3E+10	1.13E+10	9.92E+09	3411	2168
0.3	85.65	41.82	260	-1.7659	-1.7639	0.0008	0.161	2.31E+10	1.13E+10	9.93E+09	3412	2169
0.4	85.34	42.02	259.2	-1.5757	-1.5747	-0.0001	0.162	2.3E+10	1.14E+10	9.91E+09	3414	2168
0.5	85.06	42.03	258.7	-1.7729	-1.7704	0.0014	0.162	2.3E+10	1.14E+10	9.9E+09	3412	2166
0.6	84.84	42.02	257.6	-1.6525	-1.649	0.0024	0.163	2.31E+10	1.14E+10	9.91E+09	3416	2167
0.7	83.48	41.28	253.1	-1.7435	-1.741	0.0013	0.163	2.31E+10	1.14E+10	9.92E+09	3418	2169
0.8	83.16	41.33	252.8	-1.7432	-1.7406	0.0015	0.163	2.3E+10	1.14E+10	9.9E+09	3415	2166
0.9	83.87	41.68	254.9	-1.694	-1.6919	0.001	0.164	2.3E+10	1.14E+10	9.9E+09	3415	2166
1	83.13	41.23	253.9	-1.5469	-1.5453	0.0005	0.162	2.29E+10	1.13E+10	9.86E+09	3405	2161
2	83.44	41.49	254.3	-1.478	-1.4767	0.0004	0.163	2.3E+10	1.14E+10	9.87E+09	3410	2163
3	83.13	41.56	252.9	-1.4769	-1.4765	-0.0005	0.164	2.3E+10	1.14E+10	9.88E+09	3414	2164
4	83.17	41.63	252.7	-1.5526	-1.5527	-0.0009	0.165	2.3E+10	1.15E+10	9.89E+09	3417	2165
5	82.89	41.72	252	-1.5391	-1.5394	-0.0009	0.166	2.3E+10	1.15E+10	9.88E+09	3417	2163
6	82.61	41.62	251.5	-1.5428	-1.5439	-0.0016	0.166	2.3E+10	1.15E+10	9.86E+09	3415	2162
7	82.42	41.62	251	-1.5423	-1.5434	-0.0014	0.166	2.3E+10	1.15E+10	9.86E+09	3415	2162
8	82.31	41.57	250.4	-1.5333	-1.5341	-0.001	0.166	2.3E+10	1.15E+10	9.87E+09	3417	2163
10	82.15	41.57	249.9	-1.5579	-1.5585	-0.0006	0.166	2.3E+10	1.15E+10	9.86E+09	3418	2162
20	81.52	41.53	247.7	-1.5141	-1.5173	-0.002	0.168	2.3E+10	1.16E+10	9.86E+09	3422	2162
30	80.74	41.4	245.2	-1.6151	-1.6195	-0.0019	0.169	2.3E+10	1.16E+10	9.86E+09	3425	2162
40	80.68	41.72	245.5	-1.5959	-1.6005	-0.0009	0.17	2.3E+10	1.16E+10	9.83E+09	3423	2159
60	79.57	41.21	242.6	-1.5652	-1.5726	-0.0012	0.17	2.3E+10	1.16E+10	9.81E+09	3420	2156
80	78.78	41.17	241.2	-1.5365	-1.5443	0.0008	0.171	2.29E+10	1.16E+10	9.76E+09	3414	2151
100	78.19	41.4	240.8	-1.6972	-1.7073	0.001	0.172	2.27E+10	1.15E+10	9.7E+09	3406	2144
120	77.3	41.61	240.3	-1.6626	-1.6753	0.0009	0.173	2.25E+10	1.15E+10	9.6E+09	3392	2133

**Table 7.3. Results of low-frequency measurements for sample 206603 (Yalgorup Member) under dry conditions. Confining pressure – 29 MPa, pore pressure – 5 MPa.**

Frequency	Axial	Radial	Axial	Phase	Phase	Extensional	Poisson	Young	Bulk	Shear	Vp	Vs
Hz	signal standard, $\mu\text{V}$	signal rock, $\mu\text{V}$	signal rock, $\mu\text{V}$	axial standard, rad	axial rock, rad	attenuation	ratio rock	modulus, Pa	modulus, Pa	modulus, Pa	m/s	m/s
0.1	83.11	58.69	311.8	-1.5671	-1.5675	0.0004	0.188	1.87E+10	9.97E+09	7.85E+09	4228	1739
0.2	82.07	59.68	324.2	-1.5657	-1.5663	0.0006	0.184	1.77E+10	9.35E+09	7.48E+09	4133	1694
0.3	81.94	59.68	320	-1.5683	-1.5697	0.0013	0.187	1.79E+10	9.53E+09	7.55E+09	4229	1701
0.4	81.53	59.77	321.4	-1.5941	-1.5952	0.0011	0.186	1.78E+10	9.42E+09	7.49E+09	4195	1694
0.5	81.16	60.64	320.6	-1.81	-1.8143	0.0043	0.189	1.77E+10	9.5E+09	7.45E+09	4237	1690
0.6	80.98	60.33	321.8	-1.6288	-1.6328	0.004	0.188	1.76E+10	9.4E+09	7.42E+09	4202	1686
0.7	79.53	60.66	312.8	-1.628	-1.6337	0.0057	0.194	1.78E+10	9.69E+09	7.45E+09	4236	1695
0.8	79.56	60.89	315.1	-1.5898	-1.5959	0.0061	0.193	1.77E+10	9.6E+09	7.41E+09	4225	1689
0.9	80.27	61.52	317.8	-1.6279	-1.6338	0.0059	0.194	1.77E+10	9.62E+09	7.41E+09	4220	1689
1	79.04	61.6	313.1	-1.5457	-1.5536	0.0079	0.197	1.77E+10	9.71E+09	7.38E+09	4270	1687
2	79.41	62.36	314.9	-1.4753	-1.4884	0.0131	0.198	1.77E+10	9.74E+09	7.37E+09	4230	1687
3	79.25	64.02	313.4	-1.5327	-1.5515	0.0188	0.204	1.77E+10	9.98E+09	7.35E+09	4212	1691
4	79.6	67.46	311.6	-1.5501	-1.5727	0.0226	0.217	1.79E+10	1.05E+10	7.35E+09	4295	1697
5	79.37	68.37	309.9	-1.5361	-1.5622	0.0262	0.221	1.79E+10	1.07E+10	7.34E+09	4308	1699
6	79.16	70.74	308.5	-1.541	-1.5681	0.027	0.229	1.8E+10	1.11E+10	7.3E+09	4309	1700
7	78.62	69.99	299.4	-1.5966	-1.6262	0.0296	0.234	1.84E+10	1.15E+10	7.45E+09	4353	1721
8	79.12	71.69	303.6	-1.6491	-1.6794	0.0303	0.236	1.82E+10	1.15E+10	7.38E+09	4331	1714
10	79.06	72.43	304.9	-1.6845	-1.7173	0.0329	0.238	1.82E+10	1.15E+10	7.33E+09	4343	1709
20	78.45	74.32	296.5	-1.625	-1.6631	0.0382	0.251	1.85E+10	1.24E+10	7.41E+09	4388	1727
30	77.66	74.61	288.7	-1.625	-1.6631	0.0382	0.258	1.88E+10	1.3E+10	7.48E+09	4434	1741
40	77.83	75.28	288.1	-1.7329	-1.7681	0.0353	0.261	1.89E+10	1.32E+10	7.5E+09	4441	1744
60	77.08	75.43	283.6	-1.5993	-1.6295	0.0302	0.266	1.9E+10	1.36E+10	7.52E+09	4405	1751
80	76.41	75.37	281.8	-1.4742	-1.4979	0.0238	0.267	1.9E+10	1.36E+10	7.49E+09	4400	1749
100	75.97	75.58	280.9	-1.6936	-1.7117	0.0181	0.269	1.89E+10	1.37E+10	7.46E+09	4394	1747
120	74.39	75.48	279.4	-1.5663	-1.5808	0.0146	0.27	1.86E+10	1.35E+10	7.34E+09	4540	1728

**Table 7.4. Results of low-frequency measurements for brine saturated sample 206603 (Yalgorup Member). Confining pressure – 14 MPa, pore pressure – 5 MPa.**

Frequency	Axial	Radial	Axial	Phase	Phase	Extensional	Poisson	Young	Bulk	Shear	Vp	Vs
Hz	signal standard, $\mu V$	signal rock, $\mu V$	signal rock, $\mu V$	axial standard, rad	axial rock, rad	attenuation	ratio rock	modulus, Pa	modulus, Pa	modulus, Pa	m/s	m/s
0.1	82.21	47.58	251.4	-1.5657	-1.5661	0.0005	0.189	2.29E+10	1.23E+10	9.63E+09	4841	1919
0.2	81.37	47.55	248.5	-1.5587	-1.562	0.0033	0.191	2.29E+10	1.24E+10	9.62E+09	4849	1920
0.3	81.09	47.65	247.6	-1.5606	-1.5651	0.0045	0.192	2.29E+10	1.24E+10	9.61E+09	4851	1920
0.4	80.92	48.24	247	-1.5883	-1.5944	0.0061	0.195	2.29E+10	1.25E+10	9.59E+09	4854	1920
0.5	79.73	47.68	243.3	-1.8056	-1.8135	0.0079	0.196	2.29E+10	1.26E+10	9.59E+09	4854	1920
0.6	80.99	48.67	245.7	-1.6264	-1.6354	0.009	0.198	2.31E+10	1.27E+10	9.63E+09	4809	1928
0.7	80.31	48.59	244.5	-1.6243	-1.634	0.0098	0.199	2.3E+10	1.27E+10	9.59E+09	4847	1923
0.8	80.45	49.22	244.8	-1.5857	-1.5963	0.0106	0.201	2.3E+10	1.28E+10	9.57E+09	4831	1924
0.9	80.28	49.23	243.7	-1.6231	-1.6351	0.0121	0.202	2.31E+10	1.29E+10	9.59E+09	4830	1927
1	78.57	48.23	237.7	-1.5394	-1.5519	0.0125	0.203	2.31E+10	1.3E+10	9.62E+09	4879	1929
2	79.78	51.15	240.3	-1.4719	-1.4884	0.0165	0.213	2.32E+10	1.35E+10	9.58E+09	4907	1932
3	79.66	52.37	238.5	-1.5309	-1.5492	0.0183	0.22	2.34E+10	1.39E+10	9.59E+09	4944	1938
4	79.6	53.23	237.6	-1.5867	-1.6053	0.0185	0.224	2.34E+10	1.42E+10	9.58E+09	4913	1941
5	79.23	53.51	236.4	-1.6444	-1.6636	0.0193	0.226	2.35E+10	1.43E+10	9.57E+09	4923	1942
6	79.11	53.87	235.7	-1.7013	-1.7203	0.019	0.229	2.35E+10	1.44E+10	9.56E+09	4923	1943
7	78.98	53.82	234.7	-1.6841	-1.7032	0.0191	0.229	2.36E+10	1.46E+10	9.61E+09	4931	1949
8	78.88	53.92	233.9	-1.6492	-1.6676	0.0185	0.23	2.37E+10	1.46E+10	9.62E+09	4931	1951
10	78.59	54.01	232.4	-1.6605	-1.6787	0.0182	0.231	2.38E+10	1.47E+10	9.65E+09	4965	1954
20	77.83	53.83	228.1	-1.6241	-1.6405	0.0164	0.235	2.4E+10	1.51E+10	9.73E+09	4994	1965
30	76.89	53.52	223.9	-1.6375	-1.6522	0.0147	0.239	2.42E+10	1.54E+10	9.76E+09	5021	1971
40	77.02	53.78	223.7	-1.7334	-1.7464	0.0129	0.24	2.43E+10	1.56E+10	9.78E+09	5027	1974
60	76.27	53.79	221.2	-1.5993	-1.6104	0.0111	0.245	2.44E+10	1.59E+10	9.79E+09	4980	1980
80	75.46	53.9	219.6	-1.4746	-1.4852	0.0106	0.246	2.41E+10	1.58E+10	9.66E+09	5080	1963
100	75.11	54.18	219.5	-1.5666	-1.5755	0.0088	0.247	2.4E+10	1.58E+10	9.61E+09	5119	1957
120	73.74	54.38	218.5	-1.6943	-1.702	0.0077	0.249	2.36E+10	1.57E+10	9.46E+09	5154	1942

**Table 7.5. Results of low-frequency measurements for brine saturated sample 206603 (Yalgorup Member). Confining pressure – 29 MPa, pore pressure – 5 MPa.**



Frequency	Axial	Radial	Axial	Phase	Phase	Extensional	Poisson	Young	Bulk	Shear	Vp	Vs
Hz	signal standard, $\mu\text{V}$	signal rock, $\mu\text{V}$	signal rock, $\mu\text{V}$	axial standard, rad	axial rock, rad	attenuation	ratio rock	modulus, Pa	modulus, Pa	modulus, Pa	m/s	m/s
0.1	110.42	29.02	155.88	-1.575	-1.5802	0.0052	0.186	4.96E+10	2.63E+10	2.09E+10	4844	3008
0.2	109.06	29.07	153.98	-1.5699	-1.5753	0.0053	0.189	4.96E+10	2.66E+10	2.09E+10	4851	3004
0.3	108.53	29.2	153.62	-1.5718	-1.5769	0.0051	0.19	4.95E+10	2.66E+10	2.08E+10	4848	2999
0.4	108.32	29.22	153.26	-1.5988	-1.6031	0.0043	0.191	4.95E+10	2.67E+10	2.08E+10	4851	2999
0.5	106.62	28.73	150.67	-1.8169	-1.8218	0.0049	0.191	4.95E+10	2.67E+10	2.08E+10	4854	3001
0.6	107.52	28.57	151.72	-1.6353	-1.64	0.0047	0.188	4.96E+10	2.65E+10	2.09E+10	4851	3006
0.7	107.37	28.47	152.29	-1.6349	-1.6399	0.0051	0.187	4.94E+10	2.63E+10	2.08E+10	4835	3000
0.8	107.49	28.53	152.32	-1.5976	-1.6034	0.0058	0.187	4.94E+10	2.63E+10	2.08E+10	4838	3001
0.9	107.06	28.51	151.58	-1.6343	-1.6398	0.0055	0.188	4.94E+10	2.64E+10	2.08E+10	4842	3001
1	106.3	28.04	150.47	-1.5541	-1.5602	0.0061	0.186	4.95E+10	2.63E+10	2.08E+10	4838	3004
2	106.39	28.25	150.74	-1.4842	-1.4897	0.0055	0.187	4.94E+10	2.63E+10	2.08E+10	4839	3001
3	105.46	27.84	149.64	-1.4841	-1.4902	0.0061	0.186	4.93E+10	2.62E+10	2.08E+10	4831	3001
4	105.05	27.85	148.49	-1.7198	-1.7264	0.0066	0.188	4.95E+10	2.64E+10	2.09E+10	4845	3004
5	104.7	27.63	147.94	-1.6663	-1.6723	0.006	0.187	4.95E+10	2.64E+10	2.09E+10	4843	3006
6	104.52	27.65	147.52	-1.6718	-1.6786	0.0068	0.187	4.96E+10	2.64E+10	2.09E+10	4848	3007
7	103.14	27.35	145.51	-1.7608	-1.7672	0.0064	0.188	4.96E+10	2.65E+10	2.09E+10	4850	3007
8	104.16	27.67	147.74	-1.6596	-1.6665	0.0069	0.187	4.94E+10	2.63E+10	2.08E+10	4835	2999
10	103.92	27.65	147.3	-1.6946	-1.7018	0.0072	0.188	4.94E+10	2.64E+10	2.08E+10	4838	3000
20	102.99	27.43	145.53	-1.6356	-1.6439	0.0083	0.188	4.95E+10	2.65E+10	2.08E+10	4848	3004
30	102.03	27.29	144.31	-1.648	-1.6566	0.0087	0.189	4.95E+10	2.65E+10	2.08E+10	4847	3002
40	102.01	27.29	144.46	-1.7438	-1.7519	0.0081	0.189	4.94E+10	2.65E+10	2.08E+10	4844	3000
60	101.2	27.23	142.74	-1.6113	-1.6202	0.0089	0.191	4.96E+10	2.68E+10	2.08E+10	4859	3004
70	101.01	27.24	143.07	-1.7091	-1.7183	0.0092	0.19	4.94E+10	2.66E+10	2.08E+10	4848	2998
80	101.06	27.24	142.72	-1.4876	-1.4961	0.0085	0.191	4.96E+10	2.67E+10	2.08E+10	4856	3002
100	101.19	27.25	143.41	-1.6279	-1.6353	0.0073	0.19	4.94E+10	2.66E+10	2.08E+10	4845	2997
120	101.03	27.39	142.4	-1.4972	-1.503	0.0059	0.192	4.97E+10	2.69E+10	2.08E+10	4865	3003

**Table 7.6. Results of low-frequency measurements for sample 206663 (Wonnerup Member) under dry conditions. Confining pressure – 24 MPa, pore pressure – 0.1 MPa.**

Frequency	Axial	Radial	Axial	Phase	Phase	Extensional	Poisson	Young	Bulk	Shear	Vp	Vs
Hz	signal standard, $\mu\text{V}$	signal rock, $\mu\text{V}$	signal rock, $\mu\text{V}$	axial standard, rad	axial rock, rad	attenuation	ratio rock	modulus, Pa	modulus, Pa	modulus, Pa	m/s	m/s
0.1	100.3	28.21	141.18	-1.3984	-1.5351	0.1367	0.2	4.97E+10	2.76E+10	2.07E+10	4767	2920
0.2	99.74	28.45	141.15	-1.4023	-1.5305	0.1282	0.202	4.95E+10	2.76E+10	2.06E+10	4759	2909
0.3	98.95	28.32	139.16	-1.4114	-1.5326	0.1212	0.203	4.98E+10	2.8E+10	2.07E+10	4780	2916
0.4	98.66	28.28	138.21	-1.4429	-1.5589	0.116	0.205	5E+10	2.82E+10	2.07E+10	4792	2921
0.5	97.2	28.21	136.89	-1.6595	-1.7724	0.113	0.206	4.97E+10	2.82E+10	2.06E+10	4784	2911
0.6	97.99	28.32	137.62	-1.4859	-1.5946	0.1087	0.206	4.98E+10	2.82E+10	2.07E+10	4790	2916
0.7	97.76	28.46	138.46	-1.4883	-1.594	0.1057	0.206	4.94E+10	2.8E+10	2.05E+10	4769	2903
0.8	97.8	28.19	138.23	-1.455	-1.5561	0.1011	0.204	4.95E+10	2.79E+10	2.06E+10	4769	2908
0.9	97.56	28.19	137.17	-1.493	-1.5929	0.0999	0.206	4.98E+10	2.82E+10	2.06E+10	4786	2914
1	96.41	28.22	135.86	-1.4125	-1.5119	0.0995	0.208	4.97E+10	2.83E+10	2.06E+10	4788	2908
2	96.84	28.32	136.77	-1.3614	-1.4446	0.0831	0.207	4.96E+10	2.82E+10	2.05E+10	4781	2906
3	96.25	28.22	135.43	-1.3685	-1.4434	0.0748	0.208	4.98E+10	2.84E+10	2.06E+10	4794	2910
4	96.14	28.21	135.43	-1.448	-1.5175	0.0696	0.208	4.97E+10	2.84E+10	2.06E+10	4791	2908
5	95.98	28.39	136.01	-1.4368	-1.5045	0.0676	0.209	4.94E+10	2.83E+10	2.04E+10	4778	2899
6	95.4	28.38	135.68	-1.5601	-1.6268	0.0667	0.209	4.92E+10	2.82E+10	2.04E+10	4771	2893
7	95.33	28.42	134.92	-1.5625	-1.6257	0.0632	0.211	4.95E+10	2.85E+10	2.04E+10	4787	2898
8	95.3	28.29	134.4	-1.5521	-1.614	0.0619	0.211	4.96E+10	2.86E+10	2.05E+10	4795	2904
10	95.04	28.28	134.16	-1.588	-1.6482	0.0602	0.211	4.96E+10	2.86E+10	2.05E+10	4794	2902
20	94.27	28.06	133.88	-1.5421	-1.5887	0.0466	0.21	4.93E+10	2.83E+10	2.04E+10	4776	2895
30	93.37	27.55	131.82	-1.5584	-1.5997	0.0413	0.209	4.96E+10	2.84E+10	2.05E+10	4788	2904
40	93.68	27.48	131.94	-1.6579	-1.694	0.0362	0.208	4.97E+10	2.84E+10	2.06E+10	4791	2908
60	93.21	27.6	131.5	-1.5347	-1.562	0.0273	0.21	4.96E+10	2.85E+10	2.05E+10	4792	2904
70	92.96	27.47	131.41	-1.6317	-1.6569	0.0252	0.209	4.95E+10	2.84E+10	2.05E+10	4785	2902
80	92.89	27.27	131.57	-1.4171	-1.4394	0.0223	0.207	4.94E+10	2.81E+10	2.05E+10	4774	2901
100	93.03	28.31	133.19	-1.6367	-1.6531	0.0165	0.213	4.89E+10	2.84E+10	2.02E+10	4766	2879
120	92.59	27.56	131.45	-1.5149	-1.5274	0.0124	0.21	4.93E+10	2.83E+10	2.04E+10	4776	2895

**Table 7.7. Results of low-frequency measurements for brine saturated sample 206663 (Wonnerup Member). Confining pressure – 29 MPa, pore pressure – 5 MPa.**

Frequency	Axial	Radial	Axial	Phase	Phase	Extensional	Poisson	Young	Bulk	Shear	Vp	Vs
Hz	signal standard, μV	signal rock, μV	signal rock, μV	axial standard, rad	axial rock, rad	attenuation	ratio rock	modulus, Pa	modulus, Pa	modulus, Pa	m/s	m/s
0.1	96.17	26.47	157.39	-1.5625	-1.5646	0.0021	0.168	4.28E+10	2.15E+10	1.83E+10	4391	2773
0.2	96.34	26.75	158.21	-1.5619	-1.5649	0.003	0.169	4.26E+10	2.15E+10	1.82E+10	4386	2768
0.3	96.14	27.72	158.95	-1.5648	-1.568	0.0033	0.174	4.23E+10	2.17E+10	1.8E+10	4382	2752
0.4	95.6	27.92	159.19	-1.5891	-1.5957	0.0066	0.175	4.2E+10	2.16E+10	1.79E+10	4369	2741
0.5	94.45	27.51	156.97	-1.807	-1.8123	0.0052	0.175	4.21E+10	2.16E+10	1.79E+10	4373	2744
0.6	95.01	27.69	158.66	-1.6261	-1.6297	0.0036	0.175	4.19E+10	2.15E+10	1.78E+10	4361	2738
0.7	94.91	27.61	158.39	-1.6253	-1.6277	0.0024	0.174	4.19E+10	2.15E+10	1.79E+10	4362	2739
0.8	94.86	27.63	158.09	-1.587	-1.5883	0.0013	0.175	4.2E+10	2.15E+10	1.79E+10	4366	2741
0.9	94.48	27.52	157.02	-1.6245	-1.6251	0.0005	0.175	4.21E+10	2.16E+10	1.79E+10	4373	2744
1	93.81	27.34	156.39	-1.5416	-1.543	0.0015	0.175	4.2E+10	2.15E+10	1.79E+10	4365	2740
2	93.44	27.16	155.54	-1.4735	-1.4772	0.0037	0.175	4.21E+10	2.15E+10	1.79E+10	4368	2742
3	93.11	27.13	154.94	-1.4727	-1.4748	0.0021	0.175	4.21E+10	2.16E+10	1.79E+10	4370	2742
4	93.26	27	154.77	-1.5478	-1.5481	0.0003	0.174	4.22E+10	2.16E+10	1.8E+10	4374	2747
6	93.02	26.87	153.85	-1.5387	-1.5389	0.0002	0.175	4.23E+10	2.17E+10	1.8E+10	4382	2751
8	92.63	26.86	153.09	-1.5302	-1.5306	0.0004	0.175	4.24E+10	2.18E+10	1.8E+10	4386	2751
10	92.31	26.87	152.52	-1.555	-1.5555	0.0004	0.176	4.24E+10	2.18E+10	1.8E+10	4388	2751
20	91.69	25.73	150.37	-1.5103	-1.5109	0.0006	0.171	4.27E+10	2.16E+10	1.82E+10	4393	2767
40	90.95	25.54	148.15	-1.5911	-1.5927	0.0015	0.172	4.3E+10	2.19E+10	1.83E+10	4411	2775
60	89.98	25.39	146.05	-1.5589	-1.5607	0.0018	0.174	4.31E+10	2.2E+10	1.84E+10	4422	2778
80	89.3	25.27	145.03	-1.5306	-1.535	0.0044	0.174	4.31E+10	2.21E+10	1.84E+10	4421	2777
100	88.99	25.32	144.62	-1.6885	-1.6884	-0.0001	0.175	4.31E+10	2.21E+10	1.83E+10	4422	2775
120	88.53	25.22	143.81	-1.6532	-1.651	-0.0022	0.175	4.31E+10	2.21E+10	1.83E+10	4423	2775

**Table 7.8. Results of low-frequency measurements for sample 206664 (Wonnerup Member) under dry conditions. Confining pressure – 24 MPa, pore pressure – 0.1 MPa.**

Frequency	Axial	Radial	Axial	Phase	Phase	Extensional	Poisson	Young	Bulk	Shear	Vp	Vs
	signal	signal	signal	axial	axial	attenuation	ratio	modulus,	modulus,	modulus,		
Hz	standard,	rock,	rock,	standard,	rock, rad		rock	Pa	Pa	Pa	m/s	m/s
	$\mu V$	$\mu V$	$\mu V$	rad								
0.1	78.78	25.06	125.93	-1.8883	-1.8906	0.002276	0.199	4.38E+10	2.42E+10	1.83E+10	4428	2715
0.2	78.05	25.25	125.05	-1.5622	-1.56537	0.00318	0.202	4.37E+10	2.44E+10	1.82E+10	4431	2708
0.3	77.59	25.25	124.49	-1.5635	-1.56662	0.003158	0.203	4.36E+10	2.45E+10	1.81E+10	4431	2705
0.4	77.2	25.43	124.04	-1.5741	-1.57583	0.001762	0.205	4.36E+10	2.46E+10	1.81E+10	4434	2701
0.5	77.06	25.22	123.61	-1.7687	-1.76971	0.000965	0.204	4.36E+10	2.46E+10	1.81E+10	4435	2704
0.6	76.65	24.9	123.11	-1.6484	-1.65124	0.002811	0.202	4.36E+10	2.44E+10	1.81E+10	4427	2705
0.7	75.42	24.39	121.09	-1.7396	-1.74049	0.000939	0.201	4.36E+10	2.43E+10	1.81E+10	4425	2706
0.8	75.25	24.33	120.6	-1.7401	-1.7412	0.0011	0.202	4.37E+10	2.44E+10	1.82E+10	4430	2708
0.9	75.96	24.6	121.41	-1.6914	-1.69166	0.000232	0.203	4.38E+10	2.45E+10	1.82E+10	4439	2711
1	76.74	24.56	122.38	-1.5283	-1.52804	-0.000279	0.201	4.39E+10	2.44E+10	1.83E+10	4438	2716
2	72.88	23.52	116.96	-1.6955	-1.6919	-0.003608	0.201	4.36E+10	2.43E+10	1.82E+10	4425	2707
3	72	23.46	115.67	-1.6937	-1.69152	-0.00217	0.203	4.36E+10	2.44E+10	1.81E+10	4428	2703
4	72.71	23.75	117.14	-1.5495	-1.54562	-0.003916	0.203	4.35E+10	2.44E+10	1.81E+10	4421	2700
5	71.35	23.22	114.68	-1.7639	-1.76246	-0.00143	0.202	4.36E+10	2.44E+10	1.81E+10	4426	2703
6	72.04	23.45	115.73	-1.6604	-1.65657	-0.003849	0.203	4.36E+10	2.44E+10	1.81E+10	4427	2704
7	71.86	23.4	115.33	-1.6603	-1.65766	-0.002658	0.203	4.36E+10	2.45E+10	1.81E+10	4430	2705
8	71.62	23.29	115.04	-1.6483	-1.64568	-0.002621	0.202	4.36E+10	2.44E+10	1.81E+10	4427	2704
10	71.34	23.18	114.91	-1.6827	-1.682	-0.000711	0.202	4.35E+10	2.43E+10	1.81E+10	4419	2701
20	70.58	22.85	113.53	-1.6217	-1.62066	-0.001028	0.201	4.35E+10	2.43E+10	1.81E+10	4420	2703
30	69.76	22.5	111.83	-1.6345	-1.63607	0.001594	0.201	4.37E+10	2.44E+10	1.82E+10	4428	2708
40	70.15	22.56	112.22	-1.7295	-1.72658	-0.002901	0.201	4.38E+10	2.44E+10	1.82E+10	4432	2711
60	69.57	22.38	111.41	-1.5956	-1.59393	-0.001663	0.201	4.37E+10	2.44E+10	1.82E+10	4429	2710
70	69.02	22.36	110.92	-1.6929	-1.69287	1.0E-05	0.202	4.36E+10	2.43E+10	1.81E+10	4424	2704
80	69.14	22.31	110.67	-1.4714	-1.4705	-0.000906	0.202	4.37E+10	2.44E+10	1.82E+10	4433	2710
100	69.06	22.14	111.13	-1.6913	-1.69326	0.001955	0.199	4.35E+10	2.41E+10	1.81E+10	4414	2705
120	68.15	21.94	109.21	-1.5647	-1.56779	0.003077	0.201	4.37E+10	2.43E+10	1.82E+10	4428	2709

**Table 7.9. Results of low-frequency measurements for brine saturated sample 206664 (Wonnerup Member). Confining pressure – 29 MPa, pore pressure – 5 MPa.**

## 8 Summary and conclusions

The goal of the multidisciplinary work presented here is to help enable and further understand the geological and geophysical parameters that will affect the safe and efficient storage of CO<sub>2</sub> at the proposed SW-Hub site in the Southern Perth Basin. In particular the study aimed at providing a first geological, petrophysical and geomechanical description of the units crossed by the Harvey-1 stratigraphic well. The well was drilled by the geological survey of Western Australia in support of the assessment of the SW-Hub as a potential CO<sub>2</sub> geosequestration site. The deep saline aquifer equivalent to the Wonnerup Member of the Triassic Lesueur Sandstone represents the targeted reservoir, whereas the Yalgorup Member and the Basal Eneabba Shale (not cored) may act as possible stratigraphic seals.

By adopting a comprehensive multidisciplinary and multiscale study of the cored sections and the data recovered from the Harvey-1 well, the following conclusions can be made:

- The targeted storage reservoir in Wonnerup Member of the Lesueur Sandstone has thick continuous intervals of clean, coarse-grained sediments with very little mudstone intervals. This is confirmed via both sedimentary logging of the cores and interpretation of the wireline log. In terms of vertical stratigraphy the Wonnerup Member may therefore act as a suitable storage reservoir for the SW-Hub project.
- The Yalgorup Member shows a strongly interbedded facies succession with depth and with relatively thin, vertically continuous thicknesses. The shale/mudstone in cores 2-4 are significantly intruded by sandstone dykes and affected by brittle deformation at the cm-to m scale. These brittle features are interpreted as desiccation cracks in the paleosols; sedimentary logging indicates that they are confined within specific lithofacies, i.e. they are not likely to provide interconnected escape paths to underground fluids through the thickness of the Yalgorup. Nevertheless, their mechanical stability as a consequence of changes in the effective stress could not be investigated in this study and should be the focus of future examinations. Overall, the presence of inter-layered shale and sands on top of the Wonnerup Member reservoir may act as a barrier to vertical fluid movement.
- Drilling operations have identified the presence of the Basal Eneabba shale (625-704m) overlying the Lesueur Sandstone, unfortunately, the Basal Eneabba Shale was not cored in Harvey-1, but due to its mineralogical content (i.e. clay rich), and based on the observations collected on the cored section of the Pinjarra-1 well, it could provide additional sealing potential to the geosequestration site.
- Nine lithofacies were identified from core logging. The Yalgorup Member consists of mixed-thickness, interbedded high to low energy channel-fill facies, and swampy/ overbank deposits and palaeosols. The Wonnerup Member consists of thick, continuous, high energy channel-fill facies, with minor intercalations of moderate to low energy channel-fill/stacked rippleforms and rare swampy deposits. The stratigraphy in Harvey-1 is comparable to that of Pinjarra-1, when the same facies scheme is applied. The comparison of facies and rock properties distribution between the two wells allows for a better understanding of the lateral and vertical extent of reservoir and seals at the regional scale and can be used to better constrain the interpretation of seismic lines collected in the area.
- Core gamma response was compared to lithofacies interpreted from core logging. There was a moderate correlation between low core gamma (high energy channel fill and barforms, facies Ai-Aiii), moderate core gamma (low to moderate energy barforms, rippleforms and palaeosols, facies B-D) and high core gamma (swampy/overbank deposits and crevasse splays, facies E-G). There is a 50-90% probability that the core gamma, in counts per seconds, for facies Ai-Aiii, B-C and E-G are 10-50, 50-70 and 70-100+, respectively. However, facies D (palaeosols) have two components in Harvey-1. The sandstone component exhibits a low core gamma response and the silty mudstone exhibits a high core gamma response. The total core gamma varies depending on the proportion of

each of these lithotypes. The comparison between core gamma, log gamma and facies analysis done on the Harvey-1 units can be used as a guide to recognise facies in wells where there is no core using the wireline gamma ray log. This, in turn, may generate new information about the subsurface geology from the historical wells that were not cored to get a better interpretation of the distribution of reservoir and seal facies at depth around the SW-Hub area.

- Petrographic analysis on thin sections taken from the Yalgorup and Wonnerup samples indicate significant compaction and cementation (primarily kaolinite, and to a lesser extent illite, smectite and chlorite cement) in all samples, increasing with depth. The sub-hedral nature and size (reflecting the size of adjacent grains) of clay-occluded pores suggests that secondary porosity was created through weathering of feldspars. Authigenic quartz cement is rare and thought to be transported out of the system by formation waters. All the facies appear to have an inverse trend of porosity and permeability with depth due to diagenesis and compaction. Facies Aii (i.e. the most abundant one in the Wonnerup Member) is seen to maintain reasonably good reservoir suggesting that injectivity and storage potential are favourable along the Wonnerup Member even at elevated depths (>2km).
- Analysis of the suite of log data including GR, density, neutron, PE, sonic, array resistivity and NMR indicate that with increasing depth total porosity reduces from 26% to less 10% and permeability reduces from more than 4000mD to less than 10mD for Wonnerup. Permeability of sand intervals for Yalgorup Member ranges from more than 10,000mD to 4mD. The data quality for the Yalgorup Member is not good due to extensive washout, whereas for Wonnerup the borehole quality is good. With a shale volume cutoff of less than 20% and effective porosity larger than 8% a net to gross (NTG) values of 78% and 48% were computed for Wonnerup and Yalgorup Members respectively. A moderate contrast in resistivity is interpreted as difference in salinity of the pore water saturating the Yalgorup and Wonnerup Members, which in turn may imply the presence of an hydraulic barrier between the two aquifers.
- Laboratory measurements on core plugs show that porosity and permeability are inversely correlated with depth in agreement with the wireline log data. Within a cored section core plug porosities show a variation up to 12% and a permeability variation by up to four orders of magnitude. Similarly, continuous porosity and permeability derived from density and NMR logs, respectively, show a porosity variation of 28% and a permeability variation up to six orders of magnitude. This variation of porosity and permeability is likely controlled by lithofacies switching along the depth of the well. This data provides estimates of the vertical distribution of the transport properties of the rocks intersected by Harvey-1 and can be used to constrain forward stratigraphic models of the area and dynamic reservoir simulations to reduce the uncertainties in the estimation of spatial distribution of rock properties and of the injected CO<sub>2</sub> plume behavior.
- Samples attributed to lithofacies Aii (representing the possible injection target) show significant anisotropy in permeability: across bedding permeability ranges between 0.01 and 3md while along bedding permeability ranges between 38-216mD, resulting in anisotropy of up to 3 orders of magnitude. Assuming a laterally continuous and homogeneous reservoir the observed anisotropy may have beneficial effects in terms CO<sub>2</sub> injection as the fluid will move laterally with ease while its vertical displacement would be hindered by the structure of the sediments.
- Conventional core-flooding experiments conducted on core-plugs from the Wonnerup Member of the Lesueur Formation attributed to Facies Aii indicate relatively high residual scCO<sub>2</sub> saturations (25 to 45%) and a reduction in permeability of about 25%-51% in the samples after the scCO<sub>2</sub>-brine flooding, porosity changes in the same samples were almost negligible. Post flooding analyses of the samples support the interpretation of permeability reduction as due to formation damage by fine particles (kaolinite) migration. Sedimentary rocks assigned to Facies Aii therefore show relatively high residual trapping potential for the secure storage of CO<sub>2</sub>; variation in permeability of the storage reservoir over time should be considered in injection simulations to realistically predict the behaviour of the CO<sub>2</sub> plume in the subsurface.
- The mechanical and elastic properties of the Yalgorup and Wonnerup samples are significantly different. The Yalgorup is relatively weak (14<UCS<MPa; 2<E<10GPa) while the Wonnerup show stronger and stiffer response (29<UCS<72MPa; 16<E<23GPa). Generally the samples' response is

compatible with a linear Mohr-Coulomb failure criterion. The data provides real estimates of geomechanical properties that can be used to estimate the likelihood of fault reactivation and the safe values of injection pressure in the storage reservoir.

- Elastic wave velocities measured in the laboratory at ultrasonic frequency show little stress sensitivity in the Yalgorup while they increase with effective stress and stabilize at effective stress of 30-40 MPa in the Wonnerup samples. At simulated in-situ conditions the P- and S- wave velocities display values of approximately 3.6 and 2 km/s in the Yalgorup and 4.7 and 2.8 km/s in the Wonnerup respectively. More experiments should be performed to assess the role of different pore fluids and evaluate the agreement between theoretical models of fluid substitution and the values collected under controlled experimental conditions. This would prove beneficial to interpret time lapse seismic response acquired during CO<sub>2</sub> injection to monitor fluid movement at depth.
- There is good agreement between the laboratory measured elastic wave velocities and those measured in the well via wireline acoustic logging; this, should give confidence in the interpretation of petrophysical logs acquired in sections of the well where cores were not available.
- Elastic properties measured in the lab seem to be affected by several factors such as stress, fluid content and frequency of the elastic oscillation in the range 0.1-120Hz, i.e. comparable to that used in seismic investigations in the field. The dependency of the elastic properties upon fluid content measured in the laboratory may be used as a guide to interpret time lapse seismic imaging as monitoring tool, but more experiments would be required to calibrate the response of the rocks under conditions of partial saturation of water and supercritical CO<sub>2</sub>.

The above evaluation indicates favourable conditions in the Wonnerup unit for potential storage of CO<sub>2</sub> and residual trapping as a realistic containment strategy.

Open questions remain as to the characterization of the various lithofacies encountered in the Yalgorup Member: the conditions of the recovered core sections imposed a severe bias in the selection of the core plugs to be analysed in the laboratory towards the sandy layers, as such the results obtained cannot be considered representative of the whole stratigraphic units.

Future efforts should focus on the careful recovery, preservation and laboratory characterization of the clay-rich intervals of the Yalgorup Member and of the overlying Eneabba Formation to assess their geomechanical, elastic and transport properties for a better quantification of their sealing potential and to allow comparison with measurements collected on core plugs from nearby wells (e.g. Pinjarra-1).

Finally, no elements could be identified that suggest postponing or cancelling further investigations around the feasibility of the SW-Hub geosequestration site.





# Appendix A

Sedimentary log of the cored sections of Harvey-1: provided in digital format.

## Appendix B

Sample catalogue of 27 samples with respective name, sample type, sample orientation (H=horizontal, V=vertical), depth and description. Note that not all samples from Harvey-1 are recorded, only those where thin sections were prepared.

Sample No.	Sample Orient.	Core no.	Depth (m)	Description	Facies
206601	H	1	897.63	Very coarse sandstone	Ai
206603	H	1	903.61	Medium to coarse sandstone	B/C
206616	H	1	920.57	Fine to medium sandstone	B
206622	H	1	927.60	Medium to coarse sandstone	Aii
206626	H	2	1266.20	Fine to medium sandstone	D
206627	H	2	1271.95	Very coarse sandstone	Ai
206628	H	2	1273.90	Fine sandstone	D
206635	H	3	1323.94	Very coarse sandstone	Aii
206636	V	3	1324.00	Very coarse sandstone	Aii
206638	H	3	1329.95	V. fine sandstone	E
206642	H	4	1337.40	Medium to coarse sandstone	D
206643	H	4	1342.60	Fine to medium sandstone	D
206644	H	4	1343.75	Fine to medium sandstone	D
206645	H	5	1897.67	X-bedded coarse-gravelly sandstone	Aii
206646	V	5	1898.00	X-bedded coarse-gravelly sandstone	Aii
206647	H	5	1901.61	X-bedded coarse-gravelly sandstone	Aii
206648	V	5	1903.00	X-bedded coarse-gravelly sandstone	Aii
206653	H	5	1916.38	Laminated coarse sandstone	C
206660	H	5	1935.49	Laminated coarse-v. coarse sandstone	Aii
206662	H	5	1940.57	Fine to medium, lam.sandstone	C
206663	H	6	2480.65	X-bedded coarse sandstone	Aii
206664	V	6	2481.00	Coarse sandstone, cross-bedded	Aii
206669	H	6	2491.56	Very coarse sandstone	Aii
206672	H	6	2496.20	X-bedded medium-v. coarse sandstone	Aii
206675	H	6	2503.47	X-bedded coarse-gravelly sandstone	Aii
206683	V	6	2516.00	X-bedded, fine-coarse sandstone	Aiii
206688	H	6	2525.82	X-bedded coarse-v. coarse sandstone	Aii

## Appendix C

Catalogue of optical photomicrographs: polished thin sections were made from 25 selected samples from Harvey-1. Transmitted plane polarized and cross polarized light, and reflected plane polarized light images of each of the 25 samples were made using a Zeiss Axio Imager 2. The optical microscope has a moving stage, which captures photographs across the entire thin section and stitches these together. High resolution photomicrographs are taken, which can be converted to lower resolution images, including a scale bar. Note that thin sections contain quartzo-feldspathic grains surrounding the thin section to aid in polishing each thin section down to 30  $\mu\text{m}$ . These are not related to the samples. Photomicrographs are not captioned, instead they show scale bars, sample number, depth and their light mode (Trans. = transmitted light, Ref. = reflected light, PPL = plane-polarized, XPL = cross-polarized).

A complete catalogue of thin section images is provided in digital format.

# Appendix D

X-ray Mineralogy from samples of the Lesueur Sandstone. Values are expressed in weight %. Qtz = quartz; Alb = albite; K-f = k-feldspar; Kao = kaolinite; Cc = calcite; Mg-Cc = high-Mg calcite; Dol = dolomite; Ak = ankerite; Hal = halite; Ber = berthierine; Ill/mus = illite/muscovite; Sm = smectite; Ill-Sm = illite/smectite mixed layers. Samples were prepared and analysed by Geotech Geotechnical Services PTY LTD.

Sample	Z (m)	Qtz	Alb	K-f	Kao	Cc	Mg-Cc	Dol	Ak	Hal	Ber	Ill/mus	Sm	Ill-Sm	
206601	897.63	74		18	8										Lesueur Yalgorup Member
206603	903.62	73		14	10		3								
206609	911.53	82		12	5		1								
206616	920.56	59		23	15		2			1					
206622	927.61	77		15	8		1								
206626	1266.21	51	21	17	4							5	2		
206627	1271.95	62	12	15	4			2				3	2		
206628	1273.89	51	14	21	8			3					3		
206635	1323.93	59	8	25	4							2	2		
206636	1324	70	6	18	3							2	2		
206638	1329.94	38	14	22	7							10	8		
206642	1337.41	58	4	21	6	4						4	4		
206643	1342.6	64		19	6							6		5	
206644	1343.61	61		23	10							4	3		
206645	1897.66	86		9	6										Lesueur Wonnerup Member
206646	1897.91	85		12	3										
206647	1901.61	86		10	4										
206648	1902.92	77		13	8							2			
206653	1916.38	70		14	13		1				2				
206660	1935.5	77		12	7				4						
206662	1940.58	61		17	9						13				
206663	2480.66	75		13	8						4				
206664	2480.91	81		10	5						5				
206669	2491.56	90		8	2										
206672	2496.22	83		9	6						3				
206675	2503.46	86		8	5	1									
206683	2516	82		9	8			1				1			
206688	2525.83	77		13	6			1			2				

# Appendix E

Tabulated porosity and permeability values measured on samples from Harvey-1. Z= depth,  $\phi$  = porosity;  $k_l$  = permeability;  $Hg-\phi$  = porosity from mercury injection experiments.

Z (m)	$\phi$ (%) 5.5 MPa	KI(mD) 5.5 MPa	$\phi$ (%) 29.6 MPa	KI (mD) 29.6 MPa	Hg- $\phi$ (%)	$\phi$ (%) 500 MPa	$\phi$ (%) 2000 MPa	$\phi$ (%) 5000 MPa	KI (md) 3.4 MPa	KI (md) 13.8 MPa	KI (md) 5000 MPa	Formation
897.63	23.60	918.17	nd	nd	22.61							Lesueur Yalgorup Member
903.62	17.64	10.26	17.01	9.02	20.28	18.82	18.26	17.97	11.56	10.33	9.59	
911.53	25.66	nd	nd	nd	24.41							
920.56	19.33	5.15	18.89	4.67	18.44	19.00	18.60	18.29	6.05	5.56	5.21	
927.61	24.33	964.14	22.24	789.52	24.93							
1266.21	17.65	11.40	17.04	8.16	15.66	16.68	15.96	15.45	10.24	7.47	5.57	
1271.95	24.66	nd	nd	nd	21.10							
1273.89	15.01	0.72	14.39	0.41	16.02	13.79	13.24	12.77	1.02	0.67	0.48	
1323.93	18.50	12.40	17.77	8.63	16.43	17.31	16.45	15.93	10.97	7.93	5.94	
1324	18.34	25.83	17.04	17.52	20.43	18.01	16.56	15.61	20.64	15.01	10.76	
1329.94	6.70	<0.01	6.57	<0.01	13.16	7.75	6.98	6.14	0.23	0.09	0.03	
1337.41	10.25	0.07	9.93	<0.01	14.23	10.35	9.59	9.08	0.74	0.35	0.17	
1342.6	nd	nd	nd	nd	11.69	9.04	8.02	7.47	0.75	0.20	0.07	
1343.61	13.24	0.52	12.62	0.07	16.48	13.10	12.42	11.95	0.81	0.49	0.35	
1897.66	15.51	136.82	15.07	128.58	13.62	14.99	14.48	14.24	152.73	147.29	143.05	Lesueur Wonnerup Member
1897.91	16.05	215.01	15.34	194.35	13.28	16.48	15.84	15.55	229.62	208.50	198.79	
1901.61	16.35	578.67	15.86	527.89	16.73	16.25	15.64	15.39	597.28	547.16	525.03	
1902.92	13.92	7.28	13.37	5.89	2.21	13.65	13.10	12.86	8.60	7.04	6.04	
1916.38	10.94	0.44	10.23	<0.01	9.97	10.34	10.11	10.03	0.67	0.52	0.46	
1935.5	16.33	122.38	15.97	111.49	16.38	16.02	15.64	15.52	138.25	131.12	128.21	
1940.58	15.46	0.34	14.22	0.07	11.73	14.99	11.54	11.47	0.85	0.72	0.64	
2480.66	12.90	9.76	12.37	8.73	11.23	12.66	12.36	12.16	10.53	9.57	8.96	
2480.91	11.01	0.68	10.57	0.12	Sample	10.34	10.03	9.82	0.83	0.63	0.56	
2491.56	13.67	343.66	13.13	322.90	12.54	13.15	12.76	12.52	327.28	310.03	298.14	
2496.22	12.47	40.83	12.10	38.13	11.82	11.89	11.56	11.36	47.80	45.93	43.49	
2503.46	13.56	231.44	13.30	216.08	12.34	13.28	12.91	12.70	252.71	243.42	233.81	
2516	13.83	60.40	13.59	55.73	14.21	13.41	13.04	12.83	59.38	55.79	52.36	
2525.83	12.33	5.32	11.86	4.68	9.89	11.77	11.46	11.27	5.65	4.92	4.52	
	Geotech measurements					CSIRO measurements						

# Appendix F

1. Relative permeability data for the primary drainage flood conducted on sample 206647:

CO2 Sat.	Brine Rel Perm.
0.5500	0.0000
0.5388	0.0017
0.5276	0.0034
0.5163	0.0050
0.5051	0.0067
0.4939	0.0084
0.4827	0.0101
0.4714	0.0118
0.4602	0.0136
0.4490	0.0154
0.4378	0.0173
0.4265	0.0193
0.4153	0.0215
0.4041	0.0238
0.3929	0.0262
0.3816	0.0289
0.3704	0.0320
0.3592	0.0353
0.3480	0.0390
0.3367	0.0432
0.3255	0.0480
0.3143	0.0533
0.3031	0.0593
0.2918	0.0661
0.2806	0.0738
0.2694	0.0825
0.2582	0.0923
0.2469	0.1033
0.2357	0.1156
0.2245	0.1294
0.2133	0.1448
0.2020	0.1620
0.1908	0.1811
0.1796	0.2023
0.1684	0.2258
0.1571	0.2517
0.1459	0.2803
0.1347	0.3118
0.1235	0.3463
0.1122	0.3841
0.1010	0.4255
0.0898	0.4706
0.0786	0.5197
0.0673	0.5732
0.0561	0.6312
0.0449	0.6940
0.0337	0.7620
0.0224	0.8355
0.0112	0.9147
0.0000	1.0000

CO2 Sat.	CO2 Rel Perm.
0.5500	0.2230
0.5388	0.2152
0.5276	0.2074
0.5163	0.1999
0.5051	0.1924
0.4939	0.1851
0.4827	0.1779
0.4714	0.1708
0.4602	0.1639
0.4490	0.1571
0.4378	0.1505
0.4265	0.1440
0.4153	0.1376
0.4041	0.1313
0.3929	0.1252
0.3816	0.1192
0.3704	0.1134
0.3592	0.1077
0.3480	0.1021
0.3367	0.0966
0.3255	0.0913
0.3143	0.0862
0.3031	0.0811
0.2918	0.0763
0.2806	0.0715
0.2694	0.0669
0.2582	0.0624
0.2469	0.0581
0.2357	0.0539
0.2245	0.0499
0.2133	0.0459
0.2020	0.0422
0.1908	0.0386
0.1796	0.0351
0.1684	0.0318
0.1571	0.0286
0.1459	0.0255
0.1347	0.0226
0.1235	0.0199
0.1122	0.0173
0.1010	0.0148
0.0898	0.0126
0.0786	0.0104
0.0673	0.0084
0.0561	0.0066
0.0449	0.0050
0.0337	0.0035
0.0224	0.0021
0.0112	0.0010
0.0000	0.0000

2. Relative permeability data for the primary drainage flood conducted on sample 206660:

CO2 Sat.	Brine Rel Perm.
0.5990	0.0000
0.5868	0.0034
0.5746	0.0067
0.5623	0.0101
0.5501	0.0134
0.5379	0.0168
0.5257	0.0201
0.5134	0.0235
0.5012	0.0268
0.4890	0.0302
0.4768	0.0335
0.4645	0.0369
0.4523	0.0402
0.4401	0.0436
0.4279	0.0470
0.4156	0.0503
0.4034	0.0537
0.3912	0.0570
0.3790	0.0604
0.3667	0.0637
0.3545	0.0671
0.3423	0.0704
0.3301	0.0738
0.3178	0.0771
0.3056	0.0805
0.2934	0.0839
0.2812	0.0872
0.2689	0.0906
0.2567	0.0939
0.2445	0.0973
0.2323	0.1006
0.2200	0.1040
0.2078	0.1073
0.1956	0.1107
0.1834	0.1140
0.1711	0.1174
0.1589	0.1208
0.1467	0.1241
0.1345	0.1275
0.1222	0.1308
0.1100	0.1342
0.0978	0.1375
0.0856	0.1409
0.0733	0.1444
0.0611	0.1482
0.0489	0.1536
0.0367	0.1660
0.0244	0.2077
0.0122	0.3685
0.0000	1.0000

CO2 Sat.	CO2 Rel Perm.
0.5990	0.2060
0.5868	0.1895
0.5746	0.1741
0.5623	0.1596
0.5501	0.1461
0.5379	0.1335
0.5257	0.1217
0.5134	0.1107
0.5012	0.1005
0.4890	0.0910
0.4768	0.0822
0.4645	0.0741
0.4523	0.0666
0.4401	0.0597
0.4279	0.0533
0.4156	0.0475
0.4034	0.0422
0.3912	0.0374
0.3790	0.0329
0.3667	0.0290
0.3545	0.0253
0.3423	0.0221
0.3301	0.0192
0.3178	0.0166
0.3056	0.0142
0.2934	0.0122
0.2812	0.0104
0.2689	0.0088
0.2567	0.0074
0.2445	0.0062
0.2323	0.0051
0.2200	0.0042
0.2078	0.0035
0.1956	0.0028
0.1834	0.0023
0.1711	0.0018
0.1589	0.0015
0.1467	0.0012
0.1345	0.0009
0.1222	0.0007
0.1100	0.0006
0.0978	0.0005
0.0856	0.0004
0.0733	0.0003
0.0611	0.0002
0.0489	0.0002
0.0367	0.0001
0.0244	0.0001
0.0122	0.0000
0.0000	0.0000

3. Relative permeability data for the primary drainage flood conducted on sample 206669:

CO2 Sat.	Brine Rel Perm.
0.5835	0.0000
0.5716	0.0010
0.5597	0.0021
0.5478	0.0032
0.5359	0.0043
0.5240	0.0055
0.5121	0.0068
0.5001	0.0082
0.4882	0.0098
0.4763	0.0115
0.4644	0.0136
0.4525	0.0159
0.4406	0.0186
0.4287	0.0217
0.4168	0.0252
0.4049	0.0292
0.3930	0.0338
0.3811	0.0390
0.3692	0.0449
0.3572	0.0515
0.3453	0.0589
0.3334	0.0673
0.3215	0.0766
0.3096	0.0869
0.2977	0.0983
0.2858	0.1109
0.2739	0.1248
0.2620	0.1400
0.2501	0.1566
0.2382	0.1747
0.2263	0.1945
0.2143	0.2159
0.2024	0.2391
0.1905	0.2641
0.1786	0.2911
0.1667	0.3202
0.1548	0.3514
0.1429	0.3849
0.1310	0.4207
0.1191	0.4590
0.1072	0.4998
0.0953	0.5433
0.0834	0.5896
0.0714	0.6387
0.0595	0.6908
0.0476	0.7460
0.0357	0.8044
0.0238	0.8661
0.0119	0.9313
0.0000	1.0000

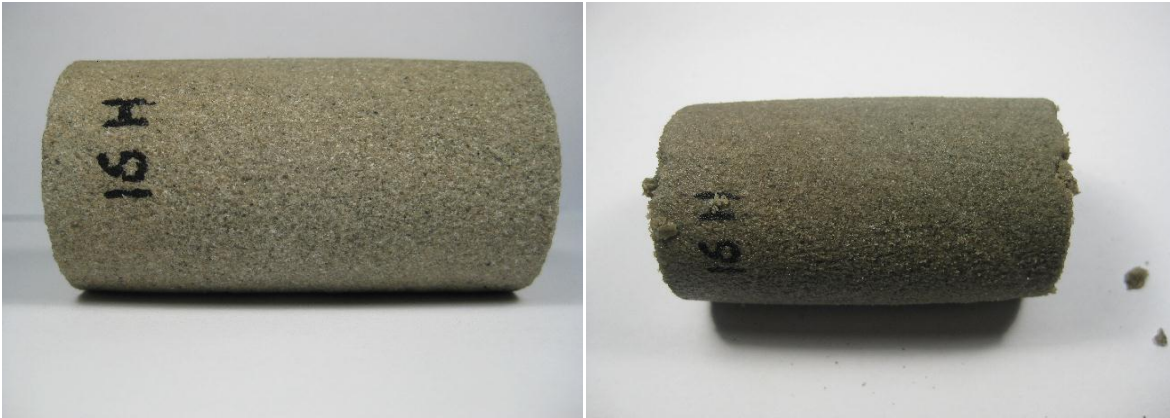
CO2 Sat.	CO2 Rel Perm.
0.58350	0.17200
0.57159	0.15795
0.55968	0.14478
0.54778	0.13247
0.53587	0.12097
0.52396	0.11024
0.51205	0.10025
0.50014	0.09096
0.48824	0.08234
0.47633	0.07436
0.46442	0.06698
0.45251	0.06017
0.44060	0.05390
0.42869	0.04814
0.41679	0.04286
0.40488	0.03803
0.39297	0.03363
0.38106	0.02962
0.36915	0.02599
0.35725	0.02271
0.34534	0.01976
0.33343	0.01710
0.32152	0.01473
0.30961	0.01262
0.29770	0.01075
0.28580	0.00909
0.27389	0.00764
0.26198	0.00638
0.25007	0.00528
0.23816	0.00433
0.22626	0.00352
0.21435	0.00283
0.20244	0.00225
0.19053	0.00177
0.17862	0.00137
0.16671	0.00105
0.15481	0.00079
0.14290	0.00058
0.13099	0.00042
0.11908	0.00030
0.10717	0.00021
0.09527	0.00014
0.08336	0.00010
0.07145	0.00007
0.05954	0.00004
0.04763	0.00003
0.03572	0.00002
0.02382	0.00001
0.01191	0.00001
0.00000	0.00000



## Appendix G

Picture of core plugs tested in multistage triaxial experiments. All samples have diameter of 38mm

### Yalgorup samples



Sample 206616 (920.56m) before (left) and after (right) geomechanical testing



Sample 206628 (1273.89) before (left) and after (right) geomechanical testing



Sample 206635 (1323.93) before (left) and after (right) geomechanical testing



**Sample 206644 (1343.61) before (left) and after (right) geomechanical testing**

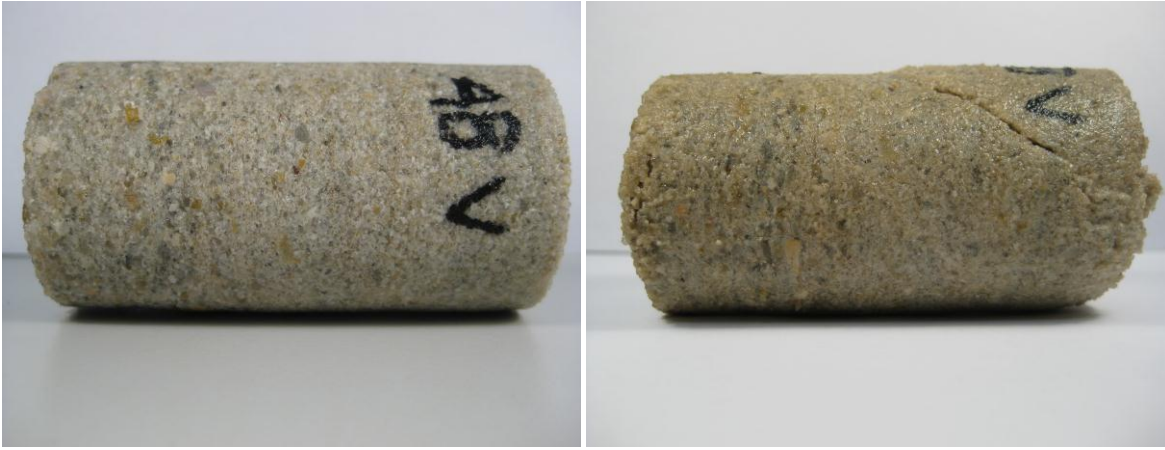
### Wonnerup samples



**Sample 206645 (1897.66) before (left) and after (right) geomechanical testing**



**Sample 206646 (1897.91) before (left) and after (right) geomechanical testing**



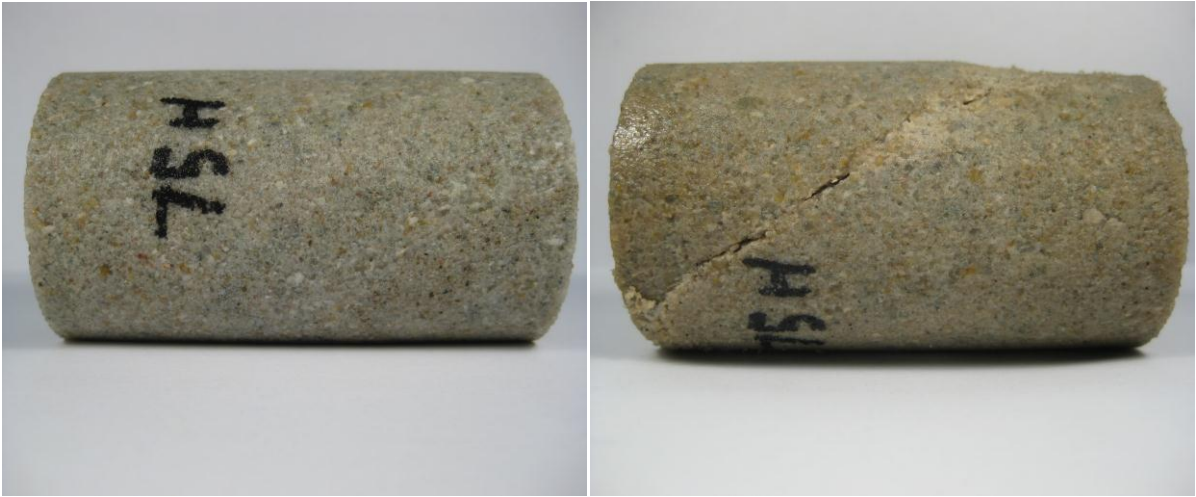
**Sample 206648 (1902.92) before (left) and after (right) geomechanical testing**



**Sample 206662 (1940.58) before (left) and after (right) geomechanical testing**



**Sample 206672 (2496.22) before (left) and after (right) geomechanical testing**



**Sample 206675 (2503.46) before (left) and after (right) geomechanical testing**



**Sample 206683 (2516.00) before (left) and after (right) geomechanical testing**

# References

## Module 1

- Bhattacharyya, A. & Morad, S. 1993. Proterozoic braided ephemeral fluvial deposits: an example from the Dhandraul Sandstone Formation of the Kaimur Group, Son Valley, central India. *Sedimentary Geology* 84(1-4), 101-114.
- Blokhuis, W. A. 1982. Morphology and genesis of vertisols. In: *Vertisols and Rice Soils of the Tropics*, Transactions: 12th International Congress in Soil Science, New Delhi, 23-47.
- Cawood, P. A. & Nemchin, A. A. 2000. Provenance record of a rift basin: U/Pb ages of detrital zircons from the Perth Basin, Western Australia. *Sedimentary Geology* 134(3-4), 209-234.
- Crostella, A. & Backhouse, J. 2000. Geology and petroleum exploration of the central and southern Perth Basin, Western Australia. Western Australia Geological Survey.
- Hjellbakk, A. 1997. Facies and fluvial architecture of a high-energy braided river: the Upper Proterozoic Segloddan Member, Varanger Peninsula, northern Norway. *Sedimentary Geology* 114(1-4), 131-161.
- Jones, D. K. & Nicholls, J. 1966. Pinjarra No.1 Well, Western Australia: Well Completion Report. West Australian Petroleum Pty Limited, Perth.
- McPherson, A. & Jones, A. 2005. Appendix D: Perth Basin geology review and site class assessment. In: *Natural Hazard Risk in Perth, Western Australia* (edited by Jones, T., Middelman, M. & Corby, N.). Geoscience Australia, Canberra, 313-344.
- Miall, A. D. 1996. *The geology of fluvial deposits: sedimentary facies, basin analysis, and petroleum geology*. Springer, New York.
- Mory, A. J. & Iasky, R. P. 1996. Stratigraphy and structure of the onshore Northern Perth Basin, Western Australia. Western Australia Geological Survey.
- Playford, P. E., Cockbain, A. E. & Low, G. H. 1976. *Geology of the Perth Basin, Western Australia*. Geological Survey of Western Australia, Perth.
- Song, T. & Cawood, P. A. 2000. Structural styles in the Perth Basin associated with the Mesozoic break-up of Greater India and Australia. *Tectonophysics* 317(1-2), 55-72.
- Spaargaren, O. C. 1994. *World Reference Base for Soil Resources*, Draft. ISSS-ISRIC-FAO, Rome.
- Timms, N. E., Corbel, S., Olierook, H., Wilkes, P., Delle Piane, C., Sheldon, H., Alix, R., Horowitz, F., Wilson, M., Evans, K. A., Griffiths, C., Stütenbecker, L., Israni, S., Hamilton, P. J., Esteban, L., Cope, P., Evans, C., Pimienta, C., Dyt, C., Huang, X., Hopkins, J. & Champion, D. 2012. A new understanding of the Perth Basin for geothermal exploration. WA Geothermal Centre of Excellence / CSIRO Report, 188.
- Timms, N. E., Olierook, H. K.H., Wilson, M. E.J., Delle Piane, C., Hamilton, P. J., Cope, P. and Stütenbecker, L. Sedimentology, mineralogy and diagenesis of the Mesozoic aquifers of the central Perth Basin. Submitted to *Marine and Petroleum Geology*.
- Wilkes, P., Timms, N. E., Horowitz, F. & Corbel, S. 2011. A new structural interpretation of the Perth Basin and the Perth metropolitan area using gravity and aeromagnetic data, geomorphology and geology. In: *WA Geothermal Centre of Excellence Confidential Report EP 117411*, Perth, 60.

## Module 2

- Cawood, P. A. & Nemchin, A. A. 2000. Provenance record of a rift basin: U/Pb ages of detrital zircons from the Perth Basin, Western Australia. *Sedimentary Geology* 134(3-4), 209-234.
- Fischer, S., Zemke, K., Liebscher, A., Wandrey, M. & CO2SINK Group. 2011. Petrophysical and petrochemical effects of long-term CO<sub>2</sub>-exposure experiments on brine-saturated reservoir sandstone. *Energy Procedia* 4, 4487-4494.
- Folk, R. L. 1965. *Petrology of Sedimentary Rocks*. Hemphill, Austin, Texas.
- Griffiths, C.M., Seyedmehdi, Z., Salles, T., Dyt, C. 2012. Stratigraphic forward modeling for South West Collie Hub: Phase one – static model. Report for ANLEC R&D Targeted Project 129. CSIRO open file report number EP13068.
- Janda, N. B. & Morrison, P. W. 2001. A Methodology for Measuring the Rate of Reaction of CO<sub>2</sub> with Brine-Rock Mixtures. In: *First National Conference on Carbon Sequestration*, Washington D.C., 8.
- Miall, A. D. 1996. *The geology of fluvial deposits: sedimentary facies, basin analysis, and petroleum geology*. Springer, New York.
- Ndlovu, B., Becker, M., Forbes, E., Deglon, D. & Franzidis, J.-P. 2011. The influence of phyllosilicate mineralogy on the rheology of mineral slurries. *Minerals Engineering* 24(12), 1314-1322.
- Selley, R. C. 1988. *Applied Sedimentology*. Academic Press, Cambridge.
- Shao, H., Ray, J. R. & Jun, Y. S. 2010. Dissolution and precipitation of clay minerals under geologic CO<sub>2</sub> sequestration conditions: CO<sub>2</sub>-brine-phlogopite interactions. *Environmental Science & Technology* 44(15), 5999-6005.
- Sircombe, K. N., & Freeman, M. J. 1999. Provenance of detrital zircons on the Western Australia coastline— Implications for the geologic history of the Perth basin and denudation of the Yilgarn craton. *Geology*, 27(10), 879-882.
- Song, T. & Cawood, P. A. 2000. Structural styles in the Perth Basin associated with the Mesozoic break-up of Greater India and Australia. *Tectonophysics* 317(1-2), 55-72.
- Stalker, L., Noble, R., Gray, D., Trefry, C., Varma, S., Ross, A., Sestak, S., Armand, S, Gong, S. 2013. Geochemical characterisation of gases, fluids and rocks in the Harvey-1 data well. CSIRO Report Number EP135208
- Summers, D., Lewis, M., Ostendorf, B. & Chittleborough, D. 2011. Visible near-infrared reflectance spectroscopy as a predictive indicator of soil properties. *Ecological Indicators* 11(1), 123-131.
- Tada, R. & Siever, R. 1989. Pressure solution during diagenesis. *Annual Reviews of Earth and Planetary Sciences* 17, 89-118.
- Timms, N., Corbel, C., Olierook, H., Wilkes, P., Delle Piane, C., Sheldon, H., Alix, R., Horowitz, F., Wilson, M., Evans, K., Griffiths, C., Stütenbecker, L., Israni, S., Hamilton, J., Esteban, L., Cope, P., Evans, C., Pimienta, L., Dyt, C., Huang, X., Hopkins, J., and Champion, D., 2012, Perth Basin Geomodel. Final Report of Project 2, Perth Basin Assessments Program, WAGCoE Report EP122443.
- Wilkinson, M., Haszeldine, R. S., Fallick, A. E., Odling, N. E., Stoker, S. J. & Gatliff, R. W. 2009. CO<sub>2</sub> - Mineral reaction in a natural analogue for CO<sub>2</sub> storage - implications for modelling. *Journal of Sedimentary Research* 79(7), 486-494.

## Module 4a

- Bernabe, Y., 1992. On the measurement of permeability in anisotropic rocks, in Coussy, O., Ed., *Fault mechanics and transport properties of rocks*: Academic Press, 147–167.
- Clennell, M. B.; Dewhurst, D. N.; Siggins, A. Raven, M. D., 2006. Shale Petrophysics: Electrical, dielectric and Nuclear Magnetic Resonance studies of shales and clays. *Transactions, SPWLA 47<sup>th</sup> Annual Logging Symposium*, June 4-7, paper KK, 13pp.
- Coates, G. R., Marschall, D., Mardon, D., Galford, J., 1998. "A new characterization of bulk-volume irreducible using magnetic resonance," *The Log Analysts*, 39, pp. 51-63.
- Dunn, K. J., Bergman, D. J., & LaTorraca, G. A. (Eds.). 2002. *Nuclear magnetic resonance: Petrophysical and logging applications* (Vol. 32). Pergamon.
- Grunewald, E., & Knight, R. 2011. A laboratory study of NMR relaxation times in unconsolidated heterogeneous sediments. *Geophysics*, 76(4), G73-G83.
- Hounsfield, G.N. 1973. Computerized transverse axial scanning (tomography): Part I. Description of system. *British Journal of Radiology* 46, 1016-1022.
- Jones, S. C. 1972. A rapid accurate unsteady-state Klinkenberg permeameter. *Society of Petroleum Engineers* 12(5), 383-397.
- Jorand, R., Fehr, A., Koch, A., & Clauser, C. 2011. Study of the variation of thermal conductivity with water saturation using nuclear magnetic resonance. *Journal of Geophysical Research*, 116(B8), B08208.
- Josh, M., L. Esteban, C. Delle Piane, J. Sarout, D. N. Dewhurst, and M. B. Clennell. 2012. Laboratory characterisation of shale properties. *Journal of petroleum science & engineering* 88: 107-124.
- Kleinberg, R. L., C. Flaum, D. D. Griffin, P. G. Brewer, G. E. Malby, E. T. Peltzer, and J. P. Yesinowski (2003a), Deep sea NMR: Methane hydrate growth habit in porous media and its relationship to hydraulic permeability, deposit accumulation, and submarine slope stability, *J. Geophys. Res.*, 108(B10), 2508, doi:10.1029/2003JB002389.
- Kleinberg, R. L., C. Flaum, C. Straley, P. G. Brewer, G. E. Malby, E. T. Peltzer III, G. Friederich, and J. P. Yesinowski. 2003b, Seafloor nuclear magnetic resonance assay of methane hydrate in sediment and rock, *J. Geophys. Res.*, 108(B3), 2137, doi:10.1029/2001JB000919.
- Walbrecker, J. O., Hertrich, M., & Green, A. G. 2011. Off-resonance effects in surface nuclear magnetic resonance. *Geophysics*, 76(2), G1-G12.
- Wellington, S.L., and Vinegar, H.J. 1987. X-ray computerized tomography. *Journal of Petroleum Technology*. Vol. 39, pp 885-898.

## Module 4b

- Bennion, B., and S. Bachu, 2005, Relative permeability characteristics for supercritical CO<sub>2</sub> displacing water in a variety of potential sequestration zones in the Western Canada sedimentary basin, SPE 95547, The SPE annual technical conference and exhibition, Dallas, Texas, USA, Society of Petroleum Engineers.
- Ennis-King, J., and L. Paterson, 2007, Coupling of geochemical reactions and convective mixing in the long-term geological storage of carbon dioxide: *International Journal of Greenhouse Gas Control*, v. 1, p. 86-93.
- Ennis-King, J., L. Paterson, J. Gale, and Y. Kaya, 2003, Rate of dissolution due to convective mixing in the underground storage of carbon dioxide, *Greenhouse Gas Control Technologies - 6th International Conference*, Kyoto, Japan.
- Grigg, R. B., and R. K. Svec, 2006, CO<sub>2</sub> transport mechanisms in CO<sub>2</sub>/brine coreflooding, SPE 103228, SPE Annual Technical Conference and Exhibition, San Antonio, Texas, USA, Society of Petroleum Engineers.
- Hayatdavoudi, A., and A. Ghalambor, 1996, Controlling Formation Damage Caused by Kaolinite Clay Minerals: Part I, SPE Formation Damage Control Symposium, Lafayette, Louisiana, Copyright 1996, Society of Petroleum Engineers Inc.
- Heaviside, J., and C. J. J. Black, 1983, Fundamentals of relative permeability: experimental and theoretical considerations, SPE 12173, SPE Annual Technical Conference and Exhibition, San Francisco, California, Society of Petroleum Engineers of AIME.
- Izgec, O., B. Demiral, H. Bertin, and S. Akin, 2008, CO<sub>2</sub> injection into saline carbonate aquifer formations I: laboratory investigation *Transport in porous media*, v. 72, p. 1-24.
- Lyons, W. C., and G. J. Plisga, 2005, *Standard Handbook of Petroleum and Natural Gas Engineering*, 2nd edition, Burlington, MA, USA, Gulf Professional Publishing- Elsevier.
- Morris, K. A., and C. M. Shepperd, 1982, The role of clay minerals in influencing porosity and permeability characteristics in the bridport sands of wytch farm, dorset: *Clay Minerals*, v. 17, p. 41-54.
- Musharova, D., I. M. Mohamed, and H. A. Nasr-El-Din, 2012, Detrimental Effect of Temperature on Fines Migration in Sandstone Formations, SPE International Symposium and Exhibition on Formation Damage Control, Lafayette, Louisiana, USA, Society of Petroleum Engineers.
- Perrin, J.-C., and S. M. Benson, 2010, An experimental study on the influence of sub-core scale heterogeneities on CO<sub>2</sub> distribution in reservoir rocks: *Transport in porous media*, v. 82, p. 93-109.
- Priisholm, S., B. L. Nielsen, and O. Haslund, 1987, Fines migration, blocking, and clay swelling of potential geothermal sandstone reservoirs, Denmark: SPE 15199, SPE Formation Evaluation, v. 2, p. 168-178.
- Rapoport, L. A., and W. J. Leas, 1953, Properties of linear waterfloods: SPE 213-G, *Petroleum Transactions, AIME*, v. 198, p. 139-148.
- Saeedi, A., R. Rezaee, B. Evans, and B. Clennell, 2011, Multiphase flow behaviour during CO<sub>2</sub> geo-sequestration: Emphasis on the effect of cyclic CO<sub>2</sub>-brine flooding: *Journal of Petroleum Science and Engineering*, v. 79, p. 65-85.
- Tiab, D., and E. C. Donaldson, 2004, *Petrophysics*: Burlington, Massachusetts, Gulf Professional Publishing, Elsevier.
- [www.globalccsinstitute.com/publications/western-australia-greenhouse-gas-capture-and-storage-tale-two-projects](http://www.globalccsinstitute.com/publications/western-australia-greenhouse-gas-capture-and-storage-tale-two-projects)



## Module 5a

- Birch, F., 1960. The velocity of compressional waves in rocks to 10kbars, *Journal of Geophysical Research*, 65, 1083-1102.
- Castagna, J. P., Batzle, M. L., & Eastwood, R. L. 1985. Relationships between compressional-wave and shear-wave velocities in clastic silicate rocks. *Geophysics*, 50(4), 571-581.
- Castagna, J.P., Batzle, M.L. Kan, T.K.. 1993. Rock physics—the link between rock properties and AVO response ,in: J.P. Castagna, M.M. Backus (Eds.), *Offset-Dependent Reflectivity-Theory and Practice of AVO Analysis, Investigations in Geophysics*, vol. 8, Society of Exploration Geophysicists (1993), pp. 135–171
- Delle Piane, C., Dewhurst, D.N., Siggins, A.F., Raven, M.. 2011. Stress-Induced Anisotropy in Brine Saturated Shale. *Geophysical Journal International*, 184 (vol.2), 897-906.
- Dewhurst, D.N. & Siggins, A.F., 2006. Impact of fabric, microcracks and stress field on shale anisotropy, *Geophysics Journal International*, 165, 135-148.
- Fjaer, E., Holt, R.M., Horsrud, P., Raaen, A.M. & Risnes, R., 1992. *Petroleum Related Rock Mechanics*, edn, Vol. 33, pp. Pages, Elsevier, Amsterdam.
- Freyburg, E. (1972). Der Untere und mittlere Buntsandstein SW-Thuringen in seinen gesteintechnischen Eigenschaften. *Ber. Dte. Ges. Geol. Wiss. A; Berlin*, 176, 911-919.
- Gassmann, F., 1951, Über die Elastizität poröser Medien. *Veri der nature Gesellschaft Zurich*, 96, 1-23.
- Han, D. H., Nur, A., & Morgan, D. 1986. Effects of porosity and clay content on wave velocities in sandstones. *Geophysics*, 51(11), 2093-2107.
- Langhi, L., Ciftci, B., Strand, J. 2013. Fault seal first-order analysis –SW Hub. CSIRO Report number EP13879.
- Lashkaripour, G.R., Dusseault, M.D. 1993. A statistical study of shale properties: relationships among principal shale properties. In: Li, K.S., Lo, S.-C.R. (eds). *Probabilistic methods in geotechnical engineering*. Balkema, pp. 195-200.
- Mavko, G., and A. Nur, 1975, Melt squirt in the asthenosphere: *Journal of Geophysical Research*, 80, 1444–1448
- Mavko, G., Mukerji, T., & Dvorkin, J. 2009. *The rock physics handbook: Tools for seismic analysis in porous media*. Cambridge University Press.
- Nauroy, J. F. (2011). *Geomechanics applied to the petroleum industry*. Editions TECHNIP.
- Plumb, R. A. (1994). Influence of composition and texture on the failure properties of clastic rocks. *Rock Mechanics in Petroleum Engineering*.
- Wang, H. F. 2000. *Theory of linear poroelasticity with applications to geomechanics and hydrogeology*. Princeton university Press 287 pp.
- Zoback, M. D. (2010). *Reservoir geomechanics*. Cambridge University Press.

## Module 5b

- Batzle, M.L., D.-H. Han, and J. Castagna, 1999, Fluids and frequency dependent seismic velocity of rocks. *69th Annual International Meeting, SEG, Expanded Abstracts*, 5-8.
- Batzle, M.L., D.-H. Han, and R. Hofmann, 2006, Fluid mobility and frequency-dependent seismic velocity - direct measurements. *Geophysics*, 71, N1-N9.
- Mavko, G., & Nur, A., 1975. Melt squirt in the asthenosphere. *Journal of Geophysical Research*, 80(11), 1444-1448.
- Mikhailsevitch, V., Lebedev, M. and Gurevich, B., 2011, A low-frequency laboratory apparatus for measuring elastic and anelastic properties of rocks. *2011 SEG Annual Meeting, San Antonio, Texas*, 2256-2260.
- Mikhailsevitch, V., Lebedev, M. and Gurevich, B., 2012, An experimental study of low-frequency wave dispersion and attenuation in water saturated sandstone. *74th EAGE Conference & Exhibition, Extended Abstracts*, P315.
- Paffenholz, J., and H. Burkhardt, 1989, Absorption and modulus measurements in the seismic frequency and strain range on partially saturated sedimentary rocks. *J. Geophys. Res.*, 94, 9493-9507.
- Spencer, J. W., 1981, Stress relaxation at low frequencies in fluid-saturated rocks: Attenuation and modulus dispersion. *J. Geophys. Res.*, 86, 1803-1812.



#### CONTACT US

**t** 1300 363 400  
+61 3 9545 2176  
**e** [enquiries@csiro.au](mailto:enquiries@csiro.au)  
**w** [www.csiro.au](http://www.csiro.au)

#### YOUR CSIRO

Australia is founding its future on science and innovation. Its national science agency, CSIRO, is a powerhouse of ideas, technologies and skills for building prosperity, growth, health and sustainability. It serves governments, industries, business and communities across the nation.

#### FOR FURTHER INFORMATION

**CSIRO Earth Science and Resource Engineering/Rock Properties Group**

Claudio Delle Piane

**t** +61 8 6436 8716  
**e** [Claudio.dellepiane@csiro.au](mailto:Claudio.dellepiane@csiro.au)